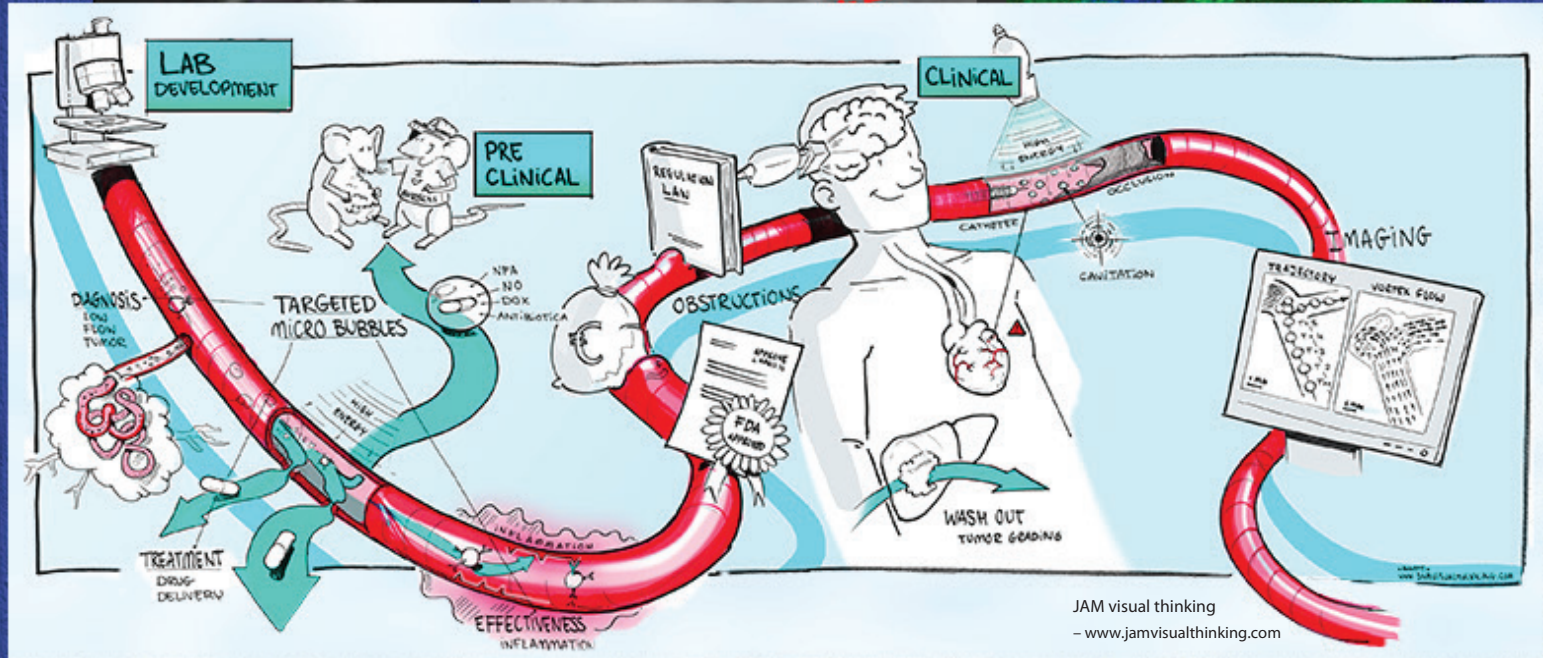
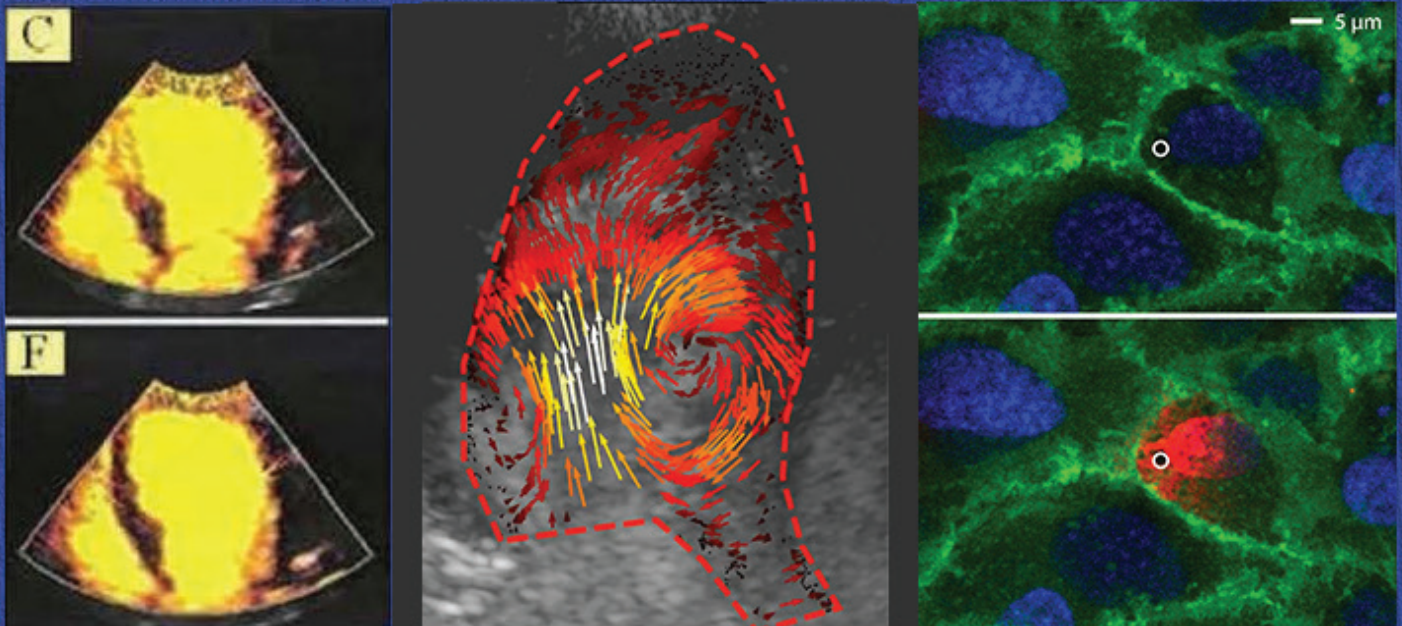


# The 27<sup>th</sup> European Symposium on Ultrasound Contrast Imaging

- An ICUS-Endorsed Conference -



## Abstract book

20-21 January 2022, Online

Organised by Klazina Kooiman, Rik Vos, Annemien van den Bosch,  
Folkert ten Cate, and Nico de Jong  
Erasmus MC Rotterdam

# 27th EUROPEAN SYMPOSIUM ON ULTRASOUND CONTRAST IMAGING

January 20&21 2022 - Online



## 27th EUROPEAN SYMPOSIUM Program

### WEDNESDAY, 19 January 2022

19.00 CET Lobby will be open – Zoom Events

### THURSDAY, 20 January 2022

14.00 – 14.10 CET	Welcome by the chairs	
14.10 – 15.05 CET	CLINICAL IMAGING.....	Chair: Rik Vos/Folkert ten Cate
14.10 Mengxing Tang	Fast super-resolution ultrasound .....	1
14.30 Paul Sidhu	Complex Renal Cysts and CEUS: The future for Bosniak Cyst Classification? .....	3
14.50 Sylvain Bodard	Ultrasound Localization Microscopy of the human kidney graft on a clinical ultrasound scanner .....	4
15.05 – 16.05 CET	CLINICAL THERAPY .....	Chair: Annemien van den Bosch
15.05 Tom Porter	Improvement in systolic function following sonothrombolysis applied after emergent percutaneous intervention in anterior ST segment elevation myocardial infarction .....	8
15.25 Sabrina Doelare	Latest Updates on Microbubbles and Ultrasound Accelerated Thrombolysis for Peripheral Arterial Occlusions .....	9
15.45 Kullervo Hynynen	Enhanced delivery of trastuzumab to Her2-positive brain metastases .....	10
16.05 – 16.30 CET	Break	
16.30 – 18.00 CET	PARALLEL ORAL SESSIONS A (Imaging) and B (Biology/Clinical) The best presentation in each session will be awarded with the ESUCI Research Award supported by	
18.00 – 18.15 CET	Break	
18.15 – 19.05 CET	THERAPY: Towards clinical use.....	Chair: Klazina Kooiman
18.15 Triantafyllos Stylianopoulos	Monitoring tumor microenvironment modifications with contrast-enhanced ultrasound and shear wave elastography for optimized immunotherapy responses .....	11
18.35 Jordan Joiner	Low-intensity focused ultrasound enhances αCD40 antitumor effect in murine pancreatic tumors .....	15
18.50 Philip Durham	Reactive Molecule Capture in Intracranial Drug Depots Following Ultrasound Mediated Delivery .....	18
19.05 – 19.10 CET	Adjourn	
19:15 – 20.30 CET	Online Social event	

Organised by: Rik Vos, Klazina Kooiman, Annemien van den Bosch, Folkert ten Cate, Nico de Jong.

Scientific board: Mike Averkiou, Mark Borden, Paolo Colonna, Olivier Couture, Beat Kaufmann, Eleanor Stride.

# 27th EUROPEAN SYMPOSIUM ON ULTRASOUND CONTRAST IMAGING

January 20&21 2022 - Online



## FRIDAY, 21 January 2022

14.00 – 14.05 CET	Welcome by the chairs	
14.05 – 14.55 CET	<b>NANODROPLETS</b> .....	<b>Chair: Klazina Kooiman</b>
14.05	Mark Borden	Engineering Nanodrops for Ultrasound Imaging..... 20
14.25	Sophie Heymans	Acoustic modulation of the degree of superheat enables nanodroplet vaporization by protons at body temperature..... 21
14.40	Yosra Toumia	Ultrasound detection of Carbon-ion dose and range using activatable polymer-shelled perfluorobutane nanodroplets ..... 23
14.55 – 16.25 CET	<b>PARALLEL ORAL SESSIONS C (Technology) and D (Bubble and Droplet Technology)</b> The best presentation in each session will be awarded with the ESUCI Research Award supported by 	
16.25 – 16.45 CET	Break	
16.45 – 17.45 CET	<b>COMPETITION: IMAGING AND/OR TREATMENT OF INFECTIONS</b> ..... <b>Chair: Nico de Jong</b>	
16.45	Joop Kouijzer	Vancomycin-decorated microbubbles for treatment and ultrasound molecular imaging of Staphylococcus aureus biofilms ..... 26
17.00	Gareth LuTheryn	Bactericidal and Anti-biofilm effects of Ultrasound-Responsive Nitric Oxide Microbubbles on Pseudomonas aeruginosa Biofilms 28
17.15	Kirby Lattwein	Ultrasound-activated microbubbles for the treatment of fibrin-based biofilms ..... 32
17.30	Virginie Papadopoulou	Ultrasound-stimulated phase-change contrast agents to eradicate methicillin-resistant Staphylococcus aureus biofilm infections in a diabetic wound model..... 34
17.45 – 18.25 CET	<b>PARALLEL PITCH SESSIONS I &amp; II</b>	
18.25 – 18.35 CET	Break	
18.35 – 19.30 CET	<b>ADVANCED CONTRAST IMAGING</b> ..... <b>Chair: Annemien van den Bosch/Folkert ten Cate</b>	
18.35	Erik Groot Jebbink	High-frame-rate, contrast enhanced, ultrasound for blood flow quantification in patients with vascular disease..... 36
18.55	Guillaume Lajoinie	AI-based Microbubble super-resolution from raw ultrasound data ..... 37
19.15	Olivier Couture	3D transcranial Ultrasound Localization Microscopy for early discrimination between ischemic and hemorrhagic stroke ..... 39
19.30 – 19.40 CET	<b>ANNOUNCEMENT OF WINNERS</b>	
19.40 – 19.45 CET	<b>ADJOURN AND CLOSING</b>	

Organised by: Rik Vos, Klazina Kooiman, Annemien van den Bosch, Folkert ten Cate, Nico de Jong.

Scientific board: Mike Averkiou, Mark Borden, Paolo Colonna, Olivier Couture, Beat Kaufmann, Eleanor Stride.



# 27th EUROPEAN SYMPOSIUM ON ULTRASOUND CONTRAST IMAGING

January 20&21 2022 - Online



Erasmus MC  
ERASMUS  
THORAX CENTRUM

THURSDAY, 20 January 2022

## Parallel oral sessions Thursday

The best presentation in each session will be awarded with the ESUCI Research Award supported by 

### Thursday 16.30-18.00

#### SESSION A: IMAGING

A1) Abderrahmane Aissani	Ultrasound Localization Microscopy of slow-moving microbubbles using Amplitude Modulation on Long Ensembles sequences .....	41
A2) Jair Castillo	Effect of Microbubble and Acoustic Radiation Force Parameters on $\alpha\beta3$ -Microbubble Targeting .....	43
A3) Chuan Chen	The unique second-wave phenomenon in contrast-enhanced ultrasound imaging with nanobubbles .....	46
A4) Peiran Chen	Solid renal cell cancer localization by contrast-ultrasound dispersion imaging .....	49
A5) Antoine Coudert	Transcranial and volumetric ultrasound localization microscopy with diverging waves.....	52
A6) Lance De Koninck	Improved tissue signal suppression through phase segmentation during amplitude modulation with Sonazoid .....	54
A7) Jonah Harmon	Quantitative nonlinear ultrasound localization microscopy .....	58
A8) Baptiste Heiles	3D Nonlinear Sound-Sheet Imaging of Acoustic Biomolecules .....	60
A9) Megan Morris	Super-resolution ultrasound and MRI imaging for monitoring breast tumour response to radiotherapy .....	65
A10) Geraldi Wahyulaksana	Porcine myocardial perfusion imaging with high frame rate contrast schemes .....	67

### Thursday 16.30-18.00

#### SESSION B: BIOLOGICAL / CLINICAL

B1) Matthew Bourn	Microfluidic Vasculature Networks for the Evaluation of Microbubble-Mediated Delivery of Targeted Liposomes .....	70
B2) Grace Conway	Ultrasound-Targeted Microbubble Cavitation Increases Blood Brain Barrier Permeability in an in vitro System.....	74
B3) Soufiane El Kadi	Feasibility of sonothrombolysis in the ambulance for ST-elevation myocardial infarction .....	76
B4) Alexandre Helbert	Sonopermeation improves the therapeutic efficacy of Caelyx in a preclinical chemo-induced breast tumor model .....	78
B5) Bram Meijlink	The OrganoPlate® as vessel-on-a-chip model to investigate microbubble-mediated drug delivery mechanisms .....	80
B6) Anurag Paranjape	Multi-Cellular Human Brain Spheroid Model to Study Sonoporation-Induced Drug Payload Penetration Beyond the Blood-Brain Barrier.....	82
B7) Dawid Przystupski	Application of calcium sonoporation to effective apoptosis induction in gastrointestinal cancer cells.....	84
B8) Sepideh Jahangiri	Ultrasound Targeted Microbubble Cavitation improves aPDL1 Cancer Immunotherapy in a mouse colon adenocarcinoma model.....	86
B9) Simon Michon	Anti-Cancer Provascular Therapy using Ultrasound Microbubbles and Nitrites to Increase Radiotherapy Efficacy.....	89
B10) Davindra Singh	Ultrasound-assisted miR-1 delivery towards the treatment of hypertrophic cardiomyopathy .....	91

Organised by: Rik Vos, Klazina Kooiman, Annemien van den Bosch, Folkert ten Cate, Nico de Jong.

Scientific board: Mike Averkiou, Mark Borden, Paolo Colonna, Olivier Couture, Beat Kaufmann, Eleanor Stride.

# 27th EUROPEAN SYMPOSIUM ON ULTRASOUND CONTRAST IMAGING

January 20&21 2022 - Online



Erasmus MC  
ERASMUS  
THORAX CENTRUM

FRIDAY, 21 January 2022

## Parallel oral sessions Friday

The best presentation in each session will be awarded with the ESUCI Research Award supported by 

### Friday 14.55 – 16.25

#### SESSION C: TECHNOLOGY

C1) Gonzalo Collado-Lara	Proton range verification with superheated droplets: influence of droplet size, concentration, and proton fluence on the range verification precision	93
C2) Hongchen Li	20 Mfps interleaved ultra-high-speed imaging by coupling two Shimadzu HPV-X2 cameras	95
C3) Marianna Horn	Environmental contrast enhanced ultrasound imaging: visualizing perfusion changes in rainbow trout bowel after induction of inflammation	98
C4) Connor Krolak	Evaluation and early detection of hepatocellular carcinoma with quantitative contrast-enhanced ultrasound	102
C5) Alina Kuliesh	A physics-informed simulation framework for ultrasound localization microscopy	105
C6) Shouqiang Li	Delineation of right and left regional ventricular function with selective microvascular enhancement following perfluoroprane droplet activation imaging	109
C7) Agisilaos Matalliotakis	Multiple scattering inside a population of nonlinear oscillating microbubbles excited by a cloud of acoustic point sources	111
C8) Romain Melich	In vivo circulation of fluorescent lipid-coated perfluorocarbon nanodroplets determined using three detection methods	114
C9) Sander Spiekhouf	Acoustical Sizing of Individual Microbubbles using an 'Acoustical Camera'	117
C10) Martin van den Broek	Transient disruption of a blood-brain barrier on-chip using ultrasound and monodisperse microbubbles	121

### Friday 14.55 – 16.25

#### SESSION D: BUBBLE AND DROPLET TECHNOLOGY

D1) Damien Batchelor	The Influence of Nanobubble Size and Stability on In Vitro Ultrasound Mediated Sonoporation	124
D2) Fabio Domenici	Microdroplet-DNA assemblies for tailored coalescing interaction and tumour cells transfection	129
D3) Dragana Dubey	Encoding stimulus-responsiveness into microbubbles through lipid shell crosslinking	133
D4) Una Goncin	Ultrasound molecular imaging using an anti-P-selectin aptamer for imaging bowel inflammation	136
D5) Mohammed Soheb Anwar	Fibrin-Targeted Phase Shift Microbubbles Outperformed Fibrin-Targeted Microbubbles in Microvascular Obstruction Treatment	138
D6) J. Angel Navarro-Becerra	In vivo Pharmacokinetics of Microbubble Volume Dose: A Direct Blood Characterization Study	141
D7) Charlotte Nawijn	Shell characterization of single microbubbles using a novel stress-strain analysis	144
D8) Antoine Presset	First in-vivo metabolomics characterization of acoustically-mediated blood-brain barrier opening	147
D9) Pedro N. Azevedo	Freeze-dried Monodisperse Microbubbles as Ultrasound Contrast Agent	150
D10) Guowei Wang	Ultrasonic Cavitation-Assisted and Acid-Activated Transcytosis of Liposomes for Universal Active Tumor Penetration	153

Organised by: Rik Vos, Klazina Kooiman, Annemien van den Bosch, Folkert ten Cate, Nico de Jong.

Scientific board: Mike Averkiou, Mark Borden, Paolo Colonna, Olivier Couture, Beat Kaufmann, Eleanor Stride.



Erasmus MC  
ERASMUS  
THORAX CENTRUM

# 27th EUROPEAN SYMPOSIUM ON ULTRASOUND CONTRAST IMAGING

January 20&21 2022 - Online



FRIDAY, 21 January 2022

## PARALLEL PITCH SESSIONS I & II

Friday 17.45 – 18.25

### SESSION I - TECHNICAL.....

I.1)	Muhammad Wahab Amjad	Development and Characterization of Nitro-Fatty Acid Microbubbles (NFABs) for the Treatment of Microvascular Obstruction	156
I.2)	Christopher Campbell	Evaluating the Stability of Perfluorocarbon Nanodroplets for Antimicrobial Therapies.....	159
I.3)	Georges Chabouh	Can Ultrasound Contrast Agents swim? .....	162
I.4)	Peiran Chen	Investigating microvascular phantom and case materials for ultrasound perfusion imaging.....	165
I.5)	Gwennou Coupier	Refined models for oscillations of ultrasound contrast agents in the spherical and buckled configurations .....	169
I.6)	Yi Huang	Normalized Singular Spectrum Area Measurement of Simulated Microbubble Signals in a Vessel Phantom.....	171
I.7)	Boudewine Ossenkoppelle	Volumetric Imaging of Microbubbles Using a Sparse Array and Deep Learning based Adaptive Beamforming .....	173
I.8)	Alexis Vivien	Size-Dependence of Microbubble Cavitation Threshold.....	175

Friday 17.45 – 18.25

### SESSION II - BIOLOGICAL / CLINICAL.....

II.1)	James Bezer	Microbubble dynamics in brain microvessels.....	178
II.2)	Christa Brown	Smart biomaterials: Exploiting protein mechanics for ultrasound stimulated drug release .....	179
II.3)	Yanou Engelen	High-intensity focused ultrasound to induce and boost anti-tumor immunity.....	181
II.4)	Stephanie He	Ultrasound-mediated delivery of microRNA-126 to endothelial cells.....	185
II.5)	Melina Mühlenpfordt	Acoustic Cluster Therapy (ACT®) increases blood-brain barrier permeability and enhances accumulation of .....	187
		core-crosslinked polymeric micelles.....	
II.6)	Oliver Pattinson	Ultra-High Speed Quantification of Cell Strain During Cell-Microbubble Interactions .....	189
II.7)	Noboru Sasaki	Ultrasound-assisted intravesical chemotherapy: preliminary safety results in a dog model.....	192
II.8)	Benjamin van Elburg	On the size dependency of sonoporation efficiency: a monodisperse microbubble study .....	194

Organised by: Rik Vos, Klazina Kooiman, Annemien van den Bosch, Folkert ten Cate, Nico de Jong.

Scientific board: Mike Averkiou, Mark Borden, Paolo Colonna, Olivier Couture, Beat Kaufmann, Eleanor Stride.



## Fast super-resolution ultrasound

*Kai Riemer<sup>1</sup>, Matthieu Toulemonde<sup>1</sup>, Marcelo Lerendegui<sup>1</sup>, Peter Weinberg<sup>1</sup>, Chris Dunsby<sup>2</sup>  
Meng-Xing Tang<sup>1</sup>*

<sup>1</sup>*Department of Bioengineering, Imperial College London, London, U.K. [Mengxing.tang@ic.ac.uk](mailto:Mengxing.tang@ic.ac.uk)*

<sup>2</sup>*Department of Physics and Centre for Pathology, Imperial College London, London, U.K.*

Recent advances in super-resolution ultrasound (SRUS) through localisation of microbubble contrast agents (also known as ultrasound localisation microscopy or ULM) have shown that it was able to break the wave diffraction limit and achieve microscopic resolution in imaging microvascular flow in deep tissue in vitro [1-2] and in vivo [3-4]. The technique can not only map microvascular morphology, but also the flow dynamics within these tiny vessels, offering insights into tissue perfusion relevant to a wide range of biomedical applications. Microbubble based SRUS techniques have shown unprecedented vasculature details in vivo, although the lack of control in the agent concentration and the dependence on flow means a compromise has to be made between agent concentration, data acquisition time and SRUS image quality. Higher contrast agent concentration can potentially shorten the acquisition time, but could significantly degrade SRUS image quality when bubble signals starts to overlap and cannot be localised individually. Lower agent concentration would help with high quality localisation and tracking of individual bubbles and result in high image quality, but it would take longer to accumulate sufficient localisations for a similar amount of microvasculature to be covered [5]. Longer acquisition time would also pose extra challenges to tissue motion correction.

A number of studies have attempted to address this challenge through more advanced signal/image processing algorithms for detection, separation and tracking of bubbles in higher concentrations [6-9]. We have recently demonstrated the use of Acoustic Wave Sparsely-Activated Localization Microscopy (AWSALM [10] and fast-AWSALM [11]) to achieve fast SRUS on a cross-tube phantom using phase change nanodroplets. Such nanodroplets enable local microbubble generation and destruction on demand, making real-time SRUS possible. In this study we examine the impact of different fluorocarbon nanodroplet formulations on the vaporisation of the nanodroplets, and demonstrate the feasibility of in vivo sub-second SRUS imaging on a rabbit kidney using AWSALM and fast-AWSALM.

Three different low boiling point fluorocarbon nanodroplets were imaged with an ultrasound research platform and a linear array. Pulsed ultrasound were used to activate, deactivate, and image the intravenously injected contrast agents in the kidney of three New Zealand White rabbits. In AWSALM higher amplitude ultrasound pulses were used for droplets activation/deactivation and lower amplitude ones used for imaging, while in fast-AWSALM the same plane wave pulses were used. All experiments complied with the ASPA 1986 and were approved by the Animal Welfare and Ethical Review Body of ICL. The acquired data were beamformed, clutter filtered, and individual bubble signals localised and tracked.

The results show that we are able to activate and deactivate phase change nanodroplets in vivo achieving contrast on demand with ultrasound mechanical indices (MIs) well below the recommended safety limit, and such activation and deactivation heavily depends on the droplet formulation. We are also able to demonstrate the feasibility of in vivo fast SRUS imaging and velocity mapping of rabbit kidneys using AWSALM, and sub-second SRUS imaging of the kidneys using fast-AWSALM. Remaining challenges in SRUS are also discussed.

## References

- [1]. O. Viessmann, R. Eckersley, K. Christensen-Jeffries, M.-X. Tang, and C. Dunsby, "Acoustic super-resolution with ultrasound and microbubbles," *Physics in Medicine & Biology*, vol. 58, no. 18, p. 6447, 2013.
- [2]. Y. Desailly, O. Couture, M. Fink, and M. Tanter, "Sono-activated ultrasound localization microscopy," *Applied Physics Letters*, vol. 103, no. 17, p. 174107, 2013.
- [3]. K. Christensen-Jeffries, R. J. Browning, M.-X. Tang, C. Dunsby, and R. J. Eckersley, "In vivo acoustic super-resolution and super-resolved velocity mapping using microbubbles," *IEEE Transactions on Medical Imaging*, vol. 34, no. 2, pp. 433–440, 2015.
- [4]. C. Errico, J. Pierre, S. Pezet, Y. Desailly, Z. Lenkei, O. Couture, and M. Tanter, "Ultrafast ultrasound localization microscopy for deep superresolution vascular imaging," *Nature*, vol. 527, no. 7579, pp. 499–502, 2015.
- [5]. Kirsten Christensen-Jeffries, Jemma Brown, Sevan Harput, Ge Zhang, Jiaqi Zhu, Meng-Xing Tang, Christopher Dunsby, Robert J Eckersley, Poisson statistical model of ultrasound super-resolution imaging acquisition time, *IEEE transactions on ultrasonics, ferroelectrics, and frequency control* 66(7), Page1246-1254, 2019
- [6]. T. Opacic, S. Dencks, B. Theek, M. Piepenbrock, D. Ackermann, A. Rix, T. Lammers, E. Stickeler, S. Delorme, G. Schmitz et al., "Motion model ultrasound localization microscopy for preclinical and clinical multiparametric tumor characterization," *Nature communications*, vol. 9, no. 1, pp. 1–13, 2018.
- [7]. A. Bar-Zion, O. Solomon, C. Tremblay-Darveau, D. Adam and Y. C. Eldar, "SUSHI: Sparsity-Based Ultrasound Super-Resolution Hemodynamic Imaging," in *IEEE Transactions on Ultrasonics, Ferroelectrics, and Frequency Control*, vol. 65, no. 12, pp. 2365-2380, Dec. 2018
- [8]. C. Huang, M. R. Lowerison, J. D. Trzasko, A. Manduca, Y. Bresler, S. Tang, P. Gong, U.-W. Lok, P. Song, and S. Chen, "Short acquisition time super-resolution ultrasound microvessel imaging via microbubble separation," *Scientific reports*, vol. 10, no. 1, pp. 1–13, 2020.
- [9]. Ruud JG van Sloun, Oren Solomon, Matthew Bruce, Zin Z Khaing, Hessel Wijkstra, Yonina C Eldar, Massimo Misch, Super-resolution ultrasound localization microscopy through deep learning, *IEEE Transactions on Medical Imaging*, V40(3), Pages 829-839, 2020
- [10]. G. Zhang, S. Harput, S. Lin, K. Christensen-Jeffries, C. H. Leow, J. Brown, C. Dunsby, R. J. Eckersley, and M.-X. Tang, "Acoustic wave sparsely activated localization microscopy (awsalm): Super-resolution ultrasound imaging using acoustic activation and deactivation of nanodroplets," *Applied Physics Letters*, vol. 113, no. 1, p. 014101, 2018.
- [11]. G. Zhang, S. Harput, H. Hu, K. Christensen-Jeffries, J. Zhu, J. Brown, C. H. Leow, R. J. Eckersley, C. Dunsby, and M.-X. Tang, "Fast acoustic wave sparsely activated localization microscopy: Ultrasound super-resolution using plane-wave activation of nanodroplets," *IEEE Transactions on Ultrasonics, Ferroelectrics, and Frequency control*, vol. 66, no. 6, pp. 1039–1046, 2019.

## **Complex Renal Cysts and CEUS: The future for Bosniak Cyst Classification?**

*Paul S. Sidhu*

The CT diagnosis of the complex renal cyst is based on the well-established 'Bosniak Renal Cyst Classification,' stratifying the malignant risk; Grade I is a simple cyst, and Grade IV is almost certainly a malignant tumour that requires surgical management. The confidence in the grading of these complex renal cysts is predominantly based on the enhancement of the complex cyst following the administration of iodinated contrast media during a CT examination. This has been shown to be an adequate method for the analyses and the grading of these cystic lesions. However, ultrasound may be a better choice for the assessment and classification of complex cystic renal tumours. Often ultrasound is the first line investigation that establishes the presence of a complex renal cyst, but previously without contrast media, ultrasound was limited in further assessment. There are inherent capabilities of the addition of ultrasound contrast to the study that gives temporal and spatial improvements in the examination, not attained by a CT examination. The ability to visualise subtle vascularisation in a renal lesion, a possible hallmark of malignancy, may improve on the risk stratification of a complex renal cyst. In addition, the use of contrast in the ultrasound examination may negate the need for downstream costs of a CT examination, and avoids ionising radiation and morbidity associated with the administration of iodinated contrast media. EFSUMB has produced a position statement on this subject, detailing the usefulness of this additional technique and suggests that the classification may need to be altered to accommodate the improvements in identifying vascularisation using ultrasound contrast. Medical practice may need to evolve to accommodate the improved imaging capabilities of contrast enhanced ultrasound of complex renal cysts.

# Ultrasound Localization Microscopy of the human kidney graft on a clinical ultrasound scanner

***Sylvain Bodard<sup>1,2,3\*</sup>, Louise Denis<sup>3\*</sup>, Vincent Hingot<sup>3</sup>, Olivier Hélénon<sup>1+2</sup>, Olivier Couture<sup>2</sup>, Jean-Michel Correas<sup>1+2+3</sup>***

*\* These authors contributed equally to this work*

<sup>1</sup> *Department of Adult Radiology Necker University Hospital (APHP), Paris, France*

<sup>2</sup> *Paris University, Paris, France*

<sup>3</sup> *Sorbonne Université, CNRS, INSERM Laboratoire d'Imagerie Biomédicale, Paris, France*

*Corresponding authors: sylvain.bodard@aphp.fr, louise.denis@sorbonne-universite.fr*

## Introduction

The assessment of the renal microvasculature is a key feature for both diagnosis and prognosis of renal vascular disorders, including chronic kidney [1]. Ultrasound Localization Microscopy (ULM) enables noninvasive and quantitative monitoring of the vasculature for vessels smaller than 0.5 mm, which cannot be achieved with any other non invasive diagnostic tools. This technique simultaneously improves sensitivity and spatial resolution for visualization of the vascular system down to the micrometer scale at several centimeters in depth [2]. High frame-rate ultrasound scanners have been used in clinical studies and have shown promising results [3]; unfortunately these techniques are not yet available for large scale human use [4]. The goal of our study is to investigate the feasibility of renal ULM using a commercially available ultrasound (US) system.

## Methods

Experiments presented in this study were performed on kidney transplant patients at Necker Hospital after validation by an ethic committee. The US examination was performed using the convex abdominal transducer i8CX1 on the Aplio i800 system (Canon MS, Nasu, Japan) with B-mode, Doppler and micro-Doppler techniques followed with Contrast-Enhanced Ultrasound (CEUS) using the convex abdominal probe (harmonic frequency 2.8 MHz). A bolus of 1,2mL of Sonovue® (Bracco) was injected for clinical indication, and specific ULM acquisitions were performed during delayed phase. Acquisitions were divided into blocks of 200 frames each. The depth and the frame rate were optimized (4-11 cm; 14 to 65 Hz). ULM was achieved with classical steps : filtering, localization of microbubbles, tracking with Hungarian algorithm method [5] and accumulation of tracks to form a vascular maps. The regions of interest used to compare velocities between cortex area and large vessels, including arcuate arteries and interlobar arteries, were hand-drawn. A t-test was performed to compare the speeds in the different regions. All the data processing was done with Matlab.

## Results

As we can observe in Figure 1a), interlobar arteries, arcuate arteries, cortical radiate arteries and a bit of medullar organization are visible by ULM density map in each patients. Smaller structures are not clearly identifiable by clinical ULM at low frame rate.

As shown in Figure 1b), directivity maps highlighted cortical radiate veins and arteries more precisely. The medullary arteries and veins can be seen in the first patient, but are less clear in the second one.

Speed maps in Figure 2a) and speed histograms in Figure 2b) indicate significant differences ( $p < 0.01$  with a t-test) between speeds in the cortical area and in the main vessels of the kidney, including interlobar arteries and arcuate arteries. The highest speed that can be detected with the actual frame rate and the ULM parameters has been indicated : velocities above this value should not be taken into account.

## Conclusions

This study shows the feasibility of ULM in human kidney graft with a conventional clinical scanner and simple post processing tools. It also highlighted the significant difference between the cortical area and the main vessels of the kidney with speeds ranges already observed in the literature [3]. Future work will involve a larger number of human subjects and the identification of biomarkers to help in the diagnosis of renal pathologies such as acute and chronic renal failure or renal tumors.

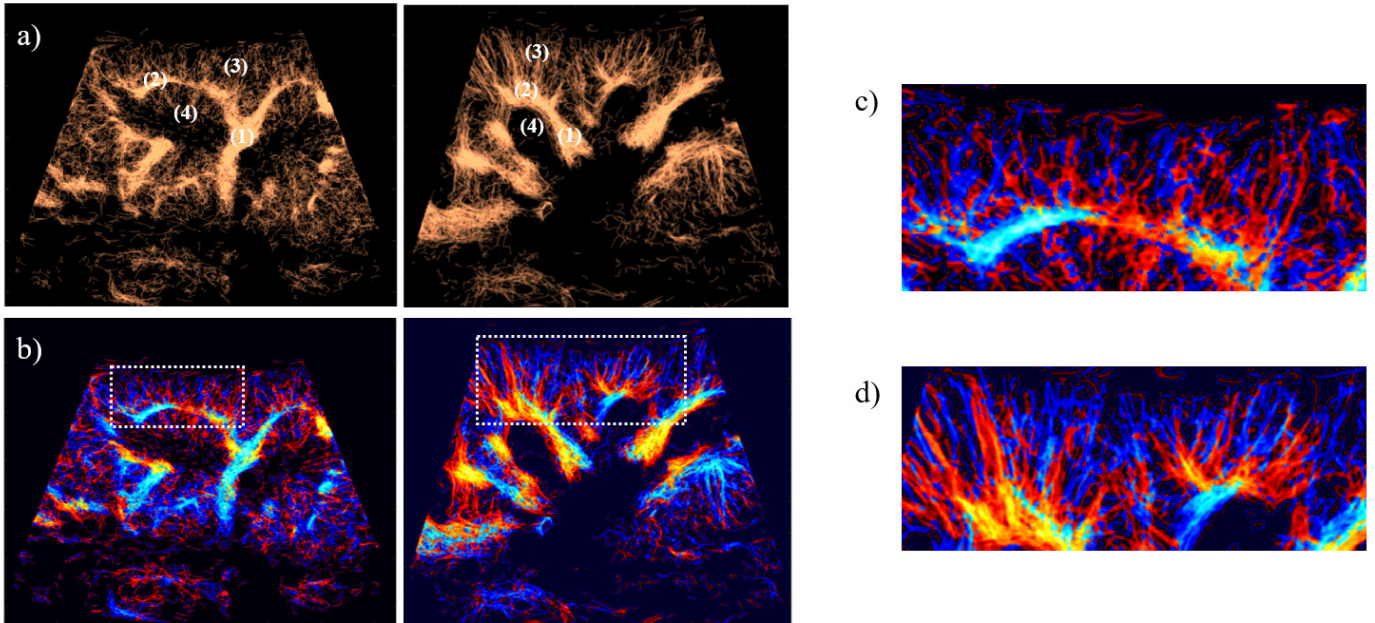


Figure 1. a) ULM density maps in two patients highlight interlobar arteries (1), arcuate arteries (2), cortical radiate arteries (3) and a bit of medullar organization (4)  
b) ULM directivity maps in two patients (with frameworks of the zoomed regions in c) and d))  
c) Close-up of the first patient ULM directivity map  
d) Close-up of the second patient ULM directivity map

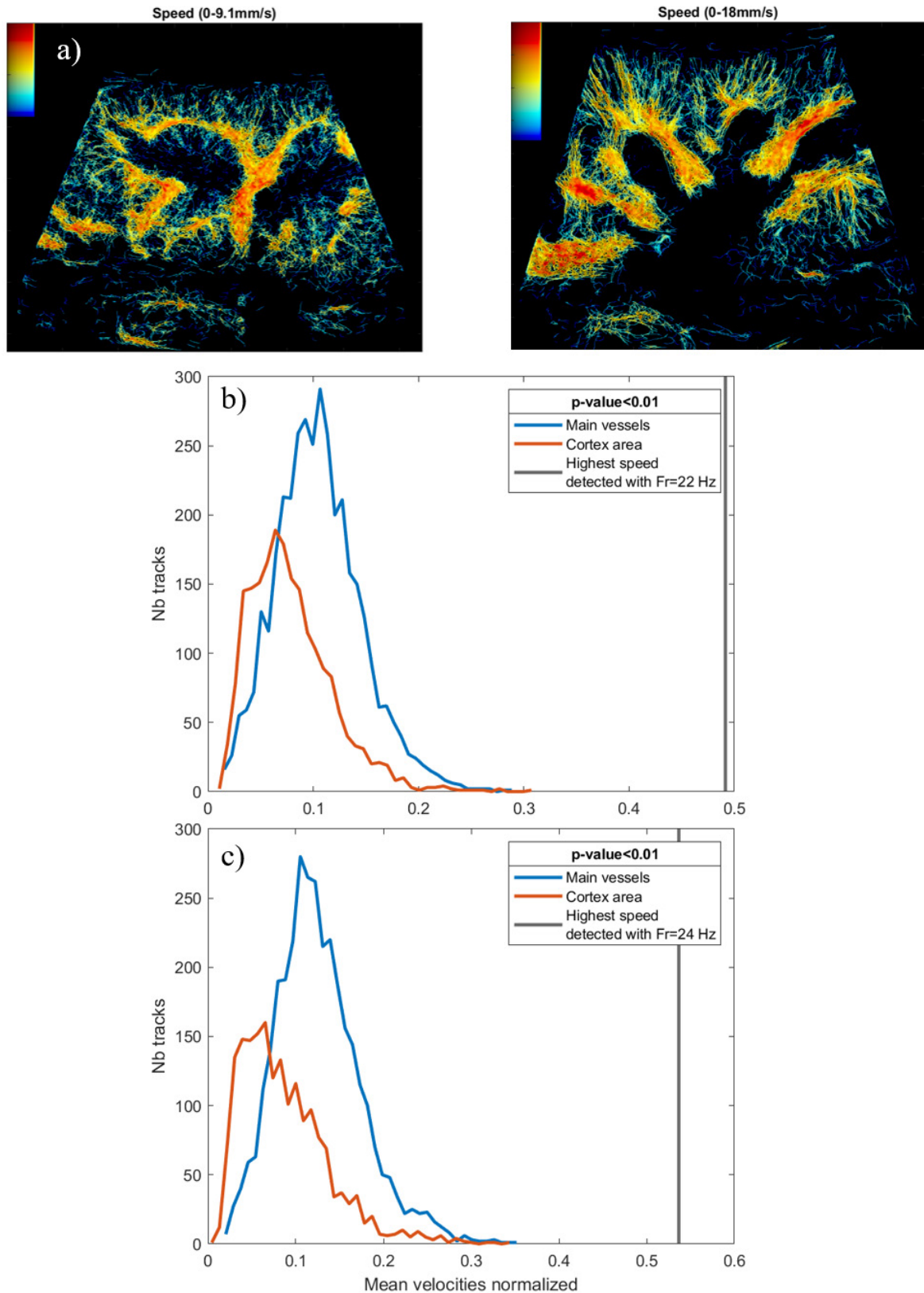


Figure 2. a) ULM speed maps in two patients  
 b) Speed histogram of the first patient.  
 c) Speed histogram of the second patient.

Speed histograms indicate significant differences between the cortical area and the main vessels of the kidney ( $p < 0.01$  with a t-test). Highest speed that can be detected by ULM with the actual frame rate is noted.

### References

- [1]. L Zafrani, C Ince, Microcirculation in Acute and Chronic Kidney Diseases, American Journal of Kidney Diseases, 2015.
- [2]. O Couture, V Hingot, B Heiles, P Muleki-Seya, M Tanter, Ultrasound Localization Microscopy and Super-Resolution: A State of the Art, IEEE Transactions on Ultrasonics, Ferroelectrics, and Frequency Control, Vol 65, No 8, 2018.
- [3]. C Huang, W Zhang, P Gong, U-W Lok, S Tang, T Yin, X Zhang, L Zhu, M Sang, P Song, R Zheng, S Chen, Super-Resolution Ultrasound Localization Microscopy Based on a High Frame-rate Clinical Ultrasound Scanner: An Inhuman Feasibility Study, Physics in Medicine & Biology, Volume 66, No 8, 2021.
- [4]. T Opacic, S Dencks, B Theek, M Piepenbrock, D Ackermann, A Rix, T Lammers, E Stickeler, S Delorme, G Schmitz, F Kiessling, Motion model ultrasound localization microscopy for preclinical and clinical multiparametric tumor characterization, Nature Communication, Vol 9, 2018.
- [5]. J-Y Tinevez, simpletracker (<https://github.com/tinevez/simpletracker>), GitHub, 2019.

## Improvement in systolic function following sonothrombolysis applied after emergent percutaneous intervention in anterior ST segment elevation myocardial infarction

*Thomas Richard Porter, Ping Zeng, Feng Xie, Shouqiang Li, Joan Olson, Yiannis Chatzizisis, Andrew Goldsweig, David Barton, Poonam Velagapudi, Arif Albulushi, John Higgins*  
*University of Nebraska Medical Center, Omaha, NE, USA*

### **Background:**

Microvascular obstruction (MVO) and stunning result in significant left ventricular systolic dysfunction following emergent percutaneous coronary intervention (PCI) in left anterior descending (LAD) ST segment elevation myocardial infarction (STEMI). Diagnostic ultrasound (DUS) mediated high mechanical index (MI) impulses may reduce MVO during a microbubble infusion. The high MI short pulse duration impulses may have a shear effect on the endothelium and red blood cells that alter coronary and microvascular flow. We hypothesized that the improvement in microvascular flow induced by sonothrombolysis may have a long term effect on systolic function (LVEF).

### **Methods:**

Thirty-nine acute anterior STEMI patients who received emergent PCI of the LAD underwent diagnostic real time myocardial contrast echo within two hours of completion of the PCI. All patients had TIMI 2-3 flow in the infarct vessel post PCI. Patients were randomized to low MI (<0.2) imaging only during a 20 minute commercially available enhancing agent infusion (3% Definity), or to low MI imaging with repeated high MI impulses (1.1 MI) in the apical (4, 2, 3) chamber views guided by replenishment. Gadolinium enhanced magnetic resonance imaging (MRI) was performed at two intervals (three days and 6-8 weeks post PCI) to assess for microvascular obstruction (MVO), infarct size, and LVEF.

### **Results:**

During the randomized treatment, the segmental extent of MVO decreased in the intermittent high MI group ( $5.0 \pm 2.5$  pre treatment to  $4.1 \pm 2.7$  post treatment;  $p=0.05$ ) but no significant change occurred in the low MI only group. However, at three days post PCI, infarct size and extent of MVO (as a percent of LV mass) were not significantly different between low MI only and intermittent high MI groups. LVEF at 3 days was not different as well ( $44 \pm 11\%$  low MI only and  $43 \pm 10\%$  intermittent high MI). However MRI at 8 weeks post PCI demonstrated a significant increase in LVEF in the intermittent high MI group ( $50 \pm 12\%$ ;  $p=0.001$ ) while no change in LVEF occurred in the low MI only group ( $45 \pm 12\%$ ).

### **Conclusion:**

A 20 minute application of sonothrombolysis immediately post PCI in acute LAD STEMI results in a reduction in MVO that ultimately results in a sustained improvement in systolic function at two month follow up. Microvascular sonothrombolysis may be an important adjunctive treatment to reduce MVO and improve systolic function following anterior wall STEMI.

## Latest Updates on Microbubbles and Ultrasound Accelerated Thrombolysis for Peripheral Arterial Occlusions

***Kak K. Yeung<sup>1,2</sup>, Sabrina A.N. Doelare<sup>1,2</sup>, Dayanara M. Jean Pierre<sup>1</sup>, Johanna H. Nederhoed<sup>1</sup>, Stefan P.M. Smorenburg<sup>1</sup>, Rutger J. Lely<sup>3</sup>, Vincent Jongkind<sup>1,4</sup>, Arjan W.J. Hoksbergen<sup>1</sup>, Harm P. Ebben<sup>1,2</sup> and MUST collaborators***

<sup>1</sup>*Department of Surgery, Amsterdam University Medical Centers (AMC), Amsterdam, The Netherlands*

<sup>2</sup>*Department of Physiology, Amsterdam University Medical Centers (VUmc), Amsterdam, The Netherlands*

<sup>3</sup>*Department of Radiology, Amsterdam University Medical Centers (AMC), Amsterdam, The Netherlands*

<sup>4</sup>*Department of Surgery, Dijklander Hospital, Hoorn, The Netherlands*

Corresponding author: [k.yeung@amsterdamumc.nl](mailto:k.yeung@amsterdamumc.nl)

### Introduction

Catheter-directed thrombolysis (CDT) for acute peripheral arterial occlusion is time consuming and still accompanied by the risk of major hemorrhages [1]. Contrast-enhanced sonothrombolysis (CEST) might enhance outcomes compared with standard CDT by improvement of thrombus susceptibility to thrombolytic agents [2]. This article reports the clinical outcomes of the safety and feasibility of this novel technique.

### Methods

In this single arm phase II trial, 20 patients with acute lower limb ischaemia received CDT combined with an intravenous infusion of microbubbles and locally applied ultrasound during the first hour of standard intra-arterial thrombolytic therapy. The primary endpoint was safety, i.e., occurrence of serious adverse events (haemorrhagic complications and/or amputation) and death within one year. Secondary endpoints included angiographic and clinical success, thrombolysis duration, additional interventions, conversion, and quality of life.

### Results

The study included 20 patients (16 men; median age 68.0 years; range, 50.0 – 83.0; and 40% native artery and 60% bypass graft). In all patients, the use of microbubble contrast enhanced sonothrombolysis could be applied successfully. There were no serious adverse events related to the experimental treatment. Duplex examination showed flow distal from the occlusion after 23.1 hours (range 3.1 – 46.5) with a median thrombolysis time of 47.5 hours (range 6.0 – 81.0). The short term ABI and pain scores significantly improved; however, no changes were observed before or after thrombolysis in the microcirculation. Overall mortality and amputation rates were both 2% within one year. The one year patency rate was 55%.

### Conclusions

Treatment of patients with acute peripheral arterial occlusions with contrast enhanced sonothrombolysis is feasible and safe to perform in patients. Further research is necessary to investigate the superiority of this new treatment over standard treatment.

### References

- [1]. Ebben HP, Jongkind V, Wisselink W, Hoksbergen AWJ, Yeung KK, Catheter directed thrombolysis protocols for peripheral arterial occlusions: a systematic review 2019, *Eur J Vasc Endovasc Surg*, 57: 667-675, 2019
- [2]. Tachibana K, Enhancement of fibrinolysis with ultrasound energy 1992, *J Vasc Interv Radiol*, 3: 299-303, 1992

# Enhanced delivery of trastuzumab to Her2-positive brain metastases

Kullervo Hynynen

*Department of Medical Biophysics, University of Toronto and Sunnybrook Research Institute, Toronto, Ontario, Canada. email: khynynen@sri.utoronto.ca*

Local modulation of the Blood-Brain barrier (BBB) using focused ultrasound (FUS) has been explored for targeted drug delivery into the brain in animal models and is now in clinical testing. One of the most interesting treatments is to enhance the delivery of molecularly targeted therapeutic delivery into the brain. One of such therapeutics is trastuzumab that has been shown to increase survival of patients with human epidermal growth factor receptor 2 (Her2)-positive breast cancer. However, incidence of brain metastases has increased in this patient population presumably because the large molecular size of the drug prevents its penetration through the BBB and the Blood-Tumor barrier (BTB). The first preclinical studies demonstrated both increase in the amount of trastuzumab in the tumours and survival<sup>1</sup>. Over the past few years our clinical team has explored the feasibility of taking this therapy into clinical testing and to quantify the increased drug delivery into the tumours.<sup>2</sup> In this study we used the MRI-guided InSightec Exablate Neuro 4000 type 2 220kHz device with microbubbles (Definity; Lantheus, North Billerica, MA, USA) infused intravenously via a saline bag gravity drip at an infusion rate of 4  $\mu\text{L}/\text{kg}$  per 5 min (up to a max of 150 $\mu\text{L}/\text{kg}$ ). Each target location was sonicated with 10 ms bursts repeated once every second (1% duty cycle), for a total duration of 2 minutes. The operator could draw an arbitrary-shaped grid up to 32 spots that were sonicated sequentially during the 1 s duty cycle. Multiple grids were used to cover the tumour volume. The effect of FUS BBB modulation on the delivery of trastuzumab in the brain was measured through SPECT imaging with <sup>111</sup>In-BzDTPA-NLS-trastuzumab. Each study consisted of one <sup>111</sup>In-BzDTPA-NLS-trastuzumab injection (111 MBq; 5 mg) followed by at 4 hours and 48 hours a SPECT scan to quantify the drug delivery. The potential adverse events were monitored via standard T2-, T2\*-weighted, and non-contrast enhanced and contrast-enhanced T1-weighted sequences acquired within an hour of and at 18 to 24 hours after the sonications.

A total of twenty treatments in four patients demonstrated an average increase of the standardized uptake value ratio (SUVR) of 101 $\pm$ 17% and up to 450% increase in some voxels. There were significant heterogeneity in the drug concentration from location to location. Although the small number of tumours makes it difficult to conclude much on tumour response, the targeted tumors appeared either stable or reduced in size on the last follow-up MRI scans relative to baseline<sup>2</sup>

The results are promising demonstrating significant increase in drug concentration in the targeted tissue volume without major adverse events. Therefore, larger studies are justified to establish the treatment impact on the tumor progressions and patient survival.

## References

- [1]. Kinoshita, M.; McDannold, N.; Jolesz, F. A.; Hynynen, K., Noninvasive localized delivery of Herceptin to the mouse brain by MRI-guided focused ultrasound-induced blood-brain barrier disruption. *Proc Natl Acad Sci U. S. A* 2006, 103 (31), 11719-11723.
- [2]. Meng, Y.; Reilly, R. M.; Pezo, R. C.; Trudeau, M.; Sahgal, A.; Singnurkar, A.; Perry, J.; Myrehaug, S.; Pople, C. B.; Davidson, B.; Llinas, M.; Hyen, C.; Huang, Y.; Hamani, C.; Suppiah, S.; Hynynen, K.; Lipsman, N., MR-guided focused ultrasound enhances delivery of trastuzumab to Her2-positive brain metastases. *Sci Transl Med* 2021, 13 (615), eabj4011.

# Monitoring tumor microenvironment modifications with contrast-enhanced ultrasound and shear wave elastography for optimized immunotherapy responses

*Triantafyllos Stylianopoulos<sup>1</sup>*

<sup>1</sup>Cancer Biophysics Laboratory, Department of Mechanical and Manufacturing Engineering, University of Cyprus, Nicosia, Cyprus

<sup>2</sup>Department of Bioengineering, University of Washington, Seattle, USA  
Corresponding author: [tstylian@ucy.ac.cy](mailto:tstylian@ucy.ac.cy)

## Introduction

Immunotherapy has revolutionized the treatment of multiple cancers and has already become a standard of care for some tumor types. However, a majority of patients do not benefit from current immunotherapeutics and many develop severe toxicities. Therefore, the identification of strategies to optimize immunotherapy is a timely task. Biomechanical aspects of the tumor microenvironment mediate resistance to immunotherapy [1]. Specifically, many tumors stiffen as they grow and also, tumor growth within the host tissue generates mechanical forces, termed solid stress. Tumor stiffening and solid stress can compress intratumoral blood vessels, causing hypo-perfusion and hypoxia. Systemic administration of immunotherapeutics requires a well-perfused vasculature, whereas hypo-perfusion and hypoxia promote immunosuppression, helping cancer cells to evade immune responses (Figure 1). Contrast enhanced ultrasound (CEUS) and shear wave elastography (SWE) can be used to monitor changes in tumor perfusion and specific measures of CEUS and SWE could be considered as potential markers of tumor response. To test this hypothesis we performed experiments in tumor-bearing mice.

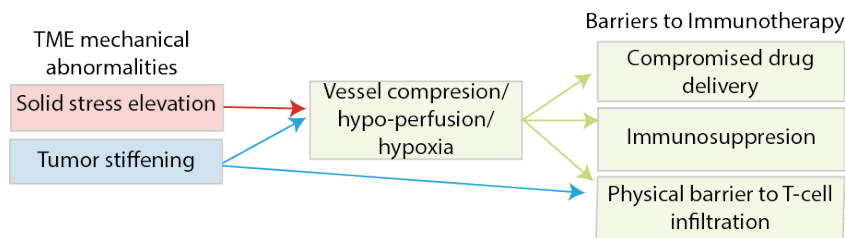


Figure 1. Tumor stiffening and solid stress elevation are two distinct mechanical abnormalities of the tumor microenvironment (TME) that induce hypo-perfusion and hypoxia, posing barriers to immunotherapy. SWE and CEUS are two clinically applied methods that could be used to monitor tumor stiffness and perfusion in order to predict tumor response to immunotherapy and to lead to patient-specific therapies.

## Methods

**Tumor model:** Orthotopic murine models of breast tumors were generated by implantation of 4T1 cells into the mammary fat pad of 6-8week-old BALB/c female mice. **Treatment Protocol:** When tumors reached an average size of 150mm<sup>3</sup> treatment with Doxil was initiated. Three different treatment schedules of Doxil were employed to investigate its effect on reducing stiffness and improving perfusion in the tumors: i) 1mg/kg (daily for six days), ii) 2mg/kg (every other day) and iii) 6mg/kg (once a week). All treatments were administered intravenously and consisted of two cycles. For the first cycle we intended to observe whether low but more frequent doses of Doxil can induce stiffness and perfusion changes. For the second cycle of treatment, an immune checkpoint inhibitor (anti-PD-L1) was added to the treatment regimen. The anti-PD-L1 antibody was administered at 10mg/kg every 3 days alone or in combination with Doxil.

Tumor stiffness and perfusion monitoring: We performed ultrasound measurements i) before the initiation of any treatment, ii) before the initiation of the second cycle of Doxil and the first dose of anti-PD-L1 and iii) at the end of all treatment protocol.

Dynamic contrast-enhanced ultrasound. Tumor perfusion was assessed with DCEUS on a Philips EPIQ Elite scanner and with the L12-5 transducer [3,4]. Image analysis was performed offline using Philips' quantification software (QLAB, Phillips Medical Systems). From the produced time intensity curves, we used as measures of perfusion the wash in slope and time to peak. SWE was employed on the same Philips EPIQ Elite system using a linear array transducer (eL18-4), according to previous research [5].

## Results

The experimental data are summarized in Figure 2. We observe that the two lower and more frequent doses of Doxil can reduce stiffness (data not shown) and improve perfusion effectively, while the highest but least frequent dose of the nanomedicine can still cause effects but not as prominent as the other two doses. The average elastic modulus of the control tumors increased from 38kPa at the initiation of the treatments to 65kPa at the end of the experimental protocol. The groups that were treated with the two more frequent but lower doses of Doxil, had an average elastic modulus decrease from 40kPa to 20kPa (1mg/kg group) and 26 kPa (2mg/kg group). We further observed an increase in the perfusion measures, and particularly a significant increase in the slope of the wash in part of the time intensity curve and the time to peak.

The addition of the anti-PDL1 immune checkpoint inhibitor did not have any anti-tumor effects when it was administered as a single agent. However, anti-PDL1 caused a significant tumor regression when it was combined with Doxil for the groups that exhibited the highest perfusion rates (i.e, 1mg/kg and 2mg/kg Doxil), whereas anti-tumor effects were less dominant but still statistically significant compared to the control group for the 6mg/kg Doxil group (Figure 3).

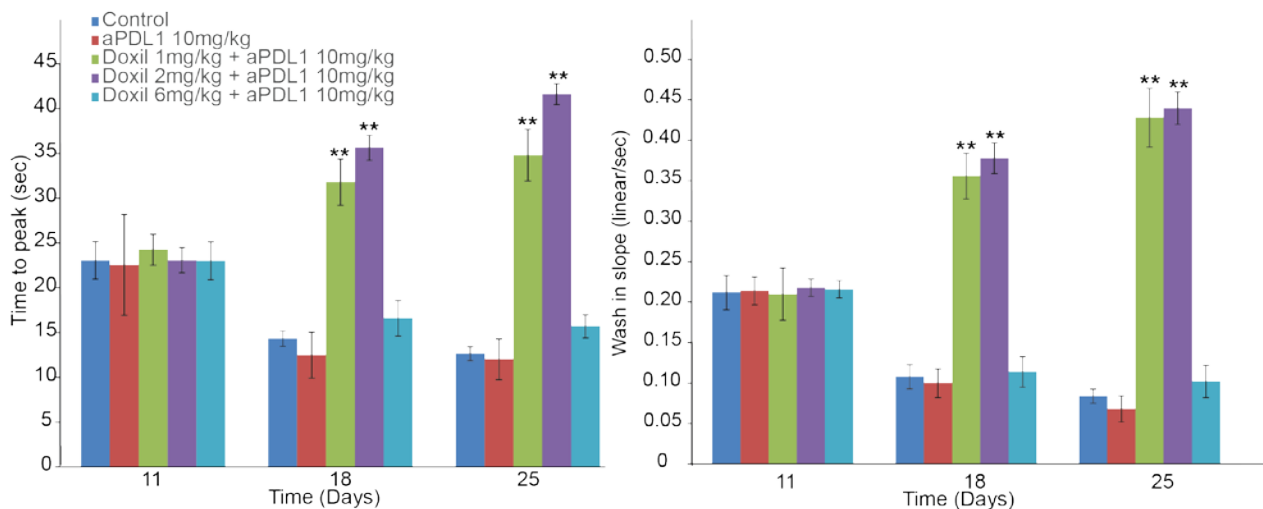


Figure 2. Results of CEUS studies. Quantification of the time to peak and the slope of the wash-in part of the time intensity curve. Average values and standard errors are depicted. An asterisk denotes statistically significant difference compared to the control group (n=5-6).

## Conclusions

Our results provide evidence that there is a good correlation between tumor stiffness and perfusion, which in turn are related to improved therapeutic outcomes, confirming our rationale as illustrated in Figure 1. Our findings also highlight the important role of biomechanical properties of solid tumors in the efficacy of anti-cancer treatments and suggest that re-engineering the physical microenvironment of tumors can improve therapy [1]. It is important also to notice that the use of SWE and CEUS to monitor tumor stiffness and perfusion can be transferred to the clinic given that both methods are already clinically applied for other

applications in oncology and for the diagnosis of other diseases. Therefore, our methodology has the potential to drive and optimize, patient-specific cancer therapies.

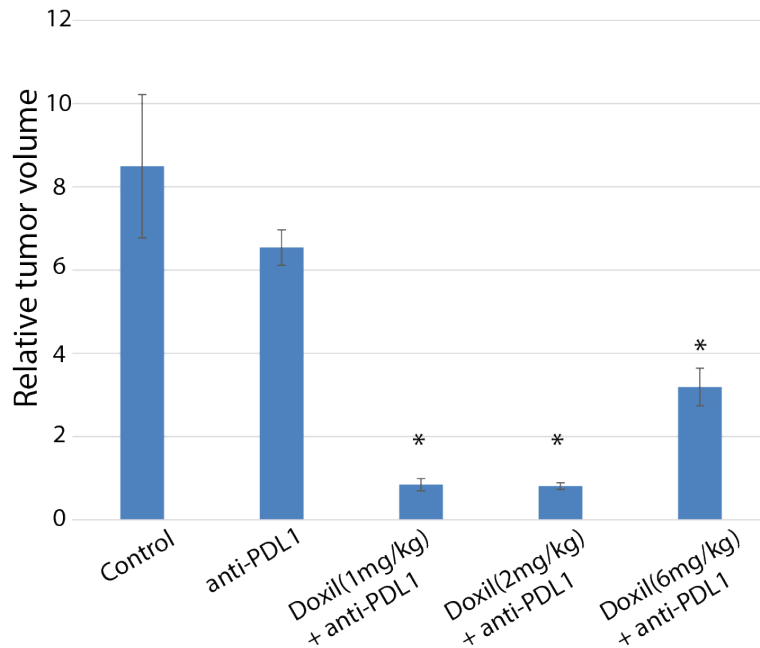


Figure 3. Relative increase in tumor growth calculated as the ratio of tumor volume at the end of the treatment protocol to the volume of the tumor at the initiation of the treatment. Average values and standard errors are depicted. An asterisk denotes statistically significant difference compared to the control group (n=5-6).

## References

- [1]. Stylianopoulos T, Munn LL, Jain RK, Reengineering the physical microenvironment of tumors to improve drug delivery and efficacy: From math modeling to bench to bedside, *Trends in Cancer*, 4(4):292-319, 2018.
- [2]. Schimid P, et. al., Atezolizumab and Nab-Paclitaxel in Advanced Triple-Negative Breast Cancer, *N Engl J Med.*, 379:2108-2121, 2018.
- [3]. Averkiou M, Keravnou CP, Izamis ML, Leen E, Evaluation of Perfusion Quantification Methods with Ultrasound Contrast Agents in a Machine-Perfused Pig Liver, *Ultraschall in der Medizin*, 39(1):69-79, 2018.
- [4]. Strouthos C, Lampaskis M, Sboros V, McNeilly A, Averkiou M, Indicator dilution models for the quantification of microvascular blood flow with bolus administration of ultrasound contrast agents, *IEEE transactions on ultrasonics, ferroelectrics, and frequency control* 57(6):1296-1310, 2010.
- [5]. Voutouri C, et al., Endothelin Inhibition Potentiates Cancer Immunotherapy Revealing Mechanical Biomarkers Predictive of Response, *Advanced Therapeutics*, 2000289, 2021.



# Low-intensity focused ultrasound enhances $\alpha$ CD40 antitumor effect in murine pancreatic tumors

**Jordan B. Joiner<sup>1</sup>, Nancy P. Kren<sup>2</sup>, Philip G. Durham<sup>1</sup>, Jinwook Kim<sup>3</sup>, Colleen Steward<sup>4</sup>, Yuliya Pylayeva-Gupta<sup>2</sup>, Paul A. Dayton<sup>1,3</sup>**

<sup>1</sup>Pharmaceutical Sciences, Eshelman School of Pharmacy, University of North Carolina at Chapel Hill, Chapel Hill, USA

<sup>2</sup>Department of Genetics, University of North Carolina at Chapel Hill, Chapel Hill, USA

<sup>3</sup>Joint Department of Biomedical Engineering, University of North Carolina at Chapel Hill & North Carolina State University, Chapel Hill, USA

<sup>4</sup>Department of Microbiology and Immunology, University of North Carolina at Chapel Hill, Chapel Hill, USA

Corresponding author: [padayton@email.unc.edu](mailto:padayton@email.unc.edu)

## Introduction

Pancreatic cancer has a poor 5-year survival rate as a consequence of late diagnosis and therapy resistance [1]. The use of immunotherapies, including checkpoint blockade, to invigorate anti-tumor immune responses to pancreatic cancer have been unsuccessful, highlighting the need to understand barriers that impede activity of immunotherapy [2]. Profound immunosuppression, as well as desmoplasia-driven compression of tumor vasculature, have been shown to account for the failure of drugs and immune cells to successfully reach tumor cells. Agonist CD40 ( $\alpha$ CD40) has been shown to have synergistic anti-tumor immune effects in combination with gemcitabine (GEM) in the murine KPC models of pancreatic cancer and has improved overall survival in combination with GEM, nab-paclitaxel (nP) and immune checkpoint blockade in humans [3,4]. Non-invasive, low-intensity focused ultrasound (LoFU) and microbubble (MB) treatments have emerged as a potential immunomodulatory treatment modality in several cancer types. One of the main consequences of focused ultrasound (FUS) application at the tumor site is a transient increase in vascular permeability and availability of antigens that may boost delivery of therapeutics and augment anti-tumor immune responses. However, optimized FUS parameters and defined immune mechanisms that may achieve such effects precludes its current application in patient care. This work will inform the design of FUS-directed immunotherapy strategies for pancreatic cancer.

## Methods

To understand how LoFU + MB treatment modulates anti-tumor immunity and vascular parameters, we used murine syngeneic models of pancreatic cancer. 57 female C57BL/6J mice were subcutaneously injected with  $1 \times 10^5$  KPC cells in 0.1 mL HBSS in the right flank [5]. Eleven days after tumor inoculation, mice were stratified into 5 groups as seen in **Figure 1**. Mice were treated by intravenously infusing decafluorobutane microbubbles (MBs) with a DSPC-PEG2k lipid shell ( $3 \times 10^8$  MBs total) and scanning the tumor with a Philips Therapy and Imaging Probe System (TIPS). Ultrasound parameters were as follows: 100 Hz pulse repetition frequency (PRF), 1 MHz frequency, 0.5 MPa peak negative pressure (PnP), 10% duty cycle, and 5 seconds/spot for a total treatment time of 5-10 minutes. Animals were sacrificed at 2 days ( $n=32$ ) to evaluate immune cell filtration in the tumor and lymph node or assessed for survival benefit ( $n=25$ ) at an endpoint of 1.5 cm length (Figure 1A) [6]. Additionally, in order to compare the immune effects of varying high-intensity focused ultrasound (HIFU) with previous LoFU treatments, we optimized focused ultrasound parameters using a SonoVol Vega system retrofitted with a 1 MHz focused transducer as shown in Table 1 [7]. H&E staining was performed on tumors collected 1 hour or 1 day post-treatment.

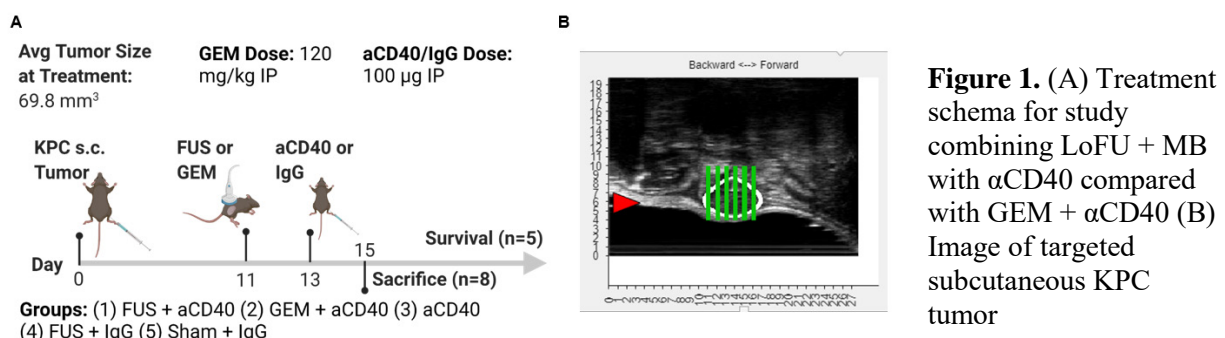


**Table 1.** Focused ultrasound parameters used to induce varying bioeffects in s.c. KPC tumors

Treatment Type	LoFU + MB	M-HIFU + MB	Hyperthermia	Thermal Ablation
Parameters	0.5 MPa PnP 10% Duty Cycle 5 sec/spot (~5 min total) 3x10 <sup>8</sup> MB total dose	6 MPa PnP 0.002% Duty Cycle 20 sec/spot (~4 min total) 3x10 <sup>8</sup> MB total dose	3.7 MPa PnP 30% Duty Cycle 2 minutes (1 spot) 40-50°C	5 MPa PnP 60% Duty Cycle 30 seconds (1 spot) >65°C

## Results

Evaluation of tumor growth revealed that  $\alpha$ CD40, GEM +  $\alpha$ CD40 and FUS +  $\alpha$ CD40 conferred similar survival benefit; however one mouse (20%) from the FUS +  $\alpha$ CD40 group had no tumor from Day 60 until the end of the study, which was censored at Day 127 (**Figures 2A and 2B**). We observed increase in frequency of total CD8<sup>+</sup> T cells in the tumor, early-activated CD8<sup>+</sup>CD69<sup>+</sup> T cells in the tumor and lymph node, and early-activated CD4<sup>+</sup>CD69<sup>+</sup> T cells in the lymph node (**Figures 2C, D, F and G**). Activated CD86<sup>+</sup> B cells were increased in the tumor and total CD19<sup>+</sup> B cells in the lymph node 2 days post-treatment (**Figures 2E and H**).

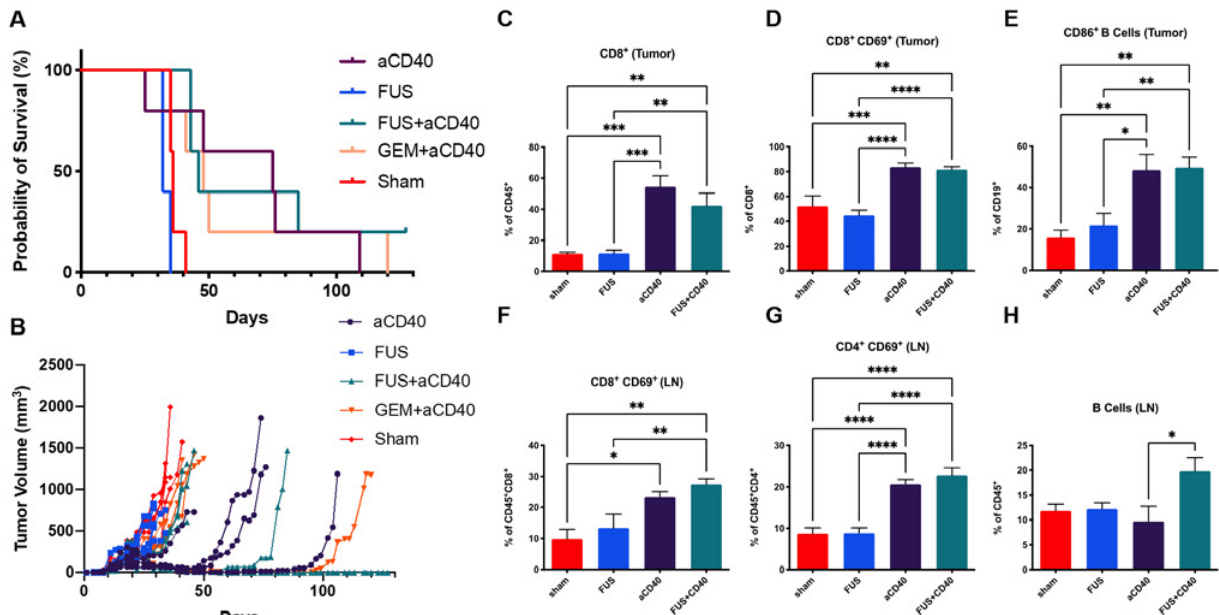


**Figure 2.** Survival and tumor growth of KPC mice treated with  $\alpha$ CD40 combined with either LoFU + MB or GEM; one FUS +  $\alpha$ CD40 mouse was cured of its tumor 127 days post-treatment. Increased CD8<sup>+</sup> T cells, CD4<sup>+</sup> T cells and B cells were recruited 2 days post-treatment.

To evaluate whether additional FUS modalities could confer enhanced anti-tumor immune effects combined with immunotherapy, we determined parameters that would induce varying ultrasound-induced bioeffects, including high-intensity mechanical ablation (M-HIFU + MB), thermal ablation, hyperthermia. These parameters were determined in an *ex-vivo* chicken breast model and tested in s.c. mice with KPC tumors (n=3). H&E images show increased presence of myeloid cells recruited 1 hour post-treatment with mechanical treatments LoFU + MB or M-HIFU + MB. Increased recruitment of lymphocytes and inflammation were observed in thermally-treated tumors (thermal ablation and hyperthermia) 1 day post-treatment.

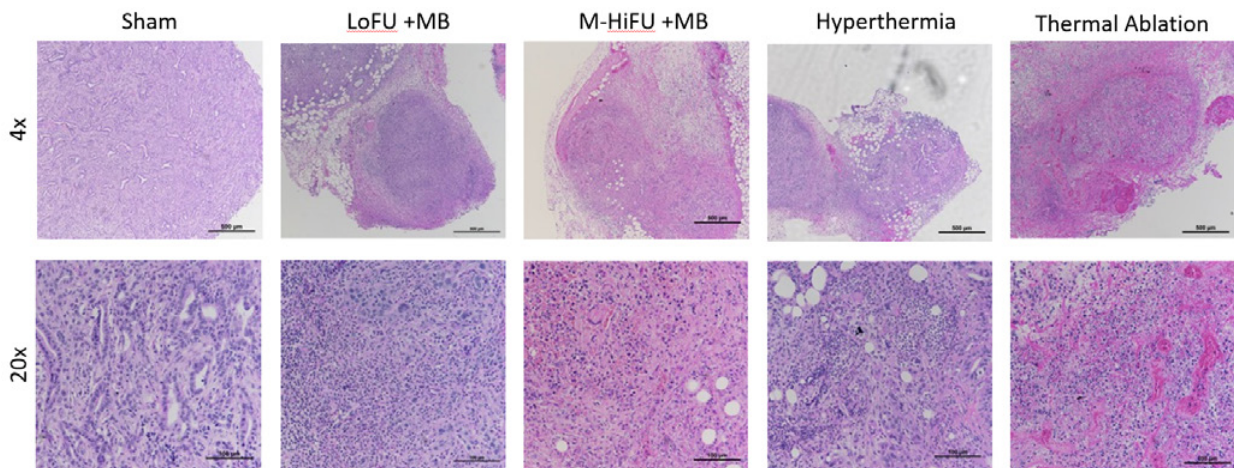


**Figure 3.** Subcutaneous KPC tumors treated with varying ultrasound parameters stained with H&E show varying levels of inflammation as well as presence of myeloid cells and lymphocytes.

### Conclusions

Low-frequency FUS combined with microbubble contrast agents and  $\alpha$ CD40 can ameliorate tumor growth via recruitment of nearby B cells and T cells. Further studies with increased animal numbers should be performed in order to understand the mechanism behind one mouse being cured of a subcutaneous KPC tumor. FUS parameters can be utilized to induce a wide variety of bioeffects, which will be combined with immunotherapies in future studies based on specific immune cell recruitment.

### References

- [1] Siegel RL, Miller KD, Jemal A. Cancer statistics, 2016. *CA Cancer J Clin.* 2016;66(1):7-30. Epub 2016/01/09. doi: 10.3322/caac.21332. PubMed PMID: 26742998.
- [2] Royal RE, Levy C, Turner K, Mathur A, Hughes M, Kammula US, Sherry RM, Topalian SL, Yang JC, Lowy I, Rosenberg SA. Phase 2 trial of single agent Ipilimumab (anti-CTLA-4) for locally advanced or metastatic pancreatic adenocarcinoma. *J Immunother.* 2010;33(8):828- 33. Epub 2010/09/16. doi: 10.1097/CJI.0b013e3181eec14c. PubMed PMID: 20842054.
- [3] Beatty, G. L., Chiorean, E. G., Fishman, M. P., Saboury, B., Teitelbaum, U. R., Sun, W., Huhn, R. D., Song, W., Li, D., Sharp, L. L., Torigian, D. A., O'Dwyer, P. J., & Vonderheide, R. H. (2011). CD40 agonists alter tumor stroma and show efficacy against pancreatic carcinoma in mice and humans. *Science (New York, N.Y.)*, 331(6024), 1612–1616. <https://doi.org/10.1126/science.1198443>
- [4] O'Hara MH, O'Reilly EM, Wolff RA, Wainberg ZA, Ko AH, Rahma OE, Fisher GA, Lyman JP, Cabanski CR, Karakunnel JJ, Gherardini PF, Kitch LJ, Bucktrout S, Christopher E, Mick R, Chen R, Trifan OC, Salvador L, O'Donnell-Tormey J, Vonderheide RH. Gemcitabine and nab-paclitaxel +/- nivolumab +/-  $\alpha$ CD40 agonistic monoclonal antibody APX005M in patients with untreated metastatic pancreatic adenocarcinoma: Phase 2 Final Results. *Journal of Clinical Oncology* 39 (15) Supp. 4019-4019.
- [4] Pylayeva-Gupta, Y., Das, S., Handler, J. S., Hajdu, C. H., Coffre, M., Koralov, S. B., & Bar-Sagi, D. (2016). IL35-Producing B Cells Promote the Development of Pancreatic Neoplasia. *Cancer Discovery*, 6(3), 247 LP-255. <https://doi.org/10.1158/2159-8290.CD-15-0843>
- [6] Mirlekar, B., Michaud, D., Searcy, R., Greene, K., & Pylayeva-Gupta, Y. (2018). IL-35 hinders endogenous anti-tumor T cell immunity and responsiveness to immunotherapy in pancreatic cancer. *Cancer Immunology Research*, 6(September), canimm.0710.2017. <https://doi.org/10.1158/2326-6066.CIR-17-0710>
- [7] Joiner JB, Pylayeva-Gupta Y, Dayton PA. Focused Ultrasound for Immunomodulation of the Tumor Microenvironment. *J Immunol.* 2020 Nov 1;205(9):2327-2341. doi: 10.4049/jimmunol.1901430. PMID: 33077668; PMCID: PMC7583653.

# Reactive Molecule Capture in Intracranial Drug Depots Following Ultrasound Mediated Delivery

*Phillip G. Durham<sup>1</sup>, Christopher Moody<sup>2</sup>, Yevgeny Brudno<sup>2</sup>, Paul A. Dayton<sup>2</sup>*

<sup>1</sup>*Eshelman School of Pharmacy, UNC Chapel Hill, NC, USA*

<sup>2</sup>*Joint Department of Biomedical Engineering, UNC/NCSU, Chapel Hill NC, USA*

*Corresponding author: pgdurham@email.unc.edu*

## Introduction

Despite advances in surgical resection, stereotactic radiosurgery and drug development, glioblastoma maintains a poor prognosis, with an average survival of 12-18 months and a 5 year survival rate less than 10%. One significant “barrier” to improved treatment efficacy is the blood-brain barrier, limiting the transport of chemotherapeutics from systemic circulation to the cancer cells. Locally releasing drug reservoirs have demonstrated efficacy, but long-term survival is not significantly changed as the drug eventually depletes. Ultrasound can be used to deliver drugs to the brain non-invasively, but many exogenous compounds are cleared rapidly from the brain and thus repeat delivery may be necessary to achieve high concentrations.

A reloadable drug reservoir could enable systemically administered drugs to be captured by the depot and released over an extended period, providing high local drug concentration with reduced off-target effects. A chemically functionalized depot has been developed that allows the capture of drugs administered intravenously, which can be released over time. This system of complimentary reactive chemistries has already demonstrated improved tumor control in an intradermal tumor model [1]. To evaluate the potential of non-invasive, ultrasound-mediated drug delivery to an intracranially implanted drug reservoir, we previously demonstrated that DBCO-Cy7 is excluded from the brain in the absence of ultrasound. We present here the elimination kinetics of DBCO-Cy7 from the brain following ultrasound-mediated delivery, and have demonstrate enhanced fluorophore retention in the brain when the depot is present.

## Methods

For determining capture efficacy and retention of the delivered fluorophore DBCO-Cy7, intracranial drug reservoirs were implanted in CD-1 mice in the right hemisphere by injecting 2 $\mu$ L of 20 mM azide-sNHS into the striatum (2 mm laterally right, 1 mm anterior from bregma, 2.5 mm depth). To track the location of the reservoir, AF647-sNHS was coadministered with the reservoir. For ultrasound treatments, an animal imaging system (Vega, SonoVol) was outfitted and co-registered with a single element focused transducer (H201-MR, Sonic Concepts). Approximately 4 weeks following intracranial injection (after the incision healed), mice were treated with focused ultrasound. Animals were anesthetized under 1.5-2.5% isoflurane inhalation carried on 100% oxygen. First, a volumetric image was aquired of the head and used to direct the focused beam for ultrasound therapy. Ultrasound was then applied at 1 MHz at a peak negative pressure of 0.5 MPa, 1000 cycles at 100 Hz pulse repetition frequency for 5 minutes following a bolus injection of 1e8 lipid shelled perfluorocarbon microbubbles (prepared as published in [2]) and DBCO-Cy7.

For kinetic analysis of DBCO-Cy7 clearance from the brain, depot-free animals were treated as stated above, and sacrificed and perfused at 3hrs, 24hrs, and 7 days after injection (n=3). The brain was removed and imaged via whole organ fluorescence imaging (IVIS Spectrum, PerkinElmer). For depot retention studies, animals were divided into 3 groups : +N<sub>3</sub>-US, -N<sub>3</sub>+US, and +N<sub>3</sub>+US (N<sub>3</sub> designating presense (+) or absence (-) of intracranial azide depot, US designating application of focused ultrasound). Animals receiving depots were implanted 4 weeks prior to ultrasound. All animals received an injection of DBCO-Cy7 and microbubbles, but only two groups received ultrasound. After 28 days, animals were perfused and the brains were collected for ex-vivo whole organ imaging. Fluorescence images were aquired in the AF647 (Ex:640nm, Em:680nm) and Cy7 (Ex:745nm, Em:800nm) channels to quantify DBCO-Cy7

retention. Regions of interest were drawn around the targeted and contralateral hemispheres and quantified (Living Image Software, PerkinElmer). Representative specimens were sectioned coronally and imaged to visualize spatial distribution.

## Results

Fluorescence images of DBCO-Cy7 following ultrasound mediated disruption in depot-free animals showed significant enhancement in the targeted hemisphere 3 hours after treatment, which diminished substantially by 24 hours and further decreased after 7 days (Figure 1a, 1b). In experiments testing depot capture (Figure 1c), animals with an intracranial depot that did not receive ultrasound (+N<sub>3</sub>-US, n=4) exhibited less fluorescence signal 28 days after treatment than animals without depots that did receive ultrasound (-N<sub>3</sub>+US, n=6). In animals treated with both depot and ultrasound (+N<sub>3</sub>+US, n=5) there was significantly more fluorescence signal in the targeted hemisphere than animals receiving ultrasound alone.

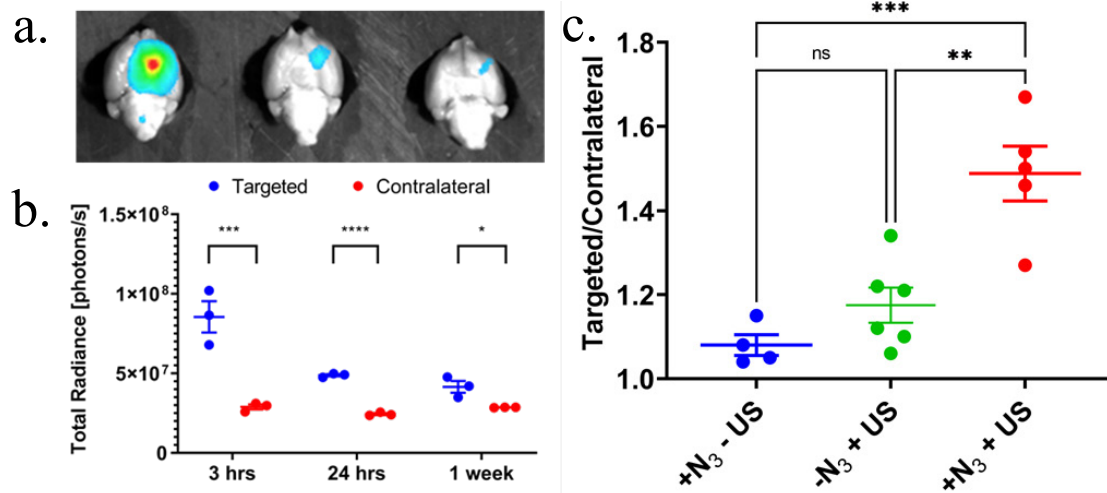


Figure 1. DBCO-Cy7 delivery, clearance and capture with focused ultrasound.

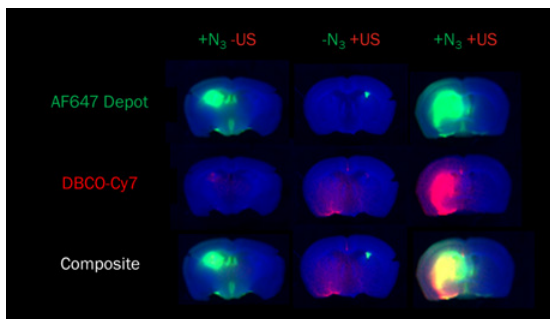


Figure 2. Spatial distribution of DBCO-Cy7 retention 28 days after delivery

While there was still detectable fluorescence in animals receiving ultrasound without depots, intracranial depots significantly enhanced DBCO-Cy7 retention 28 days after injection, indicating drug capture by the depot. Presence of the depot alone did not result in substantial fluorophore accumulation. Representative sectional images (Figure 2) depict substantial overlap in the retained DBCO-Cy7 signal and the location of the AF647 labelled depot.

## Conclusions

Refillable drug depots in the brain could be a useful tool in the long term treatment of glioblastoma, offering substantial advantages to traditional systemic chemotherapy. We demonstrate here that intracranially implanted depots can be filled non-invasively following systemic injection and blood-brain barrier disruption with focused ultrasound, significantly increasing the longevity of delivered molecules. Future studies will investigate efficacy against experimental cancer using chemically reactive drugs.

## References

- [1] Brudno, Y. et al. Replenishable drug depot to combat post-resection cancer recurrence. *Biomaterials* 178, 373–382 (2018).
- [2] Fix, S. M. et al. Accelerated Clearance of Ultrasound Contrast Agents Containing Polyethylene Glycol is Associated with the Generation of Anti-Polyethylene Glycol Antibodies. *Ultrasound Med. Biol.* 44, 1266–1280 (2018).

# Nanodrop Engineering for Ultrasound Imaging

*Mark Borden*

*Biomedical Engineering Program, Mechanical Engineering Department  
University of Colorado, Boulder, CO, USA  
mark.borden@colorado.edu*

## Abstract

Nanodrops are submicron, liquid drops suspended in an aqueous medium. Their submicron size makes nanodrops useful for targeting leaky or inflamed vasculature, for example in early diagnosis of type-1 diabetes [1]. For ultrasound imaging, a liquid perfluorocarbon core is chosen to be sufficiently volatile so that the nanodrop can phase-change into an echogenic microbubble by the process of acoustic droplet vaporization. However, vaporizability must be balanced with colloidal stability, or the nanodrops will not be sufficiently durable for storage and *in vivo* circulation [2]. In this talk, it will be shown by theory and experimental results how perfluorocarbons that are too volatile may experience rapid dissolution [3] or bubble inflation [4]. The key finding is that vapor pressure, not Laplace pressure, drives instability. Additionally, the shell material must balance the need for rigidity to stabilize the nanodrop suspension with the flexibility to expand and coat the newly formed gas/water interface on the microbubble resulting from acoustic droplet vaporization. In this talk, one such biomimetic shell will be introduced to satisfy these seemingly opposing constraints [5]. The key result is that monolayer melting, spreading and resolidification can stabilize the vaporized microbubble. Together, these findings may aid the engineering of nanodrops for applications in ultrasound imaging.

## References

- [1] D. G. Ramirez, M. Ciccaglione, A. K. Upadhyay, V. T. Pham, M. A. Borden, and R. K. P. Benninger, "Detecting insulinitis in type 1 diabetes with ultrasound phase-change contrast agents," *Proc. Natl. Acad. Sci. U. S. A.*, vol. 118, no. 41, p. e2022523118, Oct. 2021, doi: 10.1073/pnas.2022523118.
- [2] M. A. Borden, G. Shakya, A. Upadhyay, and K.-H. Song, "Acoustic Nanodrops for Biomedical Applications," *Curr. Opin. Colloid Interface Sci.*, vol. 50, p. 101383, Dec. 2020, doi: 10.1016/j.cocis.2020.08.008.
- [3] P. A. Mountford, W. S. Smith, and M. A. Borden, "Fluorocarbon nanodrops as acoustic temperature probes," *Langmuir ACS J. Surf. Colloids*, vol. 31, no. 39, pp. 10656–10663, Oct. 2015, doi: 10.1021/acs.langmuir.5b02308.
- [4] C. J. Brambila, J. Lux, R. F. Mattrey, D. Boyd, M. A. Borden, and C. de Gracia Lux, "Bubble Inflation Using Phase-Change Perfluorocarbon Nanodroplets as a Strategy for Enhanced Ultrasound Imaging and Therapy," *Langmuir ACS J. Surf. Colloids*, vol. 36, no. 11, pp. 2954–2965, Mar. 2020, doi: 10.1021/acs.langmuir.9b03647.
- [5] A. N. Thomas *et al.*, "Contrast-Enhanced Sonography with Biomimetic Lung Surfactant Nanodrops," *Langmuir ACS J. Surf. Colloids*, vol. 37, no. 7, pp. 2386–2396, Feb. 2021, doi: 10.1021/acs.langmuir.0c03349.

# Acoustic modulation of the degree of superheat enables nanodroplet vaporization by protons at body temperature

Sophie V. Heymans<sup>1,2,3</sup>, Gonzalo Collado-Lara<sup>2</sup>, Marta Rovituso<sup>4</sup>, Hendrik J. Vos<sup>2</sup>, Jan D'hooge<sup>3</sup>, Nico de Jong<sup>2</sup>, and Koen Van Den Abeele<sup>1</sup>.

<sup>1</sup>Department of Physics, KU Leuven Campus Kulak, Kortrijk, Belgium

<sup>2</sup>Department of Biomedical Engineering, Erasmus Medical Center, Rotterdam, The Netherlands

<sup>3</sup>Department of Cardiovascular Sciences, KU Leuven, Leuven, Belgium

<sup>4</sup>Holland Proton Therapy Center, Delft, The Netherlands

Corresponding author: [sophie.heyman@kuleuven.be](mailto:sophie.heyman@kuleuven.be)

## Introduction

The vaporization of superheated, injectable nanodroplets by ionizing radiation was recently demonstrated, opening the door to *in vivo* proton range verification and dosimetry. In previous studies, perfluorobutane (PFB, b.p. -2°C) was employed as the nanodroplet liquid core [1,2,3], as PFB is a popular superheated nanodroplet formulation, owing to its excellent stability at body temperature combined with a relatively low energy threshold for vaporization. Unfortunately, direct proton detection by PFB nanodroplets is not feasible at 37°C, as their degree of superheat is too low for vaporization by protons. Instead, PFB nanodroplets are only sensitive to rare secondary particles at physiological temperature [2], which limits the achievable accuracy for *in vivo* range verification. In this study, we investigate the feasibility of increasing the degree of superheat of PFB nanodroplets using an acoustic field, aiming at direct nanodroplet vaporization by protons at body temperature.

## Methods

A tube containing a flowing water dilution of PFB nanodroplets encapsulated in a polyvinyl alcohol shell [4] was simultaneously irradiated with a 158 MeV proton beam (Holland PTC, Delft, the Netherlands) and sonicated with a 1.1 MHz focused transducer (acoustic modulation), using increasing Peak Negative Pressures (PNP: 0-900 kPa). A linear ultrasound array (L12-5), driven by a Verasonics Vantage platform, was positioned parallel to the tube and recorded nanodroplet vaporization during irradiation (Fig. 1(a)). The tube was positioned in the wake of the proton range in order to specifically detect nanodroplet vaporization induced by primary protons. The temperature was progressively decreased from 50°C to 29°C, in order to determine the acoustic pressure thresholds for proton-induced vaporization as a function of temperature.

## Results

At 50°C, nanodroplet vaporization by protons was observed in the absence of acoustic modulation, in agreement with previous studies [2,3]. The number of vaporization events progressively decreased until proton sensitization was lost at 41°C. At this point, the effect of acoustic modulation was evaluated, alone and in combination with proton irradiation. We observed an increase in vaporization events when acoustic modulation was used during proton irradiation, with a PNP threshold increasing with decreasing temperature (from 200 kPa at 40.5°C to 800 kPa at 29°C, Fig. 1(b)). In contrast, nanodroplet vaporization was not observed at those PNPs when acoustic modulation was used alone, which confirms that vaporization is induced by the combined effect of the acoustic modulation field and energy deposition by proton radiation.

## Conclusions

This study demonstrates that acoustic modulation can decrease the vaporization threshold of PFB nanodroplets, making the latter vaporizable by protons at temperatures below the proton sensitization temperature at ambient (atmospheric) pressure, and acoustic pressures below the acoustic droplet vaporization threshold. Importantly, the PNP threshold for proton-induced nanodroplet vaporization at body temperature was as low as 400 kPa, bringing clinical translation within reach: acoustic modulation could be

achieved with plane waves and a conventional ultrasound array, ideally switching between acoustic modulation and detection of vaporization events.

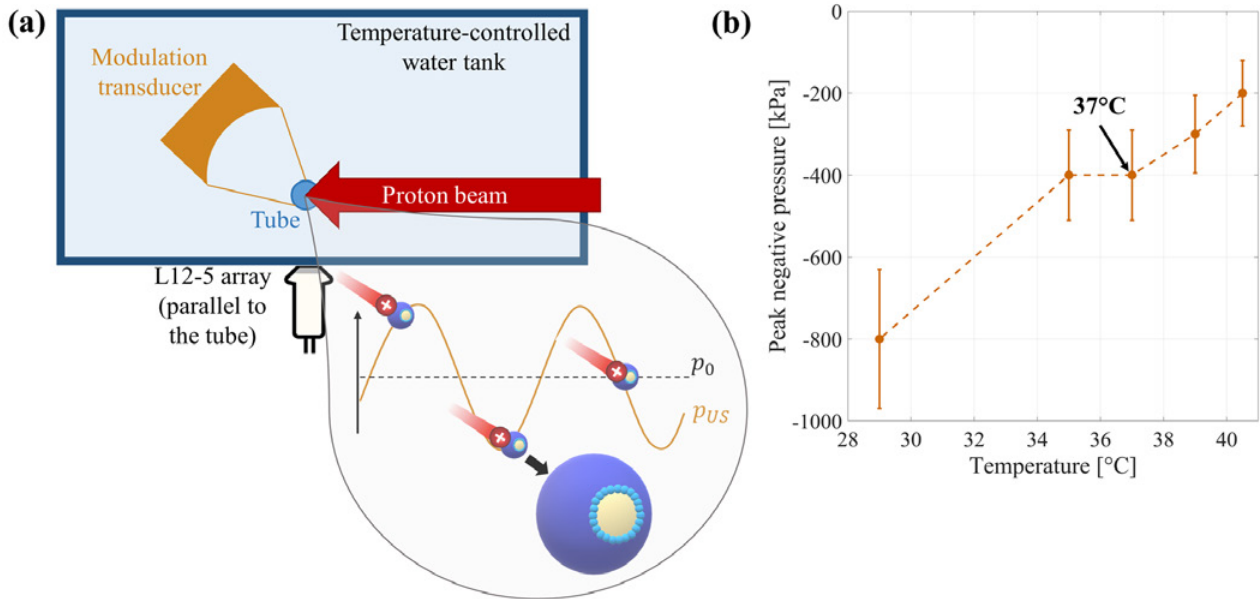


Figure 1. (a) Experimental setup for simultaneous proton irradiation and acoustic pressure modulation. The insert shows the expected mechanism: during the rarefactional phase of the acoustic pulse, the pressure inside the nanodroplet liquid core decreases, which increases the droplet degree of superheat and enables proton-induced nanodroplet vaporization. (b) Peak Negative Pressure thresholds required to sensitize nanodroplets to protons at different temperatures. At physiological temperature, nanodroplet vaporization by protons was observed for PNP<sub>s</sub>  $\geq 400$  kPa.

## References

- [1]. Carlier B, Heymans SV, Nooijens S, et al., Proton range verification with ultrasound imaging using injectable radiation sensitive nanodroplets: a feasibility study, *Physics in Medicine and Biology*, 65: 065013, 2020.
- [2]. Heymans SV, Carlier B, Toumia Y, et al., Modulating ultrasound contrast generation from injectable nanodroplets for proton range verification by varying the degree of superheat, *Medical Physics*, 48(4), 2021.
- [3]. Collado-Lara G, Heymans SV, Rovituro M et al. Spatiotemporal distribution of nanodroplet vaporization in a proton beam using real-time ultrasound imaging for range verification, *Ultrasound in Medicine and Biology* (Online) 2021.
- [4]. Toumia Y, Miceli R, Domenici F, et al., Ultrasound-assisted investigation of photon triggered vaporization of poly(vinylalcohol) phase-change nanodroplets: A preliminary concept study with dosimetry perspective, *Physica Medica*, 89, 2021.

## Acknowledgments

This project has received funding from the European Union's Horizon 2020 research and innovation Programme under grant agreement 766456 (AMPHORA).

# Ultrasound detection of Carbon-ion dose and range using activatable polymer-shelled perfluorobutane nanodroplets

*Yosra Toumia<sup>1,2</sup>, Marco Pullia<sup>3</sup>, Fabio Domenici<sup>1,2</sup>, Angela Facoetti<sup>3</sup>, Michele Ferrarini<sup>3</sup>, Emiliano D'Agostino<sup>4</sup>, Sophie V. Heymans<sup>5,7</sup>, Bram Carlier<sup>6</sup>, Damiano Palmieri<sup>1</sup>, Edmond Sterpin<sup>6</sup>, Koen Van Den Abeele<sup>5</sup>, Jan D'hooge<sup>7</sup>, Gaio Paradossi<sup>1,2</sup>*

<sup>1</sup>*Department of Chemical Science and Technology, University of Rome Tor Vergata, Rome, Italy*

<sup>2</sup>*INFN sez. Tor Vergata, Rome, Italy*

<sup>3</sup>*CNAO, Pavia, Italy*

<sup>4</sup>*DoseVue, Hasselt, Belgium*

<sup>5</sup>*Department of Physics, KU Leuven Campus Kulak, Kortrijk, Belgium*

<sup>6</sup>*Department of Oncology, KU Leuven, Leuven, Belgium*

<sup>7</sup>*Department of Cardiovascular Sciences, KU Leuven, Leuven, Belgium*

*Corresponding author: Yosra.Toumia@uniroma2.it*

## Introduction

Ultrasound contrast agents based on phase-change nanodroplets (NDs) have received great interest in the past decade due to their ability to extravasate in tumors. While acoustic and optical droplet vaporization have been commonly reported to enable the conversion of NDs into echogenic microbubbles (MBs), it was recently proven that superheated NDs, i.e. having a perfluorocarbon core above its boiling point, can be successfully vaporized by LINAC photons and 'hadron' particles (such as protons) when their degree of superheat is tuned [1-3]. These findings open a new application of NDs in radiotherapy towards *in vivo* dosimetry and, in particular, range verification of 'hadron' beams. The sensitivity of NDs to ionizing radiation strictly depends on the linear energy transfer (LET), i.e. the energy transferred by the ionizing particles per unit of length, and on the degree of superheat of the core: the higher the superheat degree, the lower is the LET required to trigger the vaporization [2].

Hadron beams feature a finite range in the body with a sharp distal fall-off known as the Bragg peak, which is the position at which the particles deposit the maximum of their energy before stopping. Nowadays, efforts are ongoing to build advanced radiotherapy centers combining proton and Carbon-ion hadron beams. Carbon-ions (C-ions) are even higher LET particles compared to protons and are characterised by a narrower Bragg peak and by higher relative biological effects against resistant tumors [4].

In this contribution, tissue-mimicking phantoms containing superheated perfluorobutane NDs encapsulated by a crosslinked poly(vinylalcohol) shell were exposed to a clinical C-ion beam at different doses and beam ranges. Ultrasound imaging (US) pre-and post-radiation exposure was performed to confirm the specific vaporization of NDs induced by C-ions, and to evaluate their dosimetry and range verification performance.

## Methods

PVA-shelled perfluorobutane nanodroplets (PVA/PFB NDs), with average diameter of  $700 \pm 100$  nm, were homogenously embedded in tissue-mimicking phantoms of polyacrylamide (PAM) hydrogel at a concentration of  $4 \cdot 10^6$  NDs/ml. The phantoms were irradiated at  $37^\circ\text{C}$  with a 311 MeV (180 mm range) C-ion beam, at the CNAO hadron therapy facility (Pavia, Italy), using doses between 0.1-4 Gy measured at the Bragg peak. Phantoms were positioned in such a way that the range was located within the phantom. Control experiments were performed on non-irradiated phantoms as well as on irradiated ND-free phantoms.

In order to assess the C-ion beam radiation effect on the PVA/PFB NDs, the phantoms were scanned pre-and post-radiation exposure with a clinical US apparatus (Mindray DP50, China) equipped with a linear transducer array ( $f_c = 7.5\text{MHz}$ ). All images were acquired at the same gain under a mechanical index

MI=0.1 (well below the acoustic vaporization threshold), and subsequently analyzed by extracting the grayscale value profile using ImageJ freeware.

The specific vaporization-response of the NDs to the C-ions was further assessed by modifying the phantom position within the beam path, by performing a spread-out Bragg peak (SOBP) irradiation (i.e. accumulation of Bragg peaks at different energies) and by modifying the beam range from 180 mm to 50 mm.

## Results

Ultrasound images of PVA/PFB NDs in PAM phantoms after exposure to C-ions at various doses between 0.1-4 Gy are shown in Figure 1a. The phantom images exhibit a narrow distinct zone of high contrast (i.e. generated microbubbles) matching with the predicted C-ions Bragg peak position. This implies that NDs' vaporization is triggered only at these positions where the C-ions deposit their maximal energy, i.e when the particles achieve a sufficient LET above  $145 \text{ keV}/\mu\text{m}$ , which was previously determined to be the threshold for PFB vaporization at  $37^\circ\text{C}$  [2]. Moreover, the ultrasound images show a gradual contrast enhancement at the predicted Bragg peak position with the increase of the dose, with an apparent saturation of the signal at 4 Gy. This visually observable trend was confirmed by quantifying the grayscale value profiles over the full ultrasound frames as a function of the beam depth (Fig 1.b). The grayscale plots show Gaussian-shaped peaks attributed to the NDs' vaporization, whose intensity increases as a function of the dose up to 2 Gy and saturates for a dose of 4 Gy.

The superposition of the simulated Bragg peak on the position of the grayscale peaks within the beam path results in a sub-millimeter shift of  $0.3 \pm 0.1 \text{ mm}$ . In addition to these initially performed range verification tests, experiments using a spreadout Bragg peak irradiation and range modification confirmed the precise matching between the ND vaporization profile and the Bragg peak location. These results further highlight the specific sensitivity of PVA/PFB NDs to C-ions beams and show their promising potential for dosimetry and range verification.

## Conclusions

This contribution demonstrates a proof-of-concept on the feasibility of C-ion dosimetry and range verification, using perfluorobutane phase-change NDs and ultrasound detection. The PVA/PFB NDs exhibited excellent sensitivity and dose-dependence to C-ion ionizing radiation at clinically relevant doses and at physiological temperatures of  $37^\circ\text{C}$ . In agreement with the thermal spike theory and previous studies, the vaporization of NDs occurs only in the zone where the C-ions achieve a high LET at the end of their range, i.e around the Bragg Peak. Based on previously reported promising results of PVA/PFB NDs with protons beams, we believe that NDs could be prospected in the future as injectable non-invasive multimodal dosimeters allowing for a high precision range verification.

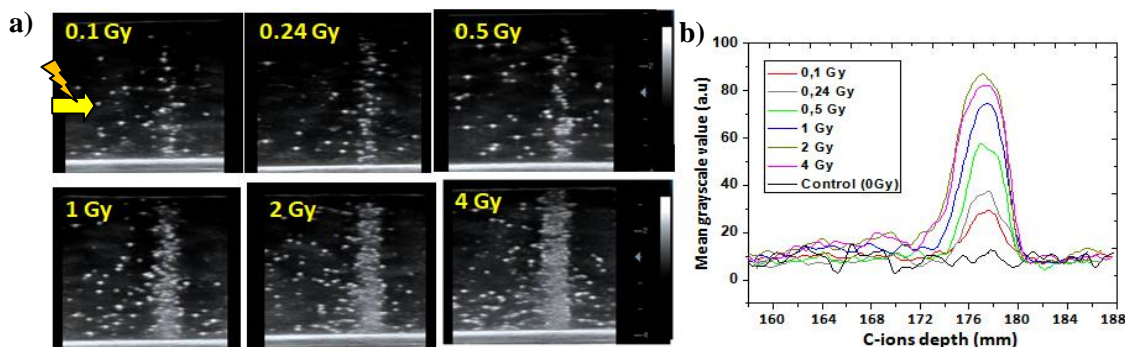


Figure 1. PVA/PFB NDs triggered vaporization by C-ions at various doses (311 MeV, 180mm range, @ $37^\circ\text{C}$ ): Ultrasound images of vaporized NDs dispersed in PAM phantom post-C-ions exposure at each tested dose; Comparison of the average grayscale value profiles at the different doses as a function of the distance traveled by C-ions (beam depth) b). Each profile is the average of grayscale values from ultrasound imaging scans of two phantoms per each dose (3 Frames/phantom,  $n_{\text{tot}}=6$ ).

## References

- [1]. Carlier B *et al.*, Proton range verification with ultrasound imaging using injectable radiation sensitive nanodroplets: a feasibility study, *Phys. Med. Biol.* 65: 065013, 2020.
- [2]. Heymans SV *et al.*, Modulating ultrasound contrast generation from injectable nanodroplets for proton range verification by varying the degree of superheat, *Med. Phys.* 48: 1983-1995, 2021.
- [3]. Toumia Y, *et al.*, Ultrasound-assisted investigation of photon triggered vaporization of poly(vinylalcohol) phase-change nanodroplets: A preliminary concept study with dosimetry perspective, *Physica Medica*, 89: 232–242, 2021.
- [4]. Tinganelli W, Durante M, Carbon Ion radiobiology, *Cancers*, 12: 3022, 2020.

## Acknowledgement

This project has received funding from the European Union’s Horizon 2020 research and innovation Programme under grant agreement 766456 (AMPHORA).

# Vancomycin-decorated microbubbles for treatment and ultrasound molecular imaging of *Staphylococcus aureus* biofilms

*J.J.P. Kouijzer<sup>1</sup>, K.R. Lattwein<sup>1</sup>, D.I. Beekers<sup>1</sup>, S.A.G. Langeveld<sup>1</sup>, H.M. Leon-Grooters<sup>1</sup>, J. Strub<sup>2</sup>, E. Oliva<sup>3</sup>, G.L.A. Mislin<sup>4</sup>, N. de Jong<sup>1,5</sup>, A.F.W. van der Steen<sup>1,5</sup>, A. Klibanov<sup>6</sup>, W.J.B. van Wamel<sup>7</sup>, K. Kooiman<sup>8</sup>*

<sup>1</sup> Department of Biomedical Engineering, Thoraxcenter, Erasmus MC University Medical Center Rotterdam, Rotterdam, the Netherlands

<sup>2</sup> CNRS/University of Strasbourg UMR 7178, Institut Pluridisciplinaire Hubert Curien, Laboratoire de Spectrométrie de Masse Bio-Organique, Strasbourg-Cedex, France

<sup>3</sup> Faculté de Pharmacie de Strasbourg, Plateforme d'Analyse Chimique de Strasbourg-Illkirch (PACSI), Illkirch-Graffenstaden, France

<sup>4</sup> CNRS/University of Strasbourg UMR7242, Illkirch-Graffenstaden, France

<sup>5</sup> Laboratory of Acoustical Wavefield Imaging, Faculty of Applied Sciences, Delft University of Technology, Delft, the Netherlands

<sup>6</sup> Cardiovascular Division, Department of Medicine, University of Virginia, Charlottesville, Virginia, United States of America

<sup>7</sup> Department of Medical Microbiology and Infectious Diseases, Erasmus MC, Rotterdam, the Netherlands  
Corresponding author: j.kouijzer@erasmusmc.nl

## Introduction

Most bacterial infections are associated with biofilms [1], which contain bacteria protected by a matrix of proteins, sugars and extracellular DNA. This protective environment hinders the effectiveness of antibiotic treatment [2]. Therefore, biofilms can cause a multitude of life-threatening and persistent infectious diseases. Currently there is no theranostic tool available in the clinic which combines the detection of biofilms with treatment possibilities. In this study, we aimed to develop targeted vancomycin-decorated microbubbles (vMB) [3] and demonstrate their potential for ultrasound-mediated treatment, and early detection of biofilms.

## Methods

First, the antibiotic vancomycin was covalently coupled to DSPE-PEG(3400)-NHS to produce a DSPE-PEG(3400)-vancomycin conjugate. Then, vMB were produced by probe sonication. DSPC (86.4 mol%), PEG-40 stearate (8.3 mol%) and the custom-made DSPE-PEG(3400)-vancomycin conjugate (5.3 mol%) were used as the phospholipid components of the microbubble shell with a perfluorobutane (C<sub>4</sub>F<sub>10</sub>) gas core. For the production of control microbubbles (cMB), the DSPE-PEG(3400)-vancomycin conjugate was substituted for DSPE-PEG(3400). vMB and cMB were incubated with a FITC-labeled anti-vancomycin antibody and imaged using high-axial resolution 4Pi confocal microscopy. A patient-derived *Staphylococcus aureus* strain was used to cultivate biofilms *in vitro* in human plasma-coated IbiTreat  $\mu$ -slides under continuous laminar flow (5 dyn/cm<sup>2</sup>, 14.4 mL/min) in IMDM medium at 37 °C for 24 h. Adherence of vMB to biofilms was evaluated under increasing physiological flow conditions (1.5-12.0 dyn/cm<sup>2</sup>; 4.3-34.5 mL/min) and compared to cMB. For the treatment of biofilms, vMB were introduced to the biofilm under a shear stress of 1.3 dyn/cm<sup>2</sup> (3.7 mL/min). After 5 min of incubation, bound vMB were insonified (2 MHz, 250 kPa, 5,000 or 10,000 cycles) under flow conditions (5 dyn/cm<sup>2</sup>). vMB oscillation during insonification was recorded with the Brandaris 128 ultra-high-speed camera coupled to a custom-built Nikon A1R+ confocal microscope [4]. Furthermore, biofilms were imaged using the Vevo3100, a high frequency pre-clinical scanner, in combination with an ultra-high frequency linear array transducer operated at 18 MHz and 10% transmit power. First, biofilms were imaged in non-linear contrast mode without vMB. After this, vMB were introduced to the biofilm and after 5 min of incubation, a shear stress of 1.5 dyn/cm<sup>2</sup>

was applied for 60 s to remove unbound vMB from the biofilm. Biofilms were imaged again and compared to baseline measurements. To locally destroy vMB, burst mode was used 1, 5 and 10 times.

## Results

high-axial resolution 4Pi confocal microscopy confirmed vancomycin to be distributed heterogeneously over the vMB coating. The adherence of vMB to biofilms under increasing shear stress was significantly higher in comparison to cMB. Upon ultrasound exposure of bound vMB under flow, microbubble oscillations were recorded (Fig.1B). Confocal microscopy recordings revealed  $19.6\% \pm 11.5\%$  biofilm removal ( $n = 7$ ) after insonification with 5,000 cycles (Fig.1A,C) while a more constant biofilm reduction effect was observed after insonification with 10,000 cycles ( $20.8 \pm 6.3\%$ ;  $n = 4$ ). During ultrasound molecular imaging, the contrast-to-tissue ratio was dramatically increased by 18.1 dB compared to the biofilm non-linear contrast signal without vMB (Fig. 1D,E). To confirm that the non-linear signal was generated by bound vMB, bursts were applied on three different places resulting in three individual lines across the biofilm (Fig.1F).

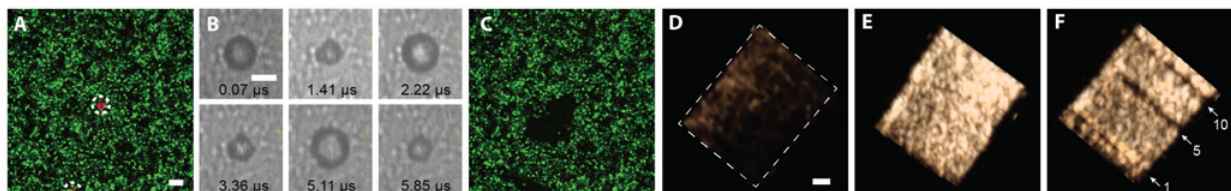


Figure 1. Theranostic potential of vancomycin-decorated microbubbles (vMB). (A) Confocal image of the initial biofilm state (vMB in red with dashed circles; bacteria in green). Scale bar is  $10 \mu\text{m}$  and also applies to C. (B) Selected frames of Brandaris 128 ultra-high-speed camera recording showing the oscillating vMB during ultrasound insonification. Scale bar is  $5 \mu\text{m}$ . (C) Confocal image after vMB ultrasound exposure showing biofilm disruption. (D) 3D rendered non-linear contrast image of the biofilm before addition of vMB, (E) after incubation and washing away unbound vMB, and (F) after applying 1, 5 or 10 flash bursts (white arrows followed by 1, 5 and 10). Scale bar is  $1 \text{ mm}$  and applies to D-F.

## Conclusions

These results demonstrate successful incorporation of the antibiotic vancomycin to the microbubble coating and the potential of vMB to be utilized as a theranostic agent. vMB bound to the biofilm enhanced the ultrasound signal during ultrasound molecular imaging and could improve biofilm detection. Mechanical effects induced upon ultrasound insonification have promising potential to enhance treatment through biofilm removal.

## Acknowledgements

This project has received funding from the European Research Council (ERC) under the European Union's Horizon 2020 research and innovation program [grant agreement 805308].

## References

- [1]. Romling, U. and C. Balsalobre, Biofilm infections, their resilience to therapy and innovative treatment strategies. *J Intern Med*, 2012. 272(6): p. 541-61
- [2]. Mah, T.F. and G.A. O'Toole, Mechanisms of biofilm resistance to antimicrobial agents. *Trends Microbiol*, 2001. 9(1): p. 34-9
- [3]. Kouijzer, J.J., et al., Vancomycin-decorated microbubbles as a theranostic agent for *Staphylococcus aureus* biofilms. *International Journal of Pharmaceutics*, 2021. 609: p. 121154
- [4]. Beekers, I., et al., Combined Confocal Microscope and Brandaris 128 Ultra-High-Speed Camera. *Ultrasound Med Biol*, 2019. 45(9): p. 2575-2582

# Bactericidal and Anti-biofilm effects of Ultrasound-Responsive Nitric Oxide Microbubbles on *Pseudomonas aeruginosa* Biofilms

Gareth LuTheryn<sup>1</sup>, Charlotte Hind<sup>2</sup>, Peter Glynne-Jones<sup>3</sup>, J. Mark Sutton<sup>2</sup>, Jeremy S. Webb<sup>4</sup>, Sandra A. Wilks<sup>4</sup>, Michael Gray<sup>5</sup>, Eleanor Stride<sup>5</sup>, Dario Carugo<sup>1</sup>

<sup>1</sup>UCL School of Pharmacy, Department of Pharmaceutics, University College London, London, England.

<sup>2</sup>UKHSA, Porton Down, Manor Farm Road, Salisbury, England

<sup>3</sup>Faculty of Engineering and Physical Sciences, University of Southampton, Southampton, England.

<sup>4</sup>National Biofilms Innovation Centre (NBIC), Faculty of Environmental and Life Sciences, University of Southampton, Southampton, England.

<sup>5</sup>Institute of Biomedical Engineering, University of Oxford, Oxford, England.

Corresponding author: G.LuTheryn@ucl.ac.uk

## Introduction

Bacterial biofilms are an ongoing major concern for public health, featuring both inherited genetic resistance traits and a conferred innate tolerance to traditional antibiotic therapies. Biofilms are implicated in over 90% of chronic wounds, the management of which represents an annual cost of £5.6 billion to the NHS (UK) as well as significant patient morbidity and mortality<sup>1</sup>. Consequently, there is a growing need for novel methods of drug delivery, to increase the efficacy of antimicrobial agents. Acoustically stimulated microbubbles (MBs) may have the capacity to enhance the efficacy of antibiotics, thus reducing the dosage required to achieve successful treatment<sup>2</sup>. Similarly, nitric oxide (NO) has been shown to instigate biofilm dispersal mechanisms in clinically relevant biofilms<sup>3</sup>. However, a major problem in the delivery of NO is that it is highly reactive, which translates to a half-life in air of only seconds. By encapsulating it as the gaseous core of an ultrasound-responsive MB, NO is shielded from the external environment. The volumetric oscillations and collapse of MBs upon exposure to an ultrasound field, facilitates physical perturbation of the biofilm and provides the means to control drug delivery both temporally and spatially<sup>4</sup>. Capitalising on the mechanical action of oscillating MBs and the biological effect of NO; dispersal and perturbation of the biofilm induced by nitric oxide microbubbles (NOMBs), can negate the physical barrier imposed by the extracellular matrix and improve treatment outcomes. This work has evaluated the anti-biofilm and bactericidal effects of uncharged room-air microbubbles (RAMBs) and NOMBs, as well as their cationic charged counterparts (RAMBs<sup>+</sup> and NOMBs<sup>+</sup>). The therapeutic efficacy of these formulations *in vitro* was evaluated with cell viability assessments and fluorescence imaging techniques, using relevant pathophysiological models of biofilm infection.

## Methods

All MBs were produced by sonication, with all NOMB formulations produced using degassed medium under a constant flow of nitrogen. NOMBs and RAMBs with mean post-production diameters of 3.3  $\mu\text{m}$  and 3.5  $\mu\text{m}$  (SD  $\pm$  2  $\mu\text{m}$ ), were composed of 1,2-dibehenoyl-sn-glycero-3-phosphocholine (DBPC) and polyoxyethylene (40) stearate (PEG40s) in a 9:1 molar ratio. NOMBs<sup>+</sup> and RAMBs<sup>+</sup> with mean post-production diameters of 5.3  $\mu\text{m}$  and 3.2  $\mu\text{m}$  (SD  $\pm$  2  $\mu\text{m}$ ), were composed of DBPC:PEG40s and 1,2-Distearoyl-sn-Glycero-3-EthylPhosphocholine (DSEPC) in a 9:05:1 molar ratio.

*Pseudomonas aeruginosa* biofilms were grown in IbiDi<sup>®</sup> dishes (ibiTreat,  $\mu$ -Dish 35 mm, Polymer coverslip bottom, Thistle Scientific), containing 1500  $\mu\text{L}$  of a proprietary wound constituent medium (WCM) that featured key pathophysiological components of the *in vivo* wound environment (haemolysed blood, plasma, meat peptones, ketones and salts). The centre of a 1  $\text{cm}^2$  area previously coated in a 50  $\mu\text{g}/\text{mL}$  fibronectin was inoculated with 10  $\mu\text{L}$  of an overnight suspension of *P. aeruginosa* diluted 1:100.

Ultrasound exposure was carried out using a modified iteration of the system for acoustic transfection (SAT) described by Gray *et al.* (2021)<sup>5</sup>. IbiDi<sup>®</sup> dishes containing MB suspensions applied topically to biofilms grown were sealed using an acoustically compatible friction fit lid (sonolid)<sup>6</sup>. Two principal

treatment conditions were used: i) Ultrasound stimulated MBs only, and ii) Ultrasound stimulated MBs with a sub-inhibitory concentration (4 µg/mL) of the antibiotic gentamicin. For all treatments, MB suspensions were diluted in a 1:5 volumetric ratio with either i) sterile PBS, for ultrasound stimulated MBs only tests, or ii) 1:5 in sterile PBS containing gentamicin. The sonolid was held in the SAT by a circular bracket in the pre-focal region of a 64 mm radius, 100 mm radius of curvature, 1.1 MHz centre frequency ultrasound transducer (Sonic Concepts, Inc. Bothell, Washington, USA). The total treatment time was 100 seconds, divided into a 60 second passive interaction period prior to 40 second ultrasound stimulation; each MB formulation was tested in triplicate. Ultrasound stimulation was carried out at 0.9 MHz, 20% duty cycle and a 500 Hz PRF; 45 Vpp was applied to the transducer to reach a peak acoustic pressure of 0.5 MPa at the target site, for 40 s.

The anti-biofilm effect of the treatment was determined by measuring the change in surface area coverage; biofilms in the 1 cm<sup>2</sup> defined area were stained with 2.5 µM Syto9 (S34854, Invitrogen™, ThermoFisher Scientific) and 9 µM propidium iodide (P3566, Invitrogen™, ThermoFisher Scientific) for 15 minutes. Four images per biofilm over the defined 1 cm<sup>2</sup> growth area dish were captured with fluorescence microscopy before treatment. After ultrasound stimulation, the treatment supernatant was removed from the Ibidi® dish. Fluorescence microscopy was used again to acquire post-treatment images of the biofilm, at identical positions over the same 1 cm<sup>2</sup> area observed in pre-treatment images. The minimum cross-entropy Li threshold was applied to images individually<sup>7</sup>; the thresholded images were used to calculate the change in surface area covered by the biofilm in pre- and post-treatment images. To determine the bactericidal effect of the treatment; the 10 mL treatment supernatant aspirated from the Ibidi® dish after ultrasound stimulation, was centrifuged (Eppendorf, 5702R, FisherScientific) at 4000 rpm for 10 minutes to form a pellet of all cellular material. The pellet was re-suspended in 5 mL sterile LB and agitated on a vortex mixer (UY-04726-01, Cole-Parmer, 0 to 3400 rpm, 115 vac), at 3400 rpm for 15 minutes to ensure homogenisation of biofilm aggregates into the medium. Culturable viable cells (CFU/mL) from the biofilm were enumerated using the Miles-Misra method<sup>8</sup>.

## Results

Although ultrasound stimulated MBs alone demonstrate a substantial capacity for biofilm detachment and reducing the proportion of culturable cells, no single formulation tested was able to achieve concurrent high levels of biofilm removal and bactericidal activity. The average reduction in surface area for the no ultrasound control biofilms was 11.1% (SD ± 0.82%) (Fig. 1A); this corresponded to relatively minor observable changes in the biofilm morphology assessed by fluorescence microscopy. Importantly, there was no detectable decrease in biofilm viability, which provided validation that the antibiotic concentration was indeed sub-inhibitory. All MB formulations assessed in conjunction with gentamicin, exhibited a highly statistically significant ( $P = < 0.0001$ ) reduction in biofilm biomass; compared to the no ultrasound control (Fig. 1A). NOMBs and NOMBs<sup>+</sup> produced the most significant reduction in biofilm biomass compared to the no ultrasound control, corresponding to a 99.9% (SD ± 5.21%) and 93.9% (SD ± 2.01%) change, respectively (Fig. 2). RAMBs<sup>+</sup> had a comparable efficacy to NOMBs<sup>+</sup>, eliciting a surface area reduction in biofilm of 92.5%. In these experiments, RAMBs achieved a maximum reduction in biomass of 81.3% (SD ± 4.43%) (Fig. 1A). The relationship between biofilm detachment by the MB-antibiotic suspensions, was consistent with the results obtained for bactericidal activity. In addition to achieving a 99.9% average reduction in biofilm surface area coverage, NOMBs also generated an important 99.9% (SD ± 0.07%) (3-log) reduction in culturable cells. All formulations tested performed significantly better than in previous tests conducted without sub-inhibitory gentamicin (Fig. 1B); the testing of each MB formulation with gentamicin showed NOMBs and both cationic RAMBs<sup>+</sup> and NOMBs<sup>+</sup> were significantly more effective than RAMBs, which attained a 99.4% (SD ± 0.19%) (2-log) reduction in culturable cells. RAMBs<sup>+</sup> and NOMBs<sup>+</sup> equally attained a 99.8% (SD ± 0.06%) (2.5-log) reduction in culturable cells, further validating the efficacy and consistency of MB-antibiotic suspensions (Fig. 1B).

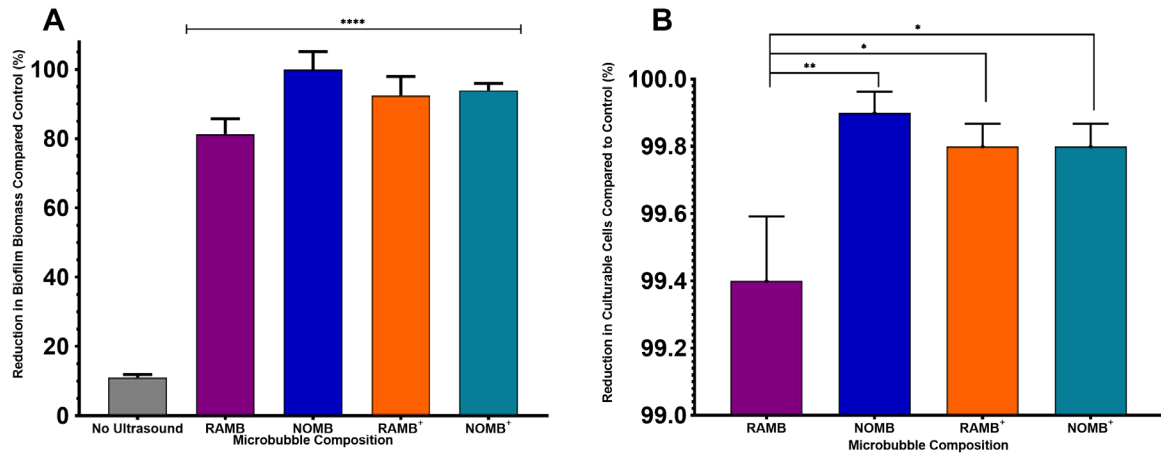


**Figure 1.** The results represent the combined efficacy of each ultrasound stimulated MB formulation co-administered with 4  $\mu\text{g/mL}$  sub-inhibitory gentamicin. (A) The percentage reduction in *P. aeruginosa* biofilm surface area reported here, was determined by calculating the change in surface area of the live/dead stained biofilm before and after treatment in a 1  $\text{cm}^2$  area. The change in surface area induced by the application of MBs and antibiotic in the absence of ultrasound was 11.1%. NOMBs elicited a 99.9% reduction in biofilm surface area, cationic NOMBs<sup>+</sup> were somewhat less effective achieving an average reduction in biomass of 93.9%. RAMBs and RAMBs<sup>+</sup> performed consistently worse than their NOMB analogues, achieving an average reduction in biofilm surface area of 81.3% and 92.5% respectively. (B) The viability of the total biofilm biomass detached during ultrasound stimulation of MBs was assessed by quantifying the average reduction in CFU/mL, compared to a control biofilm exposed to the MB application process and sub-inhibitory gentamicin without ultrasound. NOMBs achieved a 99.9% (3-log) reduction in culturable cells and were significantly more efficacious than RAMBs, which achieved a 99.4% (2-log) reduction in culturable cells. Cationic RAMBs<sup>+</sup> and NOMBs<sup>+</sup> attained an equal 99.8% (2.5-log) reduction in culturable cells, which was also significantly better than RAMBs. Significant differences are indicated as: \*  $P = < 0.05$ , \*\*  $P = < 0.005$ , \*\*\*\*  $P = < 0.0001$ ; error bars indicate standard deviation.

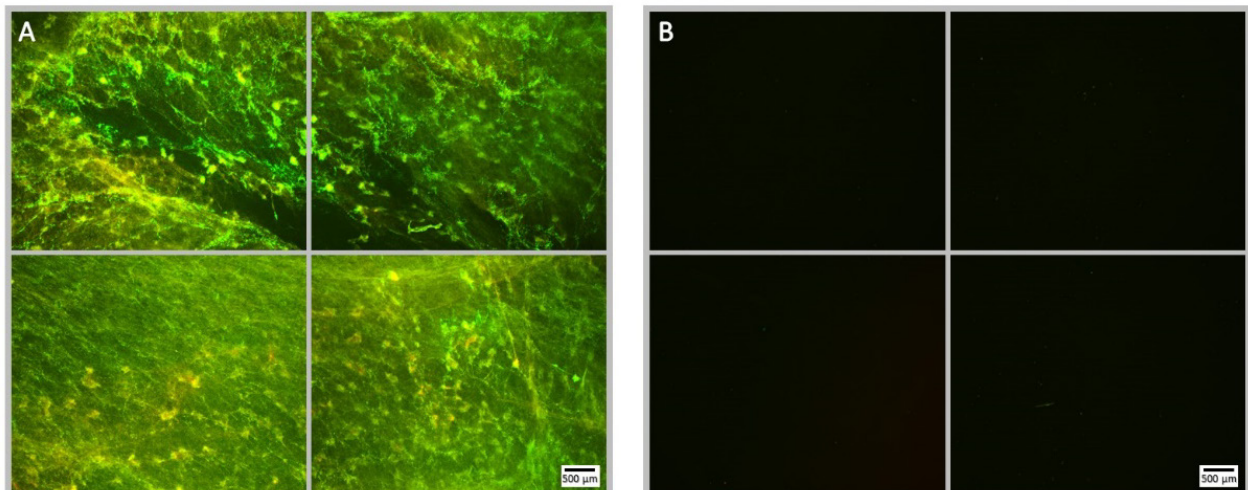


**Figure 2.** Fluorescence microscopy images of *P. aeruginosa* biofilm stained with Syto9 (green) and PI (red); Panel A images depict the pre-treatment morphology of the biofilm over a 1  $\text{cm}^2$  area. Panel B images show the changes in attached biomass after ultrasound stimulation of a NOMB suspension with antibiotic; 45 Vpp was applied to the transducer to reach an acoustic pressure of 0.5 MPa at the target site for 40 s, with a driving frequency of 0.9 MHz, duty cycle of 20% and a 500 Hz PRF. Ultrasound stimulated NOMB and sub-inhibitory gentamicin were able to significantly ( $P = < 0.0001$ ) reduce the surface area of biofilm biomass by 99.9%, compared to controls using a MB-antibiotic suspension without ultrasound.

To the best of the authors' knowledge this is the first study of the efficacy of different types of MB for the elimination of biofilms with a sub-inhibitory concentration of an antibiotic. It can be hypothesised that the differences observed between RAMB and NOMB may be due to priming of the biofilm for biological dispersal by NO which potentiates antibiotic efficacy. Subsequently, ultrasound stimulation and the oscillation of the MB proximal to the biofilm, actively drives the antibiotic deeper into the biofilm architecture and facilitates removal from the surface by mechanical agitation. The SAT device is calibrated to expose the surface of the sonolid (20 mm) to the administered pressure (0.5 MPa), consequently cationic MBs clustered closely together and strongly bound to biofilms can cause distortion of the ultrasound field and thereby reducing the efficacy of the treatment.

## Conclusions

This study has demonstrated the efficacy of ultrasound driven MB and specifically NOMB for the treatment and dispersal of bacterial biofilms *in vitro*. Importantly the biofilm system and complex growth-medium was selected to recapitulate key morphological features of *in vivo* biofilms. The results are therefore promising for the development of new clinical treatments, e.g. for chronic wounds. Future work will extend this study to investigate this approach in multispecies biofilm models.

## References

- [1]. Guest JF, Fuller GW, Vowden P. Cohort study evaluating the burden of wounds to the UK's National Health Service in 2017/2018: Update from 2012/2013. *BMJ Open*. 2020;10(12):45253. doi:10.1136/bmjopen-2020-045253
- [2]. LuTheryn G, Glynne-Jones P, Webb JS, Carugo D. Ultrasound-mediated therapies for the treatment of biofilms in chronic wounds: a review of present knowledge. *Microb Biotechnol*. August 2019;1751-7915.13471. doi:10.1111/1751-7915.13471
- [3]. Howlin RP, Cathie K, Hall-Stoodley L, et al. Low-Dose Nitric Oxide as Targeted Anti-biofilm Adjunctive Therapy to Treat Chronic *Pseudomonas aeruginosa* Infection in Cystic Fibrosis. *Mol Ther*. 2017;25(9):2104-2116. doi:10.1016/J.YMTHE.2017.06.021
- [4]. Kooiman K, Roovers S, Langeveld SAG, et al. Ultrasound-Responsive Cavitation Nuclei for Therapy and Drug Delivery. *Ultrasound Med Biol*. 2020;46(6):1296-1325. doi:10.1016/j.ultrasmedbio.2020.01.002
- [5]. Gray M, Vasilyeva A V., Brans V, Stride E. Studying Cavitation Enhanced Therapy. *J Vis Exp*. 2021;2021(170). doi:10.3791/61989
- [6]. Carugo D, Owen J, Crake C, Lee JY, Stride E. Biologically and acoustically compatible chamber for studying ultrasound-mediated delivery of therapeutic compounds. *Ultrasound Med Biol*. 2015;41(7):1927-1937. doi:10.1016/j.ultrasmedbio.2015.03.020
- [7]. Terheyden JH, Wintergerst MWM, Falahat P, Berger M, Holz FG, Finger RP. Automated thresholding algorithms outperform manual thresholding in macular optical coherence tomography angiography image analysis. Grulkowski I, ed. *PLoS One*. 2020;15(3):e0230260. doi:10.1371/journal.pone.0230260
- [8]. Miles AA, Misra SS, Irwin JO. The estimation of the bactericidal power of the blood. *J Hyg (Lond)*. 1938;38(6):732-749. <http://www.ncbi.nlm.nih.gov/pubmed/20475467>. Accessed March 18, 2019.

# Ultrasound-activated microbubbles for the treatment of fibrin-based biofilms

*K.R. Lattwein<sup>1</sup>, M. E. Starrenburg<sup>1</sup>, J.J.P. Kouijzer<sup>1</sup>, S.A.G. Langeveld<sup>1</sup>,  
H.M. Leon-Grooters<sup>1</sup>, N. de Jong<sup>2,1</sup>, A.F.W. van der Steen<sup>1,2</sup>, MP.M. de Maat<sup>3</sup>,  
W.J.B. van Wamel<sup>4</sup>, and K. Kooiman<sup>1</sup>*

<sup>1</sup> Department of Biomedical Engineering, Thoraxcenter, Erasmus University Medical Center Rotterdam, Rotterdam, the Netherlands

<sup>2</sup> Laboratory of Acoustical Wavefield Imaging, Faculty of Applied Sciences, Delft University of Technology, Delft, the Netherlands

<sup>3</sup> Department of Hematology, Erasmus University Medical Center Rotterdam, Rotterdam, the Netherlands

<sup>4</sup> Department of Medical Microbiology and Infectious Diseases, Erasmus University Medical Center Rotterdam, Rotterdam, the Netherlands

Corresponding author: [k.lattwein@erasmusmc.nl](mailto:k.lattwein@erasmusmc.nl)

## Introduction

Infective endocarditis is a life-threatening bacterial infection of the heart valves and surrounding tissue [1]. Challenges for treatment arise because the bacteria encase themselves in fibrin-based biofilms in order to shield them from both the immune system and antibiotics. One potential treatment strategy emerging in pre-clinical studies is called *sonobactericide*, which combines the use of ultrasound contrast agents and ultrasound, with or without other therapeutics, to directly or synergistically treat bacterial infections [2]. Ultrasound-mediated microbubble oscillations can induce various mechanical, chemical, and biological effects, as well as enhance thrombolytic fibrin degradation in clots [3,4]. Therefore, this study investigated the interaction of ultrasound-activated microbubbles with fibrin-based biofilms, with and without thrombolytics (rt-PA), by assessing real-time responses with high resolution fluorescence microscopy.

## Methods

*Staphylococcus aureus*, which was isolated from an infective endocarditis patient, was used to produce biofilms grown 24 h in human fresh frozen pooled plasma within IbiTreat  $\mu$ -slides under constant agitation. Microbubbles consisted of a DSPC-based coating fluorescently-labelled with the lipid dye DiI and a C<sub>4</sub>F<sub>10</sub> gas core. Fluorophores SYTO 9 and fibrinogen conjugates Oregon Green 488 or Alexa Fluor 647 were used to visualize bacteria and fibrin strands, respectively. Biofilms were exposed to multiple pulses of ultrasound (2 MHz, 400 kPa, 100 or 1000 cycles, every second for 30 s and 1 s continuous wave) every min for 10 min either alone or with a thrombolytic (rt-PA; 158 ng/mL), microbubbles, or rt-PA and microbubbles. Time-lapse confocal microscopy recordings were performed and assessed for fibrin biofilm responses to treatment.

## Results

With ultrasound-activated microbubbles, fibrin strands were observed to displace  $\sim$ 1–5.2  $\mu$ m from their original position (Fig. 1A). The majority of bending fibrin strands exhibited recovery with the longest bent strand (27.7  $\mu$ m) recovering from a 3.7  $\mu$ m displacement in 25.6 s. Bacteria dislodged from fibrin encasement (Fig. 1B) at multiple locations in only groups with ultrasound-activated microbubbles, both with and without rt-PA. Ultrasound alone did not result in fibrin strand alterations or dislodged bacteria from fibrin encasement. Ultrasound and microbubbles with rt-PA present led to fibrin strand bending without recovery and eventual breaking, and a different fibrin degradation pattern (Fig 1C) which led to complete liberation of bacteria on-demand and at a faster rate ( $322 \pm 161$  s) than rt-PA alone ( $518 \pm 86$  s; excluding  $\sim$  45 min from rt-PA exposure until degradation began).

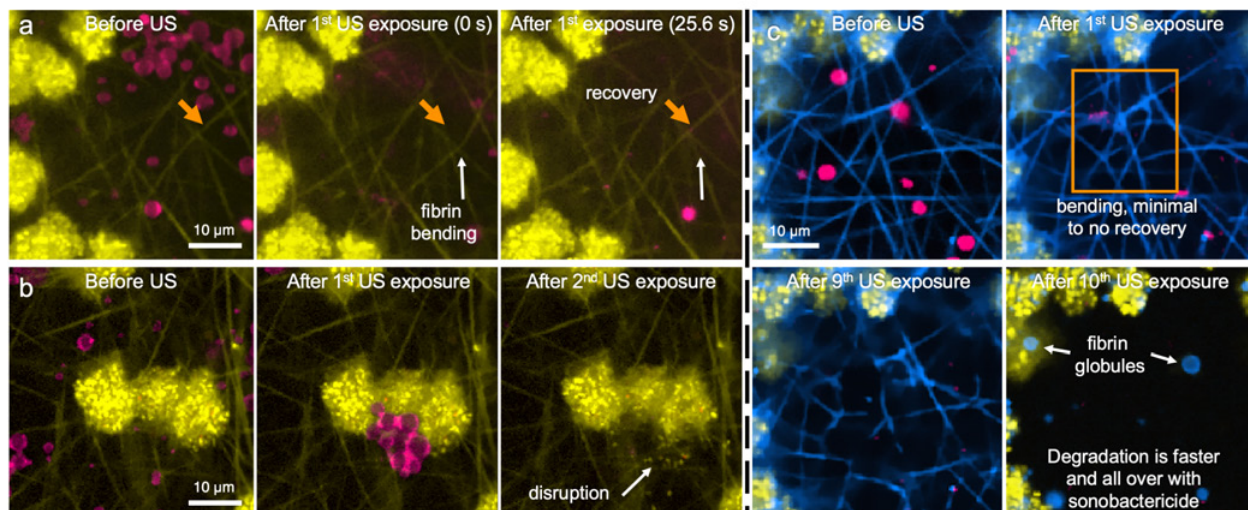


**Figure 1.** Confocal microscopy images from time-lapse recordings of typical examples of fibrin biofilms exposed to ultrasound and microbubbles (pink) without (a, b) or with (c) rt-PA (degrades fibrin). Fibrin and bacteria are yellow in (a,b) and in (c) bacteria are yellow and fibrin is blue. (a) highlights fibrin strand bending and recovery to original position. (b) microbubble clustering and dislodgment of bacteria. (c) fibrin network distortion (unrecovered bending), faster degradation of fibrin and at the same time which is not the case for rt-PA without sonobactericide. Ultrasound (US) = 2 MHz, 400 kPa, 1000 cycles, 30 s PRF of 1 Hz, and 1 s continuous wave, every min for 10 min.

## Conclusions

Ultrasound-activated microbubble effects led to the bending and breaking of fibrin strands, releasement of bacteria from fibrin encasement, and enhancement of thrombolytic efficiency. The developed cardiac-biofilm mimicking biofilm model and sonobactericide treatment settings together provide valuable insight into how ultrasound-activated microbubbles can directly alter fibrin structure and disperse encased bacteria, that both, to the best of our knowledge, have never been observed before in this manner. Harnessing these microbubble-induced effects could aid in the treatment of cardiovascular biofilm infections.

## Acknowledgements

This project has received funding from the Erasmus Medical Center Foundation (Fellowship to K.K.) and European Research Council (ERC) under the European Union's Horizon 2020 research and innovation program [grant agreement 805308 to K.K.].

## References

- [1]. Cahihll TJ, Prendergast BD. Infective endocarditis. *The Lancet*, 387(10021):882-893, 2016.
- [2]. **Lattwein KR**, Shekhar H, Kouijzer JJP, van Wamel WJB, Holland CK, Kooiman K. Sonobactericide: an emerging treatment strategy for bacterial infections. *Ultrasound Med Biol*, 46(2):193-215, 2020.
- [3]. Kooiman K, Roovers S, Langeveld SAG, Kleven RT, Dewitte H, O'Reilly MA, Escoffre JM et al. Ultrasound-responsive cavitation nuclei for therapy and drug delivery. *Ultrasound Med Biol*, 46(6):1296-1325, 2020.
- [4]. **Lattwein KR**, Shekhar H, van Wamel WJB, Gonzalez T, Herr AB, Holland CK, Kooiman K. An *in vitro* proof-of-principle study of sonobactericide. *Sci Rep*, 8:3411, 2018.

# Ultrasound-stimulated phase-change contrast agents to eradicate methicillin-resistant *Staphylococcus aureus* biofilm infections in a diabetic wound model

Sarah E. Rowe<sup>1</sup>, Ashelyn E. Sidders<sup>1</sup>, Kuan-Yi Lu<sup>1</sup>, Amanda Z. Velez<sup>1</sup>, Phillip G. Durham<sup>2,3</sup>, Duyen T. Bui<sup>1</sup>, Paul A. Dayton<sup>2,3</sup>, Brian P. Conlon<sup>1,4</sup>, Virginie Papadopoulou<sup>2</sup>

<sup>1</sup>Department of Microbiology and Immunology, University of North Carolina-Chapel Hill, Chapel Hill, North Carolina 27599, USA

<sup>2</sup>Joint Department of Biomedical Engineering, The University of North Carolina and North Carolina State University, Chapel Hill, North Carolina 27599, USA

<sup>3</sup>Eshelman School of Pharmacy, University of North Carolina, Chapel Hill, NC 27599, USA

Corresponding author: papadopoulou@unc.edu

## Introduction

Chronic wounds are a growing public health threat, with over 6.5 million people affected in the US alone. Bacterial biofilms perpetuate the inflammatory phase of wound healing and are the leading cause of delayed wound healing. The biofilm matrix acts as a protective barrier to the encased bacteria, excluding immune cells and other environmental assaults. Consequently, biofilms become encased in a host-produced matrix of pus, wound slough and immune cells. These host-produced and bacterial-produced biological barriers impede the penetration of oxygen, nutrient and certain antibiotics to the embedded bacteria. This forces the bacteria into a metabolically indolent state (also called persister cells), where they are more tolerant to conventional antibiotics, which target ATP-dependent processes. The two leading factors contributing to the remarkable tolerance of biofilms in chronic wounds are therefore the presence of antibiotic tolerant persister cells and poor drug penetration through the biological barriers. Aminoglycosides, such as gentamicin (Gent), are ineffective against biofilm cells as they maintain proton motive force below the threshold for drug uptake. We employ a novel aminoglycoside adjuvant, palmitoleic acid (PA), to facilitate drug uptake. Here we propose a dual strategy to eradicate a chronic wound infection (Fig. 1); utilizing ultrasound-stimulated phase-change contrast agents (US+PCCA) to improve the penetration of the combination drug Gent/PA that targets persister cells.

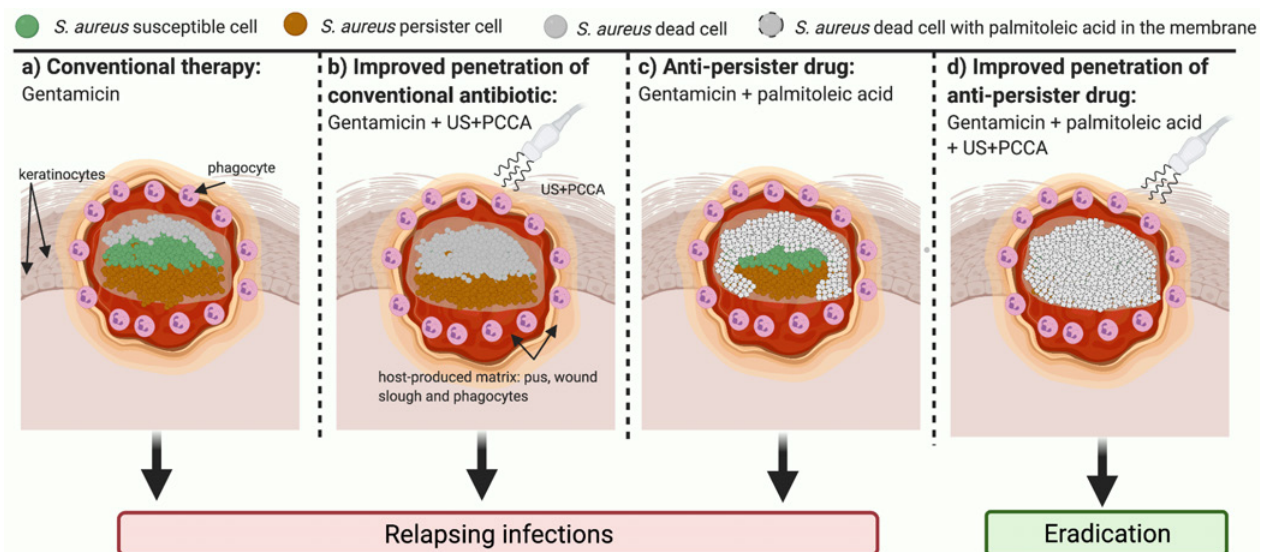


Figure 1. Proposed dual strategy for chronic wound biofilm eradication.

## Methods

A chronic, diabetic wound model of methicillin-resistant *Staphylococcus aureus* (MRSA) infection was established (Fig. 2). Briefly, SKH-1 hairless mice were treated with streptozocin to induce diabetes, then a 4mm circular wound was created on the back of the mice and infected with bioluminescent MRSA. A total of 50 mice were treated topically with gentamicin (Gent), and/or palmitoleic acid (PA), or the vehicle twice daily for 4 days. One daily antibiotic treatments was combined with ultrasound (US), topically-administered phase-change contrast agents (PCCA), combined US+PCCA, or left without additions. On day 5, mice were euthanized and the wound area was excised, homogenized and plated to enumerate colony forming units (cfu). Statistical significance was determined using Kruskal Wallis One-Way ANOVA with Dunn's multiple comparison test.

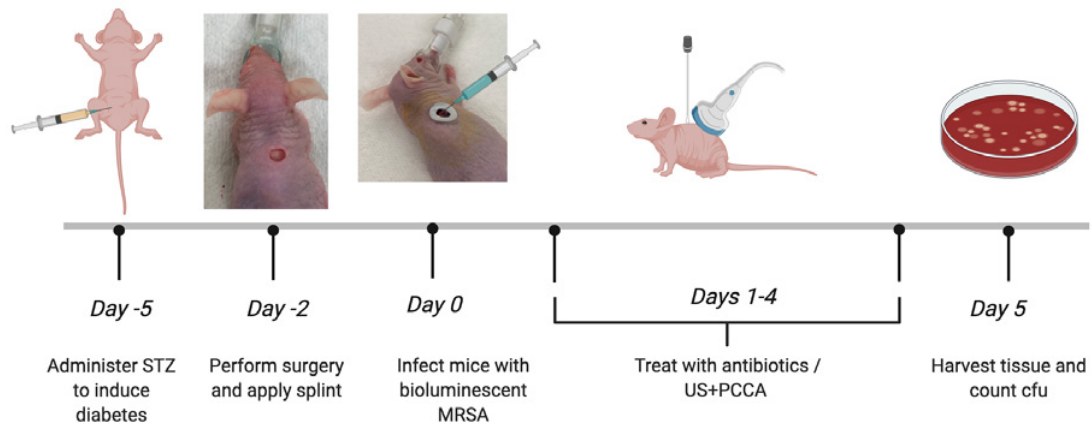


Figure 2. Schematic of our diabetic chronic wound and therapeutic treatments.

## Results

Histopathology of MRSA-infected wounds confirmed the presence of biofilm. Neither Gent nor Gent/PA significantly reduced bacterial burden in the wound. Similarly, Gent/PA combined with ultrasound alone or PCCA alone did not reduce bacterial burden. However, combining Gent with US+PCCA caused a significant reduction in bacterial burden compared to the untreated control. The anti-persister drug combination Gent/PA with US+PCCA caused the greatest decrease in bacterial burden and, importantly, 3 out of 8 mice had no detectable bacteria left (Fig. 3).

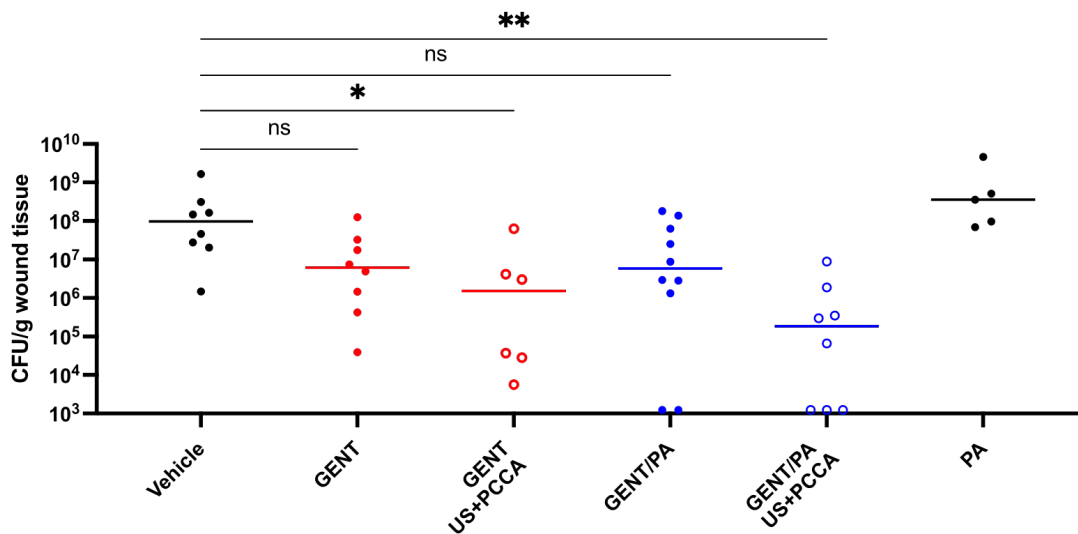


Figure 3. US+PCCA significantly improve antibiotic activity against biofilms in a chronic wound model.

## Conclusions

These data show that improving penetration of a novel anti-biofilm drug combination is a viable strategy to eradicate biofilms in chronic wounds.

# High-frame-rate, contrast enhanced, ultrasound for blood flow quantification in patients with vascular disease

**E. Groot Jebbink<sup>1</sup>**

<sup>1</sup> *Multi-Modality Medical Imaging Group, TechMed Centre, University of Twente, Enschede, The Netherlands*

*Corresponding author: e.grootjebbink@utwente.nl*

The relation between blood flow and remodeling of the vascular system is long known. However, current knowledge is mostly based on in vitro models and invasive measurements. Only since recent years techniques have become available to minimal-invasively study the interaction between blood flow, the vessel wall and (endovascular) treatment techniques in patients. A prime example is the introduction of 2D, high-frame-rate, contrast enhanced ultrasound, combined with particle image velocimetry algorithms (together coined echoPIV). EchoPIV allows for 2D flow quantification with superior temporal resolution, with subsequent heartbeat to heartbeat analysis options. The obtained spatial resolution is in good competition with MRI based flow quantification techniques.

The implementation of echoPIV in the vascular laboratory of our hospital opened up the possibility to start investigating the link between blood flow, atherosclerotic disease progression and patency of endovascular treatment modalities. However, first several feasibility studies were performed to assess if the echoPIV technique could be used to accurately quantify flow in several vessel segments. This was done in both healthy volunteers and patients with peripheral arterial disease before and after endovascular treatment. In total 133 participants were included in 4 trials. In the first trial a comparison between phase contrast MRI and echoPIV showed good agreement between the two techniques with respect to centre line flow velocities over time. Thereafter we showed echoPIV can be used to identify and quantify both disturbed and undisturbed flow, based on indices such as vorticity and flow complexity. Furthermore, limiting factors of the technique in patients with vascular disease were identified, mostly being loss of correlation in very fast and disturbed flow patterns, capturing only a short vessel segment, shadows caused by calcifications and contrast agent destruction during diastole.

Overall echoPIV is a promising candidate to become the tool for reliable flow quantification in a clinical setting. Future follow-up results will also allow us to make comparisons between blood flow, disease progression and stent patency. To overcome several existing limitations a good feedback loop between both clinical application and in vitro testing of technical improvements is crucial.

# AI-based Microbubble super-resolution from raw ultrasound data

*Nathan Blanken<sup>1</sup>, Jelmer M. Wolterink<sup>2</sup>, Hervé Delingette<sup>3</sup>, Christoph Brune<sup>2</sup>,  
Michel Versluis<sup>1</sup>, Guillaume Lajoinie<sup>1</sup>*

<sup>1</sup>*Physics of Fluids group, Techmed Centre, University of Twente, Enschede, The Netherlands*

<sup>2</sup>*Department of Applied Mathematics, Techmed Centre, University of Twente, Enschede, The Netherlands*

<sup>3</sup>*Université Côte d'Azur, Inria, EPIONE team, Sophia Antipolis, France.*

*Corresponding author: g.p.r.lajoinie@utwente.nl*

## **Introduction.**

The resolution of conventional ultrasound (US) imaging modalities is limited to the diffraction limit, which hinders the detection of small lesions. Since these lesions are first and foremost visible through a change in vasculature and flow, ultrasound contrast agents, acting as blood pool agents, seem ideally suited to tackle the challenge. Several recent super-localization strategies based on contrast microbubbles have been showing promise for capillary bed imaging down to 1/10th of the wavelength [1]-[4]. However, these studies primarily focus on high-frequency ultrasound in superficial tissue to achieve a resolution on the order of the capillary vessel sizes. Furthermore, these approaches rely on low contrast concentrations and long acquisition times. Finally, these works use beamformed images and thus do not exploit the specific bubble nonlinearities, which can dramatically improve image sensitivity and specificity. Recovering the bubble locations from the raw data is a complex problem that amounts to deconvolution of largely overlapping signals, and with a convolution kernel (the bubble response) that varies in space and time. To go beyond current limitations, we propose an alternative approach to super-resolution, which relies on both precise nonlinear bubbles simulations and original artificial intelligence (AI) techniques to localize the bubbles directly in the raw ultrasound data.

## **Methods.**

Our strategy consists of: i) generating raw ultrasound data with a custom, fast simulator and ii) training a neural network to detect bubbles within the simulated data. The simulator defines a random spatial distribution of bubbles with a narrow size distribution, i.e. monodisperse, and simulates their response to a propagating plane wave with a pressure ranging from 5 to 250 kPa. The simulator accurately describes the nonlinear dynamics of lipid-coated microbubbles. We use a dilated convolution neural network, trained with 1024 simulated RF lines, to recover the bubble locations within single RF lines (Fig. 1A). A dilated CNN provides a sufficiently large receptive field to capture a bubble signature with its larger context within the RF signal. The CNN was trained to tackle a large range of microbubble concentrations (10 to 1000 bubbles) to investigate the effect of concentration on localisation performance.

## **Results.**

Fig. 1A shows a typical simulated RF signal and the corresponding output of a trained neural network. The output signal shows multiple microbubbles within a wavelength. With a localisation tolerance of 10% of the wavelength, the precision and recall of detected microbubbles are both 0.9. Fig. 1B and C depict a delay-and-sum reconstruction with original and super-resolved RF signals (Fig. 1B) and show both the improvement in resolution, and the excellent localization accuracy.

## **Conclusions**

We have demonstrated that a neural network can accurately localize microbubbles in RF signals containing up to 1000 microbubbles. Our results show that convolutional networks are promising tools for real-time super-resolved imaging of high-density microbubble populations.

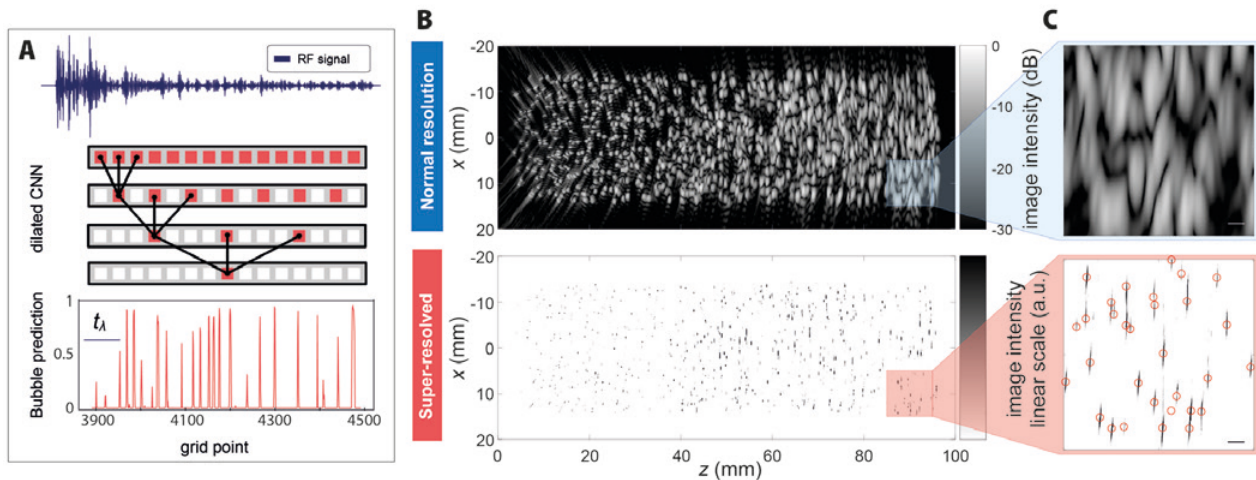


Figure 2: **A.** Concept of the AI strategy used to perform super-resolution imaging based on raw single-channel element radiofrequency (RF) data. The RF signal is fed into a dilated CNN, which outputs a vector of the same size that predicts the probability of microbubble presence at each time sample. The network is trained using a simplified plane-wave simulator and an accurate bubble simulator.  $t_\lambda$  represents the time corresponding to one acoustic wavelength **B.** Greyscale image reconstructed using delay and sum applied to the raw RF signals (top) and to the super-resolved RF signals (bottom) **C.** Zoom on the images of B. at a depth of about 9 cm, showing the applicability of the AI strategy at large depth, despite the small aperture of the transducer. The scale bar represents one acoustic wavelength and the red circles depict the ground-truth position of the bubbles.

## References

- [1]. Christensen-Jeffries K, Couture O, Dayton PA, Eldar YC, Hynynen K, Kiessling F, O'Reilly M, Pinton GF, Schmitz G, Tang MX, Tanter M, Super-resolution ultrasound imaging, *Ultrasound in Medicine & Biology*, 46(4):865-91, 2020.
- [2]. Couture O, Hingot V, Heiles B, Muleki-Seya P, Tanter M, Ultrasound localization microscopy and super-resolution: A state of the art, *IEEE transactions on ultrasonics, ferroelectrics, and frequency control*, 65 (8): 1304-20, 2018
- [3]. Errico C, Pierre J, Pezet S, Desailly Y, Lenkei Z, Couture O, Tanter M. Ultrafast ultrasound localization microscopy for deep super-resolution vascular imaging, *Nature*, 527 (7579): 499-502, 2015
- [4]. Van Sloun RJG, Solomon O, Bruce M, Khaing ZZ, Eldar YC, Misch M, Deep Learning for Super-resolution Vascular Ultrasound Imaging, *ICASSP 2019 - 2019 IEEE International Conference on Acoustics, Speech and Signal Processing (ICASSP)*: 1055-1059, 2019.

# 3D transcranial Ultrasound Localization Microscopy for early discrimination between ischemic and hemorrhagic stroke

***Arthur Chavignon<sup>1</sup>, Vincent Hingot<sup>1</sup>, Cyrille Orset<sup>2</sup>, Denis Vivien<sup>2,3</sup>, Olivier Couture<sup>1</sup>***

*<sup>1</sup>Sorbonne Université, CNRS, INSERM, Laboratoire d'Imagerie Biomédicale, Paris, France.*

*<sup>2</sup>Normandie Univ, UNICAEN, INSERM U1237, Etablissement Français du Sang, Physiopathology and Imaging of Neurological Disorders (PhIND), GIP Cyceron, Institut Blood and Brain @Caen-Normandie (BB@C), Caen, France.*

*<sup>3</sup>CHU Caen, Department of clinical research, Caen-Normandie University Hospital, Avenue de la côte de Nacre, Caen, France*

*Corresponding author: Arthur.chavignon.pro@gmail.com*

## **Introduction**

Stroke is the leading cause of adult disability and the second cause of death in the world. Ischemic strokes, associated with arterial occlusion, represent 80 % of cases. Other cases are associated with cerebral hemorrhages. Both strokes have similar symptoms, but specific and associated treatments, and the stroke must be clearly characterized with cerebral imaging (MRI, CT) [1]. Recently, the development of 3D Ultrasound Localization Microscopy (ULM) [2] has led to a volumetric angiography of the microvasculature [3]. A simpler implementation with a commercial scanner provided a transcranial and noninvasive angiography with a short acquisition time on the rat brain [4]. In this study, we demonstrate the capacity of 3D ULM to discriminate ischemic and hemorrhagic stroke in early phase in rat models.

## **Methods**

Strokes models were induced on anesthetized rats. The ischemic model [5] was performed with an injection of thrombin in the lumen of the middle cerebral artery (MCA) (N=4). For cerebral hemorrhage (N=5), collagenase was injected into the striatum. Transcranial volumetric angiography was performed at 8 MHz with a multiplexed matrix probe (Vermon, France) driven by a Vantage 256 (Verasonics, USA). Microbubbles (Bracco, Italy) were injected via a catheter in the tail vein. For each acquisition, 100k compounded volumes were acquired at 250 Hz within 7 min. RF data were processed with a custom 3D ULM algorithm [6]. ULM acquisitions were performed on animals before the stroke, in the 2 following hours and T+24h, with lesion site validated by MRI. A microvascular diffusion index (MDI) was computed to compare spatially and temporally perfusion.

## **Results**

The brain microvasculature was revealed with 3D ULM at different time points and allowed identification of hypo-perfused regions (Fig 1a). In the early phase of ischemic stroke, a large hypo-perfused area was delimited with a perfusion loss up to 90 %, compared to the reference (Fig 1b). This area can be matched with the vascular territories associated to the MCA. For the cerebral hemorrhage, the model induced a more diffused perfusion loss, mainly spherical centered on the injection site (Fig 1c). The MDI underwent a gradual loss from 39 % at 1h30 (0.61 std 0.87) to 74 % (0.26 std 0.56) at T+24h.

## **Conclusions**

Thanks to 3D ULM, we can reveal local vascular modifications induced by stroke models in the whole brain, even under the skull. The computation of MDI enables the discrimination of ischemic strokes from cerebral hemorrhages in the early phase of stroke symptoms. Its sensitivity to small vessels, such as arterioles, and its flexibility could complement CT and MRI for acute stroke management.

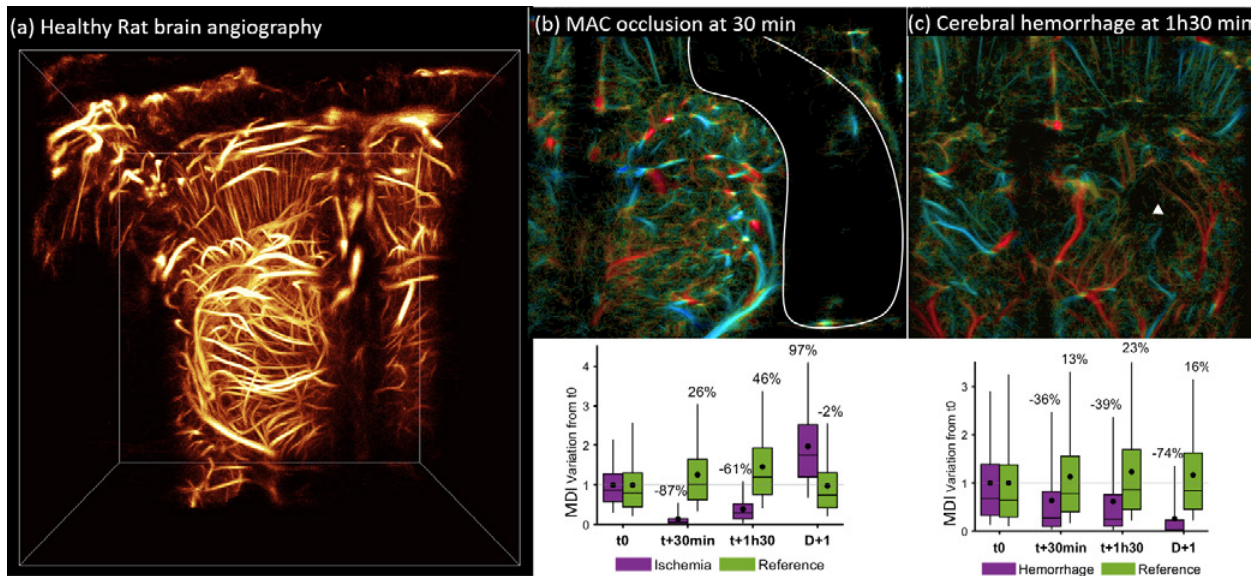


Figure 1. a) 3D ULM on a healthy rat brain. (b-c) Slices of a volumetric angiography with velocity: (b) ischemic model 30 min after injection of thrombin. White ROI: MCA vascular territory. Sudden and total loss of the microvascular index (c) Hemorrhagic stroke model at 1h30 after collagenase injection. White Array: location of the hemorrhage. Gradual and diffuse loss of the MDI.

## References

- [1]. D. Birenbaum, L. W. Bancroft, and G. J. Felsberg, "Imaging in Acute Stroke," *West J Emerg Med*, vol. 12, no. 1, pp. 67–76, Feb. 2011.
- [2]. Kirsten Christensen-Jeffries, Olivier Couture, Paul A. Dayton, Yonina C. Eldar, Kullervo Hynynen, Fabian Kiessling, Meaghan O'Reilly, Gianmarco F. Pinton, Georg Schmitz, Meng-Xing Tang, Mickael Tanter, Ruud J.G. van Sloun, Super-resolution Ultrasound Imaging, *Ultrasound in Medicine & Biology*, Volume 46, Issue 4, 2020, Pages 865-891.
- [3]. B. Heiles et al., "Volumetric ultrasound localization microscopy of the whole brain microvasculature," Sep. 2021. doi: 10.1101/2021.09.17.460797.
- [4]. A. Chavignon et al., "3D Transcranial Ultrasound Localization Microscopy in Rat with a Multiplexed Matrix Probe", *IEEE IUS*, 2020.
- [5]. C. Orset et al., "Mouse Model of In Situ Thromboembolic Stroke and Reperfusion," *Stroke*, vol. 38, no. 10, pp. 2771–2778, Oct. 2007, doi: 10.1161/STROKEAHA.107.487520.
- [6]. B. Heiles et al., "Volumetric ultrafast Ultrasound Localization Microscopy in vivo", *IEEE IUS*, 2019





# Effect of Microbubble and Acoustic Radiation Force Parameters on $\alpha_v\beta_3$ -Microbubble Targeting

*Jair I. Castillo<sup>1</sup>, J. Angel Navarro-Becerra<sup>2</sup>, Mark Borden<sup>1,2</sup>*

<sup>1</sup>*Biomedical Engineering Department, University of Colorado Boulder, Boulder, CO, USA*

<sup>2</sup>*Mechanical Engineering Department, University of Colorado Boulder, Boulder, CO, USA*

*Corresponding author: mark.borden@colorado.edu*

## Introduction

Ultrasound molecular imaging (USMI) employs targeted microbubbles (MBs) decorated with specific ligands to enhance the local visualization of vascular structures [1]. USMI has shown promising results to visualize targets that are usually associated with angiogenesis, thrombosis, and inflammation [2]. For example, angiogenesis is a crucial contributing factor that could potentially predict tumor growth and cancer progression. Overexpression of  $\alpha_v\beta_3$  integrins represents one of the key adhesion-mediated mechanisms that activate the intracellular angiogenic pathways [3]. It has been demonstrated that cyclo Arg-Gly-Asp (cRGD) targeted MBs can bind to  $\alpha_v\beta_3$  integrins providing enhanced images of the tumor vasculature [4]. It is known that acoustic radiation force (ARF) increases the number of polydisperse RGD-MBs adhered to cells [5]. Moreover, it has been demonstrated that the combination of size-selected microbubbles with specific frequencies increases the microbubble displacements [6]. Therefore, we hypothesize that the ARF can increase the number of monodisperse cRGD-MBs attached to  $\alpha_v\beta_3$ . To test this hypothesis, the main goal of this work was to study and elucidate the role of ARF and MB parameters on the targeting of cRGD-MBs using an *in vitro*  $\alpha_v\beta_3$ -coated microvessel phantom.

## Methods

Labeled polydisperse and 2  $\mu\text{m}$  size- isolated MBs (DBPC/DSPE-PEG(5000)/DSPE-PEG(2000)-PDP/Vybrant Dil) attached with cRGD and cRAD, target and control ligand respectively were synthesized. To analyze the MBs targeting, monodisperse MBs have flowed at 1 mL/h in an  $\alpha_v\beta_3$ -coated microvessel phantom ( $D=200 \mu\text{m}$ ) and pushed using UlaOp system in B-mode imaging. Two sets of experimental conditions were tested: 1)  $1 \times 10^7$  MBs/mL MBs pushed with different times (2-10 min); 2) different MB concentrations ( $1 \times 10^5 - 1 \times 10^8$  MBs/mL) pushed 4 min. Ultrasound parameters were set at 3 MHz, 20 cycles and 7 MHz, 47 cycles. To compare the targeting  $1 \times 10^7$  and  $1 \times 10^8$  polydisperse MBs were for 4 min at 7 MHz. For all the conditions cRAD- and cRGD-MBs were used. Finally, z-stack pictures of 10 different sections of the phantom were taken using bright and fluorescent contrast. The attached MBs to the microvessel wall were counted and the amount of MBs attached per  $\text{mm}^2$  was estimated. Specific interactions were obtained by subtracting RGD-MBs and RAD-MBs attached.

## Results

Polydisperse and size-isolated MBs obtained had average diameters of  $\sim 1.8 \mu\text{m}$  (Fig. 1B). Our data showed that with a fixed monodisperse MB concentration, the specific attachment follows an exponential behavior as a function of ultrasound pushing time and is independent of the frequency applied (Fig. 1C). Also, when the monodisperse MB concentration increases, the attachment is dependent on the frequency (Fig. 1D). The attachment of the MBs being pushed at 3 MHz frequency behaved linearly, while the ones being pushed at 7 MHz exhibited an exponential attachment regime. Furthermore, specific attachment interactions, presented a linear dependence and were higher when 7 MHz was applied (Fig. 1E). Finally, attachment of monodisperse population of RGD-MBs increased 8- and 3- fold, than polydisperse MBs.

## Conclusions

We present a detailed multiparametric study which revealed that the combination of ultrasound and MB parameters plays an important role to enhance the microbubble targeting. Moreover, we elucidate that the use of a monodisperse population of MBs improves the molecular specificity for  $\alpha_v\beta_3$  integrin. Finally, our results are set to deepen our knowledge of the variables behind the RGD- $\alpha_v\beta_3$  integrin bond, in order to have better control and understanding to possibly predict behaviors *in vivo* for specific purposes.

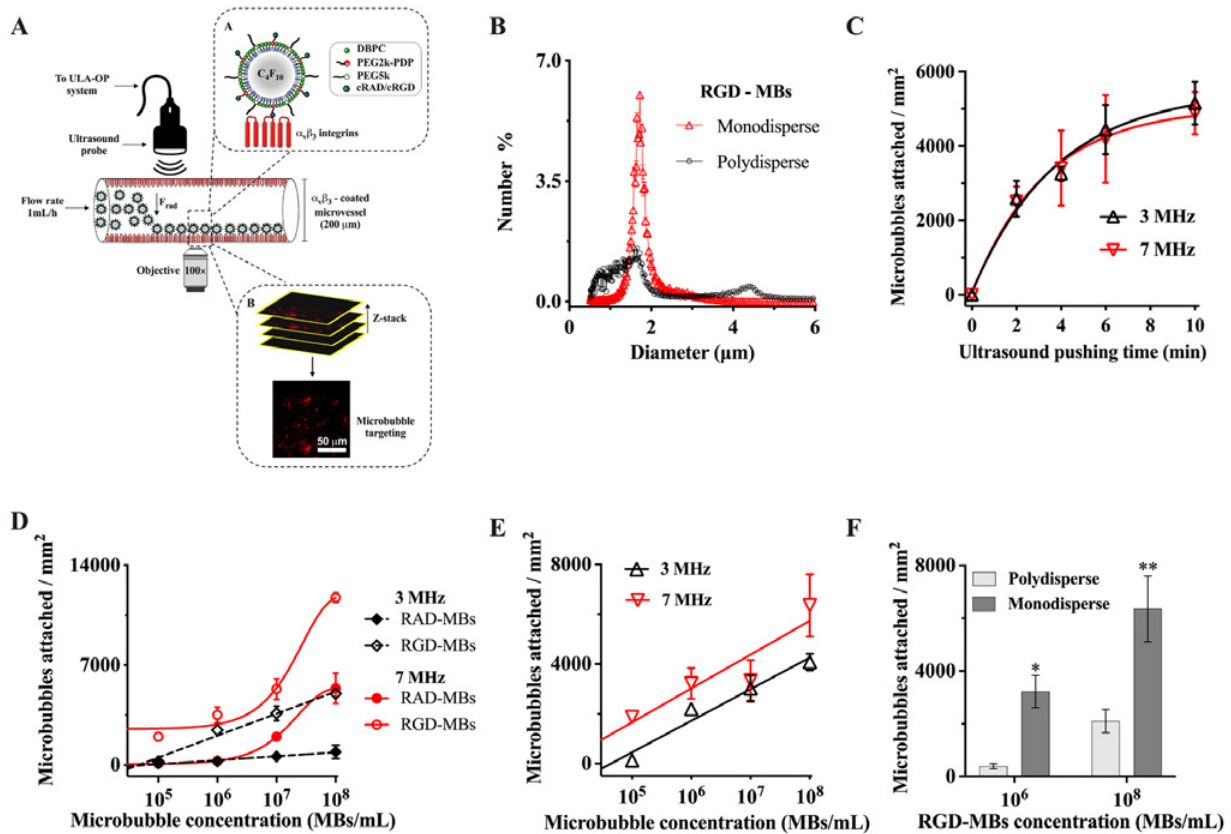


Figure 1. A) Experimental setup to study cRGD- MBs targeting. B) Number – weighted microbubble size distributions. Dependence of microbubble targeting on the C) ultrasound pushing time ( $1 \times 10^7$  MBs/mL), solid lines represent an exponential fit ( $R^2 > 0.90$ ); and D) microbubble concentration, solid lines and dashed lines represent an exponential and linear fit ( $R^2 > 0.95$ ). E) Specific interactions of cRGD-MBs at different frequencies, solid lines represent a linear fit ( $R^2 > 0.86$ ). D) Polydisperse and monodisperse microbubbles attachment comparison. 3 MHz, 20 cycles and 7 MHz, 47 cycles were applied. Data represent the mean  $\pm$  standard deviation for three different experiments.

## References

- [1] Streeter, J. E., Gessner, R., Miles, I., & Dayton, P. A. (2010). Improving sensitivity in ultrasound molecular imaging by tailoring contrast agent size distribution: in vivo studies. *Molecular imaging*, 9(2), 7290-2010
- [2] Borden, M. A., Zhang, H., Gillies, R. J., Dayton, P. A., & Ferrara, K. W. (2008). A stimulus-responsive contrast agent for ultrasound molecular imaging. *Biomaterials*, 29(5), 597-606.
- [3] Weis, S. M., & Cheresch, D. A. (2011). Tumor angiogenesis: molecular pathways and therapeutic targets. *Nature medicine*, 17(11), 1359-1370.
- [4] Borden, M. A., Streeter, J. E., Sirsi, S. R., & Dayton, P. A. (2013). In vivo demonstration of cancer molecular imaging with ultrasound radiation force and buried-ligand microbubbles. *Molecular imaging*, 12(6), 7290-2013.
- [5] Zhao, S., Borden, M., Bloch, S. H., Kruse, D., Ferrara, K. W., & Dayton, P. A. (2004). Radiation-force assisted targeting facilitates ultrasonic molecular imaging. *Molecular imaging*, 3(3), 15353500200404115.
- [6] Supponen, O., Upadhyay, A., Lum, J., Guidi, F., Murray, T., Vos, H. J., ... & Borden, M. (2020). The effect of size range on ultrasound-induced translations in microbubble populations. *The Journal of the Acoustical Society of America*, 147(5), 3236-3247.

# The unique second-wave phenomenon in contrast-enhanced ultrasound imaging with nanobubbles

*Chuan. Chen<sup>1</sup>, Reshani Perera<sup>2</sup>, Michael C. Kolios<sup>3</sup>, Hessel Wijkstra<sup>1</sup>, Agata A. Exner<sup>2</sup>, Massimo Mischi<sup>1</sup>, Simona Turco<sup>1</sup>*

<sup>1</sup>*Eindhoven University of Technology, Eindhoven, the Netherlands,*

<sup>2</sup>*Case Western Reserve University, Cleveland, Ohio, United States,*

<sup>3</sup>*Ryerson University, Toronto, Canada*

*Corresponding author: c.chen3@tue.nl*

## Introduction

Conventional contrast-enhanced ultrasound (CEUS) primarily utilizes microbubbles (MBs) as intravascular ultrasound contrast agents (UCAs) for detecting and quantifying blood perfusion. In recent years, nanobubbles (NBs) have shown promise to become new-generation UCAs [1]. Given the 100 – 300 nm diameter of NBs, which is 10 times smaller than that of MBs, it is reasonable to expect the pharmacokinetics of NBs to differ from that of larger intravascular MBs as well as from that of smaller molecular contrast agents commonly used in MRI and CT [2]. Here, we report for the first time the occurrence of a second-wave phenomenon (a second delayed peak in the contrast-enhanced ultrasound time-intensity curves) unique to NB pharmacokinetics. The first pass of the UCA bolus is usually accompanied by the appearance of a second wave within a time range of about 15 minutes. We focused on analyzing the second-wave phenomenon observed in NB-based CEUS (NB-CEUS), proposing a model for its description and possible utilization in clinical applications.

## Methods

A recently developed NB with higher stability and prolonged half-life was prepared as an UCA [3]. A total of six 4-6-weeks old athymic nude mice were employed for acquiring CEUS images. A dual-tumour model was initiated subcutaneously in the flank of each mouse, as previously described [4]. After administrating 200  $\mu$ L of the NBs in PBS via the mouse tail, a PLT-1204BT probe (frequency, 12 MHz; MI, 0.1; dynamic range, 65 dB; frame rate, 1 fps for the first 5 min and 0.2 fps for the next 25 min) connected to a Toshiba ultrasound machine (AplioXG SSA-790A) was fixed to image two tumor ROIs in the same field of view. The evolution of the NB contrast enhancement over time was recorded to obtain a time-intensity curve (TIC) at each pixel. The pixel-based TICs were fitted by a dedicated model that incorporates the second-wave phenomenon by combining a modified local density random walk (mLDRW) model with an extended retention function as [5, 6]:

$$C(t) = \alpha_1 [C_{mLDRW}(t; t_0, \kappa_1, \mu_1) + \beta_1 C_{mLDRW}(t; t_0, \kappa_1, \mu_1) * e^{-\lambda t}] + \alpha_2 [C_{mLDRW}(t; t_0, \kappa_2, \mu_2) + \beta_2 C_{mLDRW}(t; t_0, \kappa_2, \mu_2) * e^{-\lambda t}]. \quad (1)$$

Here,  $C(t)$  represents the local NB concentration, and  $C_{mLDRW}(t)$  represents the mLDRW model.  $\kappa_1$ ,  $\mu_1$ ,  $\alpha_1$  and  $\beta_1$  represent, respectively, the dispersion-related parameter, mean transit time, and the intensity scaling ratio of the retention function for the first wave. Likewise,  $\kappa_2$ ,  $\mu_2$ ,  $\alpha_2$  and  $\beta_2$  denote the corresponding parameters for the second wave. Specifically, we denote the maximum values of the first wave and the second wave as  $m_1$  and  $m_2$ , respectively.  $\lambda$  represents the decaying rate of retention function.

A number of parametric maps, including  $\lambda$  and  $\log_{10}(m_2/m_1)$  that indicates the peak intensity of the second wave relative to the first wave, were estimated by fitting the pixel-based TICs with the model. The parameter values from the two tumor ROIs and two neighbouring benign-tissue ROIs were compared by the Kolmogorov–Smirnov test (D) to evaluate the parameter ability to distinguish between malignant and benign tissue.

## Results

The model-fitting results of one dual-tumor mouse are shown in Figure 1. The second-wave phenomenon can be observed in the majority of pixel-based TICs. The parametric maps of both

$\log_{10}(m_2/m_1)$  and  $\lambda$  exhibit a clear difference between the tumor lesion and benign tissue outside the tumor. For the parameter values from twelve tumors of six mice, significantly lower  $\log_{10}(m_2/m_1)$  values ( $D > 0.25$ ) and significantly higher  $\lambda$  values ( $D > 0.25$ ) were obtained in tumor lesions compared to the surrounding benign tissues. For the  $\lambda$  values, in particular, there were more than 25.5% high values ( $\lambda > 0.6$ ) found in tumors in comparison with 3.3% high values ( $\lambda > 0.6$ ) present in benign tissue.

### Conclusions

In this study, we presented preliminary results that reveal a unique second peak in the contrast-enhanced ultrasound time-intensity curves observed in NB-CEUS (the second-wave phenomenon). We hypothesized that the formation of the second wave is mainly caused by the in-vivo kinetics of NBs within the internal vasculature and organ structures. By pharmacokinetic modeling that incorporates the second wave, several parametric maps were obtained to analyze the different pharmacokinetics of NBs in tumor and benign tissues. We obtained significantly different parameter values between tumors and benign tissues, suggesting the potential application of NBs in cancer diagnostics.

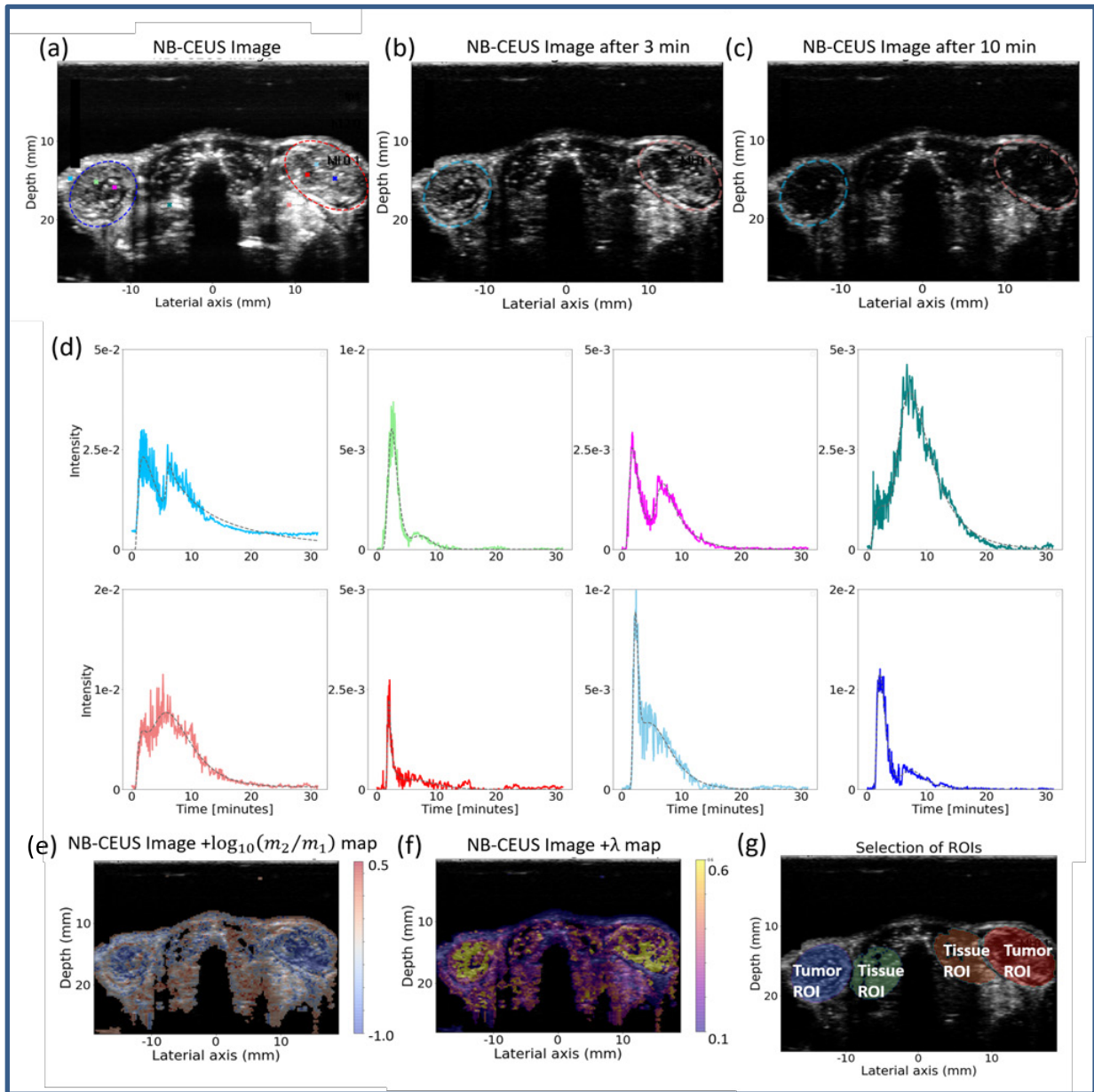


Figure 1. An example of pixel-based TICs and parametric maps in mouse dual-tumor model. (a) presents the maximum intensity projection of the NB-CEUS loop, with the left and right tumor ROIs delineated in blue and red, respectively. The NB-CEUS images acquired 3 and 15 minutes after the injection are displayed in (b) and (c), respectively. In (d), a series of experimental pixel-based TICs (colored solid lines) and corresponding model fit (gray dashed lines) are extracted from different locations which are indicated by the corresponding colored dots in (a). The scales of y-axis vary between subfigures in (d). (e) and (f) present the overlays of parametric maps of  $\log_{10}(m_2/m_1)$  and  $\lambda$  upon the NB-CEUS projection image, respectively. In (g) the ROI corresponding to tumor and benign tissue are indicated by colored masks.

## References

- [1]. Perera RH, Hernandez C, Zhou H, Kota P, Burke A, and Exner AA, Ultrasound imaging beyond the vasculature with new generation contrast agents, Wiley Interdisciplinary Reviews: Nanomedicine and Nanobiotechnology, 7.4:593-608, 2015.
- [2]. Wu H, Abenojar EC, Perera R, An T, and Exner AA, Time-intensity-curve analysis and tumor extravasation of nanobubble ultrasound contrast agents, Ultrasound in medicine & biology, 45.9:2502-2514, 2019.
- [3]. Al de Leon, et al., Contrast enhanced ultrasound imaging by nature-inspired ultrastable echogenic nanobubbles, Nanoscale, 11.33:15647-15658, 2019.
- [4]. Perera, RH. et al, "Real time ultrasound molecular imaging of prostate cancer with PSMA-targeted Nanobubbles, Nanomedicine: Nanotechnology, Biology and Medicine, 28:102213, 2020.
- [5]. Kuenen MP, Mischi M, and Wijkstra H, Contrast-ultrasound diffusion imaging for localization of prostate cancer, IEEE transactions on medical imaging, 30.8:1493-1502, 2011.
- [6]. Turco S, Frinking P, Wildeboer R, Arditi M, Wijkstra H, Lindner JR, Mischi M, Contrast-enhanced ultrasound quantification: from kinetic modeling to machine learning, Ultrasound in medicine & biology, 46.3: 518-543 2020.

# Solid renal cell cancer localization by contrast-ultrasound dispersion imaging

*P.Chen<sup>1</sup>, S. Turco<sup>1</sup>, C. Widdershoven<sup>2</sup>, Z. Liu<sup>1</sup>, J. Oddens<sup>2</sup>, H. Wijkstra<sup>1,2</sup>, M. Mischl<sup>1</sup>, P. Zondervan<sup>2</sup>*

<sup>1</sup>*Department of Electrical Engineering, Eindhoven University of Technology, Eindhoven, Netherlands*

<sup>2</sup>*Department of Urology, Amsterdam University Medical Centers, Amsterdam, Netherlands*

*Corresponding author: p.chen1@tue.nl*

## Introduction

About 9 out of 10 kidney cancers are renal cell cancers (RCCs). Typically, RCC appears asymptomatic at the early stage until progression. Nowadays, over 60% of RCCs are diagnosed incidentally with computed tomography (CT) and ultrasound (US) imaging performed for other medical purposes [1, 2]. Although contrast-enhanced CT scan is the gold standard, a more cost-effective diagnostic method is still in demand for RCC detection and screening, especially at the early stage. Tumor-driven angiogenesis is a recognized hallmark of cancer growth, resulting in a complex and irregular microvascular architecture; as a result, tumor perfusion patterns become distinguishable from those in normal tissue, establishing the basis for diagnostic imaging solutions by cost-effective, quantitative contrast-enhanced ultrasound (CEUS) [3].

In the past years, we have developed contrast-ultrasound dispersion imaging (CUDI) by quantification of CEUS acquisitions, obtaining promising results for prostate cancer localization [4, 5, 6, 7, 8, 9]. Here, we translated CUDI for the quantitative analysis of CEUS acquisitions into the kidney, aiming at investigating its feasibility for primary RCC localization.

## Methods

In this pilot study, the data acquisitions were performed on nine patients at the Amsterdam University Medical Centers (UMC, location AMC, Amsterdam) under approval granted by the local ethics committee. After signing an informed consent, the CEUS recordings were performed by using a Philips iU22 ultrasound scanner (Philips Healthcare, WA) equipped with a C5-2 convex transducer, operating in a contrast-specific mode. A low mechanical index (MI) of 0.19 was used to minimize the destruction of ultrasound contrast agents (UCAs). The scan duration was 120 s following an intravenous injection of a bolus of 2.4 mL SonoVue (Bracco, Milan, Italy) UCA and a subsequent flush of 10 mL saline. During the scanning, the patient was under anesthesia for a planned radical or partial nephrectomy and a short period of timed apnea to overcome the impact of artifacts due to respiratory motion. The first few acquisitions were used to optimize the ultrasound settings and the remaining five acquisitions were used to perform the CUDI analysis.

For each CEUS recording, dedicated pre-processing steps including spatial resolution regularization, motion correction and noise reduction were implemented to improve the image quality. Subsequently, the pre-processed data was analyzed by two different CUDI techniques, namely time-intensity curve (TIC) fitting analysis and spatiotemporal similarity analysis. In TIC analysis, a modified local density random walk model was fitted to the measured TICs, enabling the estimation of a parameter ( $\kappa$ ) related to the local contrast dispersion [4]. From the fitted TICs, typical perfusion parameters such as the appearance time (AppTime) and the full-width at half-maximum (FWHM) were also extracted. As the shape similarity between TICs is influenced by the local degree of UCA dispersion, spatiotemporal similarity analysis was employed to quantify the similarity between neighboring TICs by assessing the spectral coherence (Coherence), the temporal correlation (Correlation) and the mutual information (MutualInfo) [5, 6, 7, 8]. Both approaches aim at extracting parameters that reflect the underlying microvascular architecture. Tumor and parenchyma regions were delineated by two urologists in consensus, based on the

corresponding ultrasound B-mode images and CT scans. Pixel-based classification was then performed by the obtained CUDI parameters in each individual patient data as well as in the combined dataset of the five acquisitions. The area under the receiver-operating-characteristic curve (AUC) was calculated to assess the classification performance.

## Results

Figure 1 shows the CUDI analysis results for one patient. The parametric maps of the TIC fitting analysis and the spatiotemporal similarity analysis results demonstrate the difference between the tumor and parenchyma regions. For the TIC fitting analysis, the values of AUC are 0.61, 0.89 and 0.70 for Kappa, AppTime and FWHM, respectively; the spatiotemporal similarity analysis achieves the AUC of 0.83, 0.78 and 0.84 for Coherence, Correlation and MutualInfo, respectively, indicating that the spatiotemporal similarity analysis outperforms the TIC fitting analysis.

In the combined dataset of the five patient acquisitions, an AUC = 0.69 was obtained by the spatiotemporal similarity analysis.

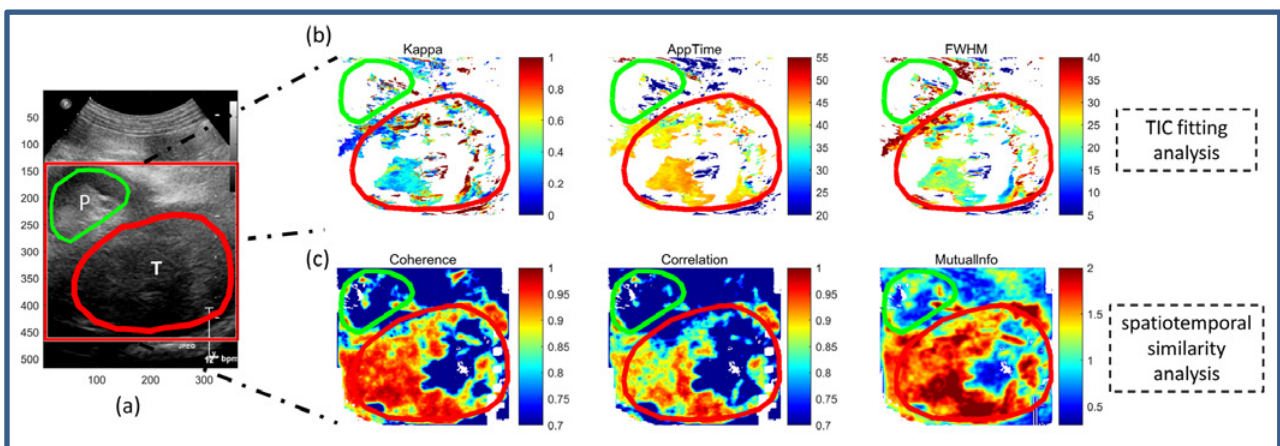


Figure 1. CUDI analysis results for one patient data. (a) is the B-mode image of the kidney. The tumor (T) and parenchyma (P) regions are indicated by red and green contours, respectively. (b) and (c) show the parametric maps of the TIC fitting and spatiotemporal similarity analysis results.

## Conclusions

Our preliminary results show the potential of CUDI for solid RCC localization. However, further validation with an extended dataset is required. It is also worth investigating a multiparametric approach combining multiple, complementary ultrasound markers of kidney cancer.

## References

- [1]. Tosaka A, Ohya K, Yamada K, Ohashi H, Kitahara S, Sekine H, Takehara Y, Oka K. Incidence and properties of renal masses and asymptomatic renal cell carcinoma detected by abdominal ultrasonography. *The Journal of Urology*, 144:1097-1099, 1990.
- [2]. Ljungberg B, Albiges L, Abu-Ghanem Y, Bensalah K, Dabestani S et al. European association of urology guidelines on renal cell carcinoma: The 2019 update. *European Urology*, 75:799-810, 2019.
- [3]. Folkman J. Role of angiogenesis in tumor growth and metastasis. *Seminars in Oncology*, 29:15-18, 2002.
- [4]. Kuenen M, Mischi M, Wijkstra H. Contrast-ultrasound diffusion imaging for localization of prostate cancer. *IEEE Trans. Med. Imaging*, 30:1493-1502, 2011.
- [5]. Mischi M, Kuenen M, Wijkstra H. Angiogenesis imaging by spatiotemporal analysis of ultrasound contrast agent dispersion kinetics. *IEEE Trans. Ultrason. Ferroelectr. Freq. Control*, 59:621-629, 2012.

- [6]. Kuenen M, Saidov T, Wijkstra H, Mischi M. Contrast-ultrasound dispersion imaging for prostate cancer localization by improved spatiotemporal similarity analysis. *Ultrasound in Medicine and Biology*, 39:1631-1641, 2013.
- [7]. Kuenen M, Saidov T, Wijkstra H, de la Rosette J, Mischi M. Spatiotemporal correlation of ultrasound contrast agent dilution curves for angiogenesis localization by dispersion imaging. *IEEE Trans. Ultrason. Ferroelectr. Freq. Control*, 60:2665-2669, 2013.
- [8]. Schalk S, Demi L, Bouhouch N, Kuenen M, Postema A, de la Rosette J, Wijkstra H, Tjalkens T, Mischi M. Contrast-enhanced ultrasound angiogenesis imaging by mutual information analysis for prostate cancer localization. *IEEE Trans. Biomedical Engineering*, 64:661-670, 2017.
- [9]. van Sloun RJG, Demi L, Postema A, de la Rosette J, Wijkstra H, Mischi M. Ultrasound-contrast-agent dispersion and velocity imaging for prostate cancer localization. *Med. Image Anal.*, 35:610–619, 2017.

# Transcranial and volumetric ultrasound localization microscopy with diverging waves

Antoine Coudert<sup>1</sup>, Arthur Chavignon<sup>1</sup>, Vincent Hingot<sup>1</sup>, Louise Denis<sup>1</sup>, Cyrille Orset<sup>2</sup>, Denis Vivien<sup>2,3</sup>, Olivier Couture<sup>1</sup>,

<sup>1</sup>Sorbonne Université, CNRS, INSERM, Laboratoire d'Imagerie Biomédicale, Paris, France

<sup>2</sup>Normandie Univ, UNICAEN, INSERM U1237, Etablissement Français du Sang, Physiopathology and Imaging of Neurological Disorders (PhIND), GIP Cyceron, Institut Blood and Brain @Caen-Normandie (BB@C), Caen, France.

<sup>3</sup>CHU Caen, Department of clinical research, Caen-Normandie University Hospital, Avenue de la côte de Nacre, Caen, France.

Corresponding author: antoine.coudert@sorbonne-universite.fr

## Introduction

Ultrasound Localization Microscopy (ULM) can map the vasculature at a micrometric scale. It has been applied on animals and humans, in 2D and 3D, deep inside tissue and even through the skull [1-6]. Unfortunately, plane-selection is difficult with 2D ULM, which also prevents appropriate flow quantification and motion correction. Moreover, several 2D ULM are needed to image a whole volume. Transcranial 3D ULM could yield a full volumetric image of the human brain microvasculature with a single bolus of contrast agents. However, it imposes new trade-offs on the insonification patterns to optimize the signal-to-noise ratio of individual microbubbles over a large field of view. In this study, we propose cylindrical multiplexing approaches to increase volume rates with diverging waves. We demonstrate its use to characterize microbubble flows behind a human skull phantom and apply it in vivo on a brain sheep.

## Methods

In agar, behind a temporal bone phantom (True Phantom, 4mm thickness, 30dB/cm), we created 2.1mm diameter wall-less vessel phantoms. A matrix probe (32 x 32, pitch 0.5 mm, 1.5 MHz, Vermon) was placed on the bone sample and connected to a Vantage 256 (Verasonics) with a 4-to-1 multiplexer. Microbubbles (Sonovue, Bracco) were injected in tubes with a throughput of 30±2 mL/min. We exploited a combination of 3 cylindrical waves in full-emission mode, in which all elements emit, and 2 spherical waves in synthetic emission instead of 5 spherical waves in synthetic emission. A total of 32k volumes were acquired at 117 Hz frame rate and reconstructed by delay-and-sum beamforming. After a singular value decomposition, microbubbles were localized by radial symmetry and tracked.

In vivo, a 2ml bolus was injected in a 18 months living sheep. The probe was placed on its shaved head. A total of 24k volumes were acquired at a 157 Hz frame rate. Same methods have been used for ULM post-treatment.

## Results

Compared to spherical synthetic emission, cylindrical in full-emission mode allowed a gain in frame rate of 35%, with an improvement in SNR. In vitro, 3D ULM allowed the reconstruction of the flow in the vessel phantom (Fig. 1 A-B). On average, 15±5 bubbles were localized in each volume, leading to a total of 3818 tracks, 14±6mm long. The average fluctuation of the microbubbles position around a linear fit was 172µm (RMSE). Aberration correction should allow to reconstruct the missing pipes (Fig. 1 B-C). Flow profiles followed a laminar flow (Fig. 1 D). First images of sheep brain showed a limited number of vessels behind the skull. (Fig. 1 E).

## Conclusions

This study confirms the possibility to perform volumetric ULM behind a skull with diverging cylindrical waves. In the future, such 3D system could be exploited to image adult human brain through the temporal window and provides diagnosis based on modification of its vascular profile.

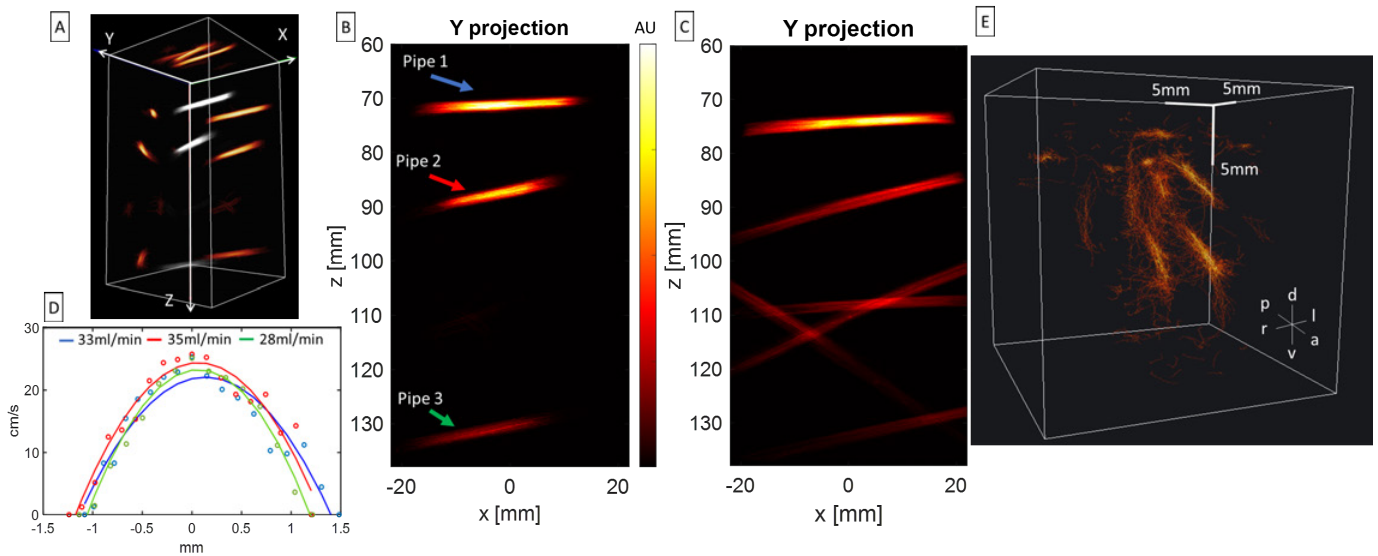


**Figure 1. (A) 3D rendering of ULM density behind skull (white) with projections (yellow). (B) ULM density projection with skull, (C) without skull. (D) Flow profiles behind skull with parabolic fits and flow measurements (pipe 1 : blue line, 2 : red, 3 : green). (E) 3D rendering of ULM density in sheep brain.**

## References

- [1]. Kirsten Christensen-Jeffries, Olivier Couture, Paul A. Dayton, Yonina C. Eldar, Kullervo Hynynen, Fabian Kiessling, Meaghan O'Reilly, Gianmarco F. Pinton, Georg Schmitz, Meng-Xing Tang, Mickael Tanter, Ruud J.G. van Sloun, Super-resolution Ultrasound Imaging, *Ultrasound in Medicine & Biology*, Volume 46, Issue 4, 2020, Pages 865-891, ISSN 0301-5629, <https://doi.org/10.1016/j.ultrasmedbio.2019.11.013>
- [2]. Errico, C., Pierre, J., Pezet, S. et al. Ultrafast ultrasound localization microscopy for deep super-resolution vascular imaging. *Nature* 527, 499–502 (2015). <https://doi.org/10.1038/nature16066>
- [3]. B. Heiles et al., "Ultrafast 3D Ultrasound Localization Microscopy Using a 32  $\times$  32 Matrix Array," in *IEEE Transactions on Medical Imaging*, vol. 38, no. 9, pp. 2005-2015, Sept. 2019, doi: 10.1109/TMI.2018.2890358.
- [4]. Baptiste Heiles et al, Volumetric ultrasound localization microscopy of the whole brain microvasculature, *bioRxiv* 2021.09.17.460797; doi: <https://doi.org/10.1101/2021.09.17.460797>
- [5]. Chavignon et al, 3D Transcranial Ultrasound Localization Microscopy in Rat with a Multiplexed Matrix Probe *IEEE IUS*, 2020.
- [6]. Demené, C., Robin, J., Dizeux, A. et al. Transcranial ultrafast ultrasound localization microscopy of brain vasculature in patients. *Nat Biomed Eng* 5, 219–228 (2021). <https://doi.org/10.1038/s41551-021-00697-x>

# Improved tissue signal suppression through phase segmentation during amplitude modulation with Sonazoid

***Lance H. De Koninck<sup>1</sup>, Connor Krolak<sup>1</sup>, Sara B. Keller<sup>1</sup>, Ting Yu Lai<sup>1</sup>, Michalakis A. Averkiou<sup>1</sup>***

*<sup>1</sup>University of Washington, Department of Bioengineering, Seattle, Washington, USA  
Corresponding author: lancedek@uw.edu*

## Introduction

Contrast-enhanced ultrasound (CEUS) has become a valuable technique for studying tumor macro- and micro-vasculature using the nonlinear microbubble echoes. This is especially useful in imaging the liver to help diagnose Hepatocellular Carcinoma (HCC), the predominant form of liver cancer and the third leading cause of cancer-related deaths worldwide [1]. Sonazoid (GE Healthcare), a contrast agent currently approved mostly in Asia, is very promising for liver oncology due to its high liver specificity (sticks to the liver parenchyma in the late phase) and its acoustic properties (it has a higher threshold of destruction than other microbubbles), lasting longer and allowing for imaging at higher mechanical indexes (MIs) [2]. However, the use of slightly higher MIs leads to an increase in amplitude-induced artifacts in the tissue that reduce the overall contrast-to-tissue ratio (CTR) of CEUS images. Therefore, there is a need for new nonlinear imaging approaches to further suppress tissue signal, specifically when elevated MIs (higher than 0.1) must be used.

Microbubble echoes exhibit an excitation amplitude-dependent phase. In amplitude modulation (AM) 2 pulses are transmitted, a first pulse ( $p_{full}$ ) and a second pulse ( $p_{half}$ ) that is half the amplitude of  $p_{full}$ . The microbubble echoes from these pulses have different phase due to nonlinear scattering. If the phase difference,  $\Delta\Phi_{AM}$ , in tissue due to nonlinear propagation is smaller than in microbubbles due to nonlinear scattering then  $\Delta\Phi_{AM}$  may be used as a criterion for image segmentation to improve CTR. Previously, it was suggested that  $\Delta\Phi_{AM}$  is the result of buckling dynamics of shelled microbubbles as described by the Marmottant model [3,4]. However, here we show that  $\Delta\Phi_{AM}$  is also linked to nonlinear propagation in tissue and nonlinear oscillations of the microbubble gas core in addition to shell properties. The goal of this work was to implement a microbubble segmentation technique based on the phase difference between the 2 pulses in AM for Sonazoid to improve the CTR of CEUS images.

## Methods

### *Bubble dynamics numerical simulations*

To better understand the behavior of microbubble oscillation, two numerical models were used to model shelled and unshelled microbubbles. The unshelled microbubble model was based on the Rayleigh-Plesset equation which describes changes in bubble radius with respect to time due to ultrasound excitation. Scattered echoes from unshelled bubbles insonified with a 1.7 MHz, 4-cycle pulse with pressures ranging from 0.005 to 0.2 MPa were modeled. Microbubble oscillation was simulated using the following parameters: density,  $\rho_L = 1000 \text{ kg/m}^3$ , acoustic pressure,  $P_0 = 100 \text{ kPa}$ , surface tension,  $\sigma_w = 0.0725 \text{ N/m}$ , polytropic exponent,  $\kappa = 1.1$ , speed of sound,  $c = 1486 \text{ m/s}$ , liquid viscosity,  $\mu_L = 0.001 \text{ Pa}\cdot\text{s}$ , for microbubble radii ( $R_0$ ) spanning from 0.5 to 3  $\mu\text{m}$  [3,4]. Radial oscillation was converted to scattered pressure ( $p_s$ ) using the following equation:

$$P_s = \frac{\rho_L R}{r} (2\dot{R} + R\ddot{R}), \quad (1)$$

where  $R$  is the radius as a function of time and  $\dot{R}$  and  $\ddot{R}$  are the first and second time derivatives of  $R$ .

The shelled microbubble model is the one developed by Marmottant. It is effectively an extension of the Rayleigh-Plesset equation that includes shell parameters [4]. The same fluid parameters were used to simulate the shelled bubbles as the free gas bubbles, with the addition of  $\kappa_s = 1.5 \times 10^{-8} \text{ kg/s}$  and  $\chi = 1.55$

[3,4]. The buckling radius and the rupture radius were defined to be 99% and 102% of the starting radius, respectively.

#### *Phase calculations*

First, echoes from the  $p_{full}$  and  $p_{half}$  pair in AM,  $Ps_{full}(t)$  and  $Ps_{half}(t)$  were filtered using an FIR bandpass filter centered around the center frequency of the transmitted pulse. The filtered echoes were then converted to their analytic signal using a Hilbert Transform, which resulted in a complex form of the wave from which phase could be extracted as follows:

$$\Phi_{full}(t) = \angle Ps_{full}(t) \quad (2)$$

$$\Phi_{half}(t) = \angle Ps_{half}(t) \quad (3)$$

where  $\angle$  is the “angle” operator on the analytic signals. The difference in phase,  $\Delta\Phi_{AM}(t)$ , between the AM echo pair was calculated at each time point as

$$\Delta\Phi_{AM}(t) = \Phi_{full}(t) - \Phi_{half}(t), \quad (4)$$

and then averaged over the pulse length to get a single value of  $\Delta\Phi_{AM}(t)$  for each AM pair.

#### *RF data acquisition in a flow phantom experiment*

A single-channel flow phantom was connected to a flow system in a closed-loop setup. A 1 L beaker of deionized water was placed on a magnetic stir plate and connected to a peristaltic pump to drive flow. Sonazoid was added to the beaker as a 1:10,000 dilution and allowed to mix before flow. A C5-1 imaging transducer connected to a Phillips iU22 scanner was coupled to the tissue phantom with ultrasound gel. The C5-1 was operating in AM contrast mode at a center frequency of 1.7 MHz and at mechanical indexes (MIs) of 0.16, 0.21, and 0.33.

Radiofrequency (RF) data were acquired using a research interface. For each MI, 3 RF frames were collected where microbubbles were allowed to flow to minimize the effect bubble destruction. The RF data was imported into MATLAB for offline processing, which consisted of post-beamformed imaging lines acquired prior to envelope detection and log compression. Two regions of interest (ROIs) were created to evaluate  $\Delta\Phi_{AM}(t)$ : one within the tube (evaluating microbubble echoes) and another ROI above the tube (evaluating tissue echoes).  $\Delta\Phi_{AM}(t)$  was first calculated between a start and end time index and then averaged over a start and end line index within the ROI. Finally,  $\Delta\Phi_{AM}$  was averaged over 3 frames for each MI tested.

## **Results**

Examples of the shelled and unshelled simulations are shown in Fig. 1. The left and middle columns show radius and scattered pressure versus time curves (respectively) at two excitation pressures for simplicity. The right column shows the  $\Delta\Phi_{AM}$  resulting from all bubble radii when all pressure cases are considered. Both shelled and unshelled bubbles show a negative phase change that is consistent with prior work. Furthermore, both shelled and unshelled bubbles show a  $\Delta\Phi_{AM}$  with a magnitude exceeding what has previously been used for phase segmentation (0.1-0.3 rad) [3]. However, where the  $\Delta\Phi_{AM}$  of the unshelled bubble seems mostly dependent on pressure, the  $\Delta\Phi_{AM}$  from the shelled bubble seems more reliant on bubble radius, where lower acoustic pressure and larger bubble radii give a greater  $\Delta\Phi_{AM}$ .

Figure 2 shows the image of the flow phantom that was used for RF data analysis (left) and the calculated  $\Delta\Phi_{AM}$  (right). The ROIs used for calculating the phase in the tissue and the bubbles are drawn in the left image. While the resultant  $\Delta\Phi_{AM}$  remains close to zero for the tissue signal, it increases with increasing amplitude for Sonazoid. This suggests that a segmentation approach based on phase would be ideal for

Sonazoid and especially important at elevated MIs. In addition, the negative  $\Delta\Phi_{AM}$  is consistent with our simulated predictions.

Fig. 3 shows the implementation of the phase segmentation technique for 2 MIs: 0.16, and 0.33. The actual images on the scanner are shown in the left column, and in the middle column the non-scan-converted images reconstructed from the RF data are shown. There are a few differences in the compression parameters between the two. The right column shows the segmented versions of the images in the middle column. The effect of segmentation at low MI (top row) is minimal whereas for the higher MI (bottom row) is more pronounced where the tissue image, including the part that comes from the so-called nonlinear propagation artifact, is effectively suppressed.

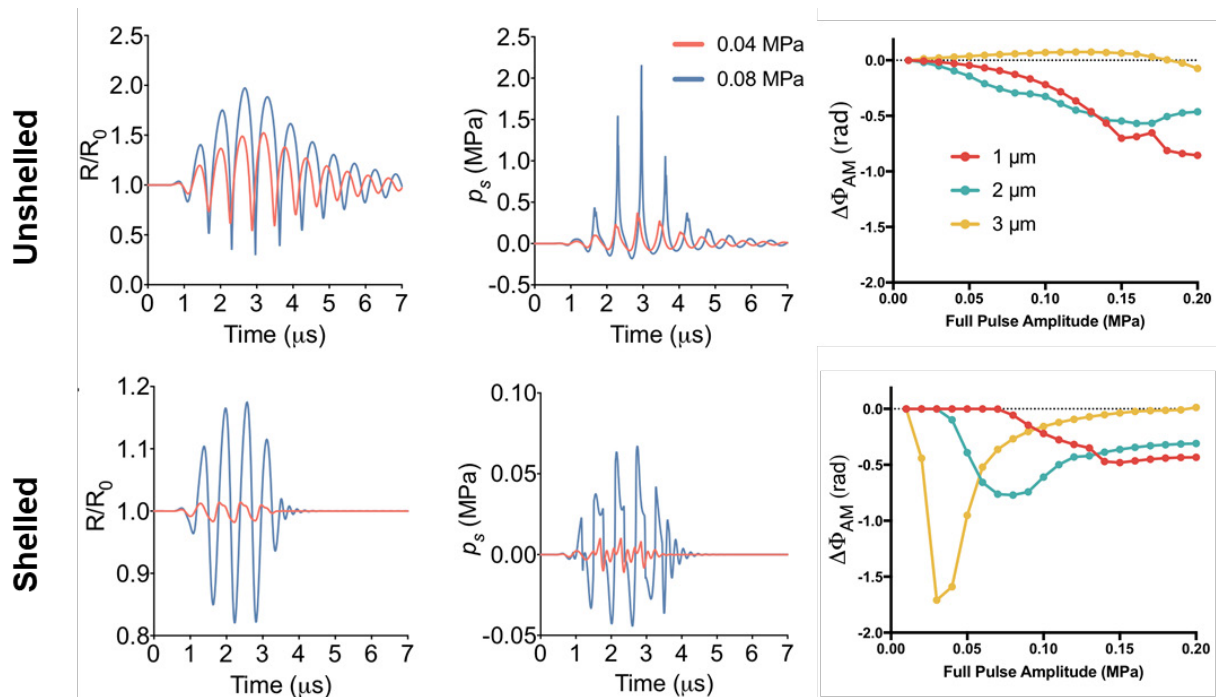


Figure 1. Example radius- (left column) and scatter pressure ( $p_s$ ) (middle column)-versus time curves from  $2 \mu\text{m}$  radius unshelled or shelled bubbles with 0.04 and 0.08 MPa pressures. (Right column)  $\Delta\Phi_{AM}$  as a function of full pulse amplitude for all radius sizes.

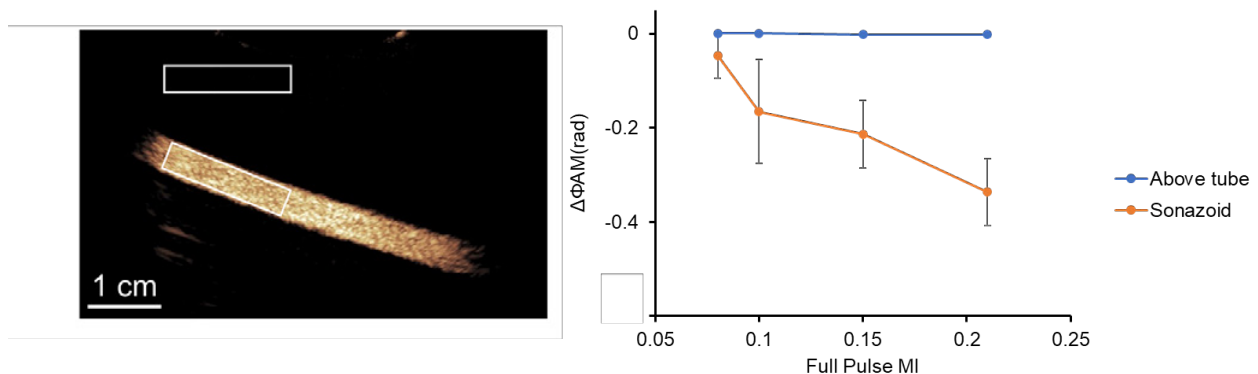


Figure 2. The left image shows the regions of interest (ROIs) selected for analyzing phase: A ROI for microbubble echoes placed in the tube and a ROI for tissue signal placed above the tube. The right image shows  $\Delta\Phi_{AM}$  measurements for Sonazoid calculated from the microbubble echoes in the radiofrequency (RF) data.

## Conclusions

The phase difference between full and half amplitude echoes during AM was investigated through simulations and RF data of Sonazoid microbubbles. From our simulations, we observed that both shelled and unshelled microbubbles resulted in a  $\Delta\Phi_{AM}$  with similar overall magnitude but some differences in trends:  $\Delta\Phi_{AM}$  was greatest at large acoustic pressures for unshelled cases, while  $\Delta\Phi_{AM}$  was greatest at large bubble radii and small acoustic pressures for the shelled cases. Regardless, evaluating  $\Delta\Phi_{AM}$  for a free gas bubble in this context has not been done before, and suggests that nonlinear oscillation is the determining mechanism of  $\Delta\Phi_{AM}$  rather than shell parameters. Finally, we offer an example of the implementation of this technique further supporting our analysis here and demonstrating effective removal of nonlinear amplitude-dependent artifacts. Implementation of this segmentation technique in real-time scanning will be very beneficial for clinical scanning of Sonazoid in the liver.

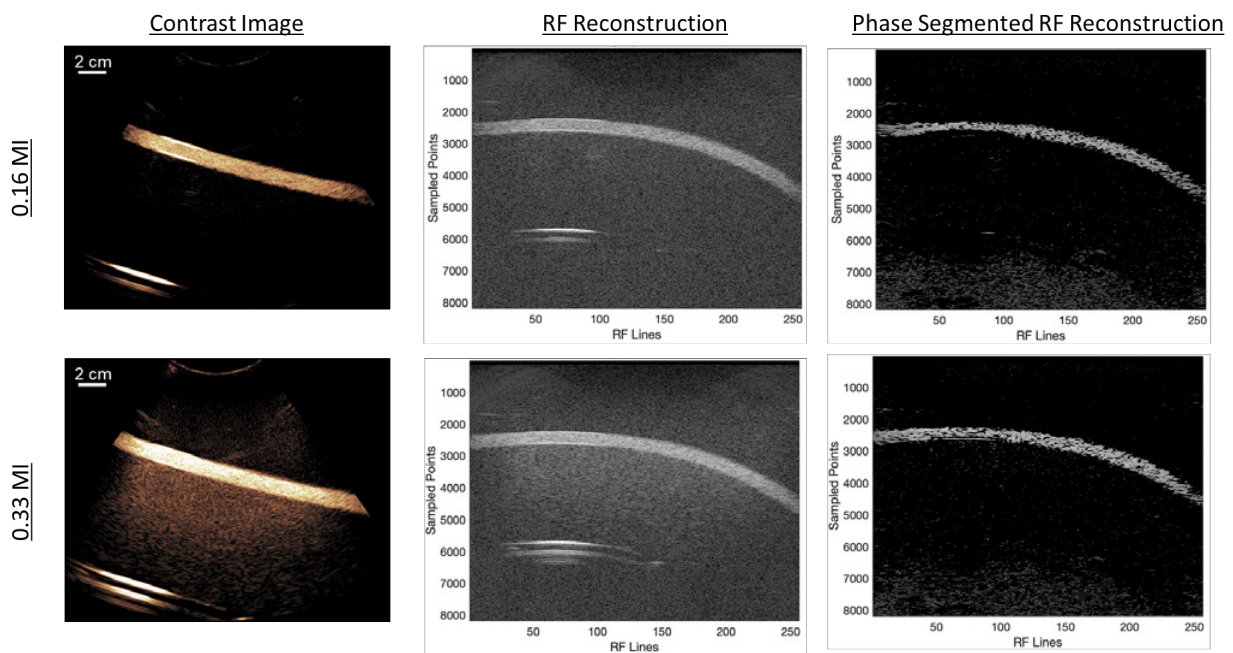


Figure 3. Implementation of the phase segmentation technique for 2 MIs: 0.16 and 0.33. (Left column) Actual contrast images of flow phantom, (middle column) the non-scan-covered images reconstructed from RF data, and (right column) phase-segmented version of middle column images.

## Acknowledgements

We would like to thank GE Healthcare for providing the Sonazoid microbubbles used in this study. This work was supported by a research grant from the GE Healthcare.

## References

- [1]. El-Serag HB, Rudolph KL. Hepatocellular carcinoma: epidemiology and molecular carcinogenesis. *Gastroenterology* 2007; 132:2557-76.
- [2]. Averkiou MA, Bruce MF, Powers JE, Sheeran PS, Burns PN. Imaging Methods for Ultrasound Contrast Agents. *Ultrasound in Medicine & Biology* 2019.
- [3]. Tremblay-Darveau et al., "The Role of Microbubble Echo Phase Lag in Multipulse Contrast-Enhanced Ultrasound Imaging," *IEEE Transactions on Ultrasonics, Ferroelectrics, and Frequency Control*, 65:8:1389–1401, 2018.
- [4]. P. Marmottant et al., "A model for large amplitude oscillations of coated bubbles accounting for buckling and rupture," *The Journal of the Acoustical Society of America*, 118:6:3499–3505, 2005.

## Quantitative nonlinear ultrasound localization microscopy

*Jonah S. Harmon<sup>1</sup>, Zin Z. Khaing<sup>1</sup>, Lindsay N. Cates<sup>1</sup>, Charles Tremblay-Darveau<sup>3</sup>, Christoph P. Hofstetter<sup>1</sup>, Matthew F. Bruce<sup>2</sup>*

<sup>1</sup>*Department of Neurological Surgery, University of Washington, Seattle, USA*

<sup>2</sup>*Applied Physics Laboratory, University of Washington, Seattle, USA*

<sup>3</sup>*Philips Medical Systems, Bothell, USA*

*Corresponding author: mbruce@uw.edu*

### Introduction

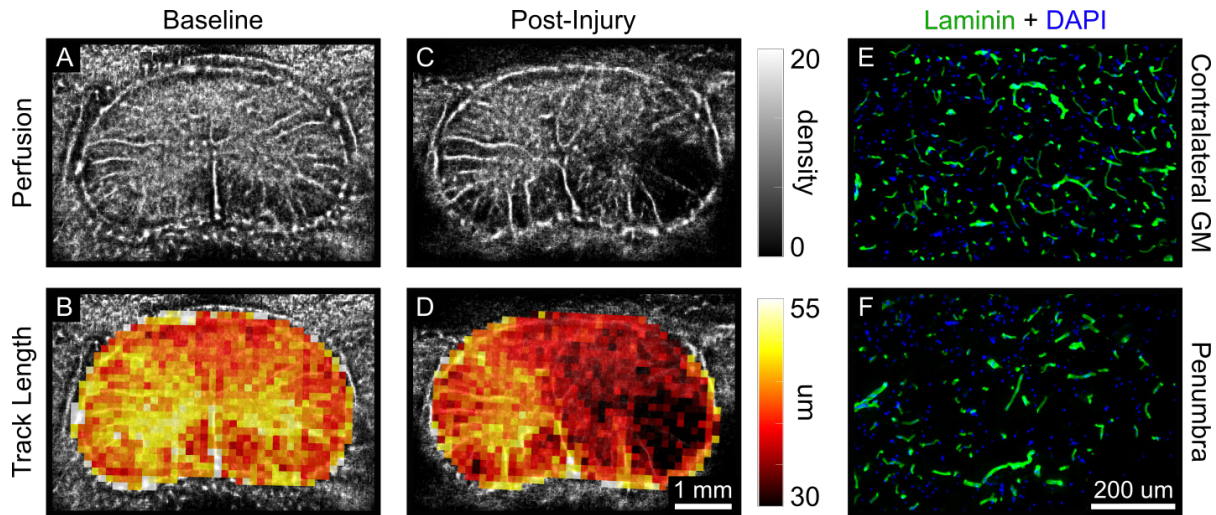
Current ultrasound localization microscopy (ULM) approaches utilize linear pulsing schemes, necessitating high-pass wall filtering in order to isolate circulating microbubbles from tissue clutter. This approach excludes signals from low velocity microbubbles due to spectral overlap with tissue motion, preventing investigation of blood flow at the level of tissue perfusion. In this work, we use ultrafast nonlinear plane wave acquisitions to segment microbubble signals independent of velocity. We then isolate the slowest microbubbles using the singular value decomposition (SVD) to produce ULM images of the microcirculation, using the rat spinal cord as a model system. In addition to generating higher resolution images, extraction of quantitative microbubble track parameters represents a novel feature set that can be utilized to describe the relative quality of microcirculatory flow.

### Methods

An amplitude modulated multiangle plane wave sequence was implemented on a Verasonics research ultrasound platform (Kirkland, WA, USA) in combination with a 15 MHz linear array transducer (Vermon, Tours, France). Imaging was conducted in the rat spinal cord at cervical level 5 at baseline and immediately following a moderate unilateral contusion injury (150 kDyn, Infinite Horizon impactor, Precision Systems, VA, USA). Ensemble acquisitions (400 Hz effective PRF) were motion corrected and SVD filtered prior to bubble localization using a weighted average method. Tracking was based on the Hungarian pairing algorithm. Tracks were accumulated across 10 ensembles (18 seconds total acquisition time) to generate output images. The total in-plane travel distance, duration, and velocity were recorded for each bubble track. Parametric maps were generated by displaying the mean values of a given track feature in 25  $\mu\text{m}^2$  bins overlaid on ULM bubble density images. Bins that contained fewer than 10 tracks were excluded from display.

### Results

Nonlinear ULM images are shown alongside parametric maps in Fig. 1 (A-D). In this case, the mean in-plane travel distance (i.e., track length) is shown in each bin. At baseline (A-B), the parametric map recapitulates meaningful biological contrast between the gray matter (center “butterfly”) and white matter (periphery). Following contusion injury, the bubble density image clearly depicted an ischemic deficit on the ipsilateral side (1.44  $\text{mm}^2$ ). The corresponding parametric map revealed a gradation in track length between the contralateral gray matter and penumbral tissue adjacent to the ischemic core ( $41.5 \pm 3.01$  vs  $33.0 \pm 2.31$   $\mu\text{m}$ , respectively; mean  $\pm$  SD). Laminin staining (E-F) depicted differences in microvessel density (504 vs 283 vessels/ $\text{mm}^2$ ) and mean vessel length ( $19.8 \pm 1.12$  vs  $16.5 \pm 1.51$   $\mu\text{m}$ ; mean  $\pm$  SEM) between the contralateral gray matter and penumbra, thereby supporting differences observed in the parametric maps.



### Conclusions

Nonlinear ultrafast imaging enables isolation of the slowest flowing microbubbles, allowing us to apply ULM processing to the microcirculation for the first time. This has utility beyond improving image resolution. Localizing and tracking individual circulating microbubble contrast agents provides a rich quantitative feature set that has not yet been comprehensively explored. In this particular example, changes in in-plane microbubble track length highlight the penumbral “tissue at risk” for further secondary damage following spinal cord injury; this is corroborated with histological analysis. In conjunction with access to true microcirculatory flow signals, nonlinear ULM may serve as a valuable new method for quantifying microcirculatory flow dynamics in the context of diagnosis and treatment guidance.

Figure 1. Nonlinear ULM images are shown in the cervical rat spinal cord before (A-B) and after (C-D) unilateral contusion spinal cord injury. Bubble density images depict a clear ischemic core following injury (A, C; right side), while parametric maps of in-plane microbubble track length reveal a clearer gradation in the penumbra immediately adjacent to the injury, and a slight impact on the contralateral gray matter as compared to baseline (B, D). Histological images illustrate a corresponding reduction in microvessel density and average vessel length between the contralateral gray matter and the penumbra (20 μm section thickness).

## 3D Nonlinear Sound-Sheet Imaging of Acoustic Biomolecules

*B. Heiles<sup>1</sup>, O. Weidlich<sup>1,2</sup>, D. Terwiel<sup>1</sup>, J. van Leeuwen<sup>1</sup>, D. Maresca<sup>1,\*</sup>*

<sup>1</sup>*Department of Imaging Physics, Delft University of Technology, Delft, The Netherlands*

<sup>2</sup>*Department of Health Technology, Technical University of Denmark, Lyngby, Denmark*

*\*Corresponding author: d.maresca@tudelft.nl*

### Introduction

The discovery of genetically encoded acoustic biomolecules known as gas vesicles (GVs) enables fundamental advances in molecular ultrasound such as imaging of gene expression [1]. GV's have been further modified to exhibit pressure-dependent nonlinear scattering [2] and successfully engineered into acoustic biosensors of enzyme [3].

Improvements in genetically encoded ultrasound contrast agents [4], as well as increasingly diverse disease models and applications, provide a strong demand for higher-speed 3D ultrasound imaging methods dedicated to GV detection. Up until now, an amplitude modulation sequence based on cross-propagating plane waves (xAM) has provided the most sensitive and specific ultrasound images of GV's [5]. Because xAM imaging performs line-by-line scanning of samples using a relatively large sliding sub-aperture, it is intrinsically limited in both framerate and field of view [6].

Here, we overcome these limitations by introducing 3D nonlinear sound-sheet imaging (NSSI), an ultrasound pulse sequence that modulates pressure amplitude across wide imaging planes at kilohertz framerates. NSSI relies on the interaction of two intersecting planar excitations of thin elongated line elements. Cross-propagation occurs at their intersection, and generates a sound sheet perpendicular to the active surface of the probe. The position of this sound-sheet can be moved by changing the elements used to transmit. We implemented NSSI at 15 MHz with a row-column addressed (RCA) probe which enabled orthogonal sound-sheet micro-scanning across a volume of 1.2 cm<sup>3</sup>. We demonstrate the imaging potential of NSSI by imaging several engineered GV variants in an in vitro context.

### Methods

**NSSI sequence.** A custom-built 15 MHz 128+128 elements RCA probe was driven using a 256 channel programmable high-framerate ultrasound scanner. Rows (and alternatively columns) were used to transmit simultaneous cross-propagating plane waves from two contiguous half-apertures  $D_{Ap/2}$  at angles  $\alpha$  and  $-\alpha$ . The two transmitted plane waves span the whole elevation width of the RCA probe and intersect along a 2D plane, referred to as the sound-sheet (**Figure 1a**). A double amplitude planar wave-front is generated at the plane waves intersection and propagates across the sound-sheet plane at a supersonic velocity  $\frac{c_0}{\cos(\alpha)}$  [5]. Image reconstruction of the echoes received by the columns of the RCA probe relies on delay-and-sum beamforming [7] with the assumption that backscattering only arises from the sound-sheet plane (**Figure 1b**).

The same sub-apertures were used for two additional transmits, each firing independently this time, and eliciting half-amplitude linear backscattering from the medium. The amplitude-modulated signal was obtained by subtracting the two single amplitude to the double amplitude received RFs (**Figure 1c**). A large volume can be captured by sweeping these 3-pulse transmissions along the rows of the array.

To increase signal-to-noise ratio, angular compounding can be implemented at every sound sheet position, covering a range of transmit angles  $\alpha$  compatible with cross-propagation. Orthogonal scans along both the rows and columns can also be realized to achieve high contrast 3D Sound Sheet Imaging (SSI) using only the double-amplitude transmit (**Figure 1d**).

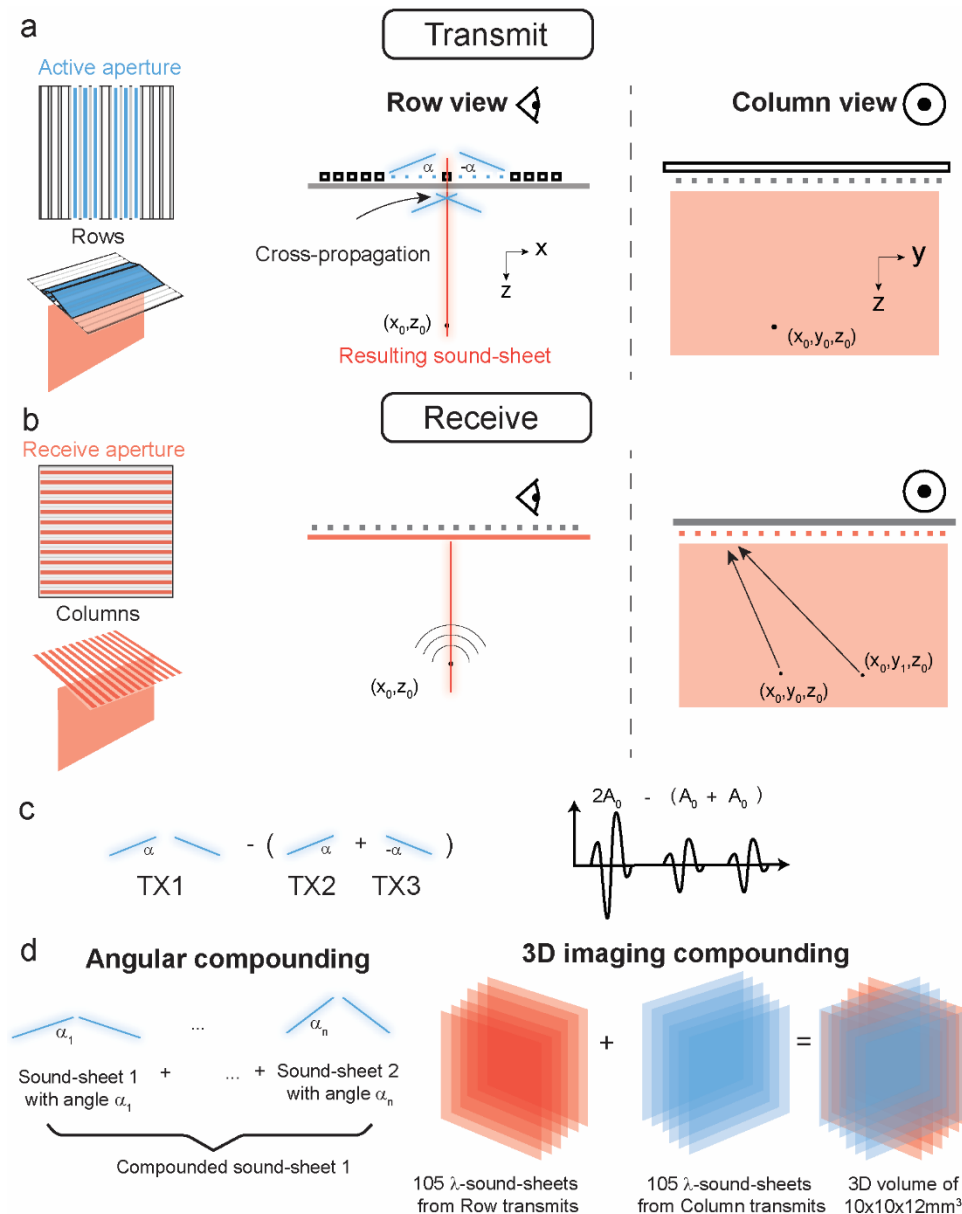


**Figure 1. Transmit and receive sequence for generation of Sound Sheets with a RCA probe**

- a) A selected active aperture is used to transmit two plane waves with opposite angles  $\alpha$  and  $-\alpha$ . Thanks to cross-propagation of the two ultrasound waves, a double amplitude is generated at the two waves intersection and due to the elongated shape of the row elements, this wave spans the entire array, resembling a sound-sheet. Left: Top and 3D view of the array. The rows used to transmit are filled in blue, inactive elements are filled in white. The two plane waves cross-propagating are also displayed in blue and form the sound-sheet in red. Middle: Row view of the two angled plane wave intersecting and creating a sound-sheet. Right: Column view of the transmitted sound-sheet
- b) In the orthogonal plane to the rows, the sound-sheet elicits scattering from an area covered by the entire array. The columns are then used to beamform the received signal and reconstruct a 2D image using a conventional Delay-And-Sum algorithm. Two points with different coordinates in the  $y$ -direction will be separable thanks to the ability to focus with the columns in the  $y$ -direction. In the  $x$ -dimension, only the points contained in the sound-sheet can back-scatter and so this imaging mode does not suffer from lack of elevation focus in the rows. Left: Top and 3D view of the array. The columns used to beamform are filled in red. The sound-sheet spans the array orthogonally to the elevation plane. Middle: Row of the sound-sheet created and

backscatter elicited from two points in the same  $y$ -position. Right: Column view of the received sound-sheet

- c) Nonlinear Sound-Sheet Imaging sequence with the first transmit being the creation of the double amplitude sound-sheet. The next two transmits are the half-aperture transmitting each a plane wave and eliciting only single amplitude backscatter. Finally, the RF signals from these last two transmits are subtracted to the sound-sheet emission to retain only non-linear signal from the medium
- d) To perform angular compounding, various sound-sheets are created with different angles while respecting the cross-propagation limit angle. The beamformed signals are then summed in post-processing. To reconstruct volumes, the sound-sheets are scanned across the entire array and a  $10 \times 10 \times 12 \text{ mm}^3$  volume is reconstructed by compounding each of these sound-sheets.

**GV phantom.** *Anabaena flos aquae* GVs were cultured and transferred to sterile separating funnels. Buoyant cells were separated from the growth media through natural flotation, and GVs were harvested after 48h of hypertonic lysis. A cycle of centrifugation and resuspension allows to purify the GVs further. A stock of wild-type GVs (wtGVs) were stripped of their GvpC protein layer with a 6-M urea solution to obtain GVs that scatter higher harmonics (hGVs). These two GV variants were either stored in phosphate buffered saline (PBS) or clustered to end up with 4 different imaging samples: wtGVs, aggregated wtGVs (wtGVs+), hGVs and aggregated hGVs (hGVs+). A 2% agar phantom comprising 2 mm in diameter wells was casted using custom-printed molds and imprints. Wells were filled with agar (control) or agar mixed with one of the 4 different GV variants prepared. The final GV concentration was measured optically at OD2.5 (285 pM)

### Results

The RCA probe was placed over the GV phantom filled with 5 different samples, agar and the 4 GV variants (**Figure 2a**). We performed NSSI scanning with a  $pitch/2$  step of the GV phantom at a pressure eliciting nonlinear scattering of hGVs (300-600 kPa range). At each sub-aperture position, 13 sound-sheet were transmitted with angles spanning  $9^\circ$  to  $21^\circ$  to increase SNR via angular compounding. 3D phantom images were reconstructed out of 210 sound-sheets positions in each orthogonal direction (**Figure 2.b**). The two bottom wells filled with hGVs were specifically retrieved by the 3D NSSI mode whereas echoes arising from the linear GV variants are extinguished as well as the artifacts below the wells. We display in **figure 2.c** one sound-sheet at a fixed position. All images were log-compressed and are displayed with a 70dB range. On the left hand side, the SSI shows all the GV-loaded wells exhibiting higher contrast than the agar-loaded wells. In the middle, the NSSI only picks up harmonic signal from the hGV/hGV+ wells.

The Contrast to Noise Ratio was found to be averaging 5.1 dB and 9.7 dB for the hGV/hGV+ respectively with maximal ratios of 11.0 dB and 13.0 dB. The Contrast To Artifact ratio for the hGV/hGV+ was 1.6 dB and 3.1 dB and was measured on another configuration with the hGV on top of the wtGV. The maximum ratios were 3.8 dB and 7.3 dB.

Finally, as reported in previous studies, we used higher pressure transmissions to selectively collapse GVs and extinguish their ultrasound contrast (**figure 2.d**).

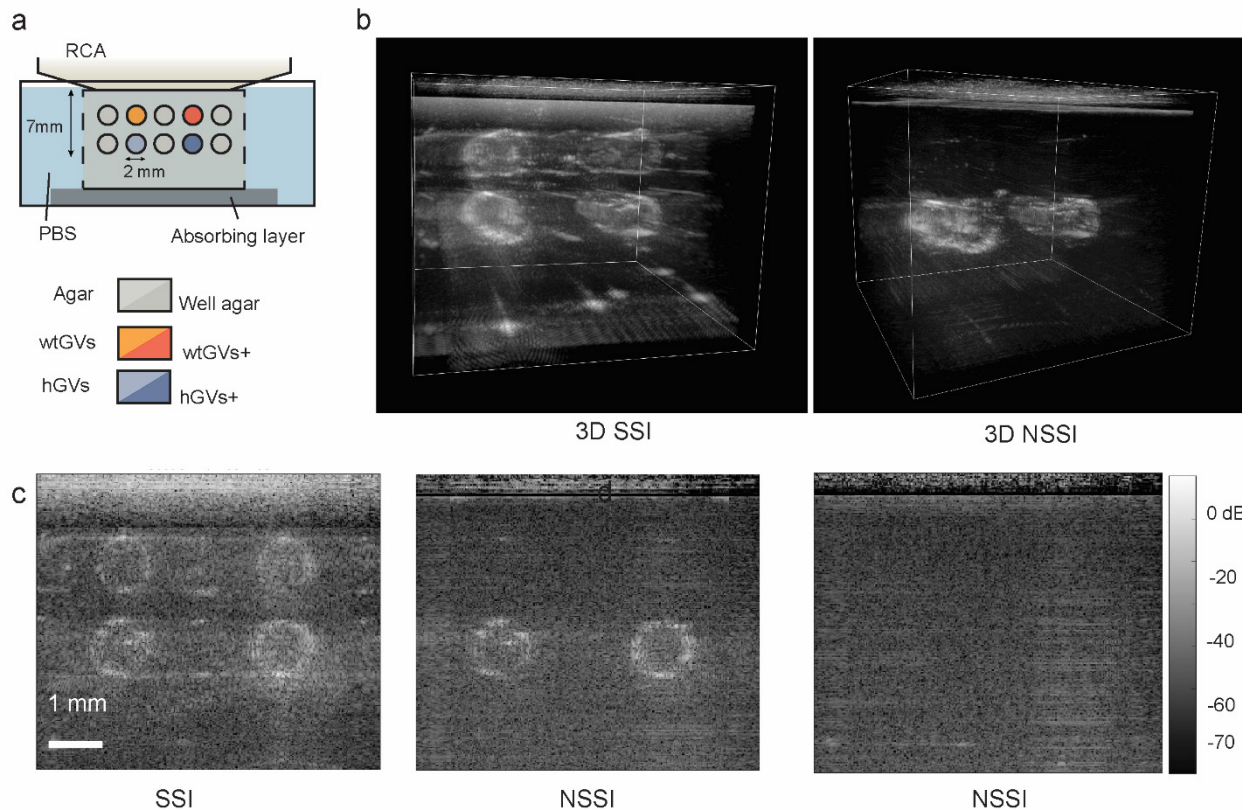


**Figure 2. Sound-Sheet and Non-linear Sound Sheet Imaging of GVs**

- e) Imaging setup showing repartition of different GVs inside the wells. Wild-type GVs are on the top wells, while harmonic GVs are on the bottom. Below the agar phantom, an absorbing layer is placed to prevent reflections, and the whole set-up sits in a PBS solution
- f) 3D renderings of linear and non-linear sound-sheet imaging modes obtained from 210 sound sheets scanned in the rows and compounded with 210 sound sheets scanned in the columns. wtGVs disappear in the non-linear mode and so do artifacts such as bubbles present in between the agar and the absorbing layer
- g) Sound sheets obtained with transmissions at low pressure to prevent GV collapse
- h) Sound sheets obtained with transmissions at high pressure to induce harmonic GV collapse

### Conclusions

We introduce 3D nonlinear sound-sheet imaging (NSSI), a new contrast-enhanced ultrasound imaging mode to visualize genetically encoded ultrasound contrast agents with high specificity in volumes larger than a cubic centimeter. Combined with an RCA probe and an ultrafast ultrasound scanner, NSSI addresses xAM limitations in terms of field-of-view and imaging speed. Specifically, kHz framerates are achieved in the sound-sheet plane, and volume rates ranging from 2.5 to 300 Hz can be reached with or without angular compounding, which is on a par with 4D fUS imaging [8]. In this first implementation with a prototype RCA probe, NSSI was capable of detecting 7 mm deep GV inclusions with a CNR of up to 13 dB. This mode is particularly well adapted to RCA probes as it relies on orthogonal micro-scanning of a sample with thin sheets of sound and restores focusing in transmission. The use of an RCA array also enabled fast 3D imaging with a single 256 channel ultrasound scanner hence simplifying usability of this imaging method.

NSSI will enable time-resolved ultrasound imaging of biological events in their native spatial arrangements.

### References

- [1]. Farhadi A, Sigmund F, Westmeyer GG, Shapiro MG. Genetically encodable materials for non-invasive biological imaging. *Nat Mater*. 2021 May;20(5):585–92.
- [2]. Lakshmanan A, Farhadi A, Nety SP, Lee-Gosselin A, Bourdeau RW, Maresca D, et al. Molecular Engineering of Acoustic Protein Nanostructures. *ACS Nano*. 2016 Aug 23;10(8):7314–22.
- [3]. Lakshmanan A, Jin Z, Nety SP, Sawyer DP, Lee-Gosselin A, Malounda D, et al. Acoustic biosensors for ultrasound imaging of enzyme activity. *Nat Chem Biol*. 2020 Sep;16(9):988–96.
- [4]. Hurt RC, Buss MT, Duan M, Wong K, You MY, Sawyer DP, et al. Genomically Mined Acoustic Reporter Genes Enable In Vivo Monitoring of Tumors and Tumor-Homing Bacteria [Internet]. *Bioengineering*; 2021 Apr [cited 2021 Nov 19]. Available from: <http://biorxiv.org/lookup/doi/10.1101/2021.04.26.441537>
- [5]. Maresca D, Sawyer DP, Renaud G, Lee-Gosselin A, Shapiro MG. Nonlinear X-Wave Ultrasound Imaging of Acoustic Biomolecules. *Phys Rev X*. 2018 Oct 4;8(4):041002.
- [6]. Rabut C, Wu D, Ling B, Jin Z, Malounda D, Shapiro MG. Ultrafast amplitude modulation for molecular and hemodynamic ultrasound imaging. *Appl Phys Lett*. 2021 Jun 14;118(24):244102.
- [7]. Rasmussen MF, Christiansen TL, Thomsen EV, Jensen JA. 3-D imaging using row-column-addressed arrays with integrated apodization - part i: apodization design and line element beamforming. *IEEE Trans Ultrason, Ferroelect, Freq Contr*. 2015 May;62(5):947–58.
- [8]. Rabut C, Correia M, Finel V, Pezet S, Pernot M, Deffieux T, et al. 4D functional ultrasound imaging of whole-brain activity in rodents. *Nat Methods*. 2019 Oct;16(10):994–7.

# Super-resolution ultrasound and MRI imaging for monitoring breast tumour response to radiotherapy

*Megan Morris<sup>1,2</sup>, Matthieu Toulemonde<sup>1</sup>, Victoria Sinnott<sup>3</sup>, Steven Allen<sup>3</sup>, Kate Downey<sup>3</sup>, Nina Tunariu<sup>2,3</sup>, Claire Lucy<sup>2,3</sup>, Lone Gothard<sup>2,3</sup>, Georgina Hopkinson<sup>3</sup>, Erica Scurr<sup>3</sup>, Emma Harris<sup>2</sup>, Matthew Blackledge<sup>2</sup>, Navita Somaiah<sup>2,3</sup> Meng-Xing Tang<sup>1</sup>*

<sup>1</sup>*Department of Bioengineering, Imperial College London, London, UK*

<sup>2</sup>*Division of Radiotherapy and Imaging, The Institute of Cancer Research, London, UK*

<sup>3</sup>*The Royal Marsden NHS Foundation Trust, London, UK*

*Corresponding author: mengxing.tang@imperial.ac.uk*

## Introduction

There is a clinical need to develop better imaging protocols to monitor response to radiotherapy (RT) that consider biological/physiological features, as opposed to relying on size measurements alone (RECIST criteria). Tumours are associated with high cellularity, and a chaotic, hyperpermeable microvasculature. We hypothesise that super-resolution ultrasound (SRUS) [1][2] combined with dynamic-contrast enhanced and diffusion-weighted (DCE/DW) MRI will enable unprecedented quantification of tumour response, including changes in microvessel structure and dynamics. This will potentially allow the identification of radioresistance and relapse earlier than is currently possible.

## Methods

In this study, patients are part of an ongoing clinical trial assessing the effectiveness of intra-tumoural H<sub>2</sub>O<sub>2</sub> as a radiosensitiser for locally advanced breast cancer (KORTUC Phase 2, ClinicalTrials.gov: NCT03946202). 2D SRUS and 3D DCE/DW-MRI of the breast tumours are acquired pre-RT and 2 weeks, 6 and 12 months post-RT (36Gy in twice-weekly fractions of 6Gy) on 6 patients. Super-resolution maps of the tumour microvasculature were generated from high frame rate (frame rate = 100-200fps) contrast-enhanced (amplitude modulated) US acquisitions by detecting intravenously injected, spatially isolated Sonovue contrast agents. 3D ADC (apparent diffusion coefficient) maps were generated from DW-MRI for measurement of cellularity and 3D AUC<sub>90</sub> (area under the curve for first 90 seconds) maps were generated from DCE-MRI contrast uptake curves for a combined measurement of vascular permeability, perfusion and density. Tumour volumes of interest were delineated and approved in both MRI and US images by a consultant radiologist and consultant breast radiographer, respectively.

## Results

Preliminary analysis confirmed that breast tumour microvasculature can be imaged using SRUS (Fig 1), and changes in microvasculature can be visually detected post-RT. A significant difference is seen between the microvasculature in healthy breast and in the tumour (Fig 1). The results from MRI show that there was an early increase in median ADC (reflecting reduced cellularity) after RT for all patients apart from one (Fig 2). At 6m and 12m, median ADC decreases. Median AUC<sub>90</sub> show an early decrease after RT for all patients apart from one (the same patient showing a decrease in median ADC), and a continued decrease at 6m and 12m (reflecting vessel disruption).

## Conclusions

We have successfully applied high frame rate CEUS and SRUS, for the first time, to study breast tumours undergoing RT. Initial pilot data shows that radiation-induced changes may be detectable at 2w post-RT, suggesting that this method can potentially be used to detect early response/resistance to RT. Further studies with more patients are required to confirm the finding. Future analysis will include correlating quantitative measurements from SRUS and MRI, and imaging the patients at further time-points

to monitor for relapse. More planes or 3D volume of the tumour will also be monitored throughout to capture the heterogeneity of the tumours.

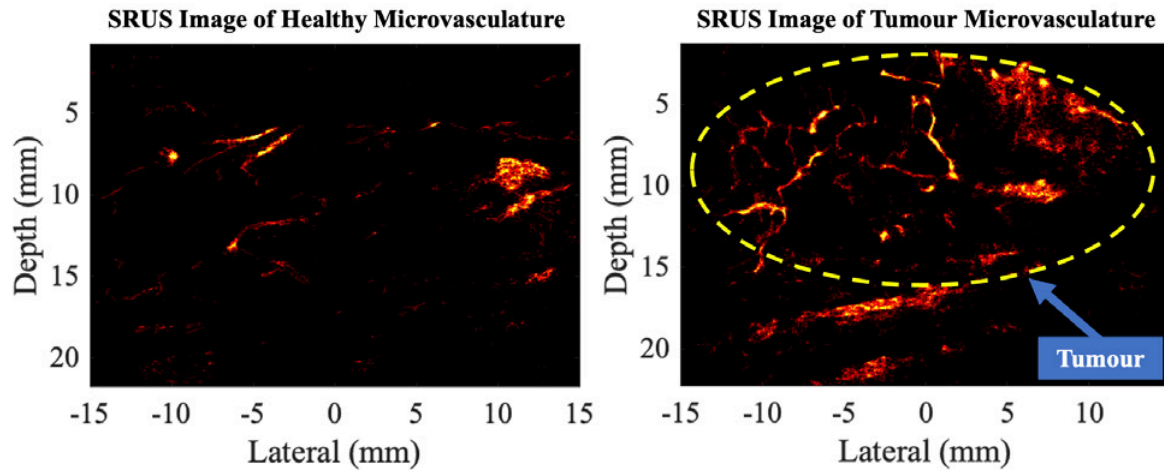


Figure 1. An SRUS map of the healthy breast microvasculature (left) and the tumour microvasculature (right).

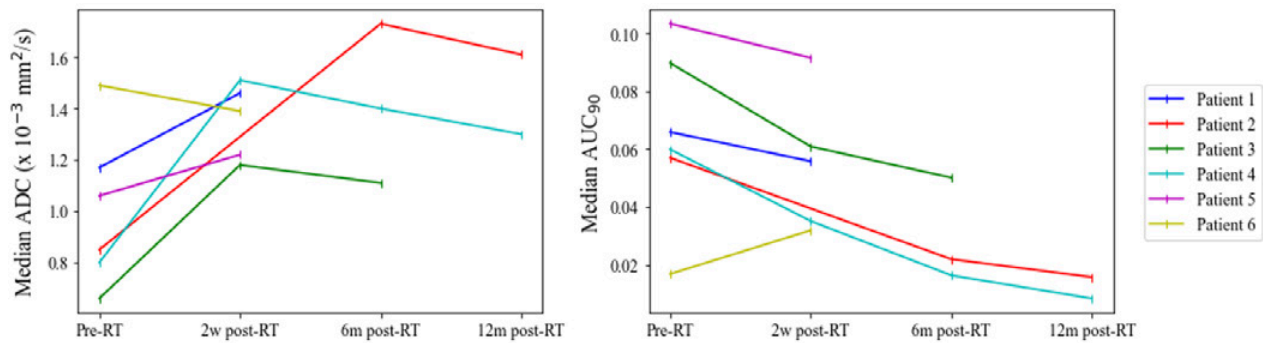


Figure 2. Median ADC (left) and median AUC<sub>90</sub> (right) values, pre-RT and 2 weeks, 6- and 12-months post-RT.

**References**

[1]. Christensen-Jeffries K, Couture O, Dayton PA, Eldar YC, Hynynen K, Kiessling F, O'Reilly M, Pinton GF, Schmitz G, Tang MX, Tanter M, van Sloun RJG, Super-resolution Ultrasound Imaging, *Ultrasound in Medicine & Biology*, 46(4): 865-891, 2020.

[2]. Opacic T, Dencks S, Theek B, Piepenbrock M, Ackermann D, Rix A, Lammers T, Stickeler E, Delorme S, Schmitz G, Kiessling F, Motion model ultrasound localization microscopy for preclinical and clinical multiparametric tumor characterization, *Nature Communications*, 9, 2018.

## Porcine myocardial perfusion imaging with high frame rate contrast schemes

***Geraldi Wahyulaksana<sup>1</sup>, Luxi Wei<sup>1</sup>, Maaike te Lintel Hekker<sup>2</sup>, Joaquim Bobi I Gibert<sup>2</sup>, Dirk-Jan Duncker<sup>2</sup>, Antonius F.W. van der Steen<sup>1</sup>, Nico de Jong<sup>1,3</sup>, Hendrik J. Vos<sup>1,3</sup>***

*<sup>1</sup>Thoraxcenter, Dept Biomedical Engineering, ErasmusMC University Medical Center Rotterdam, Rotterdam, the Netherlands*

*<sup>2</sup>Thoraxcenter, Dept Experimental Cardiology, ErasmusMC University Medical Center Rotterdam, Rotterdam, the Netherlands*

*<sup>3</sup>Medical Imaging, Faculty of Applied Sciences, Delft University of Technology, Delft, the Netherlands*  
*Corresponding author: g.wahyulaksana@erasmusmc.nl*

### Introduction

Quantifying the myocardial perfusion after infarct and intervention has high clinical value to predict outcome, and potentially can guide treatment of patients while still being present in the Cathlab. Detecting flow and perfusion in the myocardial microvasculature is challenging for contrast-enhanced ultrasound (CEUS) imaging even with the adoption of microbubbles as contrast agent. Current contrast-specific pulsing schemes contain either a single pulse (Second- or subharmonic imaging, or the experimental SVD-based fundamental imaging) or multiple pulses (power or amplitude modulation (PM, AM), and/or pulse inversion (PI)), all aiming at suppressing tissue and clutter signal. However, single-pulse second- and subharmonic schemes suffer from nonlinear tissue and bubble-cloud propagation, and the other schemes suffer from motion artefacts since tissue signal suppression reduces upon tissue motion. The latter is particularly challenging when imaging myocardial perfusion throughout the cardiac cycle, creating flash artefacts [1], [2]. High framerate CEUS generates high correlation of data both in space and time, which potentially allows for correlation-based filtering techniques not present with line by line scanning. Yet, realistic data is needed to investigate efficiency of standard and non-conventional pulsing schemes and corresponding processing of these highly correlated frames. We are using an in-vivo porcine animal model to generate such cardiac data and investigate the effect of different imaging parameters and processing to the performance of HFR CEUS to detect myocardial flow and perfusion.

### Methods

The terminal animal experiments followed European Union and institutional guidelines for the care and use of laboratory animals, with DEC protocol SP2100125 0.7, study number 172411-14. They were first sedated, next put under full anesthesia and vented mechanically. Vital signs were monitored.

RF acquisitions were performed with a phased array transducer (64-element P7-4, Philips ATL, Bothell, WA), connected to a Vantage 256 system (Verasonics Inc., Redmond, WA). Live line-based power-modulation imaging was used for navigation and pre-viewing of contrast agent arrival in the RV and LV, subsequently. One acquisition consisted of uninterrupted recording of 2s of high frame rate data, ECG gated, and the corresponding pre- and post-recorded line based live preview frames. The high frame rate transmission sequence consisted of 3 synthetic transmit apertures (21 elements to increase spatial resolution) [3], with a pulse repetition frequency ranging between 4.3 - 4.5 kHz. The pulses had a center frequency of 5.2 MHz; see Table 1 for all settings. A transmission level of 20V corresponded to a derated  $MI_{0.3dB}$  of 0.05 at 6 cm depth. Data were stored for offline processing (approx. 10s storage time per acquisition), and beamformed using the Ultrasound Toolbox [4] in Matlab (2020B, the Mathworks, Natick, 2020) on a  $0.5 \lambda$  resolution grid. Next to the conventional pulsing schemes that are appropriate for narrow-band probes such as the P7-4, we also captured data with a multi-level scheme, with the hypothesis that proper data processing of such multi-level pulse can benefit from pressure-dependent attenuation and scattering properties of microbubbles that have been recently described in [5].

**Table 1. Experimental settings**

Probe	P 7-4, PRF = 4.3kHz – 4.5 kHz
Transmission	5.2MHz, 3-cycle, diverging waves from 3 subapertures
Receive	fundamental Rx band, 10cm depth, 2s. continuous acquisition
Pulsing schemes	Checkerboard 3-pulse PM, checkerboard 3-pulse PMPI, 3- and 6-pulse Multi-level transmission *
Peak voltage	10, 20, 30, 40, 50 V
Bubble type	Definity (5 vials) and SonoVue (2 vials)
Injection type	(a) Bolus of half and full of the respective recommended weight-corrected dose; (b) Continuous infusion with Definity (2 and 4 ml/min of diluted 1:33 suspension)
View	Parasternal long and short axis, modified Apical 2 and 4 chamber

\* multi-level transmission schemes were implemented through the pulse-width modulation option of the Vantage system.

## Results

Two-hundred sixty contrast-enhanced acquisitions were recorded. After every bolus, 6 - 9 acquisitions were captured. Out of all views, the parasternal short axis view provided full view of the septal wall (Fig. 1a) and therefore are analysed first. After image reconstruction and conventional processing, the data captured with PM and PMPI showed clear suppression of tissue and clear ventricular border delineation, yet were suffering from noise (Fig. 1b). The bubble cloud in the right ventricle, right after injection, shielded part of the left ventricle. We could identify traces of contrast agent microbubbles inside the myocardium after initial PM and PMPI processing and squared incoherent summation (50 frames) in end-diastolic phase, where motion is minimal (Fig. 1c).

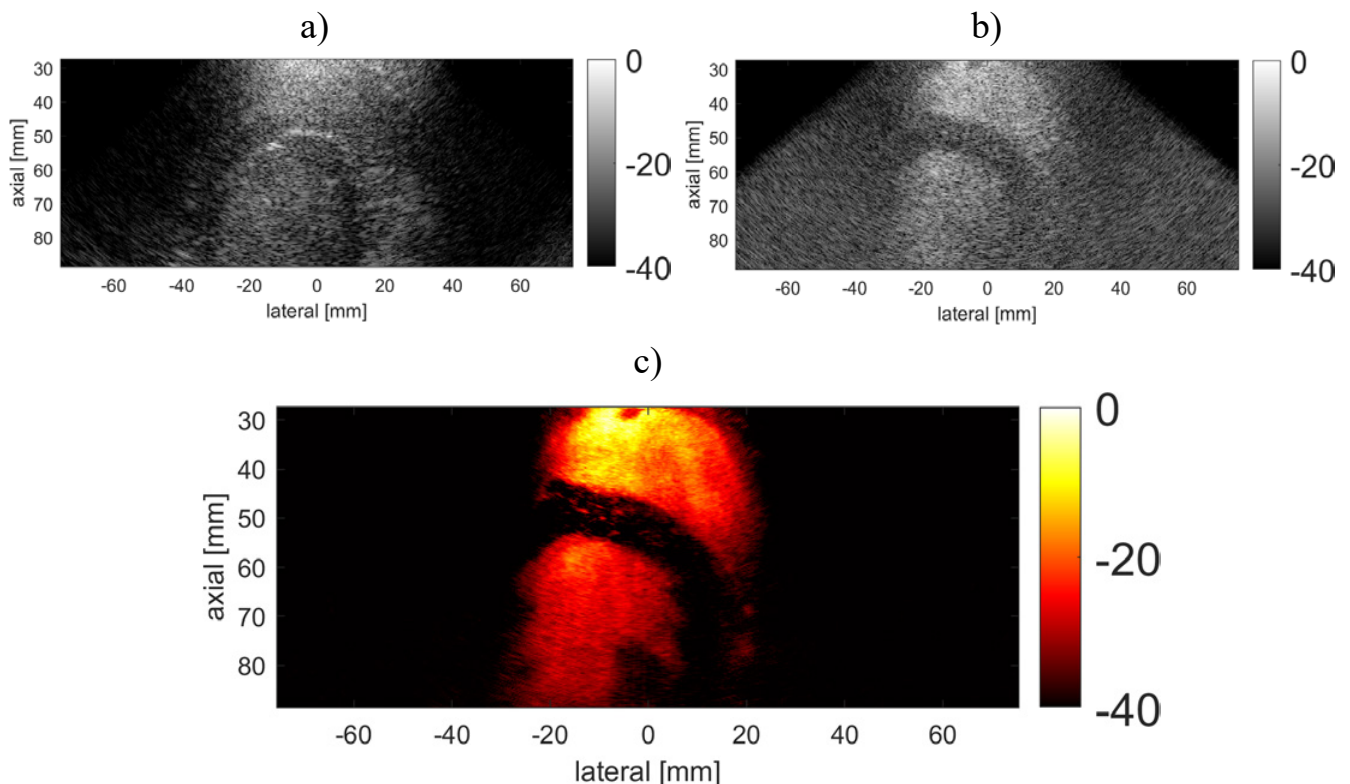


Figure 1. a) fundamental image of short-axis parasternal view with contrast agents present, end-diastolic; b) PMPI-processed frame with contrast agent; c) PMPI and squared incoherent summation (50 frames) to show the traces of the contrast agents inside the myocardium.

## Conclusions

We performed in-vivo HFR CEUS imaging with standard and unconventional contrast-specific pulsing schemes and varying transmit settings. We showed preliminary feasibility of visualizing myocardial perfusion with the combination of PMPI and incoherent summation imaging. The improved spatio-temporal correlation of high frame rate imaging, over line scanning, will enable more possibilities of implementing post-processing filtering techniques.

## References

- [1] F. Lin, C. Cachard, R. Mori, F. Varray, F. Guidi, and O. Basset, "Ultrasound contrast imaging: Influence of scatterer motion in multi-pulse techniques," *IEEE Trans. Ultrason. Ferroelectr. Freq. Control*, vol. 60, no. 10, pp. 2065–2078, 2013, doi: 10.1109/TUFFC.2013.2797.
- [2] M. Toulemonde *et al.*, "High-frame-rate contrast echocardiography using diverging waves: Initial in vitro and In vivo evaluation," *IEEE Trans. Ultrason. Ferroelectr. Freq. Control*, vol. 65, no. 12, pp. 2212–2221, Dec. 2018, doi: 10.1109/TUFFC.2018.2856756.
- [3] C. Papadacci, M. Pernot, M. Couade, M. Fink, and M. Tanter, "High-contrast ultrafast imaging of the heart," *IEEE Trans. Ultrason. Ferroelectr. Freq. Control*, vol. 61, no. 2, pp. 288–301, 2014, doi: 10.1109/TUFFC.2014.6722614.
- [4] A. Rodriguez-Molares *et al.*, "The UltraSound ToolBox," Oct. 2017, doi: 10.1109/ULTSYM.2017.8092389.
- [5] T. Segers, P. Kruizinga, M. P. Kok, G. Lajoinie, N. de Jong, and M. Versluis, "Monodisperse Versus Polydisperse Ultrasound Contrast Agents: Non-Linear Response, Sensitivity, and Deep Tissue Imaging Potential," *Ultrasound Med. Biol.*, vol. 44, no. 7, pp. 1482–1492, 2018, doi: 10.1016/j.ultrasmedbio.2018.03.019.

# Microfluidic Vasculature Networks for the Evaluation of Microbubble-Mediated Delivery of Targeted Liposomes

***Matthew D. Bourn<sup>1</sup>, Safoura Zahed Mohajerani<sup>2</sup>, Georgia Mavria<sup>2</sup>, Nicola Ingram<sup>2</sup>, P. Louise Coletta<sup>2</sup>, Stephen D. Evans<sup>1</sup>, Sally A. Peyman<sup>1,2\*</sup>***

<sup>1</sup>*Molecular and Nanoscale Physics Group, School of Physics and Astronomy, University of Leeds, LS2 9JT, United Kingdom*

<sup>2</sup>*Leeds Institute of Medical Research, Wellcome Trust Brenner Building, St James's University Hospital, Leeds, LS9 7TF, United Kingdom*

*Corresponding author: s.peyman@leeds.ac.uk*

## Introduction

Microbubble (MB)-mediated sonoporation offers a potential means of improving localised drug delivery to tumours. As with all intravenous therapeutics, the tumour-associated vasculature presents the first barrier which must be overcome if effective drug delivery is to be achieved. Several studies have investigated the impact of MB and ultrasound (US) on the endothelium, however many of these studies have been conducted on simplistic 2D cell monolayer or pre-patterned 3D models, which do not faithfully recreate the structure of vasculature [1–3]. The production of a vasculature system that mimics the structure and functionality of tumour-associated vasculature would provide a platform for the testing of potential intravenous therapeutics on a system that closely represents in vivo tumour vasculature. This study presents a fully perfusable microfluidic vasculature system that can be induced to display tumour-associated vasculature properties without the direct incorporation of tumour cells. The soluble factors and cytokines secreted by tumour cells have been shown to influence the behaviour of healthy cells, inducing them to display tumour-associated properties [4,5]. This study conditioned healthy vasculature cultures with media taken from HCT116 colorectal cancer cells, resulting in the formation of disorganised, tortuous networks which display characteristics consistent with that of tumour vasculature. The expression of integrin  $\alpha_v\beta_3$ , an integrin associated with angiogenesis, was found to be upregulated when cells were conditioned with tumour cell media (TCM) – consistent with observations in tumour vasculature [6,7]. TCM-conditioned networks were subsequently used to evaluate the efficacy of targeting liposomes (LS) to integrin  $\alpha_v\beta_3$  and further used to evaluate the efficacy of enhancing LS accumulation using microbubbles (MB) and ultrasound (US).

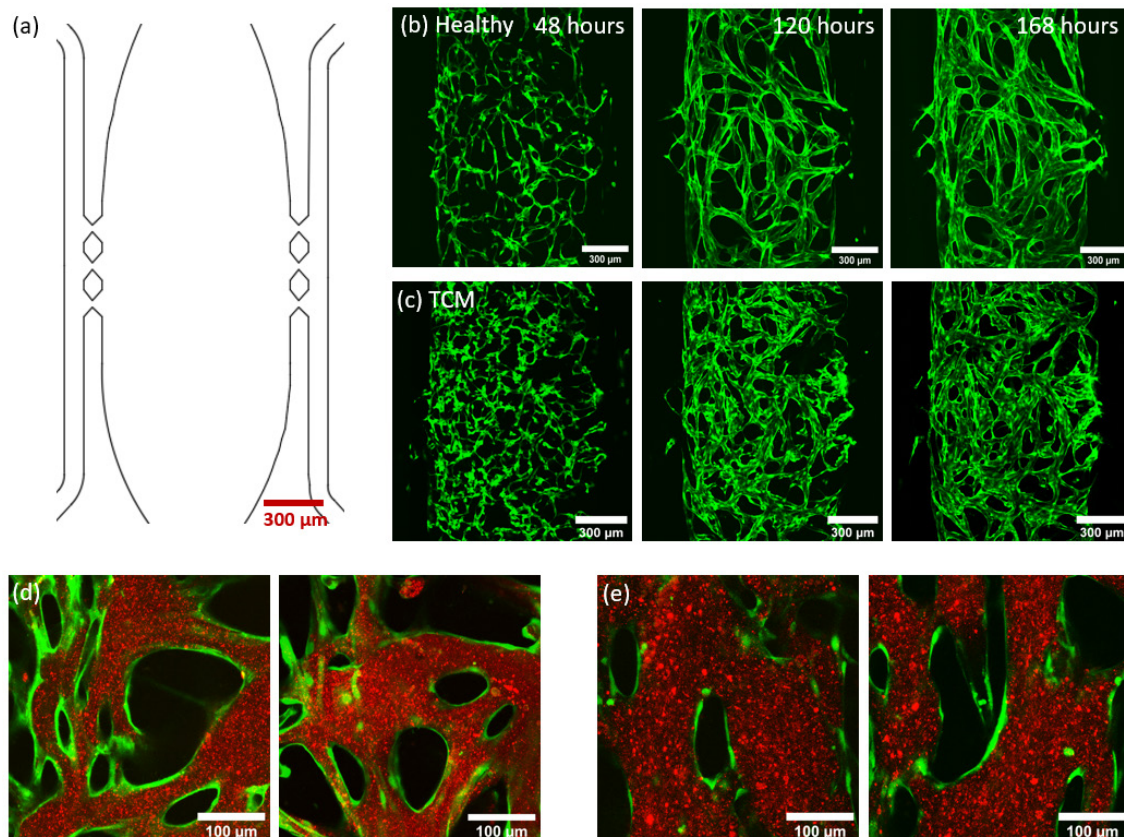
## Methods

Vasculature was produced by seeding GFP-transfected human umbilical vein endothelial cells (GFP-HUVECs) and normal human lung fibroblasts (NHLFs) in a fibrin matrix into a microfluidic device. Media-containing side channels adjacent to the cell chamber were used to provide physiological rates of interstitial flow and pressure required to induce angiogenesis – the formation of new blood vessels. Endothelial growth medium (EGM-2, Lonza) was used to supply the appropriate growth factors required to induce the self-assembly of HUVECs into a perfusable network 7 days after seeding. Vasculature was conditioned with TCM media by growing cultures in [2:1] EGM:TCM media for the final 5 days of culture. LS were prepared via extrusion from a mixture of DSPC, Cholesterol, DSPE-PEG2000 Biotin and DOPE-647N in a 55:40:4.6:0.4 M ratio with a total lipid concentration of 12mg/ml. MBs were prepared from a mixture of DPPC and DPSE-Biotin-PEG2000 in a 95:5 M ratio and a total lipid concentration of 2 mg/ml. C<sub>4</sub>F<sub>10</sub> gas was bubbled through the MB lipid solution which was then placed in a shaker (VialMix, Bristol Meyers Squibb) to form the MB. Biotin-avidin binding was used to bind biotinylated  $\alpha_v\beta_3$  antibodies (2  $\mu$ g/ml or 4  $\mu$ g/ml) to the surface of LS, creating targeted-LS (T-LS) which were then bound to MB using the same mechanism to form targeted-LS-MB conjugates (T-LS-MB). Microfluidic devices were isonated using a 2.25 MHz centre frequency unfocussed transducer (V323-SM, Olympus, US) with a 2 second, US pulse (1 % duty cycle, 1 kHz pulse repetition frequency, 400 mVpp). This was characterised to produce a peak negative pressure of  $0.81 \pm 0.04$  MPa after travelling through 1 mm of PDMS and had previously been shown to burst 99.6 % of MBs. Fluorescent LS accumulation within the vasculature networks was used to

quantify the efficacy of each treatment. Post-perfusion imaging of LS fluorescence was performed using a confocal microscope (Leica, DMi8/SP8) with a 100 x objective to acquire 1.5  $\mu\text{m}$  thick z-stack slices of entire vessels. ImageJ particle analysis was then used to quantify LS accumulation.

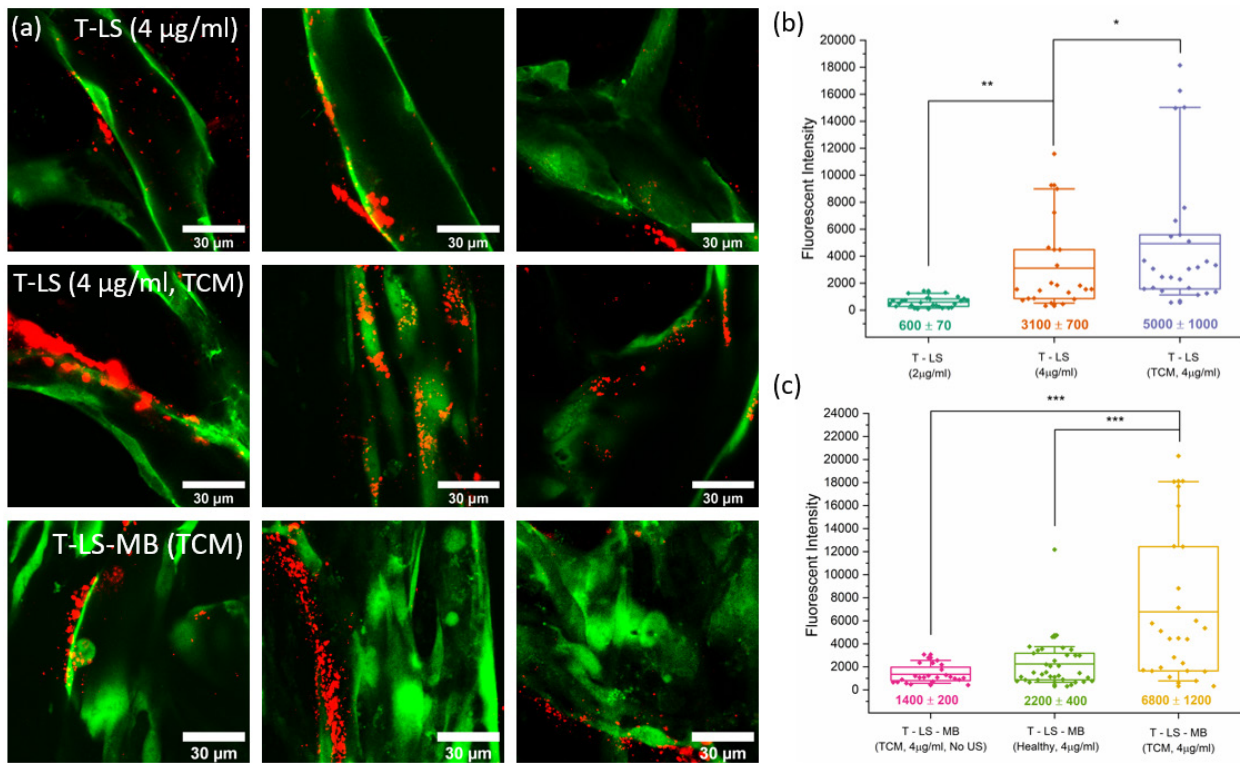
## Results

Figure 1a depicts the microfluidic device designed for the production of vasculature alongside images taken of healthy (b) and TCM-conditioned (c) vasculature networks developing across 7 days. TCM-conditioning was observed to form networks with disjointed, tortuous structures compared to the smooth continuous vessels formed in healthy networks – consistent with observations of *in vivo* tumour vasculature. Analysis of integrin  $\alpha_v\beta_3$  expression using immunostaining and flow cytometry found that  $\alpha_v\beta_3$  was upregulated in both HUVECs and NHLFs conditioned with TCM – further demonstrating that tumour-associated characteristics could be induced using TCM.



**Figure 1 – (a) AutoCAD design of the microfluidic device used for vasculature formation. (b) Fluorescent images of GFP-HUVECs self-assembling into a healthy vasculature network 48, 120 and 168 hours after cell seeding. (c) Fluorescent images of GFP-HUVECs self-assembling into a TCM-conditioned vasculature network 48, 120 and 168 hours after cell seeding. (d) Fluorescent images taken of T-LS (red) perfusing through the vasculature. (e) Fluorescent images taken of T-LS-MB (red) perfusing through the vasculature.**

T-LS and T-LS-MB were perfused throughout the networks (figure 1d and 1e, respectively) and observed to remain confined within the vessels. Perfusions were performed for one hour and US was applied shortly after MBs populated the network. Fresh media was added and allowed to perfuse for an additional hour to remove any unbound LS from the network. Perfusion of T-LS conjugated with 2  $\mu\text{g}/\text{ml}$  or 4  $\mu\text{g}/\text{ml}$   $\alpha_v\beta_3$  antibodies was initially performed to observe the effect of increasing antibody concentrations. Images captured post perfusion are shown in figure 2a. LS accumulation intensities, shown in figure 2b, were found to be  $600 \pm 70$  and  $3100 \pm 700$  for 2  $\mu\text{g}/\text{ml}$  and 4  $\mu\text{g}/\text{ml}$  T-LS perfusions in healthy networks, respectively. Comparison with antibody isotype controls at the same concentrations found that only 4  $\mu\text{g}/\text{ml}$  targeting resulted in a statistically significant increase in LS accumulation. Perfusion of 4  $\mu\text{g}/\text{ml}$  T-LS through TCM networks observed an increase in accumulation ( $5000 \pm 1000$ ) compared to healthy networks – indicating that TCM-induced  $\alpha_v\beta_3$  upregulation facilitated increased T-LS accumulation.



**Figure 2 – (a) Post-perfusion images taken of LS accumulation (red) within the vasculature networks (green) after perfusion with T-LS (4 µg/ml), T-LS (4 µg/ml, TCM) and T-LS-MB (4 µg/ml, TCM). (b) Boxplot graph of LS accumulation intensities after T-LS (2 µg/ml), T-LS (4 µg/ml) and T-LS (4 µg/ml, TCM) perfusions. (c) Boxplot graph of LS accumulation intensities after T-LS-MB (4 µg/ml, no US), T-LS-MB (4 µg/ml, healthy) and T-LS-MB (4 µg/ml, TCM) perfusions.**

Experiments progressed into evaluating the use of T-LS-MB (4 µg/ml) to enhance LS accumulation within tumour vasculature networks. Perfusions of T-LS-MB (4 µg/ml) in TCM networks without an US trigger and T-LS-MB (4 µg/ml) in healthy networks were used as controls to observe the impact of US and tumour-vasculature on LS accumulation. Post perfusion images can again be observed in figure 2a alongside a boxplot of accumulation intensities in figure 2c. Results found that the use of T-LS-MB (4 µg/ml, TCM) resulted in a significant increase in LS accumulation ( $6800 \pm 1200$ ) compared to the healthy network ( $2200 \pm 400$ ) and no US ( $1400 \pm 200$ ) control conditions. Direct comparison between the LS only and LS-MB perfusions was not considered due to the difficulty in equating the overall LS dosage in each configuration.

## Conclusions

Vasculature networks mimicking *in vivo* tumour-associated vasculature have been developed by conditioning healthy networks with TCM – presenting a novel method of producing tumour vasculature without the direct incorporation of tumour cells. Vasculature networks were fully perfusable and allowed for the subsequent evaluation of integrin  $\alpha_v\beta_3$ -targeted LS and LS-MB conjugates. Results observed increased accumulation of 4 µg/ml T-LS in TCM-conditioned networks compared to healthy networks. This was consistent with flow cytometry observations which found  $\alpha_v\beta_3$  upregulation in cells conditioned with TCM. Perfusion of 4 µg/ml T-LS-MB (with US) through TCM networks was found to increase LS accumulation 3-fold compared to similar perfusions through a healthy network. This demonstrated the potential of integrin  $\alpha_v\beta_3$  targeted MBs to increase localised LS delivery to tumour tissues. MB perfusions through TCM networks without an US trigger also resulted in significantly reduced LS accumulation. This indicated that US, and the resultant MB bursting, is necessary to facilitate the deposition of LS in tumour vasculature. Whilst further work is still required to investigate the efficacy of integrin targeting and MB-mediated sonoporation on drug delivery, experiments throughout this study have demonstrated the potential of using targeting and MBs to enhance the delivery of LS to tumour tissues.

## References

- [1]. Silvani G, Scognamiglio C, Caprini D, Marino L, Chinappi M, Sinibaldi G, et al. Reversible Cavitation-Induced Junctional Opening in an Artificial Endothelial Layer. *Small*. 2019;15(51):1–11.
- [2]. Juang EK, De Cock I, Keravnou C, Gallagher MK, Keller SB, Zheng Y, et al. Engineered 3D Microvascular Networks for the Study of Ultrasound-Microbubble-Mediated Drug Delivery. *Langmuir*. 2019;35(31):10128–38.
- [3]. Beekers I, Vegter M, Lattwein KR, Mastik F, Beurskens R, van der Steen AFW, et al. Opening of endothelial cell–cell contacts due to sonoporation. *J Control Release* [Internet]. 2020;322(March):426–38. Available from: <https://doi.org/10.1016/j.jconrel.2020.03.038>
- [4]. Katanasaka Y, Asai T, Naitou H, Ohashi N, Oku N. Proteomic characterization of angiogenic endothelial cells stimulated with cancer cell-conditioned medium. *Biol Pharm Bull*. 2007;30(12):2300–7.
- [5]. Hida K, Akiyama K, Ohga N, Maishi N, Hida Y. Tumour endothelial cells acquire drug resistance in a tumour microenvironment. *J Biochem*. 2013;153(3):243–9.
- [6]. Liu Z, Wang F, Chen X. Integrin  $\alpha\beta3$ -targeted cancer therapy. *Drug Dev Res*. 2008;69(6):329–39.
- [7]. Fabricius EM, Wildner GP, Kruse-Boitschenko U, Hoffmeister B, Goodman SL, Raguse JD. Immunohistochemical analysis of integrins  $\alpha\beta3$ ,  $\alpha\beta5$  and  $\alpha5\beta1$ , and their ligands, fibrinogen, fibronectin, osteopontin and vitronectin, in frozen sections of human oral head and neck squamous cell carcinomas. *Exp Ther Med*. 2011;2(1):9–19.

# Ultrasound-Targeted Microbubble Cavitation Increases Blood Brain Barrier Permeability in an *in vitro* System

Grace E. Conway<sup>1</sup>, Anurag N. Paranjape<sup>1</sup>, Xucai Chen<sup>1</sup>, Flordeliza S. Villanueva<sup>1</sup>

<sup>1</sup>Center for Ultrasound Molecular Imaging and Therapeutics, University of Pittsburgh, Pittsburgh, PA, USA

Corresponding author: villanuevafs@upmc.edu

## Introduction

Ultrasound-targeted microbubble cavitation (UTMC) is being explored as a technique to transiently open the blood brain barrier (BBB) for the treatment of many neurologic diseases including Alzheimer's Disease (AD). UTMC by itself has recently been shown to decrease A $\beta$  plaques in the brain and ameliorate cognitive dysfunction in murine models of AD. Due to the success of pre-clinical studies, phase I and II clinical trials for UTMC-mediated BBB opening have begun in patients with AD. While UTMC-mediated BBB opening is an exciting potential treatment for degenerative neurologic diseases, its underlying mechanisms are incompletely understood. Here, we sought to develop an *in vitro* model of the BBB that simulates increased endothelial barrier permeability after UTMC.

## Methods

We developed a transwell model with murine brain microvasculature endothelial cells (bEnd.3) on the abluminal and murine C8-D1A astrocytes on luminal side of a 1.0  $\mu$ m transwell support membrane. Lipid microbubbles (MB; mean size 3.0  $\mu$ m) were added at a 3:1 MB to endothelial cell ratio before applying pulsed ultrasound (1 MHz, 10  $\mu$ s pulse duration, 10 ms pulse interval) at 250 kPa for 20 s. To determine optimal parameters for permeability studies, cells were stained with Hoechst 33342 (nucleus), propidium iodide (sonoporation), CellMask Deep Red (cell coverage), and calcein-AM (viability). Two methods of endothelial barrier function were assessed: transendothelial electrical resistance (TEER) and permeability using 10 kDa Texas Red dextran as a model drug. Live cell imaging was performed using Fluo-4 AM (calcium indicator). Live cell imaging and TEER studies were performed in media with and without calcium. Differences between 0 and 250 kPa were compared using unpaired 2-tailed *t*-test. For multiple group comparison, one way ANOVA with correction of multiple comparison post-hoc *t*-testing was performed. Significance was defined as  $p < 0.05$ .

## Results

After 250 kPa of UTMC at a 3:1 MB:cell ratio, there was a significant increase in viably sonoporated endothelial cells (3.8%). The area of the transwell covered by cells decreased by 2.7%, and there was 0.5% endothelial cell death. These parameters (250 kPa and a 3:1 MB:cell ratio) were used in the permeability studies. There was a significant decrease in TEER two minutes after UTMC that continued for at least 60 minutes (Figure 1A). There was a significant increase in dextran flux 15 minutes after UTMC that lasted for at least 60 minutes (Figure 1B). There was an influx of calcium into 92.8% of endothelial cells after UTMC. When the co-culture was incubated in calcium-free media, this decreased to 11.0%. Additionally, the change in TEER after UTMC at 250 kPa compared to 0 kPa was attenuated when the co-culture was incubated in calcium-free media.

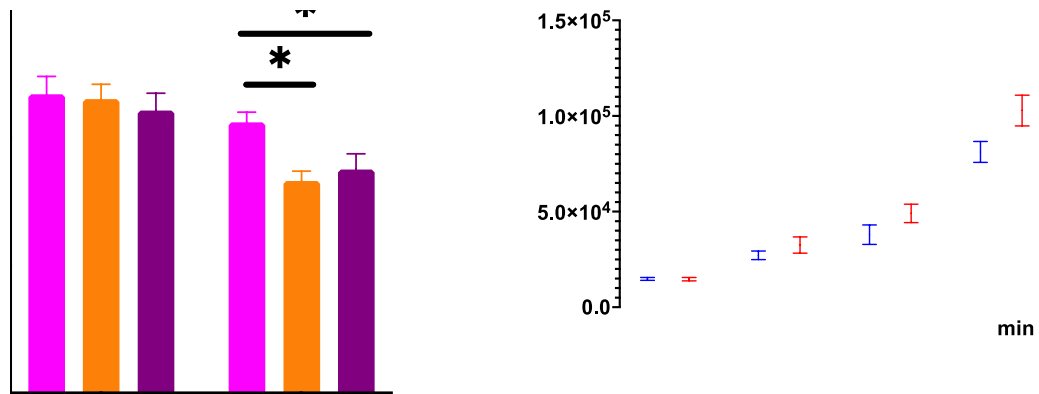


**Figure 1. UTMC increases endothelial barrier permeability in an *in vitro* model of the BBB.** Data represents mean  $\pm$  SD ( $n=3-6$ ). \*  $p<0.05$ . (A) There was a decrease in TEER starting two minutes after UTMC that remains for at least 60 minutes. (B) There was an increase in 10 kDa Texas Red dextran flux across the endothelial barrier 15 minutes after UTMC that remains for at least 60 minutes.

### Conclusions

We developed a contact co-culture transwell model utilizing brain microvascular endothelial cells and astrocytes to simulate the BBB. UTMC increased endothelial barrier permeability and induced calcium influx into porated and adjacent non-porated endothelial cells. When the influx of calcium by UTMC was decreased, the change in endothelial barrier function was attenuated, thus suggesting the importance of calcium influx in facilitating increased BBB permeability after UTMC. Future studies will utilize this model to determine how calcium increases BBB permeability after UTMC.

## Feasibility of sonothrombolysis in the ambulance for ST-elevation myocardial infarction

*S. El Kadi<sup>1</sup>, TR. Porter<sup>2</sup>, M. Zanstra<sup>3</sup>, A. Siegers<sup>3</sup>, RB. Van Loon<sup>1</sup>, LHGA. Hopman<sup>1</sup>, AC. Van Rossum<sup>1</sup>, O. Kamp<sup>1</sup>*

*<sup>1</sup>Amsterdam UMC - Location VUmc, Amsterdam, The Netherlands*

*<sup>2</sup>University of Nebraska Medical Center, Cardiology, Omaha, United States of America*

*<sup>3</sup>Ambulance Amsterdam, Amsterdam, The Netherlands*

*Corresponding author: s.elkadi@amsterdamumc.nl*

### Introduction

Patients with ST-elevation myocardial infarction (STEMI) due to coronary occlusion require immediate restoration of epicardial and microvascular blood flow (1). A potentially new reperfusion method is the use of ultrasound and microbubbles, also called sonothrombolysis. The oscillation and collapse of intravenously administered microbubbles upon exposure to high mechanical index (MI) ultrasound pulses results in thrombus dissolution and stimulates nitric oxide-mediated increases in tissue perfusion (2). The aim of this study was to assess feasibility of sonothrombolysis in the ambulance for STEMI patients.

### Methods

Patients presenting with chest pain and ST-elevations on initial electrocardiogram were included. Sonothrombolysis was applied in the ambulance during patient transfer to the percutaneous coronary intervention (PCI) center. Feasibility was assessed based on duration of sonothrombolysis treatment and number of high MI pulses applied. Vital parameters, ST-resolution, pre- and post-PCI coronary flow and cardiovascular magnetic resonance images were analyzed. Follow up was performed at six months after STEMI.

### Results

Twelve patients were screened, of which three patients were included in the study. Sonothrombolysis duration and number of high MI pulses ranged between 12-17 minutes and 32-60 flashes respectively. No changes in vital parameters were observed during and directly after sonothrombolysis. In one case, sonothrombolysis on top of regular pre-hospital care resulted in reperfusion (Fig. 1), in another case the effect was inconclusive, and in the last case no effect was seen on reperfusion or definite infarct size.

### Conclusions

Sonothrombolysis in the ambulance for STEMI patients is feasible. Large clinical trials on efficacy and safety of pre-hospital sonothrombolysis are needed.

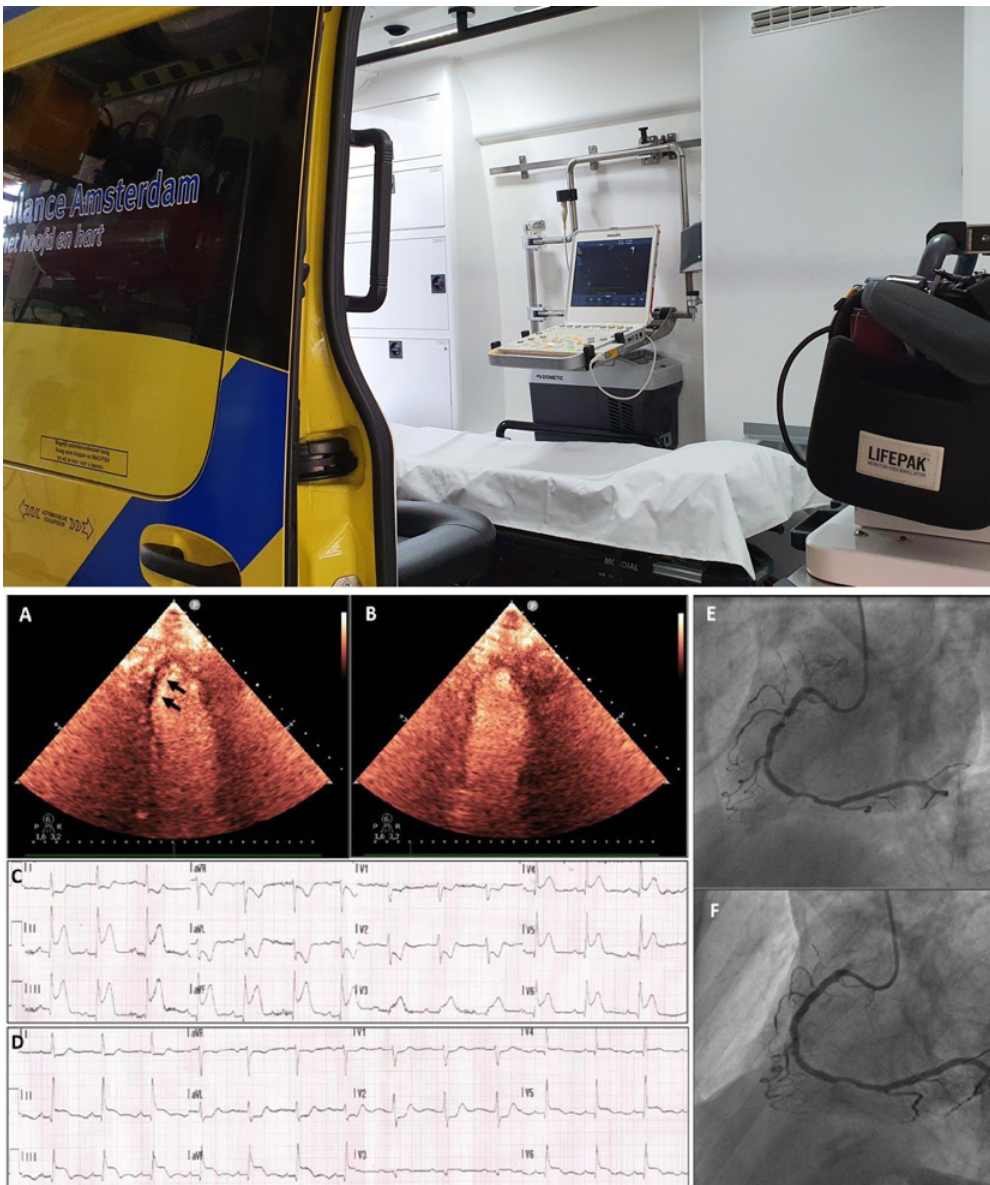


**Figure 1.** Upper image: Sonothrombolysis set-up in the ambulance. Lower image: Successful case with reperfusion of the right coronary artery prior to percutaneous coronary (PCI) after 10-minute sonothrombolysis. A: Visible contrast defect inferior (arrows) before sonothrombolysis. B: Contrast replenishment inferior after 10-minute treatment. C: Electrocardiogram before sonothrombolysis. D: Electrocardiogram after sonothrombolysis. E: Coronary angiography prior to PCI (TIMI-II flow). F: Coronary angiography after PCI.

### References

- [1] Ibanez B, James S, Agewall S, et al. ESC Guidelines for the management of acute myocardial infarction in patients presenting with ST-segment elevation: The Task Force for the management of acute myocardial infarction in patients presenting with ST-segment elevation of the European Society of Cardiology (ESC). *Eur Heart J*. 2017;2018:119–77.
- [2] El Kadi S, Porter TR, Verouden NJW, van Rossum AC, Kamp O. Contrast Ultrasound, Sonothrombolysis and Sonoperfusion in Cardiovascular Disease: Shifting to Theragnostic Clinical Trials [published online ahead of print, 2021 Oct 7]. *JACC Cardiovasc Imaging*. 2021;S1936-878X(21)00689-6. doi:10.1016/j.jcmg.2021.07.028

# Sonopermeation improves the therapeutic efficacy of Caelyx in a preclinical chemo-induced breast tumor model

*A. Helbert, E. Gaud, D. Lazarus, V. Jeannot*

*Bracco Suisse SA, 31 route de la Galaise, Plan-Les-Ouates, Geneva, Switzerland  
Corresponding author: [alexandre.helbert@bracco.com](mailto:alexandre.helbert@bracco.com)*

## Introduction

Recently, microbubbles (MBs) combined with therapeutic ultrasound sequences ( $_{th}US$ ) have been of interest to increase the therapeutic index of various medications. Indeed, the combination of MBs +  $_{th}US$  can enhance the delivery of drugs at the target site by sonopermeation. Sonopermeation includes mechanisms such as pore formation, opening of intercellular junctions or stimulation of endocytosis/transcytosis. To date, sonopermeation has been tested successfully in preclinical tumor models and clinical trials for brain, pancreas, liver and breast cancers [1].

In the present study, we aimed at delivering a liposomal doxorubicin formulation (Caelyx®) through the tumoral vessel wall to improve its therapeutic effect. To this end, we applied therapeutic ultrasound sequence associated with the administration of home-made lipid shelled microbubbles on chemo-induced rat mammary tumors.

## Methods

Mammary tumors were induced on prepubescent female rats by a single intra-peritoneal injection of 50 mg/kg of *N*-nitro-*N*-methylurea (NMU). First tumors appeared approximately 40 days after injection.

In the first part of the study, 100 nm diameter DiR fluorescent liposomes were injected in animals. Two experimental conditions were tested: liposomes alone (naïve tumors, n=13) and liposomes + MBs +  $_{th}US$  (n=7). In the group liposomes + MBs +  $_{th}US$ , four consecutive boluses of home-made phospholipid microbubbles were administered during insonation with a 5-minute delay. During twenty minutes after injection of liposomes or after the first bolus of MBs, therapeutic ultrasound sequence was applied using an unfocused single element transducer (Imasonic 1.6 MHz; 10 msec. ON time; 10 s OFF; PNP 800 kPa). Two hours or forty-eight hours after the onset of the treatment, animals were euthanized, and tumors harvested. The amount of fluorescent liposomes accumulated within tumors was evaluated *ex vivo* by fluorescence imaging using a preclinical Fluobeam 700 camera (Fluoptics, Grenoble, France), then tumors were processed for fluorescence microscopy observation.

In the second part of the study, sonopermeation was performed concomitantly with the administration of Caelyx. Four experimental conditions were tested: Caelyx alone (n=11), Caelyx +  $_{th}US$  (n=5), MBs +  $_{th}US$  (n=4) and Caelyx + MBs +  $_{th}US$  (n=9). Experimental procedures ( $_{th}US$ , MBs) were similar to those used precedently. Animals received three treatments on a weekly basis. The follow-up of tumor volume variation along the different treatments was evaluated at each session using the 3D volume reconstruction tool of the Vevo2100 ultrasound scanner (Visualsonics, Toronto, Canada). A MS200 probe was fixed to the 3D acquisition motor to perform a longitudinal scanning of the entire tumor in B-mode. 3D reconstruction of the stack of images was done with the Vevo®Lab software.

## Results

Fluorescent signal measured in tumors treated with MBs +  $_{th}$ US was respectively 3.2-fold higher and 2.1-fold higher compared to naïve tumors, 2 hrs. and 48 hrs. after the injection of DiR liposomes, Figure 1.

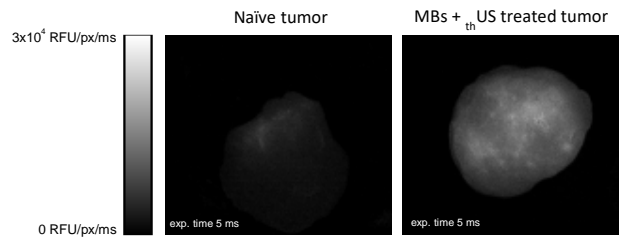
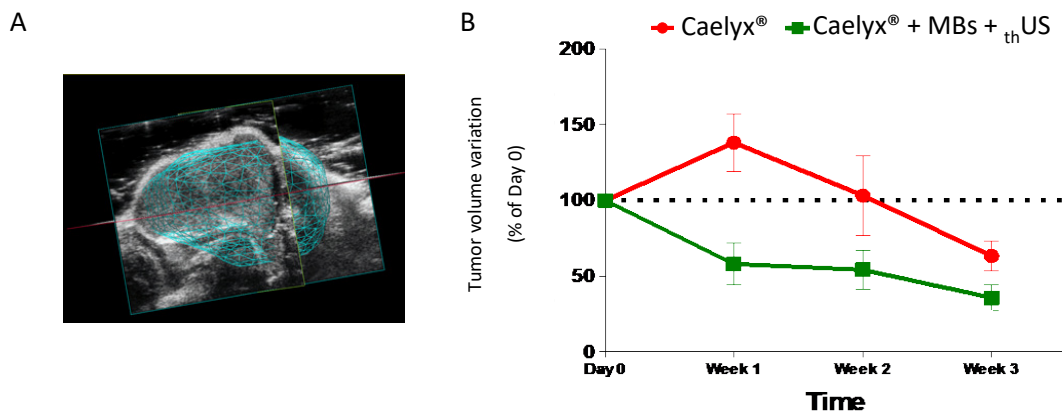


Figure 1. Illustrative fluorescent images of extravasation of 100 nm DiR, 2 hrs. after injection, in NMU tumors from naïve and MBs +  $_{th}$ US groups.

During the follow-up of tumoral volume, a significant tumor growth was observed in control groups, Caelyx +  $_{th}$ US (~2.5-fold) and MBs +  $_{th}$ US (~2.3-fold) imposing to anticipate the end of the procedure for ethical reasons after week 2. Similarly, in the animals treated by Caelyx alone, a tumor growth until week 2 was first observed (~2.1 fold). However, it was followed by a drop to 76% of the initial tumor volume at week 3. Differently, in tumors from the Caelyx + MBs +  $_{th}$ US group, a shrinkage of 23% was observed during the first week of treatment. A gradual decrease of tumor volume was observed during all the follow-up period, which was finally divided by a factor of 10 at week 3.

Beyond the increase in therapeutic efficacy of the Caelyx, the proportion of tumors responding to the treatment, and the strength of the response was higher in the Caelyx + MBs +  $_{th}$ US group (78% of tumors responding to the treatment), in comparison to Caelyx alone (27%), Figure 2.

Figure 2. A, 3D volumetric reconstruction of NMU tumors used for tumor volume estimation.



B, Tumor volume variations in tumors that respond to Caelyx® alone (27% of the treated tumors) or in combination with MBs +  $_{th}$ US (78% of the treated tumors).

## Conclusions

In these chemo-induced rat mammary tumors, sonopermeation mediated by microbubbles and therapeutic ultrasound pulses can enhance the extravasation of one hundred nanometer liposomes across the tumoral vessel wall. Furthermore, this effect can be applied to improve the therapeutic outcome of Caelyx, resulting in a faster and stronger decrease of tumoral volume and improvement of the success rate.

## References

- [1]. Snipstad, S., et al., Sonopermeation to improve drug delivery to tumors: from fundamental understanding to clinical translation. *Expert Opinion on Drug Delivery*, 2018. **15**(12): p. 1249-1261.

## The OrganoPlate<sup>®</sup> as vessel-on-a-chip model to investigate microbubble-mediated drug delivery mechanisms

***Bram Meijlink<sup>1</sup>, Inés Beekers<sup>1</sup>, Simone A.G. Langeveld<sup>1</sup>, Kristina Bishard<sup>2</sup>, Antonius F.W. van der Steen<sup>1,3</sup>, Nico de Jong<sup>1,3</sup>, Sebastiaan J. Trietsch<sup>2</sup>, Klazina Kooiman<sup>1</sup>***

<sup>1</sup>*Department of Biomedical Engineering, Erasmus MC, Rotterdam, the Netherlands*

<sup>2</sup>*Mimetas B.V., Leiden, the Netherlands*

<sup>3</sup>*Acoustical Wavefield Imaging, Delft University of Technology, Delft, the Netherlands*

*Corresponding author: k.meijlink@erasmusmc.nl*

### Introduction

The vessel wall is an important barrier hindering the delivery of drugs to the underlying diseased tissue. Microbubbles (MBs), which oscillate upon ultrasound (US) insonification, can potentially be used to locally enhance vascular permeability but more insight into this mechanism is needed for safe and efficient microbubble-mediated drug delivery. The OrganoPlate<sup>®</sup> (Mimetas B.V., Leiden, NL) provides the possibility to grow an advanced membrane free vessels-on-a-chip with which transcellular drug delivery can be investigated. These microvessels have a 3D structure, are partially grown against a soft and permeable extracellular matrix, and are cultured under flow. This makes these vessels-on-a-chip more physiologically relevant than *in vitro* 2D cell culture and provides higher throughput with less ethical objections than *in vivo* models. Additionally, the OrganoPlate<sup>®</sup> is compatible for US experiments [1]. The aim of this study was to enable and optimize the growth of a human vessel-on-a-chip in the OrganoPlate<sup>®</sup> and investigate the effect of US-activated targeted MBs on the vascular permeability.

### Methods

Collagen I matrix gel was loaded in the 3-lane OrganoPlate<sup>®</sup> 40 to form a perfusable tubular shape (300×220 μm) which was coated using fibronectin. Human Microvascular Endothelial Cells (HMEC) were seeded and cultured for 4 days under flow to form a confluent 3D microvascular tube. Phospholipid-coated MBs with a C<sub>4</sub>F<sub>10</sub> gas core were made by probe sonication and were targeted towards the angiogenic marker α<sub>v</sub>β<sub>3</sub>, as previously described [2]. To determine the vascular permeability, fluorescent dextran (FITC; 150 kDa) was added as a model drug to the microvessel at t<sub>0</sub> and the vascular permeability was measured over time using fluorescent microscopy imaging (Fig. 1A). Propidium Iodide (PI) was also added at t<sub>0</sub> to evaluate sonoporation. The microvessels were treated with MBs and 2 MHz US pulses with pressures ranging from 100-850 kPa Peak Negative Pressure (PNP) and 10×10 or 10×1000 cycles. Control microvessels were either non-treated (sham), treated with MBs only, or treated with US only (2 MHz, 850 kPa PNP and 10×10 or 10×1000 cycles). To quantify the vascular permeability, time-lapse microscopy imaging (4× air objective, A1R+ upright microscope with DS-Fi3 color camera, Nikon Instruments) was performed for up to 120 min. First, to quantify the leakage over time the fluorescent intensity outside the microvessel (i.e. middle channel) was divided by that inside the microvessel channel (i.e. upper channel). Next, the apparent vascular permeability (P<sub>app</sub>) was calculated using the trendline of the leakage, as previously reported [3].

### Results

In total, 122 microvessels were analyzed. Figure 1A shows typical examples of the leakage behaviour of the model drug over time in three different conditions. In the cell free control, the model drug perfused into all three channels directly after addition. In the sham microvessel, the model drug was visible in the microvascular channel and gradually a low leakage of the drug into the middle channel was observed over time. In the MBs and US (2 MHz, 850 kPa PNP, 10×1000 cycles) treated microvessel, the gradual low leakage of the drug before US was similar to that in the sham microvessel, but the leakage was clearly increased upon treatment. Figure 1B shows the quantification of the leakage for these three typical examples. Upon treatment with US and MBs, a clear and sudden increase in leakage was observed suggesting a

microbubble-mediated enhancement of the vascular permeability. To further examine this increased permeability, a variety of US pressures and cycle lengths combined with MBs were investigated (Fig. 1C). Before US treatment, no differences in  $P_{app}$  between the microvessels could be observed. After US treatment, within the MBs and short cycles group ( $10 \times 10$  cycles), the microvascular  $P_{app}$  was significantly increased compared to all the control microvessels only when applying the highest pressure (850 kPa  $10 \times 10$  cycles). For the microvessels that were treated with MBs and longer cycles ( $10 \times 1000$ ), both the 625 kPa and 850 kPa treated microvessels showed a significantly higher  $P_{app}$  than all the control groups. Besides this increase in  $P_{app}$ , the same increasing trend could be observed in the PI signal, suggesting a simultaneous increase in vascular permeability and sonoporation with higher pressure and longer cycle insonifications.

## Conclusions

Human vessels-on-a-chip were successfully grown in the OrganoPlate<sup>®</sup>. Due to the high throughput which can be achieved with the OrganoPlate<sup>®</sup>, the effect of MBs and a wide range of US pressures and cycle lengths on the vascular permeability and sonoporation of the microvessel could be investigated. The results showed that the pressures and cycle lengths significantly affect the increase of both the vascular permeability and PI. These results demonstrate that the vessel-on-a-chip grown in the OrganoPlate<sup>®</sup> is an excellent model to investigate microbubble-mediated drug delivery, which will aid the development of safe and efficient microbubble-mediated drug delivery.

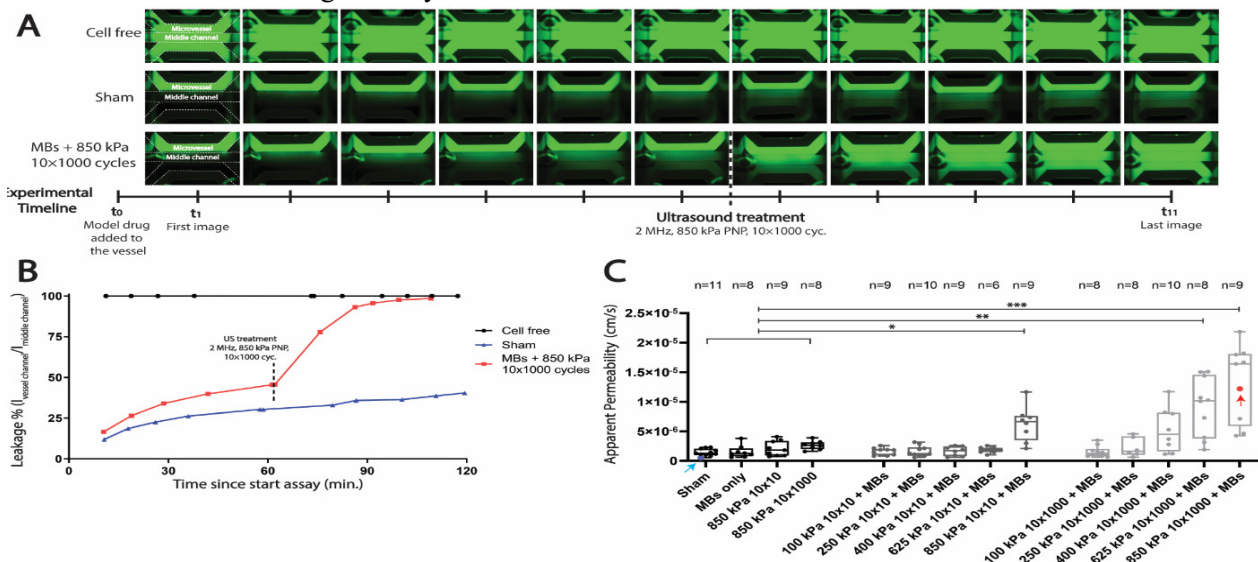


**Figure 1:** **A)** Overview of the leakage of the model drug (FITC-dextran dye; 150 kDa) over time in a cell-free, non-treated (sham), and ultrasound (2 MHz, 850 kPa PNP,  $10 \times 1000$  cycles) and microbubble treated microvessel. FITC-dextran dye was added to the microvessel (top channel) at  $t_0$  and the leakage of the drug to the middle channel was measured over time. **B)** Quantification of the fluorescent images in A. To obtain the leakage, the fluorescent intensity of the middle channel was divided by the fluorescent intensity in the top microvessel channel. **C)** Apparent permeability of the microvessels for controls and after ultrasound and microbubble treated. Typical examples from A and B are illustrated with colored datapoint and arrows (sham in blue, MB +US in red). Significant differences compared to all the control groups are indicated with \* $p < 0.05$ , \*\* $p < 0.01$ , \*\*\* $p < 0.001$ .

## Acknowledgements

This work was supported by the Applied and Engineering Sciences (TTW) (Vidi-project 17543), part of NWO. The authors thank Michiel Manten and Robert Beurskens from the Department of Biomedical Engineering, Thoraxcenter, Erasmus MC.

## References

- Beekers I, van Rooij T, Verweij MD, Versluis M, de Jong N, Trietsch SJ, Kooiman K, Acoustic Characterization of a Vessel-on-a-Chip Microfluidic System for Ultrasound-Mediated Drug Delivery, *IEEE Trans Ultrason Ferroelectr Freq Control*, VOL. 65, NO. 4, APRIL 2018.
- Langeveld SAG, Beekers I, Collado-Lara G, van der Steen AFW, de Jong N, Kooiman K, The Impact of Lipid Handling and Phase Distribution on the Acoustic Behavior of Microbubbles, *Pharmaceutics*, VOL. 13, NO. 1, JAN 2021.
- Tran TT, Mittal A, Gales T, Maleeff B, Aldinger T, Polli JW, Ayrton A, Ellens H, Bentz J, Exact kinetic analysis of passive transport across a polarized confluent MDCK cell monolayer modeled as a single barrier, *Journal of Pharmaceutical Sciences*, VOL. 93, ISSUE 8, AUGUST 2004

# Multi-Cellular Human Brain Spheroid Model to Study Sonoporation-Induced Drug Payload Penetration Beyond the Blood-Brain Barrier

*Anurag N Paranjape<sup>1</sup>, Leonardo D'Aiuto<sup>2</sup>, Wenxiao Zheng<sup>2</sup>, Xucai Chen<sup>1</sup>, and Flordeliza S Villanueva<sup>1</sup>*

<sup>1</sup>Center for Ultrasound Molecular Imaging and Therapeutics, University of Pittsburgh, Pittsburgh, PA, USA; <sup>2</sup>Department of Psychiatry, University of Pittsburgh School of Medicine Western Psychiatric Institute and Clinic, Pittsburgh, PA, USA; Corresponding author: villanuevafs@upmc.edu

## Introduction

The blood-brain barrier (BBB) acts as a major hindrance to treat various neurodegenerative diseases, gliomas and metastases. Ultrasound-targeted microbubble cavitation (UTMC) can facilitate delivery of cell-impermeant drugs across the endothelial barrier, including the BBB. To investigate the extent of payload penetration beyond the endothelial barrier and to study the bioeffects of UTMC on extravascular cells, we established a 3-dimensional (3-D) multi-cellular human brain spheroid model.

## Methods

Using neurons and astrocytes derived from human induced-pluripotent stem cells, primary human brain- microglia, brain microvascular endothelial cells (ECs) and pericytes the spheroids were generated (Fig. 1A). The architecture of the spheroids was analyzed using immunocytochemistry and confocal imaging. Ultrasound (1 MHz frequency, 250-500 kPa peak negative pressures, 10  $\mu$ s pulse duration, 10 ms pulse interval) was delivered for 10 s to the spheroids placed in a water tank with lipid microbubbles. We used propidium iodide uptake to mark sonoporation; calcein-AM and sytox red to detect cell viability; and Texas Red Dextran (10 kDa) to quantify permeability. BBB function was validated using histamine. L-NAME was used to confirm the involvement of endothelial nitric oxide synthase (eNOS) pathway in regulating UTMC-induced hyperpermeability.

## Results

As shown by immunostaining (Fig. 1B), membranous ZO-1 and CD31-positive ECs and NG2-positive pericytes were found at the spheroid periphery, while MAP2 expressing neurons, GFAP-positive astrocytes and Iba1 expressing microglia were distributed inside the spheroids. BBB functionality was confirmed with histamine treatment (Fig. 1C), which significantly increased the permeability to Texas Red Dextran (28.8% increase in mean fluorescence intensity,  $p < 0.002$ ). As shown by calcein-AM and sytox-red staining (Fig. 1D), UTMC did not induce significant cell death. Interestingly, we observed that propidium iodide uptake indicative of sonoporation was not limited to the endothelial surface coating the spheroid and in contact with microbubbles, but also occurred in cells  $\sim 200 \mu$ m beyond the BBB (Fig. 1E). UTMC increased the Texas Red Dextran penetration beyond the BBB (12.2% increase compared with no treatment), while inhibition of eNOS with L-NAME significantly reduced this UTMC-induced dextran penetration (19% decrease,  $p < 0.05$ ) (Fig. 1F).

## Conclusions

We have developed a 3-D brain spheroid model with an intact functional BBB that should be useful for systematic study of bioeffects of UTMC, including effects occurring spatially remote from the endothelial barrier. UTMC was able to breach the barrier and eNOS signalling was necessary for the UTMC-induced hyperpermeability. Importantly, for the first time we report here a remote sonoporation event occurring well beyond the endothelial barrier.

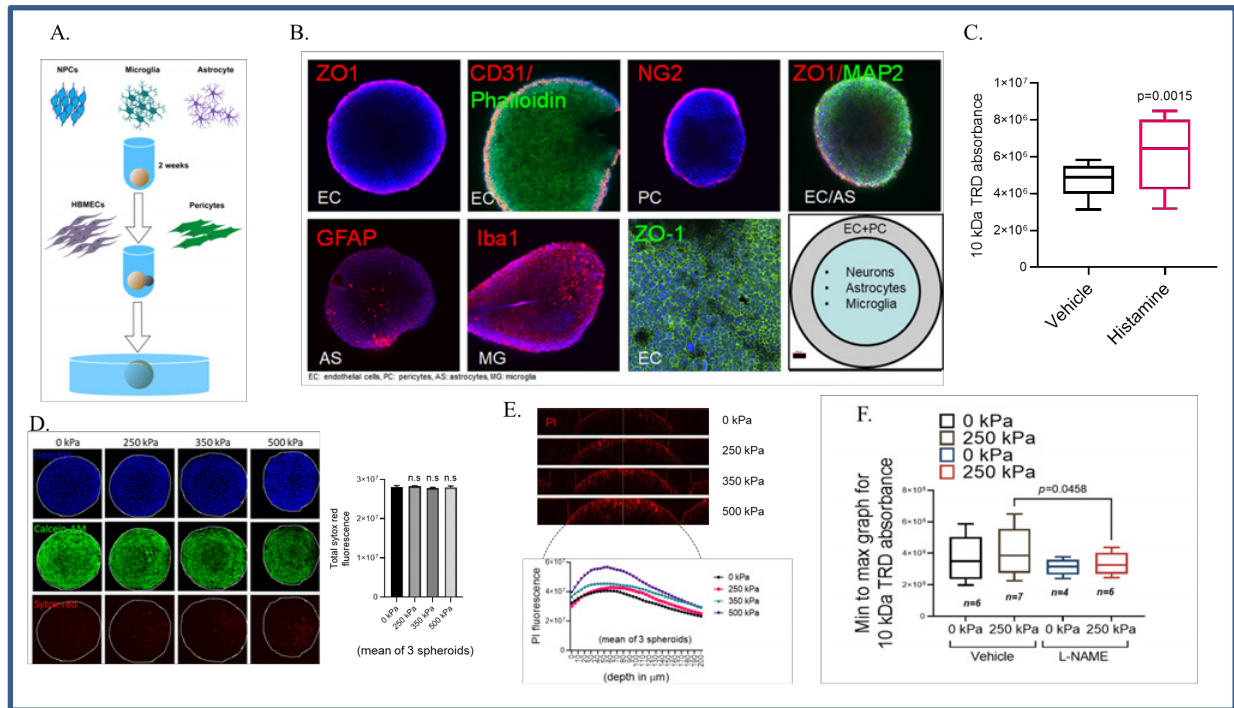


Figure 1. Establishing and validating a 3-D spheroid model for studying sonoporation-induced drug payload penetration beyond the BBB. A. Schematic showing generation of spheroids. B. Immunostaining to decipher the architecture of the spheroids (nuclei stained with DAPI, scale bar= 100  $\mu$ m). C. Graph shows enhanced Texas Red Dextran (TRD) uptake after 4.5 mM histamine treatment for 15 min ( $n=3$ ). D. Assessment of UTMC-induced cell death using calcein-AM and sytox red staining (nuclei stained with DAPI) ( $n=3$ ). E. Propidium iodide (PI) uptake (sonoporation) measured at various depths using confocal microscopy ( $n=3$ ) (images show orthogonal view of optical sections up to 200  $\mu$ m). F. The graph shows TRD absorbance after UTMC treatment in the presence of L-NAME or vehicle control. ( $n$ =number of spheroids, significance was calculated using Mann-Whitney test).

## References

- [1]. Helfield B, Chen X, Watkins S.C, and Villanueva F.S. Biophysical insight into mechanisms of sonoporation. Proc. Natl. Acad. Sci. USA 2016, 113, 9983–9988.
- [2]. D’Aiuto L, Naciri J, Radio N, Tekur S, Clayton D, Apodaca G, Di Maio R, Zhi Y, Dimitrion P, Piazza P, Demers M, Wood J, Chu C, Callio J, McClain L, Yolken R, McNulty J, Kinchington P, Bloom D, and Nimgaonkar V. 2018. Generation of three-dimensional human neuronal cultures: application to modeling CNS viral infections. Stem Cell Res Ther 9:134.

## Application of calcium sonoporation to effective apoptosis induction in gastrointestinal cancer cells

*Dawid Przystupski<sup>1</sup>, Dagmara Baczyńska<sup>2</sup>, Julita Kulbacka<sup>2</sup>,  
Joanna Rossowska<sup>3</sup>, Marek Ussowicz<sup>1</sup>*

<sup>1</sup> *Department of Paediatric Bone Marrow Transplantation, Oncology and Haematology,  
Wroclaw Medical University, Wroclaw, Poland*

<sup>2</sup> *Department of Molecular and Cellular Biology, Wroclaw Medical University, Wroclaw, Poland*

<sup>3</sup> *Ludwik Hirszfeld Institute of Immunology and Experimental Therapy, Polish Academy of Sciences,  
Wroclaw, Poland,*

*Corresponding author: dawid.przystupski@student.umw.edu.pl*

### Introduction

Some types of cancers, especially gastrointestinal cancers, display resistance to the chemotherapy which is called multi-drug resistance (MDR) phenomenon. Unfortunately, despite successful surgical treatment, the problem of cancer cell resistance to chemotherapeutics remains unsolved, resulting in the administration of ever-higher doses of cytostatic agents, which often prove to be ineffective. Due to the numerous clinical implications of the MDR phenomenon, there is a crucial need to seek treatments that abolish or modulate MDR. One of them is called sonoporation (SP) – the use of acoustic waves for temporary permeabilization of cell membranes, which allows the maximization of the targeted gene and drug delivery to tumors while minimizing their systemic toxicity. It has been reported that a rapid increase of intracellular calcium level by SP may be a new approach to cancer treatment through induction of cell death. Calcium ions are one of the most important stimuli of cell proliferation, differentiation and mostly cell death. Electroporation-based studies confirmed its efficacy in apoptosis induction, whereas the mechanisms triggered by calcium sonoporation (CaSP) remains unclear.

### Methods

The efficiency of sonoporation combined with Ca<sup>2+</sup> ions and SonoVue microbubbles was examined in this study. As a research model, we used two gastrointestinal cancer cell lines: colorectal cancer cells LoVo and pancreatic adenocarcinoma cells HPAF-II. At the beginning, we performed optimisation of sonoporation parameters (power of acoustic wave, its frequency and exposure time, duty cycle) using flow cytometry for YO-PRO-1 uptake and viability assessment. Then, we tested 3 calcium (CaCl<sub>2</sub>) concentration: 2.5 mM, 5 mM and 10 mM, combined with SonoVue microbubbles (SV) and the selected SP parameter: 2 W/cm<sup>2</sup>, 1 MHz, duty cycle 50%, 30 sec. To examine oxidative stress, we performed H<sub>2</sub>O<sub>2</sub> and mitochondrial superoxide generation assays, intracellular glutathione and lipid peroxidation analysis. Next, the mitochondria were evaluated as follows: mitochondrial membrane potential (JC-1 staining), ATP production and glucose uptake. Finally, cell death was analysed using flow cytometry for annexin-V/PI staining and cell cycle examination and Western Blot to identify caspase-3, Bax and Bcl-2 proteins.

### Results

Our studies have shown that the application of sonoporation in the presence of Ca<sup>2+</sup> ions and SonoVue microbubbles is cytotoxic for LoVo and HPAF-II cells – the lowest cell viability (app. 20%) was observed for 10 mM CaCl<sub>2</sub> combined SV. Next, we confirmed intense reactive oxygen species generation as well as lipid peroxidation 2 hours after CaSP, especially in LoVo cells. Similar tendency was observed for

intracellular glutathione assessment. However, mitochondrial superoxide production was significantly increased only for LoVo cells. Basing on these findings, we focused on mitochondria analysis in the following experiments. We revealed that calcium sonoporation is associated not only with oxidative stress but also strong mitochondrial disturbances – app. 80% of LoVo cells showed decreased mitochondrial membrane potential, ATP production as well as glucose uptake. Similar tendency for observed for HPAF-II cells but the revealed phenomena were not as intense as for LoVo cells. Flow cytometry showed a strong apoptosis induction for LoVo cells and G2/M cell cycle arrest in HPAF-II, which were proved by Western Blot analysis.

### **Conclusions**

Our studies show that SP combined with Ca<sup>2+</sup> is cytotoxic to gastrointestinal, especially colorectal cancer cells. Additionally, our experiments proved that CaSP may lead apoptosis through an intrinsic pathway induction triggered by strong CaSP-based mitochondria disturbances. The observed phenomena are also associated with intense reactive oxygen species generation. Moreover, calcium ions by themselves are non-toxic to normal cells, therefore causing no side effects as compared to well-known cytostatics. Interestingly, SP therapy based on calcium could reduce overhead and be less invasive than current therapies applied for colorectal and pancreatic cancers.

# Ultrasound Targeted Microbubble Cavitation improves aPDL1 Cancer Immunotherapy in a mouse colon adenocarcinoma model

Sepideh Jahangiri<sup>1,2</sup>, John Stagg<sup>3</sup>, Francois Yu<sup>1,4\*</sup>

<sup>1</sup> Microbubble Theranostic Laboratory, CHUM Research Center, Montreal, Canada

<sup>2</sup> Department of Biomedical Sciences, Faculty of Medicine, Université de Montréal, Montreal, Canada

<sup>3</sup> Faculty of Pharmacy, Université de Montréal, Montreal, Canada.

<sup>4</sup> Department of Radiology, Radiation Oncology and Nuclear Medicine, Faculty of Medicine, Université de Montréal.

Corresponding author: francois.yu@umontreal.ca

## Introduction

Immune checkpoint blockade (ICB) has emerged in the clinical setting, by unleashing cytotoxic immune cells against tumors, notably by blocking PD-1/PD-L1 axis, leading to complete remissions in subgroups of patients across several cancer types [1]. However, ICB fails for the majority of patients and can induce severe systemic toxicities. ICB resistance is characterized by insufficient immune cell penetration and impaired T cell function [2], which are associated with immune hostile tumor microenvironments (TME). Ultrasound Targeted Microbubble Cavitation (UTMC) can open and/or loosen the microvessel boundaries [3] and change the vascular integrity in a way that effectively improves the delivery of the therapeutic agents [4] and increase antibody extravasation to the site of interest [5, 6]. Interestingly, UTMC sonication of tumors could trigger an anticancer immunological response in mice associated with an increase in vascular permeability but the biological mechanistic signaling remains unclear [7].

Purinergic signaling is an important modulator of the tumoral microenvironment immune profile. Previous reports revealed the involvement of purinergic signaling in inflammation and cancer progression and its indispensable role in modulating cell migration, proliferation, and death [8-10]. ATP inhibits the proliferation of tumor cells and promotes cancer cell death. Hence, in tumors, ATP is rapidly hydrolyzed into adenosine (Ado) by CD39 and CD73 ectonucleotidases, often overexpressed by tumor and tumor resident immune cells. By contrast, Ado attenuates the immune response by suppressing effector cell function and stabilizing immunosuppressive T-Reg cells [11]. Since our laboratory has recently shown that UTMC can release ATP [12] and improve antibody extravasation [5], we are investigating the role of UTMC mediated ATP release and signaling in the context of improved aPDL1 efficacy. Herein, we hypothesized that we can improve the efficacy of aPDL1 by UTMC to inhibit tumor growth in a mouse model of colon adenocarcinoma (MC38) using conditions that increased tumoral perfusion (consistent with a release of ATP in the tumor) and could cause ATP release in muscle tissue.

## Methods

Tumor growth inhibition and mice survival study were performed on a syngeneic mouse colon adenocarcinoma (MC38) C57BL/6 model. Tumors implanted subcutaneously received a total of three treatments of 200 µg (i.v) of aPDL1 +/- UTMC every 3 days starting when the tumors reached 40 mm<sup>3</sup>. (N=5/group). Therapeutic US pulses (1 MHz, 850 kPa, 5000 cycles every 5 seconds, for 10 minutes) were applied using a single element transducer (A303S, Olympus) during a tail-vein MB infusion of perfluoropropane microbubbles (Definity, Lantheus). Therapy was guided by CEUS imaging using a clinical scanner (15L8, CPS7, Sequoia, Siemens) and burst replenishment imaging cineloops were analyzed offline to quantify tumoral perfusion before and after UTMC. Additionally, we quantified ATP release following UTMC by bioluminescence (Optix Mx2) using luciferin (3mg)/luciferase (270ug) in CD39 knock out mice (N=6). All statistical analyses were performed using GraphPad Prism version 8.0.2 (San Diego, USA) and p-value < 0.05 was considered statistically significant.

## Results

Tumor perfusion increased after UTMC treatment (Fig. 1A,  $p < 0.0001$ , paired t-test), consistently with a local release of ATP. In the tumor growth inhibition study (Fig. 1B), a significant effect of time and treatment groups were observed ( $p < 0.0001$ ; two way ANOVA). Differences between groups at fixed time revealed that UTMC+aPDL1 treatment caused a significantly reduced tumor size compared to the control group from day 11 onwards ( $p < 0.05$ , Fisher's LSD test). One mouse in UTMC+aPDL1 and one mouse in aPDL1 alone group showed complete rejection and did not develop tumor in re-challenge experiment indicating the role of anti-tumor immune memory (5 months follow-up). Survival rate analysis (Fig. 1C) showed a significant increase only in the UTMC+aPDL1 vs. control group ( $p = 0.001$ , Mantel-cox log rank test). Also, our preliminary results indicate UTMC can locally increase the level of eATP in muscle of CD39 knockout mice (Fig. 1D,  $p < 0.0001$ ,  $n = 6$ , test of Dunn).

## Conclusions

Hereby, we have shown UTMC+aPDL1 caused tumors growth inhibition in our murine colon carcinoma model, similarly to the finding of others [13]. This was associated with an increase in flow, consistently with a release of ATP and activation of purinergic signaling following UTMC as was observed in muscle [14]. We also confirmed that ATP can be released in the muscle of CD39 knock out mice, which was consistent with our prior findings using BALB/c mice in muscle and tumors [12]. It remains to be determined if ATP released using UTMC is implicated in the increase in efficacy of UTMC+aPDL1, which will be investigated using molecular inhibitors, antibody and genetically modified models in future studies.

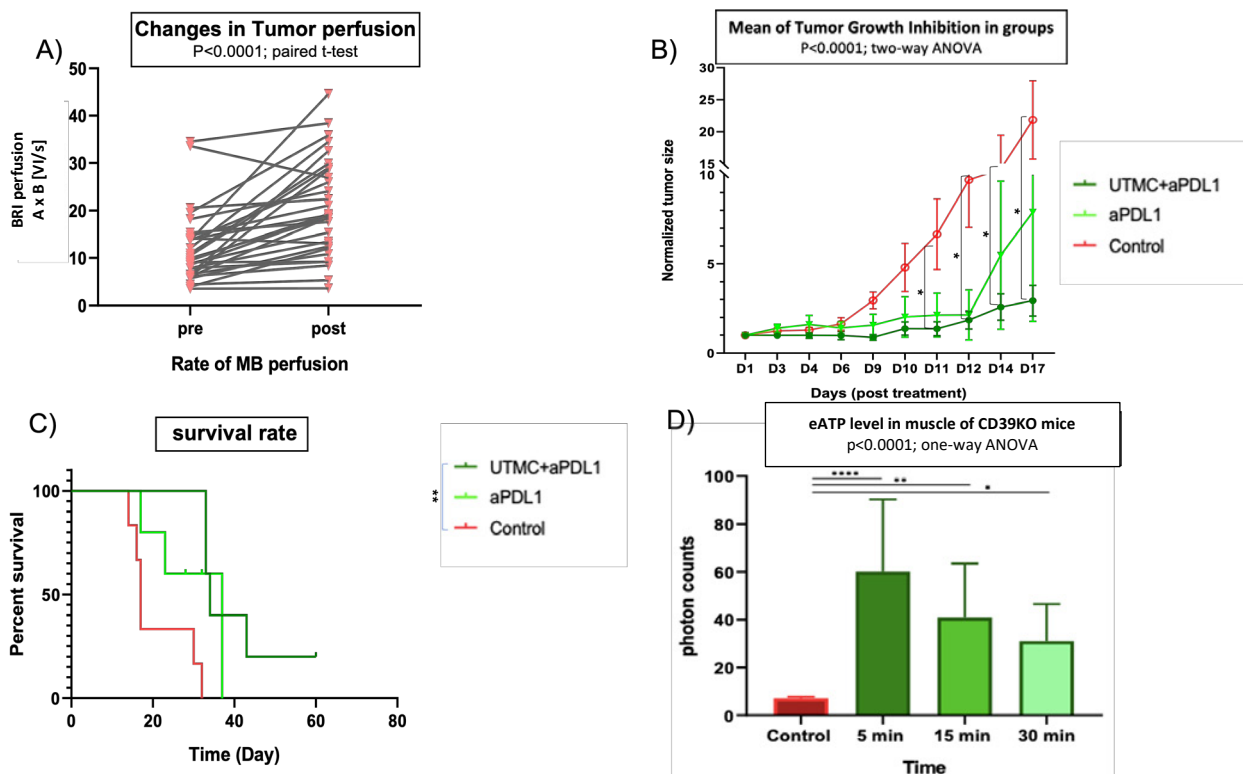


**Figure 1:** (A) Tumor perfusion increased after UTMC ( $p < 0.0001$ , paired t-test); (B) combined treatment of UTMC+aPDL1 caused growth inhibition of MC38 tumors vs control group (\*  $p < 0.05$ , Fisher's LSD test); (C) UTMC+aPDL1 treatment caused increased survival rate (\*\*  $p = 0.001$ , Mantel-Cox Log rank test); (D) UTMC treatment increased level of eATP up to 30 minutes post treatment ( $n = 6$ ,  $p < 0.0001$ , Dunn test); data are shown as mean  $\pm$  SEM.

### References

- [1] A. H. Sharpe and K. E. Pauken, "The diverse functions of the PD1 inhibitory pathway," *Nature Reviews Immunology*, vol. 18, no. 3, p. 153, 2018.
- [2] R. W. Jenkins, D. A. Barbie, and K. T. Flaherty, "Mechanisms of resistance to immune checkpoint inhibitors," *British journal of cancer*, vol. 118, no. 1, pp. 9-16, 2018.
- [3] S. R. Sirsi and M. A. Borden, "Advances in ultrasound mediated gene therapy using microbubble contrast agents," *Theranostics*, vol. 2, no. 12, p. 1208, 2012.
- [4] C. Mannaris *et al.*, "Microbubbles, nanodroplets and gas-stabilizing solid particles for ultrasound-mediated extravasation of unencapsulated drugs: an exposure parameter optimization study," *Ultrasound in medicine & biology*, vol. 45, no. 4, pp. 954-967, 2019.
- [5] M. Amate, J. Goldgewicht, B. Sellamuthu, J. Stagg, and F. T. Yu, "The effect of ultrasound pulse length on microbubble cavitation induced antibody accumulation and distribution in a mouse model of breast cancer," *Nanotheranostics*, vol. 4, no. 4, p. 256, 2020.
- [6] V. Frenkel, "Ultrasound mediated delivery of drugs and genes to solid tumors," *Advanced drug delivery reviews*, vol. 60, no. 10, pp. 1193-1208, 2008.
- [7] H.-L. Liu, H.-Y. Hsieh, L.-A. Lu, C.-W. Kang, M.-F. Wu, and C.-Y. Lin, "Low-pressure pulsed focused ultrasound with microbubbles promotes an anticancer immunological response," *Journal of translational medicine*, vol. 10, no. 1, pp. 1-14, 2012.
- [8] D. Allard, P. Chrobak, B. Allard, N. Messaoudi, and J. Stagg, "Targeting the CD73-adenosine axis in immuno-oncology," *Immunology letters*, vol. 205, pp. 31-39, 2019.
- [9] B. Allard, D. Allard, L. Buisseret, and J. Stagg, "The adenosine pathway in immuno-oncology," *Nature Reviews Clinical Oncology*, vol. 17, no. 10, pp. 611-629, 2020.
- [10] D. Allard, B. Allard, and J. Stagg, "On the mechanism of anti-CD39 immune checkpoint therapy," *Journal for immunotherapy of cancer*, vol. 8, no. 1, 2020.
- [11] I. Perrot *et al.*, "Blocking antibodies targeting the CD39/CD73 immunosuppressive pathway unleash immune responses in combination cancer therapies," *Cell reports*, vol. 27, no. 8, pp. 2411-2425. e9, 2019.
- [12] R. Grygorczyk *et al.*, "Lytic Release of Cellular ATP: Physiological Relevance and Therapeutic Applications," *Life*, vol. 11, no. 7, p. 700, 2021.
- [13] N. Li *et al.*, "Tumor perfusion enhancement by ultrasound stimulated microbubbles potentiates PD-L1 blockade of MC38 colon cancer in mice," *Cancer Letters*, vol. 498, pp. 121-129, 2021.
- [14] J. T. Belcik *et al.*, "Augmentation of muscle blood flow by ultrasound cavitation is mediated by ATP and purinergic signaling," *Circulation*, vol. 135, no. 13, pp. 1240-1252, 2017.

## Anti-Cancer Provascular Therapy using Ultrasound Microbubbles and Nitrites to Increase Radiotherapy Efficacy

***Simon Michon***<sup>1,2,3,4</sup>, ***Francis Rodier***<sup>2,4</sup>, ***Francois Yu***<sup>1,2,3,4\*</sup>

<sup>1</sup>Microbubble Theranostic Laboratory, CHUM Research Center, Montreal, Canada;

<sup>2</sup>Institut du Cancer de Montréal, Montreal, Canada;

<sup>3</sup>Institut de Génie Biomedical, University of Montreal, Canada;

<sup>4</sup>Department of Radiology, Radiation Oncology and Nuclear Medicine, Faculty of Medicine, University of Montreal, Canada

\*Corresponding author: francois.yu@umontreal.ca

### Introduction

Hypoxia is a recognized mechanism of resistance to radiation therapy in solid tumors [1]. It has recently been shown that ultrasound (US) targeted microbubble (MB) cavitation (UTMC) can increase the blood perfusion in muscles by triggering the signaling of nitric oxide [2], and that this effect was amplified also in muscle following nitrites injection [3]. We hypothesized that UTMC and nitrites injection can radiosensitize solid tumors by increasing blood perfusion and thus reduce tumor hypoxia.

### Methods

Mice were injected bilaterally with PC3 cancer cells, the right side being treated and left used as control. A therapeutic transducer (S3 probe, 1.3 MHz, SONOS 5500, Ultraharmonic Power Doppler) was used to transmit US pulses (M.I = 1.3, 1 frame) to the tissue of interest during the injection of MBs (Definity, Lantheus) via the tail vein (3-5  $\mu$ L/min). Nitrites were injected 5 minutes before treatment (4mg/kg). UTMC consisted of 60 therapeutic pulses, given at a pulse interval (10-15 seconds) adjusted to allow MB replenishment as guided by US contrast imaging (CPS 7MHz, Probe 15L8, Sequoia, Siemens), typically given in  $\sim$  15 min. The increase in perfusion in the tumor was quantified by burst replenishment imaging allowing longitudinal quantification of blood perfusion (AxB) [4]. Mice were irradiated 10 minutes after UTMC and tumor growth followed for 25 days. All statistics were performed using GraphPad Prism Software (v. 8.4.1).

### Results

In muscle, the increase in blood perfusion following UTMC + Nitrites treatment was strong and very rapid ( $13,64 \pm 8,13$  times the pre-treatment value, [\*\*\*  $p < 0.005$ , T-Test]). This significant increase in perfusion was also visible in tumors subjected to UTMC + Nitrites (Figure 1A :  $1,88 \pm 1,24$  times the pre-treatment value, [\*  $p < 0.005$ , T-Test]) and lasted for at least 10-15 minutes. Finally, there was an improved growth inhibition for the 8 Gy + UTMC + Nitrites group vs. 8 Gy + Nitrites alone (Figure 1B : +++  $p < 0.005$ , Mixed-model Analysis). This effect was not significant with mice treated by UTMC + Nitrites and receiving 0 Gy or 2 Gy, and in tumors treated with lower M.I. and without nitrites. The decrease in hypoxia post UTMC was confirmed by histology using Pimonidazole and HIF1 staining.

### Conclusions

In conclusion, UTMC + nitrites increased blood flow and reduced hypoxia in our mouse model of human prostate tumor, leading to an increased radiotherapy efficacy at 8 Gy.

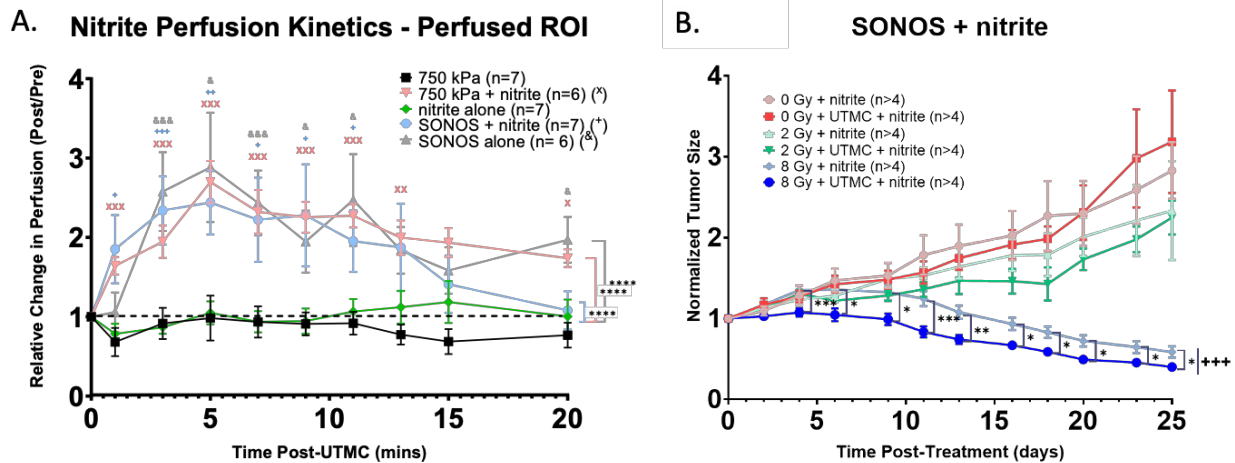


**Figure 1: A. Effect of UTMC + nitrite on tumor perfusion kinetics.** Time (\*\*\*) and treatment (\*\* =  $p < 0.02$ ) affected perfusion (two-way ANOVA). The provascular response for SONOS, SONOS + nitrite and 750 kPa + nitrite was higher than nitrite alone (\*\*\*\* =  $p < 0.0001$ , Tukey post-hoc). Significant increase vs nitrite at each timepoint is indicated (\*, +, & =  $p < 0.05$  respectively when compared to nitrite alone, Tukey post-hoc). Interestingly, the addition of nitrite induced a provascular response with the 750 kPa pulse that was not observed without nitrite ; **B. Tumor growth inhibition following UTMC Treatment with short pulses SONOS + nitrite and radiotherapy.** There was a significant difference in tumor sizes between the 8 Gy group (no-treatment) and the 8 Gy + UTMC + nitrite group (right: +++ =  $p < 0.001$ , Mixed-Model Analysis), (within 8Gy: \* =  $p < 0.05$ , \*\* =  $p < 0.01$ , \*\*\* =  $p < 0.001$ , Sidak post-hoc).

## References

- [1] L. H. Gray, A. D. Conger, M. Ebert, S. Hornsey, and O. C. Scott, "The concentration of oxygen dissolved in tissues at the time of irradiation as a factor in radiotherapy," *Br J Radiol*, vol. 26, no. 312, pp. 638-48, Dec 1953, doi: 10.1259/0007-1285-26-312-638.
- [2] F. T. H. Yu, X. Chen, A. C. Straub, and J. Pacella, "The role of nitric oxide during sonoreperfusion of microvascular obstruction," *Theranostics*, vol. 7, no. 14, pp. 3527-3538, 2017.
- [3] G. Z. Yu *et al.*, "Ultrasound-Targeted Microbubble Cavitation with Sodium Nitrite Synergistically Enhances Nitric Oxide Production and Microvascular Perfusion," *Ultrasound Med Biol*, vol. 46, no. 3, pp. 667-678, Mar 2020, doi: 10.1016/j.ultrasmedbio.2019.10.012.
- [4] K. Wei, A. R. Jayaweera, S. Firoozan, A. Linka, D. M. Skyba, and S. Kaul, "Quantification of myocardial blood flow with ultrasound-induced destruction of microbubbles administered as a constant venous infusion," (in English), *Circulation*, vol. 97, no. 5, pp. 473-483, Feb 10 1998. [Online]. Available: <Go to ISI>://000071887700012.

# Ultrasound-assisted miR-1 delivery towards the treatment of hypertrophic cardiomyopathy

*Davindra Singh<sup>1</sup>, Stephanie He<sup>1</sup>, Brandon Helfield<sup>1,2</sup>*

<sup>1</sup>*Department of Biology, Concordia University, Montreal, Canada*

<sup>2</sup>*Department of Physics, Concordia University, Montreal, Canada*

*Corresponding author: davindra.singh@concordia.ca*

## Introduction

Hypertrophic cardiomyopathy is a cardiovascular disease that results in the abnormal growth of cardiac cells, which can overtime lead to sudden cardiac arrest [1]. This disease is characterized by a downregulation of miR-1 leading to an increased upregulation of mRNA targets (e.g. TWF1, MEF2A, CX43) [2,3,4]. Cardiac miRNA therapy, while a promising alternative treatment approach to surgical and pharmacological techniques for cardiovascular disease, is currently challenged by a safe and effective delivery method [5].

Ultrasound contrast agent microbubbles, which are commonly employed as a clinical echocardiography contrast agent, offer an exciting approach to localized, image-guided cardiac gene therapy. Here, we demonstrate the feasibility of viable ultrasound-mediated miR-1 delivery to hypertrophic cardiomyocytes and simultaneously record bubble cavitation to provide correlative acoustic measurements.

## Methods

Cardiomyocytes (CMs) were isolated from neonatal rat pups between 1-3 days old. Our hypertrophy disease model was established by CM incubation with phenylphrine (100  $\mu$ M), an  $\alpha$ -1 adrenergic agonist, and confirmed via cell size measurement (29% increase,  $p=0.03$ ), RT-qPCR expression (60% decrease in miR-1,  $p=0.005$ ) and downstream protein expression (34% increase in TWF1,  $p=0.0002$ ; 50% increase in MEF2A,  $p=0.0002$ ; 45% increase in CX43,  $p=0.0003$ ). Homemade phospholipid-coated microbubbles (5e9 MBs/ml) were synthesized using a C<sub>3</sub>F<sub>8</sub> gas core and a DPPC:DPPA:DPPE-PEG5K lipid shell. Suspensions of either healthy or diseased CMs along with microbubbles (1:250 cell to bubble ratio) and free miR-1 (84nM) were placed in a chamber within a 37°C deionized, gas equilibrated water bath. Samples were insonicated for 2 minutes (1 MHz, peak-negative pressures ranging from 62.5-250 kPa; 20 cycles; 200  $\mu$ s PRI) and bubble echoes were simulatenoulsy recorded via a co-aligned 3 MHz transducer. Two days post treatment, miR-1 levels and cell viability were assessed using RT-qPCR and MTT assays respectively. Echoes were processed offline using MATLAB to extract harmonic and broadband cavitation doses.

## Results

In both healthy and diseased CMs, increasing delivery of miR-1 was observed with increasing peak-negative pressure from 62.5 to 187.5 kPa. Optimal delivery was achieved at 62.5 kPa, resulting in an 2.79 and 2.44 fold relative increase in miR-1 compared to untreated controls for healthy and diseased CM populations respectively ( $p=0.02$ ;  $p=0.07$ ), while maintaining cell viability (98% and 95% respectively). Passive cavitation data highlights that relative miR-1 expression positively correlates with inertial cavitation dose ( $r=0.76$ ,  $p=0.04$ ).

## Conclusions

We demonstrated that ultrasound-stimulated microbubbles can be used to deliver miR-1 to both healthy and hypertrophied cardiomyocytes while preserving cell viability. These findings demonstrate the feasibility of ultrasound as an image-guided delivery method for molecular therapeutics in cardiovascular disease.

## References

- [1]. Spudich, J.A. 2014. Hypertrophic and dilated cardiomyopathy: Four decades of basic research on muscle lead to potential therapeutic approaches to these devastating genetic diseases. *Biophys. J.* 106:1236–1249. doi:10.1016/j.bpj.2014.02.011.

- [2]. X.Q. Li, N. Zhu, P. Lappalainen, W.J. Yuan, Y.W. Qin, and Q. Jing. 2010. Attenuation of microRNA-1 derepresses the cytoskeleton regulatory protein twinfilin-1 to provoke cardiac hypertrophy (Journal of Cell Science 123, (2444-2452)). *J. Cell Sci.* 123:2680. doi:10.1242/jcs.077578.
- [3]. Peng, C., X. Luo, S. Li, and H. Sun. 2017. Phenylephrine-induced cardiac hypertrophy is attenuated by a histone acetylase inhibitor anacardic acid in mice. *Mol. Biosyst.* 13:714–724. doi:10.1039/c6mb00692b.
- [4]. Ye, J., M. Cardona, M. Llovera, J.X. Comella, and D. Sanchis. 2012. Translation of Myocyte Enhancer Factor-2 is induced by hypertrophic stimuli in cardiomyocytes through a Calcineurin-dependent pathway. *J. Mol. Cell. Cardiol.* 53:578–587. doi:10.1016/j.yjmcc.2012.07.013.
- [5]. Chen, H.H., P.N. Matkar, K. Afrasiabi, M.A. Kuliszewski, and H. Leong-Poi. 2016. Prospect of ultrasound-mediated gene delivery in cardiovascular applications. *Expert Opin. Biol. Ther.* 16:815–826. doi:10.1517/14712598.2016.1169268.

## Proton range verification with superheated droplets: influence of droplet size, concentration, and proton fluence on the range verification precision

Gonzalo Collado-Lara<sup>1</sup>, Sophie V. Heymans<sup>1,2,6</sup>, Marta Rovituso<sup>3</sup>, Edmond Sterpin<sup>4</sup>, Hendrik J. Vos<sup>1</sup>, Jan D'hooge<sup>6</sup>, Koen Van Den Abeele<sup>2</sup>, Nico de Jong<sup>1</sup>,

<sup>1</sup>Department of Biomedical Engineering, Erasmus Medical Center, Rotterdam, The Netherlands

<sup>2</sup>Department of Physics, KU Leuven Campus Kulak, Kortrijk, Belgium

<sup>3</sup>Holland Proton Therapy Center, Delft, The Netherlands

<sup>4</sup>Department of Oncology, KU Leuven, Leuven, Belgium

<sup>5</sup>Department of Medical Imaging, TU Delft, Delft, The Netherlands

<sup>6</sup>Department of Cardiovascular Sciences, KU Leuven, Leuven, Belgium

Corresponding author: g.colladolar@erasmusmc.nl

### Introduction

Proton therapy is an advanced cancer therapy which can optimize the spatial dose distribution compared to conventional radiotherapy. Protons, contrary to photons, completely stop within the patient's body, depositing most of their energy in a confined area known as the Bragg peak. The residual dose to surrounding healthy organs is thus minimized provided the Bragg peak position is accurately controlled. However, in practice, the proton range is affected by different sources of uncertainty. Hence, there is a coercing need for a range verification method with a sub-millimetric accuracy to optimize the treatment delivery. Range verification could be performed in vivo with superheated nanodroplets, as they vaporize upon proton beam irradiation, depicting a vaporization distribution related to the proton stopping distribution [1]. The vaporization process is stochastic, implying that the range verification precision depends on the probability of proton-induced vaporizations. In the present contribution, we propose and validate a statistical model to predict the number of vaporizations for a variety of conditions, and use the model to predict a lower limit of the range localization precision.

### Methods

The probability of proton-induced vaporization was modelled in light of the homogeneous nucleation theory [2]. Vaporization occurs if a proton deposits enough energy to nucleate a gas embryo larger than a critical size. This condition can only be met at the end of the proton track, where the deposited energy density is above the critical embryo nucleation threshold. Therefore, that the probability of a proton to vaporize a single droplet is assumed to be equivalent to the probability of a proton stopping within a droplet, i.e.  $p = 4/3\pi R_d^3 n_d$ , where  $R_d$  is the droplet radius, and  $n_d$  the droplet number concentration. Next, the distribution of vaporizations for  $N_p$  protons is modelled as a binomial distribution assuming that the vaporization probability remains constant. This model was tested experimentally by irradiating droplet solutions in a proton beam (Holland PTC, Delft, the Netherlands) and counting the vaporization events. Vaporizations of nanodroplets dispersed in a non-newtonian gel were acoustically monitored during irradiation using a linear array (L12-5) with a Vantage 256 system (Verasonics, Kirkland, USA). Individual vaporization events were detected on beamformed images using differential imaging, as described in [1]. The number of protons was determined for each irradiation using an ionization chamber (DE.TEC.TOR, Turin, Italy). Droplet dispersions were prepared from three different droplet subpopulations with mean radius of 1.0, 1.8 and 2.9  $\mu\text{m}$ , isolated by differential centrifugation. The droplet radius was kept above 0.5  $\mu\text{m}$  so they could be measured using a Coulter counter. Different droplet concentrations were studied.

Since the spatial distribution of protons follows a three-dimensional normal distribution, the range position can be estimated from the mean position of the vaporization events (i.e. the maximum likelihood estimator). Further, the range verification precision can then be estimated as the standard deviation of the mean  $\sigma_x = \sigma_x / \sqrt{N_v}$ , where  $x$  is the vaporization position, and  $N_v$  the number of vaporizations, which can then be combined with the above derived statistical model.

## Results

Individual droplet vaporizations were successfully recorded via differential imaging. Corrections were applied to remove a decay over time in the number of vaporizations. First, to isolate the effect of the droplet size, the number of counts were normalized with the number of protons and the droplet number concentration. The mean number of normalized counts were 1, 23, and 197 for increasing droplet size, compared to the expected values from the statistical model of 4, 24, and 102, respectively. The experimental results were in good agreement with theory (Fig. 1a), except for smaller droplets. Furthermore, to isolate the effect of the concentration, the counts of only one size were normalized with the number of protons (Fig. 1b). The number of vaporizations increased linearly with the droplet concentration.

After validation, the model was used to assess the range verification precision as a function of the number of protons and the droplet volume concentration for a beam energy of 154 MeV ( $\sigma_x = 3.2$  mm). Three different precision regions are depicted in Fig. 1c, i.e. good ( $\sigma_x < 0.5$  mm), acceptable ( $0.5 \text{ mm} < \sigma_x < 2$  mm), and unacceptable precision ( $\sigma_x > 2$  mm). As a reference, if  $10^7$  protons were used, which is a clinically relevant value for a single spot in proton pencil beam scanning, a droplet volume concentration of  $4 \cdot 10^{-6}$  mL/mL is the minimum to achieve a good precision ( $\sigma_x < 0.5$  mm). This concentration is in the same order of magnitude as the volume concentration of SonoVue in an average-sized vascular system [3].

## Conclusions

It was shown that the number of vaporizations can be estimated based on the number of incoming protons, the droplet size, and the droplet concentration. The number of vaporizations was then used to estimate the precision of the range verification method. The results reported here show that superheated droplets could provide sub-millimetric precision for range verification using realistic droplet concentrations.

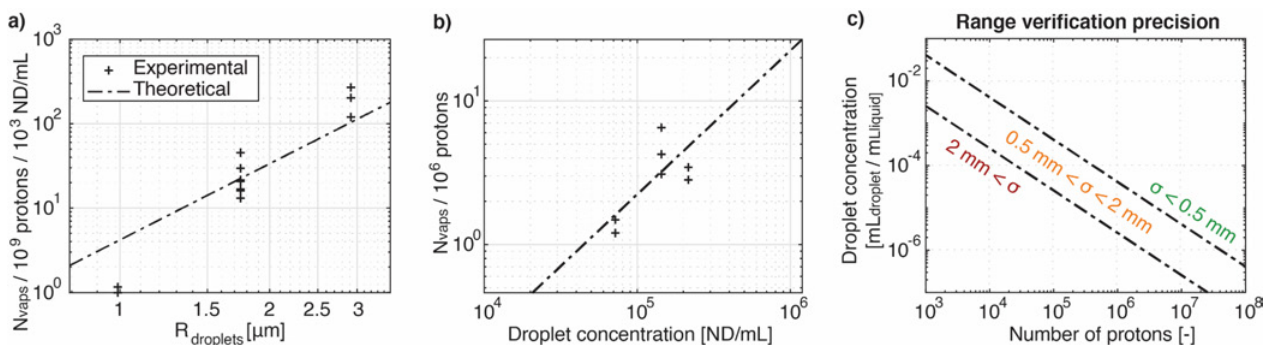


Figure 1. a) Number of vaporizations normalized with the number of protons and droplet concentration as a function of droplet size. b) Number of vaporizations normalized with number of protons as a function of droplet concentration. The crosses represent experimental results and the dotted-dashed line the prediction of the statistical model. c) Range verification precision limits as a function of number of incoming protons and droplet volume concentration.

## References

- [1]. Collado-Lara G and Heymans SV et al, Spatiotemporal distribution of nanodroplet vaporization in a proton beam using real-time ultrasound for range verification, *Ultrasound in Medicine and Biology*, In Press, 2021
- [2]. Seitz F, On the Theory of the Bubble Chamber, *The physics of fluids*, Vol. 1, No. 1, 1958
- [3]. Schneider M, Characteristics of SonoVue<sup>TM</sup>, *Echocardiography*, Vol. 16, No. 7, Part 2, 1999

# 20 Mfps interleaved ultra-high-speed imaging by coupling two Shimadzu HPV-X2 cameras

*Hongchen Li<sup>1</sup>, Xiufeng Li<sup>2</sup>, Frits Mastik<sup>1</sup>, Robert Beurskens<sup>1</sup>, Antonius F. W. van der Steen<sup>1</sup>, Martin D. Verweij<sup>1,2</sup>, Nico de Jong<sup>1,2</sup>, Klazina Kooiman<sup>1</sup>*

<sup>1</sup>Department of Biomedical Engineering, Erasmus MC, Rotterdam, the Netherlands

<sup>2</sup>Laboratory of Acoustical Wavefield Imaging, Delft University of Technology, Delft, the Netherlands

Corresponding author: [h.li@erasmusmc.nl](mailto:h.li@erasmusmc.nl)

## Introduction

Ultrasound-mediated biomedical imaging and therapy substantially rely on the dynamics of ultrasound contrast agents, such as microbubbles and nanodroplets [1,2]. The response of contrast agents to ultrasound is crucial for contrast agent design [3] and the interaction between contrast agents and tissues and/or bacteria [2]. Ultra-high-speed imaging could provide detailed insights into the responses of contrast agents such as size change and vibration mode [4]. However, current ultra-high-speed imaging systems are either not fast enough for acoustical spectroscopy [5] or custom-made requiring lots of expertise and a large budget [6], which limits the application of ultra-high-speed imaging in contrast agent research. Therefore, the aim of this study was to develop a 20 million frames per second (Mfps) ultra-high-speed imaging system by interleaving two small-sized commercially available 10 Mfps Shimadzu cameras and demonstrate the performance of the system including its flexibility to adapt to different experimental setups.

## Methods

The two Shimadzu HPV-X2 ultra-high-speed cameras were electronically coupled using their internal synchronization function, where a S/FTP Cat 6 standard network cable was used to connect the two cameras. The 20 Mfps recording speed was achieved by interleaving the two cameras which worked at 10 Mfps separately (50 ns exposure time) by triggering with a 50 ns delay in between. Because of synchronization, the two cameras were labeled as Shimadzu 1 and Shimadzu 2, which means that the Shimadzu 1 records 50 ns earlier than the Shimadzu 2. Each camera has a resolution of 400×250 pixels.

To verify the 20 Mfps recording speed, two experiments were implemented with the setups shown in Fig. 1a and Fig. 1c. In experiment one (Fig. 1a), two synchronized high-frequency green LED lights were separately placed towards the two cameras to which Tamron 60mm F/2.0 macro lenses were connected. Two LED lights were driven by a customized driver circuit at 6.67 MHz and 1/3 on/off duty cycle (50 ns on and 100 ns off) for 160 pulses. Both the LED driver and the Shimadzu 1 were triggered by the same arbitrary waveform generator, while the start of the LEDs were delayed 1550 ns according to the initialization time of the camera (850 ns), aiming to obtain dissimilar recording patterns from two cameras.

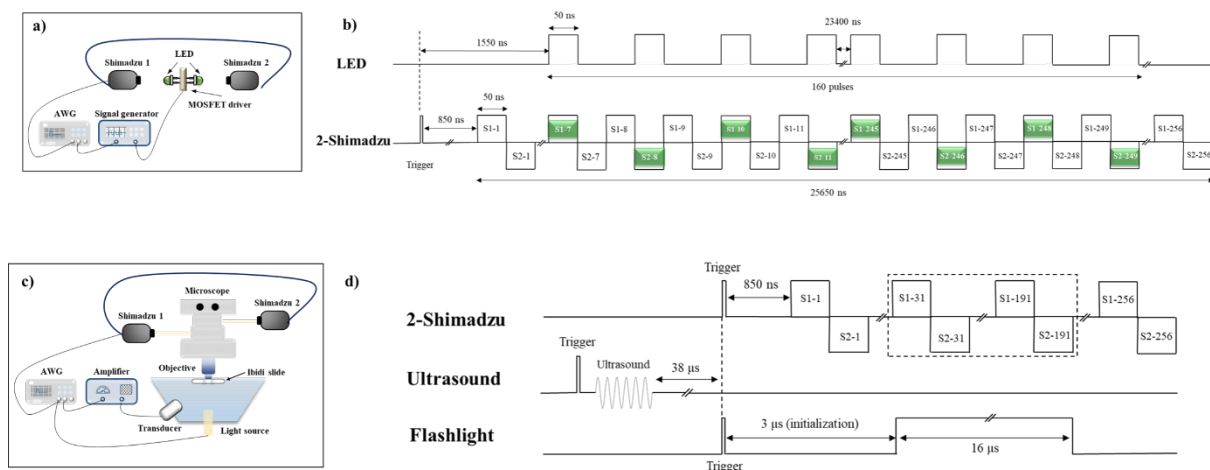


**Figure 1. Experimental setups of two Shimadzu ultra-high-speed cameras coupling and their corresponding timing diagrams. a) Sketch of the 20Mfps interleaving verification using strobe LEDs. b) The**

timing diagram of the LED and the 2-Shimadzu system in experiment one. c) Sketch of the 20Mfps interleaving recording of microbubble vibration. d) The timing diagram of the 2-Shimadzu system, ultrasound, and flashlight in experiment two.

In experiment two (Fig. 1c), the 2-Shimadzu system was air-coupled to two output ports of an Olympus bright-field microscope at 60× magnification, in order to record microbubble vibration upon ultrasound insonification. DSPC-based lipid-coated microbubbles with a C<sub>4</sub>F<sub>10</sub> gas core were made by probe sonication as described previously [7] and they were placed in an IbiTreat polymer μ-slide (80196; 0.8 mm channel height; I Luer) in a concentration of 5×10<sup>5</sup>/ml at room temperature. A single element transducer (used at 2 MHz, 100 kPa (peak negative pressure), 20 cycles) was placed underneath the microchannel at a 45° angle to insonify microbubbles. Owing to the ultrasound propagation duration, the 2-Shimadzu system and the flashlight were delayed 38 μs after the ultrasound was sent (shown in Fig. 1d). After acquiring the microbubble oscillation recordings, the microbubble vibration was tracked from each recording using the Hough transform method in MATLAB.

### Results

Each camera recorded 256 frames, so 512 frames in total were recorded for the 2-Shimadzu system, resulting in a full recording duration of 25.650 μs. The selected frames from the LED experiment (Fig. 2) show that the two cameras acquired unique intensity patterns of the flashing LED at different time points. The Shimadzu 1 showed a repeated pattern of bright, dark, dark, whereas the Shimadzu 2 showed a repeated pattern of dark, bright, dark. The patterns show that the two cameras captured the ‘on’ status of the LED in an interleaved way, thereby verifying that the exposure delay (50 ns) between the two cameras was accurately controlled.

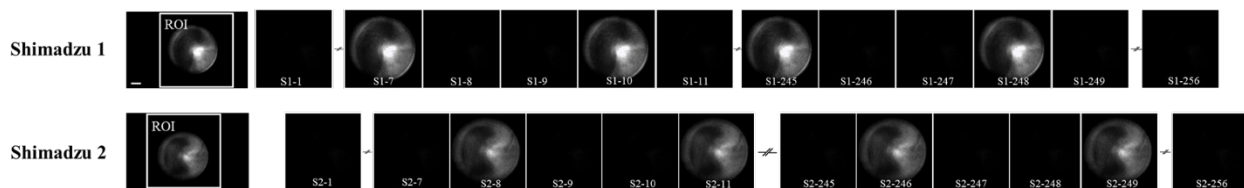


Figure 2. Selected frames from two cameras of the LED flashing experiment.

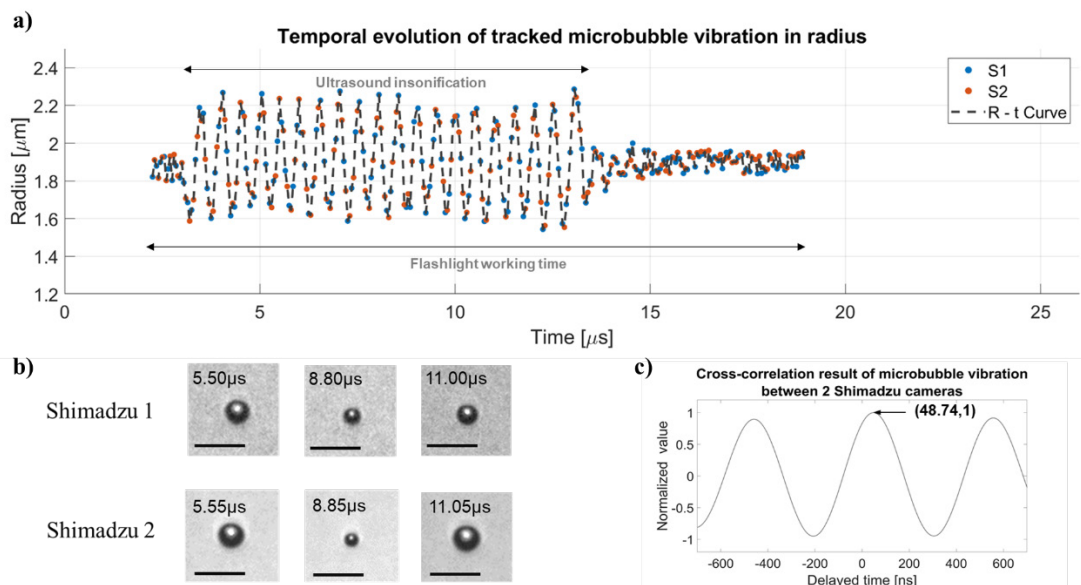


Figure 3. Results on 20Mfps interleaving recording of microbubble vibration. a) Temporal evolution of tracked microbubble vibration in radius. b) Selected recorded frames (the length of the scale bar is 10 μm). c) The cross-correlation result of radius tracked from two cameras.

Fig. 3a shows a vibrating microbubble captured by the 2-Shimadzu system. The microbubble, having a resting radius of 1.83  $\mu\text{m}$ , vibrated 20 cycles at a central frequency of 2 MHz. The recordings from the two cameras show a slightly different radius (Fig. 3b) and the extracted radius-time curves indicating a time shift of approximately 50 ns. To accurately investigate the time shift, the radius-time data were further processed by calculating the extent of the cross-correlation, which resulted in a time delay of 48.74 ns between the two cameras as shown in Fig. 3c. This time delay is 2.8% less than the required 50 ns.

### Conclusions

A novel and flexible ultra-high-speed imaging system with the recording speed of 20 Mfps was successfully developed by interleaving two Shimadzu HPV-X2 cameras. Two verification experiments validated the interleaving timing and reliability, including revealing the dynamics of the ultrasound-activated microbubble. With this advanced imaging system, we expect to further elucidate ultrasound-mediated imaging and therapy and advance the knowledge of the dynamics of ultrasound contrast agents and their interaction with living cells in an ultrasound field.

**Acknowledgements** – This project has received funding from the European Research Council (ERC) under the European Union's Horizon 2020 research and innovation program [grant agreement 805308].

### References

- [1] K. Christensen-Jeffries, O. Couture, P.A. Dayton, Y.C. Eldar, K. Hynynen, F. Kiessling, M. O'Reilly, G.F. Pinton, G. Schmitz, M.X. Tang, M. Tanter, R.J.G. van Sloun, Super-resolution Ultrasound Imaging, *Ultrasound Med Biol*, 46 (2020) 865-891.
- [2] K. Kooiman, S. Roovers, S.A.G. Langeveld, R.T. Kleven, H. Dewitte, M.A. O'Reilly, J.M. Escoffre, A. Bouakaz, M.D. Verweij, K. Hynynen, I. Lentacker, E. Stride, C.K. Holland, Ultrasound-Responsive Cavitation Nuclei for Therapy and Drug Delivery, *Ultrasound Med Biol*, 46 (2020) 1296-1325.
- [3] E. Stride, T. Segers, G. Lajoinie, S. Cherkaoui, T. Bettinger, M. Versluis, M. Borden, Microbubble Agents: New Directions, *Ultrasound Med Biol*, 46 (2020) 1326-1343.
- [4] N. de Jong, M. Emmer, A. van Wamel, M. Versluis, Ultrasonic characterization of ultrasound contrast agents, *Med Biol Eng Comput*, 47 (2009) 861-873.
- [5] G. Lajoinie, N. de Jong, M. Versluis, Brandaris Ultra-High-Speed Imaging Facility, *The Micro-World Observed by Ultra-High-Speed Cameras 2018*, pp. 49-77.
- [6] C.T. Chin, et al and also for the UPMC cam add: X. Chen, J. Wang, M. Versluis, N. de Jong, F.S. Villanueva, Ultra-fast bright field and fluorescence imaging of the dynamics of micrometer-sized objects, *Rev. Sci. Instrum.*, 84 (2013) 063701.
- [7] S.A.G. Langeveld, I. Beekers, G. Collado-Lara, A.F.W. van der Steen, N. de Jong, K. Kooiman, The Impact of Lipid Handling and Phase Distribution on the Acoustic Behavior of Microbubbles, *Pharmaceutics*, 13 (2021).

# Environmental contrast enhanced ultrasound imaging: visualizing perfusion changes in rainbow trout bowel after induction of inflammation

*Marianna E. Horn<sup>1</sup>, Una Goncin<sup>1</sup>, Ron Geyer<sup>2</sup>, Ahmed El Kaffas<sup>3</sup>, Markus Brinkmann<sup>4</sup>, Helmut Segner<sup>5</sup>, Steven Machtaler<sup>1</sup>*

<sup>1</sup>*Department of Medical Imaging, University of Saskatchewan, Saskatoon, Canada*

<sup>2</sup>*Department of Pathology, University of Saskatchewan, Saskatoon, Canada*

<sup>3</sup>*Department of Radiology and Radiation Oncology, Stanford University, Stanford, USA*

<sup>4</sup>*School of Environment and Sustainability, University of Saskatchewan, Saskatoon, Canada*

<sup>5</sup>*Centre of Fish and Wildlife Health, University of Bern, Bern, Switzerland*

*Corresponding author: marianna.horn@usask.ca*

## Introduction

Inflammatory bowel disease (IBD) disproportionately affects people in rural northern First Nations communities in Canada [1], where low water quality from pathogens and high levels of various metals [2] is a probable contributing factor. However, the precise combinations of contaminants most likely to contribute to IBD development are unknown. Establishment of an animal sentinel system could aid in identifying the combinations of contaminants leading to increased prevalence of IBD in these communities.

The immune and gastrointestinal systems of fish are similar in both structure and function to those of mammals [3]. Aquatic habitat makes fish inherently sensitive to water quality, giving them potential as an environmental sentinel [4]. If non-invasive imaging can be performed on environmentally-relevant fish, wild specimens from contaminated waters can be non-lethally used to collect epidemiological data for use in identifying bodies of water in which bowel inflammation is more prevalent.

The goal of this study is to establish a chemically-induced model of bowel inflammation in rainbow trout (*Oncorhynchus mykiss*) using the haptentizing agent Trinitrobenzene sulfonic acid (TNBS), commonly used in murine models of IBD [5], and measure changes in bowel inflammation using contrast-enhanced ultrasound (CEUS) imaging. The ultimate purpose is the development of a non-invasive tool to assess bowel inflammation in trout to detect environmental factors that may play a role in developing IBD.

## Methods

**Bowel inflammation and imaging:** Rainbow trout (30-150 g) were anaesthetized with Tricaine methane sulfonate (MS-222, 0.08 g/L water) after two days of fasting. Acute bowel inflammation was induced through rectal administration of TNBS or saline: (i) 500  $\mu$ l saline control (n = 4), (ii) 250  $\mu$ l 2.5% TNBS + 250  $\mu$ l 95% ethanol (n = 4). Trout were anaesthetized again 24 h later and prepared for imaging. Scales were carefully removed posterior to the pelvic fin and anterior to the anus, to prevent impedance in the imaging region. Rectal administration of ultrasound gel cleared the imaging region of fecal matter. Microbubbles were prepared in a VIALMIX, which agitated 1.5 ml of solution (2 g/ml of 9:1 molar ratio of 1,2-distearoyl-sn-glycero-3-phosphocholine (DSPC) and 1,2-distearoyl-sn-glycero-3-phosphoethanolamine-N-[methoxy(polyethylene glycol)-2000] (DSPE-PEG2000)) within a 3 ml vial of perfluorobutane (C<sub>4</sub>F<sub>10</sub>) for 45 s. A bolus of MBs (diameter mean  $\pm$  SD: 0.93  $\mu$ m  $\pm$  0.59, measured using a Beckman Coulter Multisizer 4e) was injected intravenously at a dosage of 1.5x10<sup>6</sup> MBs/g through the caudal tail vein and visualized using non-linear contrast mode on a small animal ultrasound system (VEVO3100 preclinical ultrasound system, MX250 – 20 MHz transducer). After imaging, trout were humanely euthanized and their bowels were harvested for histology.

**Perfusion analysis:** Using MATLAB, peak enhancement (PE) was measured by drawing a region of interest (ROI) around the bowel and a time-intensity curve (TIC) was generated using a lognormal fit.

## Results

Histology validated epithelial damage, increased villi thickness, and presence of submucosal inflammation in the TNBS-treated bowels (Fig. 1A), consistent with the response in mice.

CEUS imaging identified that the gut of rainbow trout is acoustically visible and highly vascularized (Fig. 1C). Administration of MBs in trout with inflamed bowels resulted in a mean PE value of  $0.85 \text{ a.u.} \pm 0.07$ , which was significantly lower than normal bowels, where the mean PE was  $0.94 \text{ a.u.} \pm 0.03$  ( $F_{1,8} = 6.552$ ,  $p = 0.043$ ; Fig. 1E). These data suggest that in rainbow trout, peak enhancement decreases with high levels of acute inflammation, possibly due to edema, consistent with other pre-clinical studies including in mice [6].

## Conclusions

The bowel of rainbow trout responds to TNBS administration with acute inflammation. The bowels are acoustically visible, and show a decrease in bowel perfusion 24 hours post TNBS administration. These data suggest that CEUS can be used to differentiate normal and inflamed gut, and may provide a non-invasive means of evaluating the impacts of water quality on gut inflammation in wild fish.

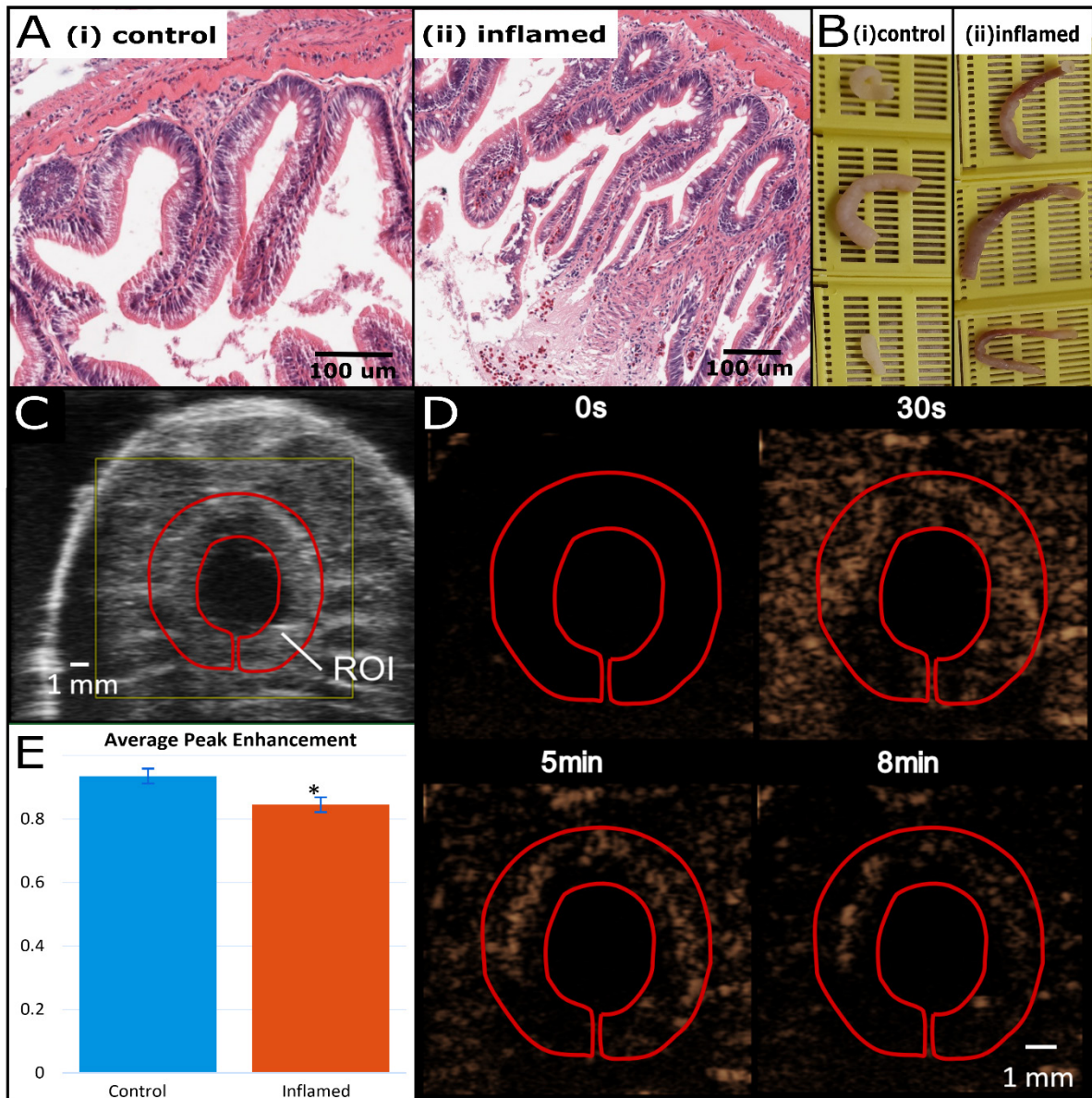


Figure 1. Contrast-enhanced perfusion imaging of rainbow trout bowel. (A) Histological staining of trout bowel (i) control without or (ii) inflamed with TNBS treatment (scale bar = 100  $\mu$ m). (B) Gross morphology of (i) control or (ii) inflamed (TNBS-treated) bowels. (C) B-mode sonograph of trout abdomen region of interest (ROI) outlining bowel of an untreated fish (scale bar = 1 mm). (D) Non-Linear Contrast mode sonographs illustrating MB intensity over time after bolus injection of an untreated fish (scale bar = 1 mm). (E) Average peak enhancement values for trout treated with TNBS was significantly lower than in control bowels ( $F_{1,8} = 6.552$ ,  $p = 0.043$ ).

**References**

- [1]. Peña-Sánchez JN, Osei JA, Marques Santos JD, *et al.* Increasing prevalence and stable incidence rates of inflammatory bowel disease among First Nations: population-based evidence from a western Canadian province. *Inflammatory Bowel Diseases*, X: 1-9, 2021.
- [2]. Bradford LEA, Bharadwaj LA, Okpalauwaekwe U, Waldner C. Drinking water quality in Indigenous communities in Canada and health outcomes: a scoping review. *International Journal on Circumpolar Health*, 75: 32336, 2016.
- [3]. Brugman S. The zebrafish as a model to study intestinal inflammation. *Developmental and Comparative Immunology*. 64: 82-92, 2016.
- [4]. Neo JPS, Tan BH. The use of animals as a surveillance tool for monitoring environmental health hazards, human health hazards and bioterrorism. *Veterinary Microbiology*, 203: 40-48, 2017.
- [5]. Wirtz, S. *et al.* Chemically induced mouse models of acute and chronic intestinal inflammation. *Nature Protocols*, 12: 1295-1309, 2017.
- [6]. Machtaler, S. *et al.* Assessment of inflammation in an acute on chronic model of inflammatory bowel disease with ultrasound molecular imaging. *Theranostics*, 5: 1175-1186, 2021.

# Evaluation and early detection of hepatocellular carcinoma with quantitative contrast-enhanced ultrasound

*Connor D. Krolak<sup>1</sup>, Alicia Clark<sup>1</sup>, Manjiri Dighe<sup>2</sup>, Michalakis Averkiou<sup>1</sup>*

<sup>1</sup>*Department of Bioengineering, University of Washington, Seattle, USA*

<sup>2</sup>*Department of Radiology, University of Washington, Seattle, USA*

*Corresponding author: krolakc@uw.edu*

## Introduction

Hepatocellular carcinoma (HCC) is the most common primary liver malignancy. HCC has a high mortality rate that can be partly attributed to a delay in diagnosis [1]. Developing methods for early detection of HCC is therefore critical, to widen treatment options and improve patient outcomes. Currently, the state-of-the-art diagnostic metric for HCC is LI-RADS (Liver Imaging Reporting and Data System), a qualitative image assessment used to evaluate tumor malignancy through analysis of lesion blood perfusion [2]. HCC is generally classified by abnormal arterial flow after an initial portal venous and hepatic arterial flow reduction [3]. These blood flow anomalies can be observed in real-time with contrast-enhanced ultrasound (CEUS), which utilizes a blood pool contrast agent consisting of 1-10  $\mu\text{m}$  gas microbubbles that are detectable in the microcirculation. Despite LI-RADS being highly specific, it has not been shown to improve the delay in diagnosis associated with HCC because the readouts are primarily qualitative and ultimately lack sensitivity [4]. We hypothesize that a quantification of tumor vascularity and perfusion with CEUS would improve LI-RADS and lead to earlier, unbiased, and more accurate diagnosis of HCC.

## Methods

### *Patient HCC Data Collection*

This study consists of data from 29 LI-RADS LR-5 patients (confirmed HCC). Lesions were located in conventional B-mode ultrasound with a Philips EpiQ C5-1 transducer, which was then spatially fixed with an articulated arm, a critical component for accurate measurements. A 1.2 mL bolus of Lumason contrast agent followed by a 5 mL saline flush was intravenously injected, and a 5-minute image video loop was collected while scanning the liver with a contrast specific mode. For preservation of contrast, scanning was performed continuously for the first 90 seconds, but then for only 15 seconds at the 2, 3, 4, and 5-minute mark (Fig. 1). The probe was then moved to evaluate another plane of the lesion, and repeated as necessary.

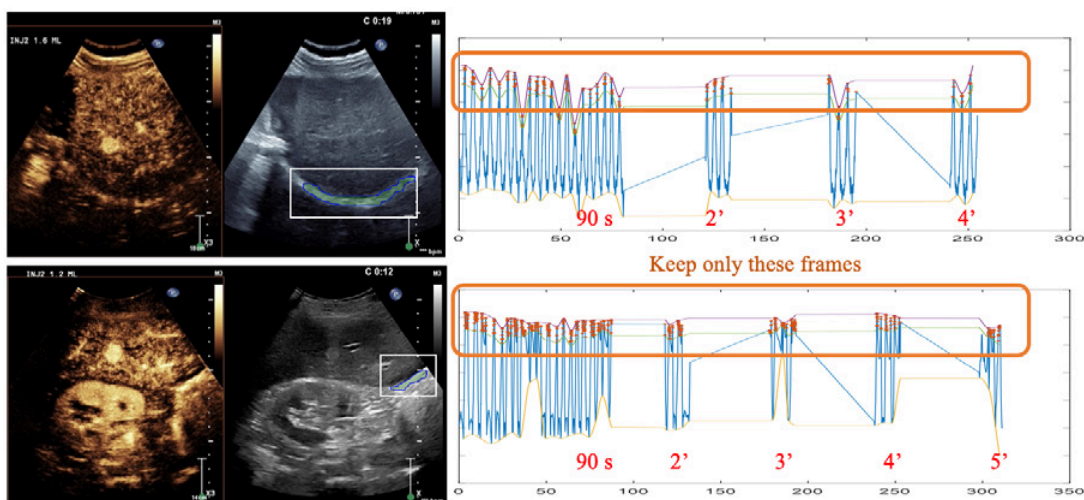


**Figure 1.** Two examples of the 5-minute scanning sequence and demonstration of the automatic respiratory gating. The white box on the fundamental image highlights the moving interface automatically detected and tracked by the algorithm.

Custom MATLAB HCC Analysis (*qDicomUW*)

Analysis of HCC image loops was performed in a MATLAB based tool operating on linearized data (with the logarithmic compression removed), acquired via a propriety data transformation script from Philips (Philips Medical Systems, Bothell, WA). DICOM loops from the 5-minute scan were stitched together, and a key frame with an optimal view of the lesion in the breathing cycle was selected. An automatic respiratory gating (ARG) algorithm was incorporated to eliminate out-of-plane motion relative to this key frame, as demonstrated in Fig. 1. To further reduce motion and improve perfusion quantification accuracy, a motion compensation algorithm operating on the fundamental image of the respiratory gated frames was used. Regions of interest (ROI) were selected for the lesion and parenchyma on the post-processed loop, and time intensity curves (TIC) were created. The rise time was then calculated for the lesion and parenchyma, determined by the elapsed time from when contrast arrived in the ROI to its peak intensity. As shown in Fig. 2, ARG reduced the TIC noise (seen as oscillations) and motion compensation further improved the TIC before the rise time measurement was made.

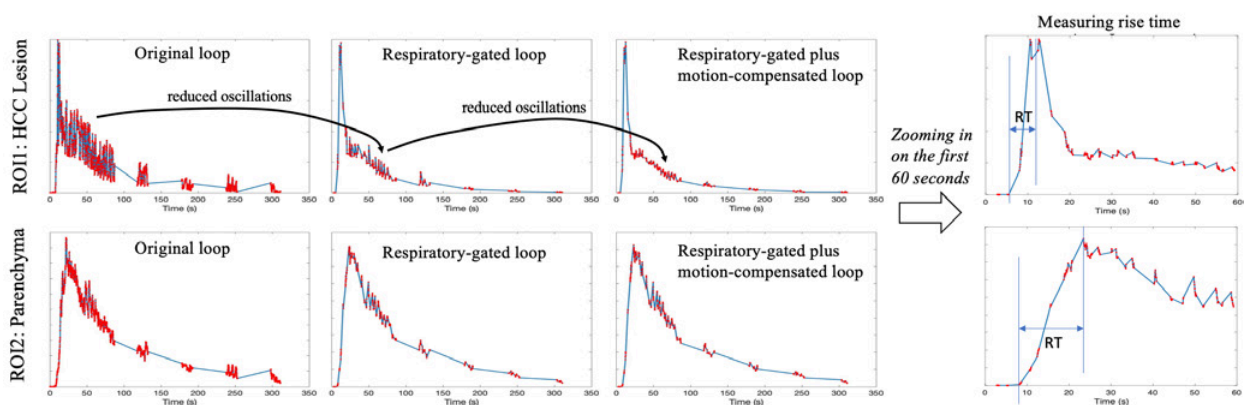


**Figure 2.** Demonstration of the effects of respiratory gating and motion compensation to reduce oscillations in the time intensity curves of the lesion and parenchyma, along with visualization of the calculation of rise time.

To quantify HCC washout, the intensity at the 2, 3, 4, and 5-minute mark were averaged to single values, and two additional metrics were calculated. For the first metric, an exponential decay curve was fit to these points, and the slope was compared between the lesion and parenchyma. For the second metric, titled degree of washout, these points were normalized to the peak intensity of their individual TIC, and a ratio of the normalized intensity of the parenchyma over the lesion at each minute mark was computed and plotted, as shown in Fig. 3.

**Results**

We were able to accurately measure arterial hyperenhancement of the studied HCCs through the calculation of rise time for both the lesion and parenchyma. For all patients, average rise time was  $11.11 \pm 4.64s$  for the lesion and  $30.36 \pm 9.95s$  for the parenchyma, with every individual's lesion rise time being shorter than the surrounding parenchyma. To fully characterize HCCs, we also quantified tumor washout with two metrics: exponential decay and degree of washout. Average patient exponential decay slope in a ratio of lesion over parenchyma slope was  $1.431 \pm 0.34$ , and similarly all patients had equal or greater decay slope in their lesion compared to surrounding parenchyma. The ratio being greater than 1 indicates that the washout of the lesion is faster than the parenchyma. Degree of washout is uniquely able to distinguish between early (2 minute) and late (4/5 minute) washout. In our dataset, the average degree of washout was  $3.3 \pm 1.8$  for the 2-minute mark, and  $4.7 \pm 3.0$  for the 5-minute mark, with this increased variability due to the fact that HCCs can exhibit varying washout behavior. Therefore, the degree of washout was compared on an individual basis, where any degree of washout greater than 1 indicates higher washout of the lesion compared to the surrounding liver. Thresholds for differentiating between mild and moderate washout have been empirically determined to be approximately 3 for early washout, and 4 for late washout. All patients

in the study had degrees of washout greater than 1, and typical results demonstrating the use of this parameter and its appearance for mild and moderate degrees of washout are depicted in Fig. 3.

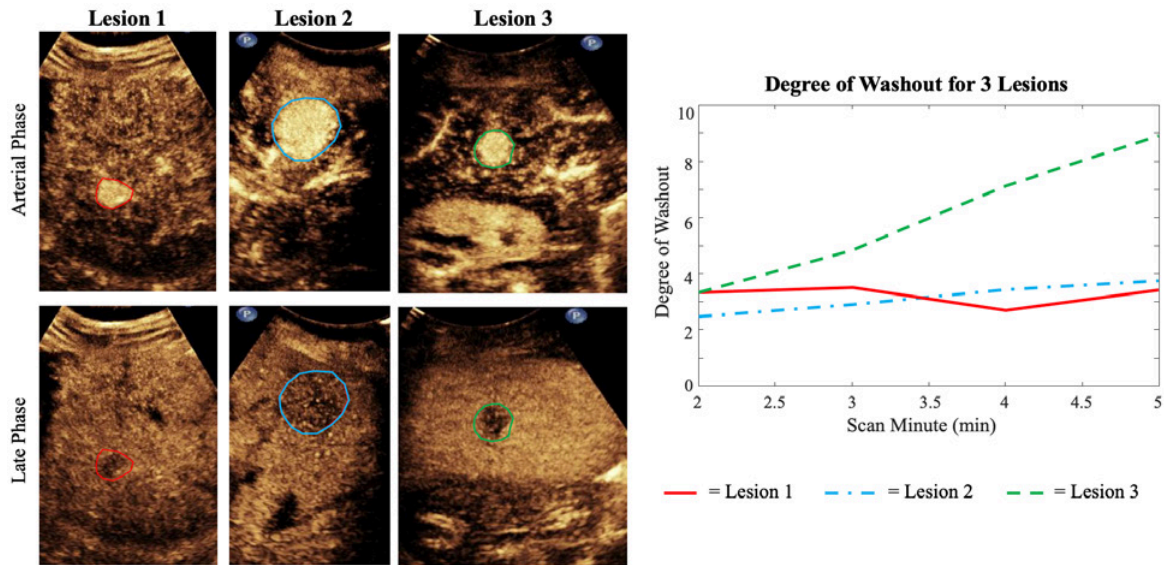


**Figure 3.** Examples of the degree of washout metric for 3 patients. Lesions 1 and 2 exhibit a mild degree of washout, while lesion 3 exhibits a moderate degree of washout. These values reflected in the plot are supported by the visual appearance of the lesion in the late phase relative to the surrounding parenchyma.

## Conclusions

We have developed an imaging protocol and analysis method to accurately characterize HCC through quantification of vascular parameters specified by CEUS LI-RADS. Through the calculation of rise time, exponential decay slope, and degree of washout, we were able to accurately identify and quantify the features of arterial hyperenhancement and washout in HCC patients. We aim to further improve this technique to complete a robust algorithm with the assistance of AI or machine learning, to improve CEUS LI-RADS and allow for an earlier and more accurate diagnosis of HCC.

## References

- [1]. El-Serag HB, Rudolph KL. Hepatocellular carcinoma: epidemiology and molecular carcinogenesis. *Gastroenterology*, 2007; 132(7):2557-2576.
- [2]. Hu J, Burak KW, et. al. Resolution of indeterminate MRI with CEUS in patients at high risk for hepatocellular carcinoma. *Abdom Radiol*, 2020; 45(1):123-133.
- [3]. Wilson SR, Burns PN, Kono Y. Contrast-Enhanced Ultrasound of Focal Liver Masses: A Success Story. *Ultrasound in Medicine & Biology*, 2020; 46(5):1059-1070.
- [4]. Kim TK, et al. Contrast-enhanced ultrasound (CEUS) liver imaging reporting and data system (LI-RADS) 2017 – a review of important differences compared to the CT/MRI system. *Clinical and molecular hepatology*, 2017; 23(4):280

# A physics-informed simulation framework for ultrasound localization microscopy

**A. Kuliesh<sup>1,\*</sup>, N. Blanken<sup>2,\*</sup>, B. Heiles<sup>1,\*</sup>, K. Jain<sup>3</sup>, D. Maresca<sup>1</sup>, G. Lajoinie<sup>2</sup>**  
(\* contributed equally)

<sup>1</sup>Department of Imaging Physics, Delft University of Technology, Delft, The Netherlands

<sup>2</sup>Physics of Fluids group, MESA+ Institute for Nanotechnology, Technical Medical (TechMed) Centre, University of Twente, Enschede, The Netherlands

<sup>3</sup>Engineering Fluid Dynamics Group, Department of Thermal and Fluid Engineering, University of Twente, Enschede, The Netherlands.

Corresponding authors: [k.jain@utwente.nl](mailto:k.jain@utwente.nl), [d.maresca@tudelft.nl](mailto:d.maresca@tudelft.nl), [g.p.r.lajoinie@utwente.nl](mailto:g.p.r.lajoinie@utwente.nl)

## Introduction

Ultrasound Localization Microscopy (ULM) is a breakthrough ultrasound technique that enables volumetric in vivo mapping of large-scale vascular networks with up to a 10-fold increase in resolution compared to standard ultrasound [1, 2]. As the use of ULM is on the rise, it becomes critical to develop tools that can objectively assess the performance of ULM localization, tracking and reconstruction algorithms by providing time-resolved ground truth information about both vascular structure and microbubble (MB) distribution. Earlier attempts to generate synthetic ULM datasets have ignored nonlinear wave propagation, nonlinear microbubble responses, and microbubble-microbubble interactions [3]. These datasets therefore fall short of being realistic enough for benchmarking.

Here, we introduce a simulation framework for ULM that takes into account vascular geometry, flow dynamics and nonlinear microbubble physics, including microbubble-microbubble interactions. This framework can be used to generate image sequences comprising thousands of frames to benchmark ULM algorithms. Through the 3D nature of the simulator we can produce data both for 2D and 3D ultrasound imaging with different probes (linear, phased, row-column arrays etc). As a first demonstration, we used our framework to generate pulse-echo radiofrequency data for phased array arising from microbubbles flowing in a realistic vascular architecture. The simulation can be run both on the CPUs and GPUs, with a significant computational acceleration for the latter.

## Methods

In order to assemble a physically sound simulation framework, we divided the simulator into three modules: (1) microbubble dynamics, (2) ultrasound wave propagation, and (3) hemodynamic simulation, Fig. 1a.

**Hemodynamic simulation.** This simulation module is based on the lattice Boltzmann solver *Musubi* [4, 5]. A mesh representing vascular geometries is used as a boundary to perform flow computations. The inflow boundary condition can be prescribed either as stationary or pulsatile inflow. For the specific example presented in the results section, blood rheology was described as a Newtonian fluid with fixed density ( $1056 \text{ kg/m}^3$ ) and viscosity ( $3.27 \times 10^{-6} \text{ m}^2/\text{s}$ ). The flow simulator is parallelized using MPI, and allows for accelerated computation on clusters. A predefined number of circulating microbubbles are then positioned along streamlines derived from the vascular flow module using a stream tracer.

**Ultrasound propagation.** The ultrasound wave propagation module is based on the acoustic toolbox k-Wave [6] and simulates the 3D pressure field of ultrasound imaging arrays. We precisely emulate our physical transducer arrays relying on experimental characterization. The propagation medium is simulated using average soft tissue properties, i.e. a speed of sound  $c_0 = 1540 \text{ m/s}$ , density  $\rho_0 = 1000 \text{ kg/m}^3$ , nonlinear parameter  $B/A = 6$ , and attenuation coefficient  $\alpha_t = 0.75 \text{ dB.MHz}^{-1.5} \text{ cm}^{-1}$ . The vasculature used in the hemodynamic module is embedded in the simulation medium with the following blood properties: density  $\rho_b = 1060 \text{ kg/m}^3$ , speed of sound  $c_b = 1584 \text{ m/s}$ ,  $B/A = 6$ , attenuation coefficient

$\alpha_b = 0.14 \text{ dB} \cdot \text{MHz}^{-1.5} \text{ cm}^{-1}$ . To mimic speckle, the speed of sound and density are modulated by a Gaussian random noise around the mean values of  $c_0 = 1540 \text{ m/s}$  and  $\rho_0 = 1000 \text{ kg/m}^3$ . Finally, pressure sensors and sources are placed at each microbubble position obtained from the previous module, and they interface with the MB simulation module.

**Microbubble dynamics:** The input pressure signals recorded at the sensor points of the propagation medium are transferred to a microbubble simulator, which solves a Rayleigh-Plesset equation [7] to compute the resulting nonlinear radial response of the microbubbles. The surface tension curve of the phospholipid shell is based on Marmottant model [7]. Iterative communications between the microbubble vibration module and ultrasound wave propagation module account for cross-talk between microbubble contrast agents. Once all scattering events and cross-talks are taken into account for one probe transmission, the hemodynamic module is used to update microbubble positions according to the pulse repetition frequency of the array. This strategy enables the simulation framework to generate time-resolved data, Fig. 1b.

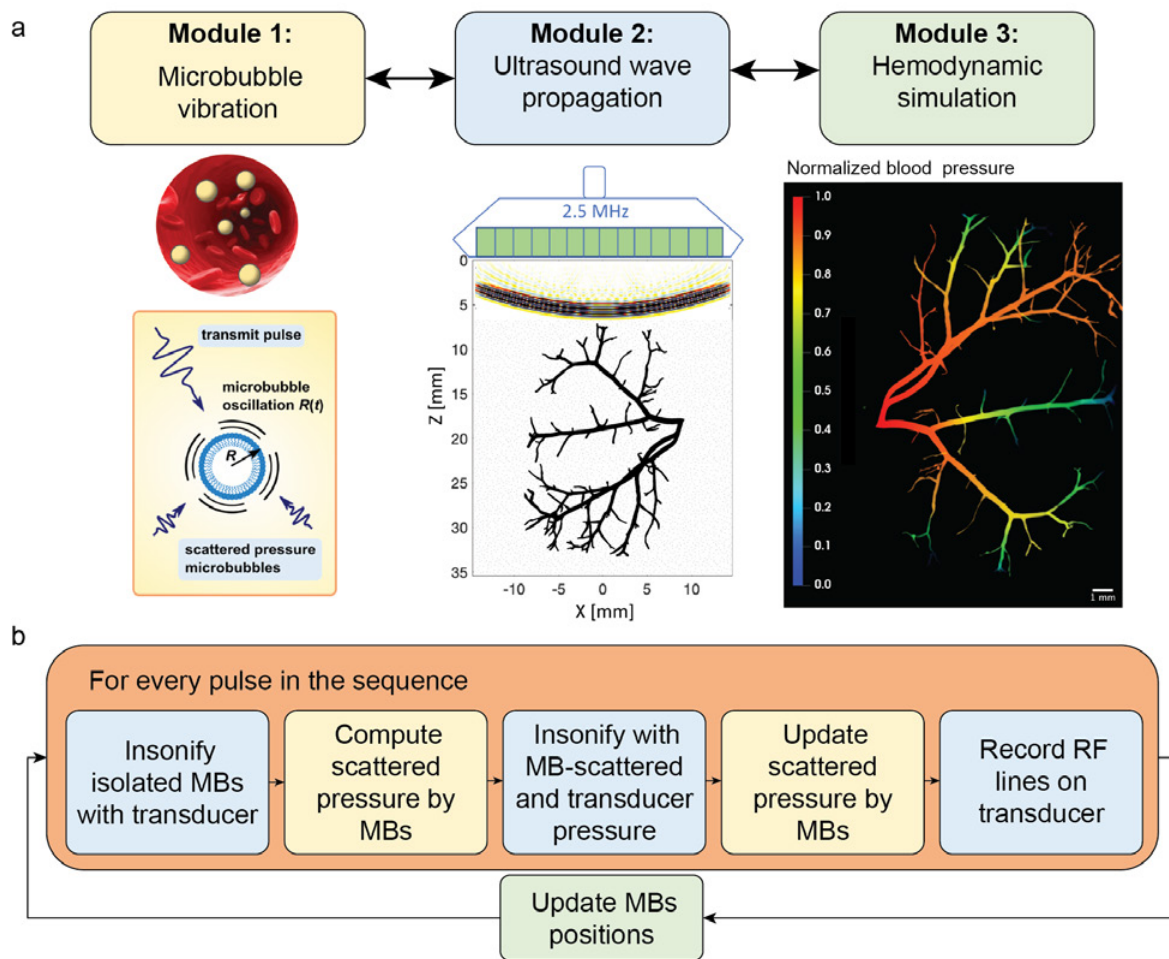


Figure 1. Modular architecture of the simulation framework.

a. The simulator includes: a microbubble dynamics module, an ultrasound wave propagation module and a hemodynamics module. Each module is shown with a representative image (from left to right): microbubble oscillations in the pressure field, transducer (top of the simulated domain) generating diverging wave, normalized blood pressure drop over the renal arterial tree (renal morphology based on [8]). b. The simulator pipeline: first, the transducer generates pressure wave. The local pressure is recorded at the MBs' locations and used to simulate their response. In the next step, pressure fields generated by the microbubbles are added to that of the transducer. The pressure wave locally experienced by the MBs' now includes the first order acoustic interactions. The last ultrasound simulation provides the RF lines sensed by the transducer that can be used for image reconstruction. The MBs' positions are then updated using the flow module and the process is repeated for each frame.

## Results

The ultrasound wave propagation module generated results are in good agreement with the experimental pressure fields of a commercial phased array probe (P4-1, Philips Healthcare, The Netherlands) as illustrated in Fig. 2a.

The vascular branch modelled in the hemodynamics module is a segment of a renal arterial system [8], Fig. 2b. In this example it was positioned at a depth of 30 mm from the probe in axial direction, or approximately 50 wavelengths at 2.5 MHz. For accuracy and stability of the numerical simulation, the voxel size was tuned to meet the k-Wave imposed criterium of 8 grid points per wavelength ( $\lambda = 600 \mu\text{m}$ ). A cineloop of 200 frames was generated on the TU Delft High Performance Computing cluster. One of these frames is displayed in Fig. 2c, and overlaid with a 2D projection of the 3D vascular geometry. In our simulation, the speckle intensity shadowed echoes arising from the single microbubbles. An amplitude modulation pulsing scheme allows to retrieve microbubble point spread functions hidden in the speckle by exploiting their nonlinear response, Fig. 2d.

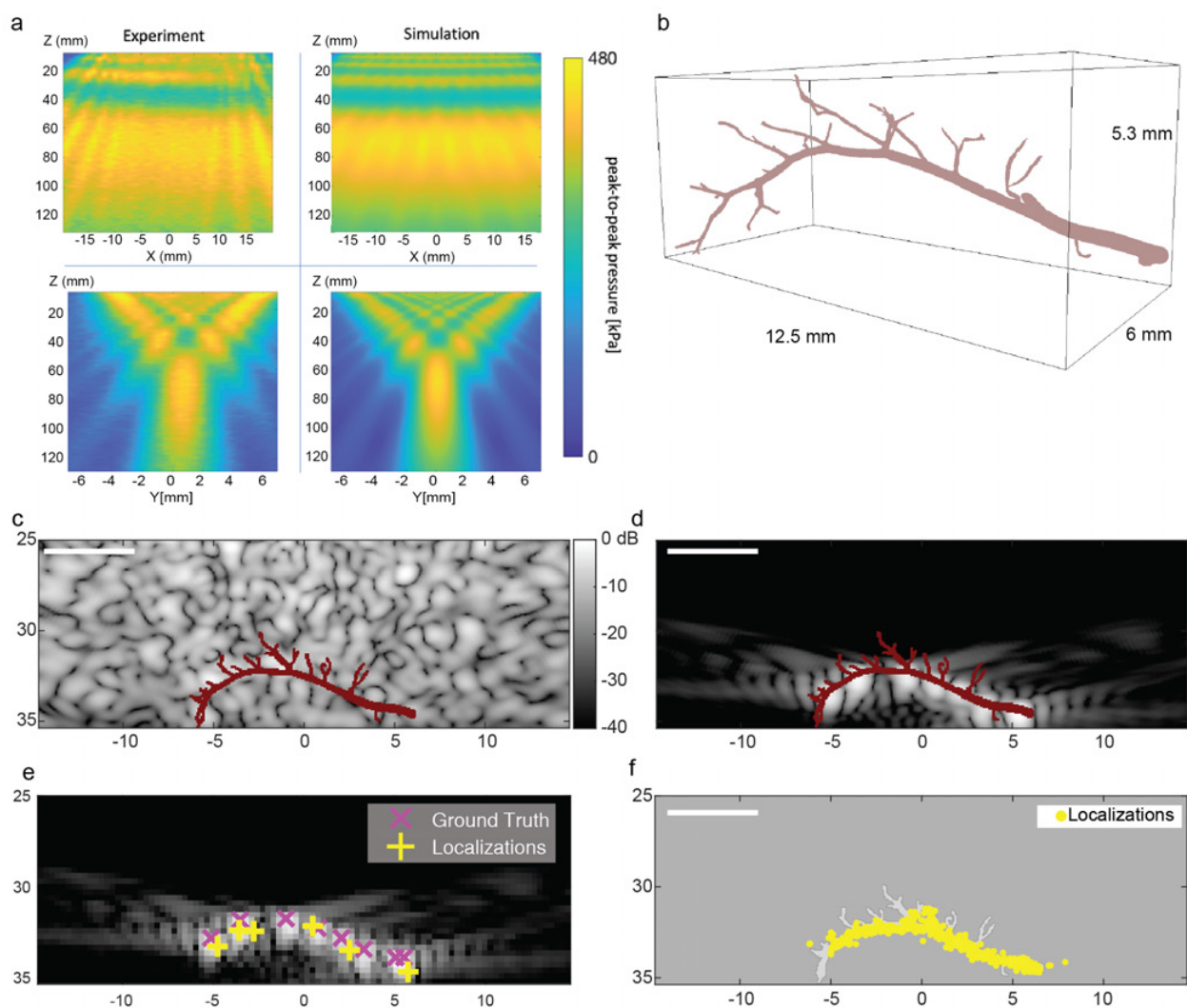


Figure 2. Modular architecture of the simulation framework.

a. Comparison between the simulated and measured pressure fields (peak-to-peak) for the P4-1 clinical transducer. The transducer is driven with an 8-cycles pulse with a center frequency of 2.5 MHz and emits a diverging wave (beam focus = -34 mm). Top panels show the imaging planes while the bottom panels show the elevation planes.

b. 3D view of the simulated vasculature geometry. The diameter of the inlet vessel is  $364 \mu\text{m}$ .

- c. 2D B-Mode image of single frame zoomed in on the vascular tree (beamforming at  $\lambda/8$ ). Speckle intensity overshadows the signal from microbubbles. The imaging plane projection of the simulated vessel geometry is overlaid on the image (scale bar = 5 mm). Display intensity range is 40 dB.
- d. 2D B-Mode image obtained after amplitude modulation (beamforming at  $\lambda/8$ ). The nonlinear microbubbles are clearly visible while the linear speckle is strongly suppressed. The imaging plane projection of the simulated vessel geometry is overlaid on the image. (scale bar = 5 mm). Display intensity range is 40 dB.
- e. Amplitude modulated B-Mode image beamformed at  $\lambda/2$  passed to the LOTUS toolbox. The ground truth coordinates are displayed with magenta crosses and the predicted coordinates using the radial symmetry localization algorithm are displayed with yellow pluses (scale bar = 5 mm). Display intensity range is 40 dB.
- f. Density map with localizations from 100 frames overlaid with the simulated geometry, scale bar = 5 mm.

To pinpoint the positions of the microbubbles circulating in the vascular branch and reconstruct a density map, we performed radial localization on the beamformed IQ data with the LOTUS toolbox [9]. The results of the localization for a single amplitude modulated frame beamformed at  $\lambda/2$  are presented in Fig. 2e. The ground truth of the retrieved and simulated MB localizations are displayed in magenta and yellow, respectively. We successfully reconstructed a density map of the vascular branch by applying the radial localization algorithm on 100 simulated frames, Fig. 2f.

### Conclusions

We present a simulation framework that treats adequately and simultaneously ultrasound propagation physics, microbubble physics and flow physics. This model can therefore generate realistic raw radiofrequency data for ULM reconstruction. Microbubble positions are updated between each ultrasound transmission within a vascular architecture of choice thanks to a hemodynamic model. Together, these three modules will enable ULM community users to generate physically sound datasets to benchmark their algorithms or train their neural networks.

### References

- [1]. Errico, C., et al., Ultrafast ultrasound localization microscopy for deep super-resolution vascular imaging. *Nature*, 2015. **527**(7579): p. 499-502.
- [2]. Heiles, B., et al., Volumetric ultrasound localization microscopy of the whole brain microvasculature. *bioRxiv*, 2021.
- [3]. Belgharbi, H., et al., An Anatomically and Hemodynamically Realistic Simulation Framework for 3D Ultrasound Localization Microscopy. *bioRxiv*, 2021.
- [4]. Klimach, H., K. Jain, and S. Roller, End-to-end parallel simulations with apes, in *Parallel computing: accelerating computational science and engineering (CSE)*. 2014, IOS Press. p. 703-711.
- [5]. Available from: <https://apes.osdn.io>.
- [6]. Treeby, B.E. and B.T. Cox, k-Wave: MATLAB toolbox for the simulation and reconstruction of photoacoustic wave fields. *Journal of biomedical optics*, 2010. **15**(2): p. 021314.
- [7]. Marmottant, P., et al., *A model for large amplitude oscillations of coated bubbles accounting for buckling and rupture*. *The Journal of the Acoustical Society of America*, 2005. **118**(6): p. 3499-3505.
- [8]. Nordsletten, D. A., Blackett, S., Bentley, M. D., Ritman, E. L., & Smith, N. P. (2006). Structural morphology of renal vasculature. *American Journal of Physiology-Heart and Circulatory Physiology*, *291*(1), H296-H309.
- [9]. Heiles and Chavignon, et al, Performance benchmarking of microbubble-localization algorithms for ultrasound localization microscopy, [in press], *Nat. Biomed. Eng.*, 2021

## **Delineation of right and left regional ventricular function with selective microvascular enhancement following perfluoropropane droplet activation imaging.**

*Shouqiang Li<sup>1</sup>, Ping Zeng<sup>1</sup>, Chen Cheng<sup>2</sup>, John Lof<sup>1</sup>, Elizabeth Stolze<sup>1</sup>, Xucai Chen<sup>2</sup>, John J. Pacella<sup>2</sup>, Flordeliza S. Villanueva<sup>2</sup>, Terry Matsunaga<sup>3</sup>, Carr Everbach<sup>4</sup>, Feng Xie<sup>1</sup>, Thomas R. Porter<sup>1</sup>*

*1University of Nebraska Medical Center; Omaha, NE, USA*

*2University of Pittsburgh Medical Center; Pittsburgh, PA; USA*

*3University of Arizona Medical Center; Tucson, AZ; USA*

*4Swarthmore College; Swarthmore, PA; USA*

### **Introduction**

Lipid-encapsulated perfluoropropane droplets (LEPD) transfer across endothelial borders and persist within the myocardium for several minutes post intravenous injection (IVI). LEPD are activated with high mechanical index (HMI) ultrasound, and imaged at a low MI<sup>1</sup>. We hypothesized that post activation imaging at a low MI would permit improved right and left ventricular regional function analysis, and better delineation of the infarct zone.

### **Methods**

In 16 rats undergoing 60 minutes of left anterior descending ischemia followed by reperfusion (I/R), we performed transthoracic harmonic imaging at 3 and 6 minutes following LEPD IVI. Background subtracted myocardial intensity (BSI) was compared between I/R zones and remote myocardium at the different time points, and confocal microscopy utilized to confirm LEPD location kinetics. Post mortem staining confirmed infarct zone and size..

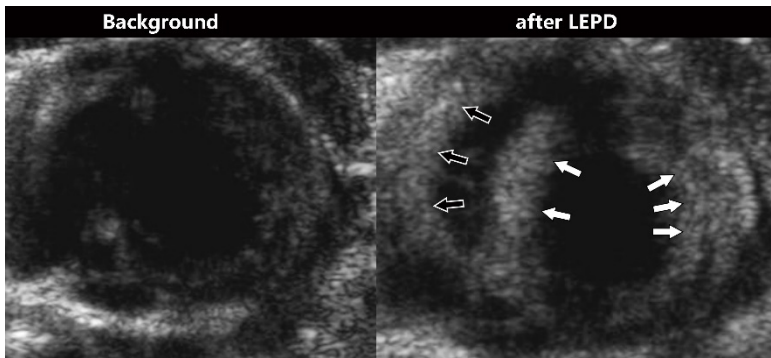
### **Results**

At 3 minutes post IVI, post activation low MI imaging selectively enhanced left and right myocardium without cavity enhancement (black arrows, Figure 1), along with significantly higher BSI within the IZ (white arrows; BSI ratio  $2.60 \pm 1.21$  at 3 minutes versus  $1.44 \pm 1.25$  at six minutes;  $p = 0.002$ ). This corresponded to fluorescent intensity ratios on confocal microscopy at the different time points following IVI.

### **Conclusions**

Droplet activation imaging sequences can be utilized to selectively a) enhance left and right ventricular borders without cavity contrast for regional function analysis, b) enhance and quantify the IZ, and c) reduce the effects of attenuation created by LV cavity contrast .

Figure 1. Acoustic activation Imaging in rat model of acute anterolateral myocardial infarction.



### References

- [1]. Choudhury S, Xie F, Kutty S, Lof J, Stolze E, Porter TR Selective infarct zone imaging with intravenous acoustically activated droplets. PLoS One 2018; 13(12):e0207486

# Multiple scattering inside a population of nonlinear oscillating microbubbles excited by a cloud of acoustic point sources

A. Matalliotakis<sup>1</sup>, X. Li<sup>1</sup>, M.S. van der Heiden<sup>3</sup>, P.L.M.J. van Neer<sup>1,3</sup>, N. de Jong<sup>1,2</sup>, M.D. Verweij<sup>1,2</sup>

<sup>1</sup>Medical Imaging, ImPhys, Delft University of Technology, Delft, the Netherlands

<sup>2</sup>Biomedical Engineering, Thorax Center, Erasmus MC, Rotterdam, the Netherlands

<sup>3</sup>TNO, The Hague, the Netherlands

Corresponding author: a.matalliotakis@tudelft.nl

## Introduction

Proton therapy is used for cancer treatment as an unconventional alternative to radiotherapy. The advantage over the conventional photon therapy is the local dose deposition, reaching a peak at the stopping range of the protons. This is called the Bragg peak, behind which the energy deposited is significantly smaller. A big challenge of this technology is to control the range uncertainties of the energy deposition from the beam. . Acoustic localization is a promising technology to monitor the position of the Bragg peak. Unfortunately, the signal generated from the thermal expansion due to an entire proton beam (ionoacoustics) is a broadband acoustic signal in the kHz range, rendering the submillimeter localization impossible. On the other hand, a single proton (protonacoustics) emits a broadband signal in the GHz range, which will suffer too much from attenuation to be detected at the outside of the body. Our idea of tackling this challenge is combining monodisperse microbubbles with protons. Their mutual interactions can result in in-phase vibrations in the order of 1-2 MHz, which result in an amplified signal that is detectable by an optoacoustic sensor outside the body. Because of the difficulty of in vivo trials, a suitable simulation model should be implemented to find the optimal configuration of the aforementioned procedure. For this purpose, we have extended the Iterative Nonlinear Contrast Source (INCS)[1] method with the inclusion of acoustic point sources and microbubbles.

## Methods

The INCS method is intended to compute the nonlinear acoustic pressure field from sources apertures with a pulsed excitation in a four dimensional spatiotemporal domain. Initially, INCS was implemented to deal with sources with a planar aperture [1]. Recently, we have extended INCS with the inclusion of microbubbles, each as an individual and independent pointscatterer that is represented as a contrast source term [ref. to previous symposium abstract]. Their nonlinear oscillations were described by a model created by Marmottant[2], providing the temporal signature of each microbubble. The spatial signature of the latter is a dirac function. By using a Neumann iterative scheme, the multiple interactions between microbubbles is taken into account. In this way, each iteration adds an order of multiple scattering. A significant advantage of our approach is that the location of the scatterers is independent of the gridpoints' position. Moreover, the concentration of the point scatterers is not limited by the number of the gridpoints, giving the ability to try different configurations efficiently. Starting from this implementation, we have now extended INCS with the addition of point sources that represent the source pressure that is generated by impacting protons. The summation of all these point sources constitutes the primary source term. Each point source has an amplitude, a temporal signature and a Dirac function as its spatial signature, as mentioned before. To simulate a realistic case, they are randomly positioned in a cubic domain and their position is independent of the microbubbles' location. In order to imitate the protons, the temporal signature of each source is a short bipolar pulse, all with the same phase delay.

## Results

In Fig. 1 , the computational domain that is used for the simulations is depicted in a total , focused and sliced view. The locations of both the point sources (red asterisks) and the microbubbles (blue circles) are shown. Furthermore, on the right part of the figure, the time signature and the frequency spectrum of the

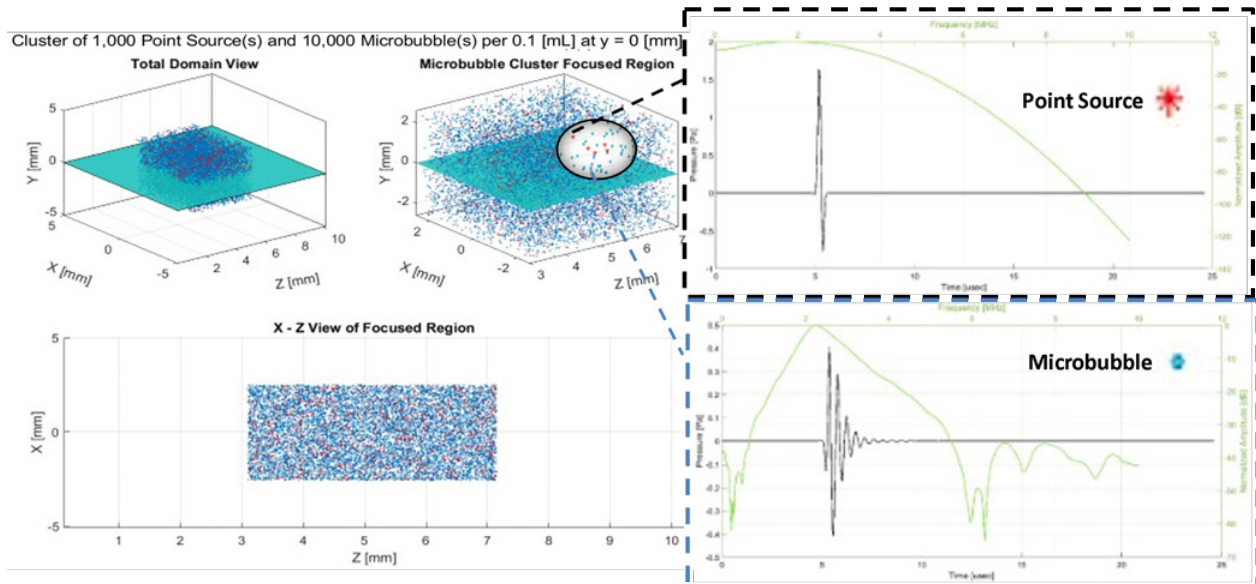


**Figure 1.** Computational domain containing the microbubbles and the point sources. On the top right is the time signature and frequency spectrum of the pressure generated from a point source ( red asterisk). On the bottom right is the time signature and the frequency spectrum of the scattered pressure from a microbubble (blue circle).

mentioned are presented, respectively. From Fig. 1 it can be deduced that the simulation took place in a domain with dimensions of 10 mm x 10 mm x 10 mm in X,Y and Z , respectively. For this simulation a center frequency of 1.7 MHz and a sampling frequency of 20.4 MHz was used. A concentration of  $10^4$  monodisperse microbubbles with a radius of  $2.4 \mu\text{m}$  was used in a domain of 0.1 ml volume . Their resonance frequency @ 100 kPa is close to the center frequency used. The linear field was generated by  $10^3 / 0.1 \text{ ml}$  point sources with an amplitude of 78 Pa @ a distance of  $1 \mu\text{m}$ . Medium attenuation was not included.

In Fig 2., the results of the simulation are presented. On the left part of the image, the incident pressure field is depicted with a peak amplitude of around 0 db. At the left part of the image, the scattered pressure from a microbubble cloud is presented. Due to low excitation pressure, the scattered pressure is relatively low compared to the former. Moreover, because the acoustic pulse is a broadband acoustic signal, microbubbles are not resonating at their resonance frequency. This results on a weaker scattered pressure. Furthermore, the 2<sup>nd</sup> harmonic is relatively high compared to the fundamental. This can be explained due to the fact that although the microbubbles are oscillating in the linear regime, the scattering includes

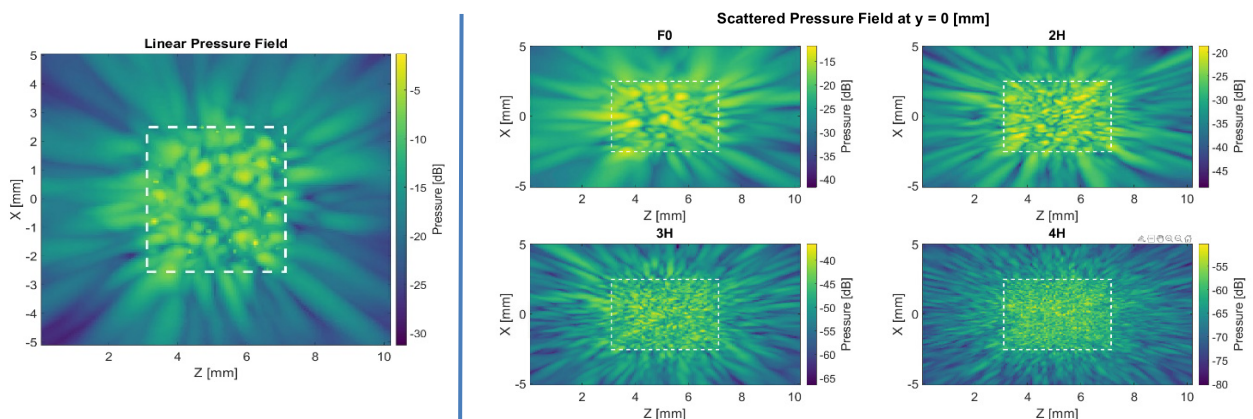


**Figure 2.** (Left) Incident Pressure field generated from  $10^3$  Point sources / 0.1 ml . (Right Panel) Scattered Pressure Field generated from  $10^4$  Microbubbles / 0.1 ml. In the same panel, the pressure field for the fundamental (F0), 2<sup>nd</sup> (2H), 3<sup>rd</sup> (3H), 4<sup>th</sup> (4H) Harmonic is depicted. Both the acoustic sources and the microbubbles are located randomly inside the dotted white square. All the results are from 8<sup>th</sup> iteration, where convergence is achieved.

nonlinear components. An interesting fact is the detailed image in the 4<sup>th</sup> harmonic (4H) compared to the one in fundamental (F0), as expected.

Despite the low excitation amplitude of the scattered pressure, these results are promising because of the low excitation pressure that was used. In the case of higher excitation amplitudes, different signatures, or higher concentrations, the scattered pressure may be higher than currently obtained

### Conclusions

INCS has been successfully extended to efficiently simulate the scattered pressure of a microbubble cloud when excited by the pressure field generated from a cloud of point sources representing protons. The nonlinear oscillatory behaviour of microbubbles can be detected in higher harmonics at the location of the cluster. This gives the opportunity to study the destructive and constructive behaviour of a microbubble cluster, when combined with acoustic sources. Moreover, INCS provides the ability to try different configurations with polydisperse microbubble concentrations. In this way, it is possible to characterize the behavior of a microbubble configuration and implement this in a practical application in the future. One of these is the extraction of a patient-specific treatment plan for proton therapy when microbubbles are used.

### References

- [1]. J. Huijssen, M. D. Verweij, An iterative method for the computation of nonlinear, wide-angle, pulsed acoustic fields of medical diagnostic transducers, *The Journal of the Acoustical Society of America*, vol. 127, no. 1, pp. 33-44, Jan. 2010. doi: 10.1121/1.3268599
- [2]. Marmottant et al., A model for large amplitude oscillations of coated bubbles accounting for buckling and rupture, *The Journal of the Acoustical Society of America*, vol. 118, no. 1, pp. 3499 - 3505, Dec. 2005. doi: 10.1121/1.210942
- [3]. Matalliotakis et al. Nonlinear propagation of medical ultrasound through a microbubble cluster in view of multiple scattering effects, *The 26<sup>th</sup> European symposium on Ultrasound Contrast Imaging*,

## ***In vivo* circulation of fluorescent lipid-coated perfluorocarbon nanodroplets determined using three detection methods**

***Romain Melich, Patricia Emmel, Carole Mandaroux, Philippe Bussat, Isabelle Tardy & Samir Cherkaoui***

*Bracco Suisse SA, 31 route de la Galaise, 1228 Plan-Les-Ouates, Switzerland  
Corresponding author: romain.melich@bracco.com*

### **Introduction**

Liquid perfluorocarbon nanodroplets (PFC-NDs), also known as Phase Change Contrast Agents (PCCAs), are able to vaporize into gaseous echogenic microbubbles via an external ultrasound stimulus called acoustic droplet vaporization (ADV). Thanks to the nanometric size and the liquid core composition, they have gained much attention for new diagnostic and therapeutic applications [Durham and Dayton., 2021]. In fact, sub-micron NDs present several advantages in terms of increased *in vivo* circulation, deeper penetration into the tissues via the extravascular space, on-demand vaporization allowing localized drug delivery and the possibility to carry payload. To further unlock the full potential of these agents and enable successful clinical translation, it is of utmost importance to better understand their *in vivo* behavior.

In this study, we investigated the *in vivo* circulation time (pharmacokinetic properties) of fluorescent lipid-coated perfluorobutane (PFB, C<sub>4</sub>F<sub>10</sub>) nanodroplets (F-NDs) after intravenous bolus injection in rat using three detection procedures. Firstly, the NDs vaporization over time was evaluated in the abdominal vein using a B-mode imaging detection. Secondly, two analytical methods were used to determine the F-NDs behavior in the blood circulation namely C<sub>4</sub>F<sub>10</sub> assay by gas chromatography coupled with mass spectrometry (GC-MS) and the fluorescence measurements in collected blood samples.

### **Methods**

Phase-shift droplets were generated and adapted from the microbubble condensation method previously described by Sheeran et al., 2011. In this study, a research grade lipid shelled microbubble formulation, comprising perfluorobutane gas stabilized by a lipid shell and labelled with a fluorescent cyanine dye was prepared as precursor microbubbles in a lyophilized form (Bracco Suisse S.A., Plan-les-Ouates, Switzerland). After redispersion, the vial containing the C<sub>4</sub>F<sub>10</sub> microbubble suspension was immersed in an isopropanol bath controlled by a cryostat at -5°C and gently swirled for 3 min. Then, the headspace of the vial was pressurized using 12 mL of ambient air from a syringe.

First, physicochemical characterization was used to determine the size, the size distribution, the particle concentration, and the PFB concentration. For the *in vivo* study, each rat (Sprague-Dawley, n = 14) received a dose of  $8.0 \times 10^9$  particles/kg as a single intravenous bolus injection in tail vein. The *in vivo* decay, measured by a B-mode imaging, was adapted from an experimental *in vitro* set-up described in a previous study [Melich et al., 2020]. Briefly, a linear ultrasonic probe (L11-4V) connected and driven by a Vantage 256 system (Verasonics) was used to activate and image the NDs vaporization on five aligned focal points at an acoustic pressure corresponding to 1.4 times to ADV threshold pressure. The US probe was placed longitudinally above the abdominal vein of a rat to acquire the echogenicity from vaporized NDs. VueBox™ (Bracco, Switzerland) quantification software was used to determine the mean echo-power value decay of NDs over time.

For the fluorescence measurements and C<sub>4</sub>F<sub>10</sub> assay, blood samples were collected over time from the catheter placed in the left carotid artery. Fluorescence signal was determined using three drops (20 µL) of each blood sample visualized using the preclinical Fluobeam®700 camera (Fluoptics), while PFB concentrations were measured in collected blood samples using a GC-MS (Gas chromatography - mass spectrometry) bioanalytical method. For pharmacokinetic data analysis, a non-compartmental analysis was applied to determine T<sub>α ½</sub> and T<sub>β ½</sub> values using WinNonlin 8.2 software (Certara USA, Inc). The first half-life corresponds to the time required for 50% of a given dose to be distributed into the systemic circulation called distribution half-life (T<sub>α ½</sub>), while the elimination half-life (T<sub>β ½</sub>) corresponding to the second phase

was determined using at least three time points in semi-logarithmic concentration-time curve to select the best adjusted  $R^2$  value.

## Results

A Multisizer Coulter Counter 4e (20  $\mu\text{m}$  aperture, size range 0.4-12  $\mu\text{m}$ ; Beckman Coulter) was used to confirm the size decrease after MBs condensation to formulate a submicron droplet suspension. From the MBs size distribution, the concentration was extracted and was assumed to be equal to the NDs concentration after condensation. Indeed, the  $\text{C}_4\text{F}_{10}$  assay by GC-FID (Gas Chromatography - Flame Ionization Detector) method provided similar PFB concentrations from MBs and NDs samples, namely  $134.1 \pm 3.9$  and  $119.3 \pm 3.0$   $\mu\text{g}/\text{mL}$ , respectively ( $n=3$  vials).

For the *in vivo* half-life measurements determined by NDs vaporization, the contrast enhancement data were normalized to the maximum value and were plotted versus time. As observed in **Figure 1**, a large echogenic NDs cloud was created in the vaporization region and decreased over time. As a result, the echogenicity half-life ( $T_{\alpha/2}$ ) determined was  $8.8 \pm 2.1$  min ( $n = 5$  rats).

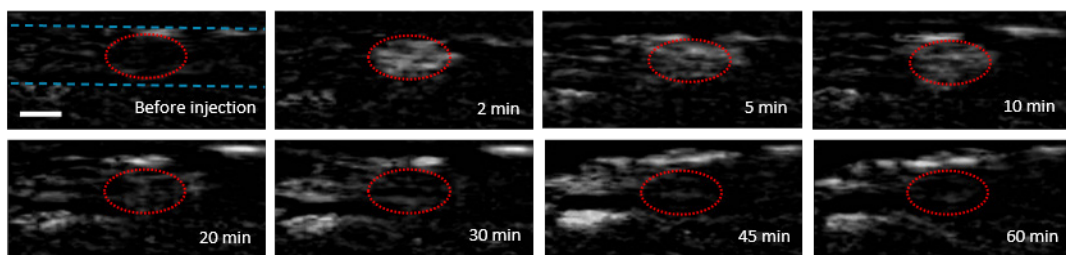


**Figure 1.** *In vivo* B-mode images of the F-NDs vaporization in the abdominal vein over time (vein walls were delimited by the blue dotted line, scale bar : 2 mm and red circle : region of interest)

At a bolus dose of  $8.0 \times 10^9$  particles/kg, no signs of respiratory distress or discomfort were seen, similar to what has been observed by **Sheeran et al., 2015** where a 7-fold higher dose was injected in terms of particles/kg. In fact, the large difference of the injected dose is due to the technology used to measure the NDs concentration (Nanoparticle Tracking Analysis, NTA versus Coulter Multisizer). In terms of PFB concentration/kg, both studies injected similar doses with  $2.12 \times 10^{-4}$  g/kg and  $3.2 \times 10^{-4}$  g/kg for Sheeran's team and our study, respectively. Moreover, they found a similar *in vivo* half-life by vaporisation in the kidney of mice ( $10.84 \pm 1.63$  min).

At the end of the kinetic study (1 hour), the NDs vaporization was assessed in various organs (spleen, liver, kidney). Vaporization could be observed in organs of the reticuloendothelial system (RES) such as the spleen and the liver (**Figure 2**).

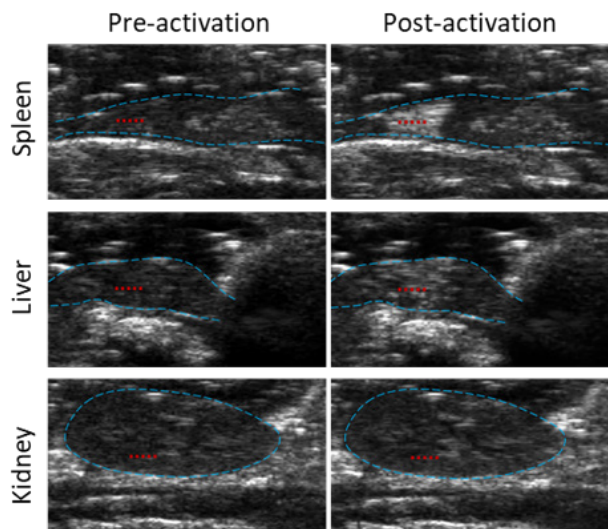


**Figure 2.** *In vivo* B-mode images of the F-NDs vaporization in various organs of rat namely spleen, liver and kidney at 1 hour after NDs administration (organs were delimited by the blue dotted lines and the red dots correspond to five focal points for the vaporization)

For the three detection methods, a decrease in signal response was observed over time with a decline being essentially bi-phasic characterized by a rapid initial phase (distribution phase) and a slower later phase (elimination phase) (**Figure 3**). The NDs decay profile is in line with that observed in the case of other gas-filled microbubble-based ultrasound contrast agents and thus two half-times could be determined for both phases. The C<sub>4</sub>F<sub>10</sub> monitoring by GC-MS confirmed the expected longer NDs circulation time with a distribution half-life ( $T_{\alpha 1/2}$ ) corresponding to 3.1-fold that of MBs of similar composition [**Schneider et al., 2011**]. A rapid NDs elimination from the blood compartment was determined with a C<sub>4</sub>F<sub>10</sub> elimination half-life ( $T_{\beta 1/2}$ ) of 19.1 min like observed with MBs of 14.5 min. In this sense, around 100 min is necessary to eliminate approximately 97% of the C<sub>4</sub>F<sub>10</sub> contained in administered NDs from the rat blood.

Finally, the NDs distribution half-life ( $T_{\alpha 1/2}$ ) determined by fluorescence has shown a longer time of 23.8 min which is most probably due to the circulating remnant fluorescence into the blood from F-NDs but also from F-liposomal and other F-lipidic structures generated by lipids shedding during the MBs condensation process.

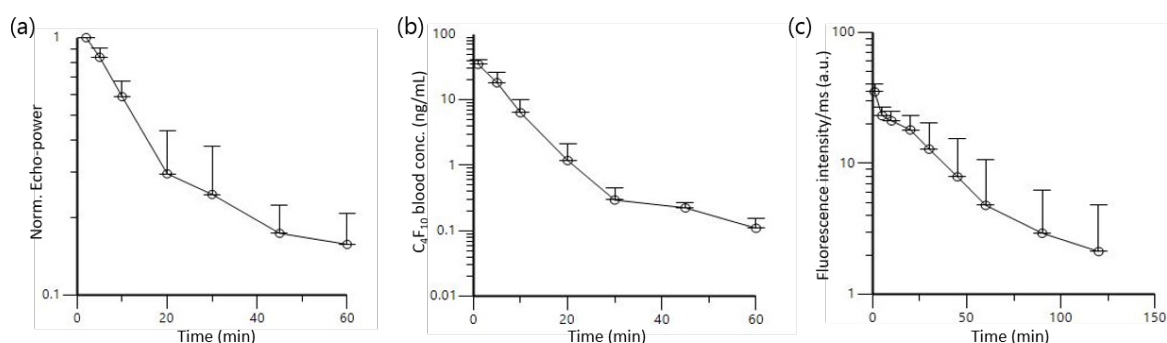


**Figure 3.** *In vivo* F-NDs decay over time using three detection methods namely (a) Normalized Echo-power values (n=5) following F-NDs vaporization, (b) C<sub>4</sub>F<sub>10</sub> blood concentration (n=4) as determined by GC-MS measurement and (c) fluorescence intensity from blood (n=5)

## Conclusion

In this study, three different experimental procedures were applied to monitor the circulation behavior of fluorescent lipid shelled nanodroplets in healthy Sprague-Dawley rat. This includes NDs vaporization and imaging in the abdominal vein, F-NDs fluorescence measurement in the collected blood samples and finally the PFB core gas assay using a sensitive GC-MS bioanalytical method. The results collected so far further confirm the longer circulation time of lipid-coated NDs compared to clinically available microbubbles. In addition, F-NDs accumulation in organs (mainly liver and spleen) was observed by the fluorescence evaluation and confirmed by the vaporization. The present study paves the way to additional *in vivo* studies to investigate the extravasation behavior of US responsive NDs to define the appropriate time point for applications requiring this property.

## References

- [1]. Durham, P. G. & Dayton, P. A. Applications of sub-micron low boiling point phase change contrast agents for ultrasound imaging and therapy. *Current Opinion in Colloid & Interface Science* 101498 (2021) doi:10.1016/j.cocis.2021.101498.
- [2]. Melich, R. *et al.* Microfluidic preparation of various perfluorocarbon nanodroplets: Characterization and determination of acoustic droplet vaporization (ADV) threshold. *International Journal of Pharmaceutics* 587, 119651 (2020).
- [3]. Sheeran, P. S. *et al.* Contrast-Enhanced Ultrasound Imaging and *In Vivo* Circulatory Kinetics with Low-Boiling-Point Nanoscale Phase-Change Perfluorocarbon Agents. *Ultrasound in Medicine & Biology* 41, 814–831 (2015).
- [4]. Schneider, M. *et al.* BR38, a New Ultrasound Blood Pool Agent: *Investigative Radiology* 46, 486–494 (2011)

# Acoustical Sizing of Individual Microbubbles using an ‘Acoustical Camera’

S. Spijkhou<sup>1</sup>, J.D. Voorneveld<sup>1</sup>, G. Renaud<sup>2</sup>, B. van Elburg<sup>3</sup>, T. Segers<sup>4</sup>, M. Versluis<sup>3</sup>,  
M. Verweij<sup>1,2</sup>, N. de Jong<sup>1,2</sup>, J. Bosch<sup>1</sup>

<sup>1</sup>Department of Biomedical Engineering, Erasmus MC, Rotterdam, the Netherlands

<sup>2</sup>Imaging Physics, Technical University of Delft, Delft, the Netherlands

<sup>3</sup>Physics of Fluids Group, TechMed Center, University of Twente, The Netherlands

<sup>4</sup>BIOS Lab-on-a-Chip group, MESA+ Institute, University of Twente, The Netherlands

Corresponding author: s.spijkhout@erasmusmc.nl

## Introduction

The nonlinear response of a suspension of microbubbles (MBs) to specific acoustical excitations forms the basis of many advanced ultrasound (US) imaging techniques. Measuring the response from a single MB, however, typically requires ultra high-speed optical imaging, which is costly and can be labour intensive. A relatively simple acoustical setup called an ‘Acoustical Camera’ (AC)<sup>[1]</sup> - provides a more-scalable alternative to high-speed imaging. An AC employs a high-frequency (HF) probing pulse with a frequency well above the resonance frequency of MBs, while modulating the size of the bubbles with a low-frequency (LF) pulse. The scattered pressure amplitude scales linearly with the instantaneous bubble size, and as such allows to capture the relative size change  $dR(t)/R_0$  of single MBs. However, the AC lacks the ability to measure the resting radius  $R_0$ . An experimental study by Fouan et al.,<sup>[2]</sup> reported a potential way to estimate  $R_0$  from the acoustic signal measured with an AC. This method utilizes the phase change of the scattered HF pressure to estimate the absolute wall displacement  $dR$ . Combined with the relative change  $dR/R_0$  from amplitude demodulation – the principle used in the original AC<sup>[1]</sup> - this results in the size of single MBs. In this study we further develop this approach and compare the AC sizing method with the Coulter Counter (CC) sizing method on size-sorted commercial MBs with a size  $R_0$  down to 1.5  $\mu\text{m}$ .

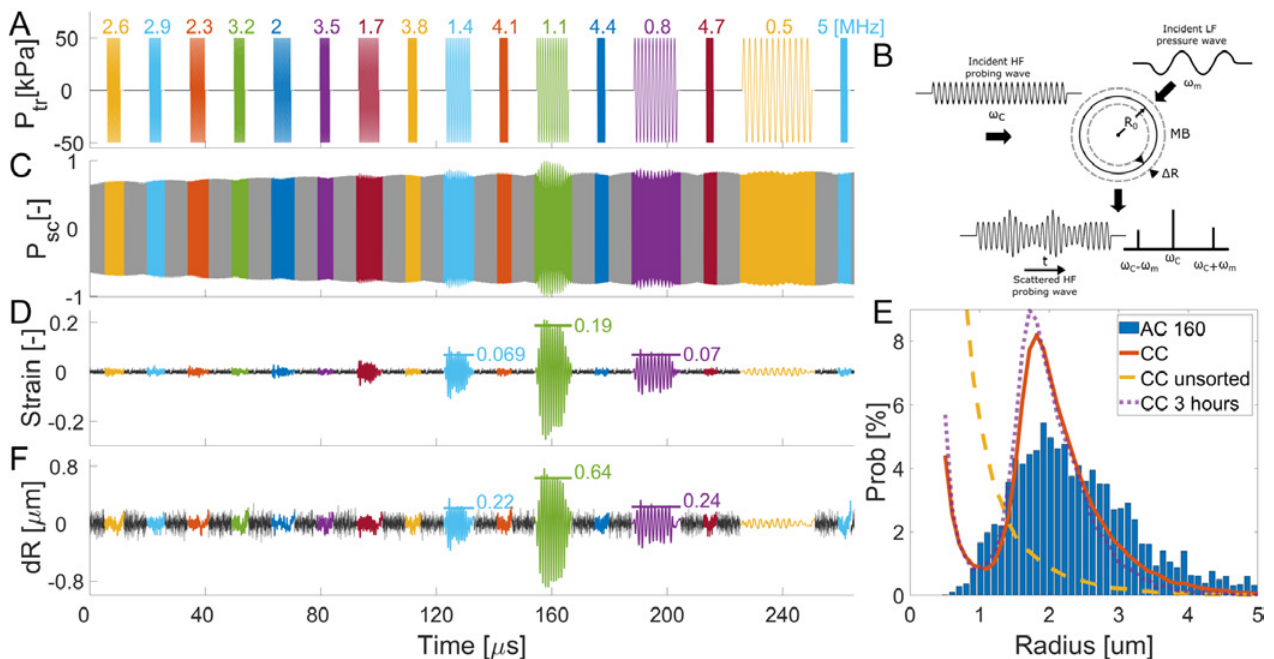


Figure 1. (A) LF signal sequence used to induce bubble vibrations consisting of 16 individual – 12 cycle – pulses. (B) Schematic of the situation inside the AC, with a vibrating microbubble following the LF pressure wave, and separately a HF probing wave which is modulated in amplitude following the time-variant bubble size. (C) Example of a detected bubble signal, with sections of LF excitation colour-matched to the LF sequence in A. (D) Example of demodulated amplitude strain signal, and (F) example of

*demodulated phase dR signal. Sizing uses the stronger sections (with strain > 0.025) and works by dividing dR magnitude with strain magnitude – both indicated with horizontal line and labelled. (E) Size distribution obtained with this acoustical method after measuring 453 individual MB in blue bar plots, CC obtained distributions of unsorted MB in yellow dashed line, size sorted MB in red, and the CC size distribution after 3 hours in purple dotted line.*

## **Methods**

### *HF scattering from a vibrating microbubble*

A vibrating MB with frequency  $\omega_m$ , and vibrational (strain) magnitude  $m$ , insonicated by a pressure field with a frequency  $\omega_c$  well above the fundamental resonance, will scatter a time-varying pressure amplitude  $P_{sc}(t)$  following:

$$P_{sc}(t) = (1 + m \sin(\omega_m t)) \sin(\omega_c t + \Delta\phi \sin(\omega_m t)),$$

where an amplitude modulation with magnitude  $m$  occurs from volumetric oscillations, simultaneously with a phase modulating effect with magnitude  $\Delta\phi$  from wall displacement of the vibrating MB. For this, it is assumed that a linear relation between scattered HF pressure phase and instantaneous bubble size exist, similar to the scattered HF pressure phase (see Fig. 1 in [1]). Additionally, a spherical symmetry in this scattered HF pressure phase is assumed – which is the case for the Rayleigh regime (scatterer dimension < wavelength) – we can isolate  $\Delta R$  from phase demodulation by multiplying the phase with the probing wavelength since:

$$\Delta\phi = -\Delta R \frac{\omega_c}{c},$$

with  $c$  being the speed of sound in the medium.

### *Experimental steps*

The headspace of freeze-dried SonoVue (Bracco, Milano, Italy) MBs was replaced by C<sub>4</sub>F<sub>10</sub> before being mixed with the 5 mL solution. MBs were then sized in a CC (Beckman Coulter, Mijdrecht, The Netherlands), setting aside 2 mL of MB solution in a syringe. To remove MB with resting radius  $R_0 < 1.5 \mu\text{m}$ , this syringe was centrifuged for one minute at 160 relative centrifugal force (RCF) after which the top 0.5 mL-layer (i.e., the cake) was kept and re-immersed to a 2 mL saline solution, following a protocol described in [3]. Centrifugation was repeated 8 times and CC sizing was performed on the resulting size-sorted MBs. Removal of the larger amount of small MBs was performed because a lower detection limit for MB sizes was assumed – since scattered pressure decreases with size. These size-sorted MBs were then measured three times in the AC for 20 minutes using 30 kPa LF driving pressure, and two times using 50 kPa LF pressure. CC sizing was performed ten times over the course of 20 minutes to confirm the MB stability in solution. The MBs were sized in the CC once more after the ~3 hours of AC experiments to confirm MB stability on that timescale.

A solution of 0.5  $\mu\text{L}$  of size-sorted MBs in 210 mL phosphate buffered saline was mixed inside the AC and measured for 20 minutes before refreshing the MB. The probing signal was set to 25 MHz at 500 kPa using a single-element focused HF transducer (V324, Olympus Industrial, Essex, UK) and amplifier (150A100B, Amplifier Research, Bothell, WA, USA). The LF signal to induce MB pulsations - displayed in Fig. 1A - is a sequence of 16 individual sections, of 12 cycles each at a pressure of 50/30 kPa, in alternating frequencies ranging from 0.5 to 5 MHz, with a 10  $\mu\text{s}$  rest in between. The LF pulses were programmed into an arbitrary waveform generator (AWG) (WW2572A, 250 MS/s, Tabor Electronics, Tel Hanan, Israel), and transmitted 15 times per second - together with the HF signal following a pulse from a secondary AWG (33220A, Agilent, Palo Alto, CA, USA) - using an amplified (310L, ENI, Rochester, NY, USA) transducer (PA081, Precision Acoustics, Dorchester, UK).

Scattered HF signals are recorded - following the pulse from the second AWG, by a second HF transducer (V324, Olympus Industrial, Essex, UK), amplified (AU-1519-10289, Miteq, Hauppauge, NY) and finally digitized (M4x.4420-x4, Spectrum Instrumentation, Limerick, Ireland). The scattered HF signal

is modulated both in amplitude and in phase due to the vibrational response of the MB to the LF signal. One example recording is shown in Fig. 1C. Initially, signals with a high frequency (HF) scattered amplitude exceeding the background noise by at least 20 dB were included following [1]. Later, we found a significant improvement in sizing performance if a 30 dB threshold was used instead.

### *Signal processing*

To acoustically size a MB, the HF signal (Figure 1.C) is demodulated in amplitude and phase, from which the strain (Figure 1.D) and  $dR$  (Figure 1.F) magnitudes are computed for each driving LF frequency (colours matched in Figures 1A, C, D and F). From signals with a strain value exceeding 0.025,  $R_0$  is computed by dividing  $dR$  by the strain. Each individual MB measurement then yields up to 16  $R_0$  estimates, from which a distribution is generated with a count weighed by the number of valid  $R_0$  estimates for that MB. To illustrate, in the MB measurement displayed in Fig. 1C, 3 estimates are included with values of  $0.22/0.069=3.19 \mu\text{m}$ ,  $0.64/0.19=3.37 \mu\text{m}$  and  $0.24/0.07=3.43 \mu\text{m}$ , each with a count of 1/3.

### **Results**

A total of 465 MBs were recorded with the AC, of which 453 included at least one LF pulse where the strain threshold ( $\geq 0.025$ ) was met. An average of 5.3 LF pulses were included per MB (i.e., 5.3  $R_0$  estimates) to form the size distribution shown by blue bar plots in Fig. 1E. The AC-obtained size distribution peaked at a  $R_0$  of  $1.9 \mu\text{m}$ , whereas the CC measured at  $1.8 \mu\text{m}$ . The AC full width at half maximum (FWHM) is approximately twice that of the CC ( $1.7$  versus  $0.83 \mu\text{m}$ ). We found the threshold value of the SNR (scattered HF signal versus random noise) to significantly influence sizing performance.  $R_0$  estimates from acquisitions with lower than 30 dB SNR were less likely to fit inside the CC sizing distribution, indicating that the sizing technique is sensitive to noise.

The sizing depends on the phase demodulation, which was found to be more sensitive to noise than the amplitude demodulation – hence the higher required SNR. The modulation ( $m$ ) threshold is another important parameter to consider, but has a smaller effect on the distribution than the SNR. A higher threshold for both  $m$  and SNR is better in general, but eventually ( $\text{SNR} > 35 \text{ dB}$ ) this results in rejection of most of the MB signals, and a sparse distribution of high  $R_0$  estimates is found, since only the largest MBs will scatter with sufficient pressure amplitudes. It is also clear that there is indeed a lower limit to the bubble sizes that can be reliably measured, which appears to be around  $1\text{-}2 \mu\text{m}$ . This lower limit may be lowered by higher HF signal levels, better SNR of the signal processing chain or tuning of the LF excitation signal. This is subject of further investigation.

The normalized CC size distribution is shown by the red line in Figs. 1E, which is calculated as the mean distribution from the 10 runs over 20 minutes. For reference, the original unsorted MB distribution is shown by the dashed yellow line, and the sorted MB, sized after 3 hours in solution by the dotted purple line. Size sorting resulted in significant changes on the CC-obtained size distribution, as can be seen from comparing the solid red line with the dashed yellow line in Fig 1E. The MB distribution remained stable in solution for over 3 hours, as can be seen from comparing the dotted purple curve with the solid red line in Fig. 1E.

On average, strain magnitudes were higher ( $0.0335$  versus  $0.0196$ ) for 50 kPa excitations than 30 kPa, which results in a greater relative contribution of 50 kPa excited bubble signals in the size distribution. No significant differences in the mean resonance curves were found between the 30 and 50 kPa driving frequencies.

### **Discussion**

Larger HF pressures (increased SNR) likely will improve sizing performance, and will allow smaller MB sizes to be measured. Similarly, an increased LF pressure improves sizing performance through  $m$ , but potentially introduces permanent changes to the MB's behaviour or size through deflation, which may interfere with the goal of the AC user - to study MB behaviour. SNR can also be improved by increasing the probing frequency, as a higher  $\omega_c$  increases the phase modulating magnitude, reducing noise in the  $dR$  estimate, but eventually interfering with the Rayleigh scattering regime assumption.

## Conclusions

The AC-obtained distribution from the 160 RCF MB ( $R_0 > 1.5 \mu\text{m}$ ) agreed well with the CC distribution in both shape and peak probability, although there is a bias for larger  $R_0$  estimates, and a 100 % increase in FWHM in the case of the AC. This likely follows from the fact smaller MBs scatter insufficient HF ultrasound ( $P_{sc}$  scales with  $R$ ), which can, additionally, introduce a detection limit for smaller MBs. An overall improvement in sizing performance is expected from higher HF pressure and frequency.

## References

- [1]. Renaud G, Bosch JG, Van Der Steen AF, De Jong N. Low-amplitude non-linear volume vibrations of single microbubbles measured with an "acoustical camera". *Ultrasound Med Biol.* 2014 Jun;40(6):1282-95. doi: 10.1016/j.ultrasmedbio.2013.12.018. Epub 2014 Mar 7. PMID: 24613552.
- [2]. Fouan D, Achaoui Y, Payan C, Mensah S. Microbubble dynamics monitoring using a dual modulation method. *J Acoust Soc Am.* 2015 Feb;137(2):EL144-50. doi: 10.1121/1.4905883. PMID: 25698042
- [3]. Feshitan J, Chen C, Kwan J, Borden M, Microbubble size isolation by differential centrifugation, *Journal of colloid and interface science*, 329, 316-24, 2008.

# Transient disruption of a blood-brain barrier on-chip using ultrasound and monodisperse microbubbles

*Martin R.P. van den Broek<sup>1\*</sup>, Mariia Zakharova<sup>1\*</sup>, Pieter A.M. Persijn van Meerten<sup>1</sup>, Jolien Wichers-Schreur<sup>1</sup>, Michel Versluis<sup>2</sup>, Albert van den Berg<sup>1</sup>, Loes I. Segerink<sup>1</sup>, Tim Segers<sup>1</sup>*

<sup>1</sup>*BIOS Lab-on-a-Chip Group, Max-Planck Center for Complex Fluid Dynamics, MESA+ Institute for Nanotechnology, University of Twente, Enschede, The Netherlands*

<sup>2</sup>*Physics of Fluids Group, University of Twente, Enschede, The Netherlands*

Corresponding author: [m.r.p.vandenbroek@utwente.nl](mailto:m.r.p.vandenbroek@utwente.nl)

*\*Both authors contributed equally*

## Introduction

The blood-brain barrier (BBB) inhibits the passage of molecules from the vasculature to the brain and thereby protects it from harmful pathogens [1]. For the same reason, the BBB prevents intravenously injected therapeutics from reaching their target site in the brain which highly complicates the treatment of brain tumors and neurodegenerative diseases, as well as brain tumor detection using liquid biopsy. Microbubbles injected into the bloodstream combined with focused ultrasound has proven to be a successful method to temporarily open the BBB in pre-clinical models as well as in humans. However, to date, fundamental questions remain as to the detailed mechanism(s) by which oscillating microbubbles induce BBB permeation. The questions include (i) whether drug transport is facilitated through bubble-induced disruption of the intercellular tight-junctions and/or through endocytosis and, (ii) what the intricate correlation is between microbubble dynamics and BBB permeability. Here, we aim to understand the fundamentals of BBB permeation using bubbles and ultrasound by employing novel organ-on-a-chip technology allowing detailed characterization of (i) the acoustic microbubble response using ultra-high-speed imaging, (ii) BBB permeability using fluorescence imaging *and* trans-endothelial electrical resistance (TEER) measurements, and (iii) the time-resolved dynamics of tight-junctions also through fluorescence imaging. By using a monodisperse microbubble suspension, we keep the physical parameter of the bubble size constant such that (in our future work) microbubble response can be correlated with membrane permeability and the dynamics of tight-junctions.

## Methods

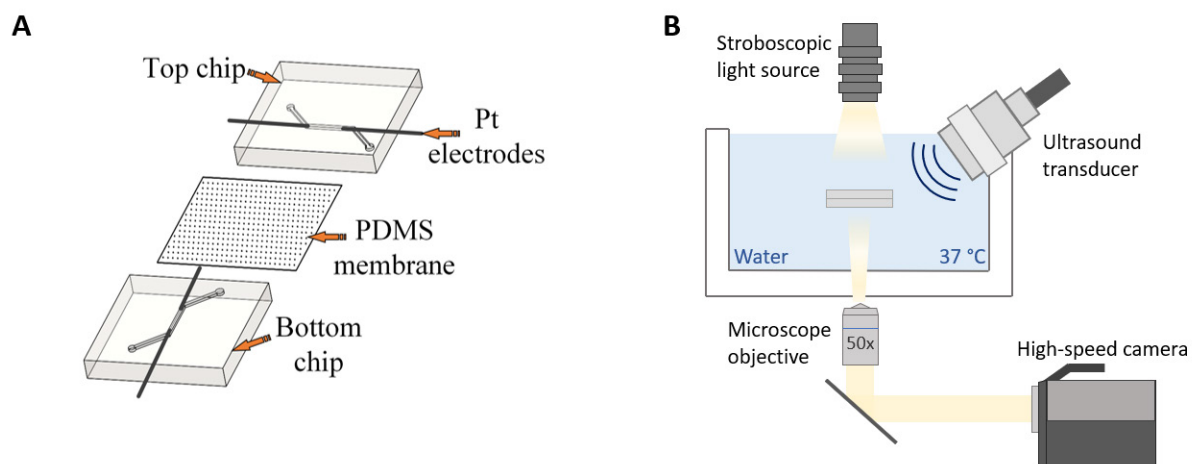


**Figure 1.** A) Schematic representation of the microfluidic chip. The cross-section between the top and bottom channel is separated by a 2 μm thick PDMS membrane with a grid of 3 μm diameter pores. The endothelial cells were cultured on this membrane. B) Schematic representation of the ultrasound setup. Focused ultrasound

was generated by a transducer placed at a 45° angle with respect to the chip surface. The microbubbles were imaged from below using a high-speed camera operated at 10 million frames/s.

A BBB-on-chip was fabricated as previously described by our group [2]. In short, two chips of polydimethylsiloxane (PDMS), both containing a channel, were plasma-bonded on top of each other with a 2 μm thick porous PDMS membrane in between such that the area over which diffusive transport can take place from one channel to the other comprised 500 x 500 μm<sup>2</sup> (Fig. 1A). The hCMEC/D3 cells were seeded on the membrane in the bottom channel and were cultured for 4 days. On the 4<sup>th</sup> day, BBB disruption was performed using monodisperse 2.9-μm radius microbubbles. A concentration of 1 million bubbles/mL was injected in the bottom channel of the chip. The chip was placed in a 37 °C water bath in the acoustic setup (Fig. 1B). A single 25-cycle ultrasound burst at a frequency of 1 MHz and an acoustic pressure amplitude of 500 kPa was used to insonify the monodisperse bubbles. The monodisperse bubbles were formed in a flow-focusing device at 55 °C as described in [3] using a gas-mixture (13 v% C<sub>4</sub>F<sub>10</sub> in CO<sub>2</sub>) and an aqueous lipid mixture comprising DSPC and DPPE-PEG5000 mixed at a 9:1 molar ratio. BBB permeability was measured using the fluorescent marker FITC-dextran (4 kDa and 1 mg/mL) that was injected into the bottom channel (also containing the cells) immediately after ultrasound insonation. The fluorescent intensity in the top channel was then measured over a period of 1 hour and compared to that of a BBB on-chip that did not undergo ultrasound insonation.

## Results

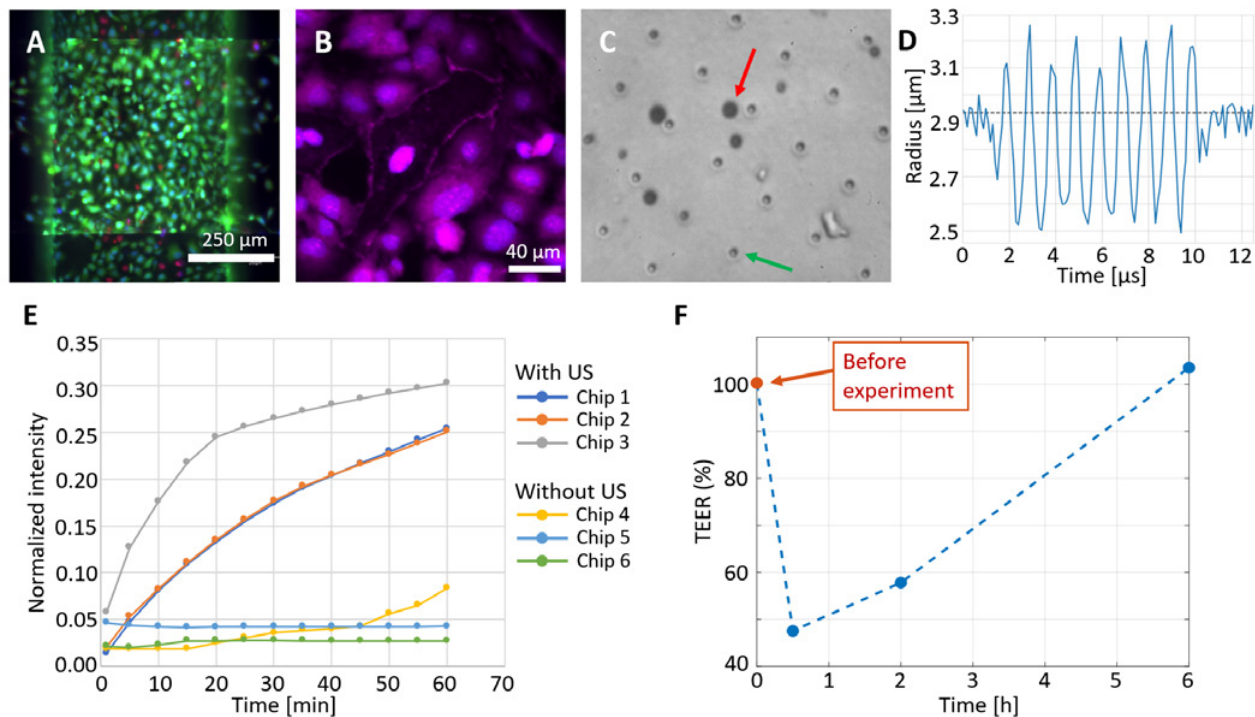


**Figure 2.** A) Live-dead staining of the hCMEC/D3 cells inside the BBB chip. B) ZO-1 staining of cells inside the chip highlighting the tight junctions and cell nuclei. C) High-speed movie frame of oscillating microbubbles floating against the porous PDMS membrane during the bubble-expansion phase. The red arrow points toward a microbubble and the green arrow to a membrane pore. D) Radius-time curve of a microbubble oscillating against the membrane. E) Fluorescent intensity in the top channel normalized to that in the bottom channel compared for BBBs on-chip with and without ultrasound insonation. F) Average change in TEER values after exposure to ultrasound and microbubbles (n=2).

Figure 2A shows a live-dead staining where the green signal indicates live cells, red indicates dead cells, and blue indicates cell nuclei. The image shows that our BBB on-chip is viable, i.e., with little dead cells. Figure 2B shows the presence of tight junctions visualized using the ZO-1 tight junction marker. Figure 2C displays a frame of a high-speed recording showing microbubbles inside the chip floating against

the porous membrane (without cells). Figure 2D presents a radius-time curve of an oscillating microbubble against the porous membrane imaged at a frame rate of 10 million frames/s.

The oscillating microbubbles resulted in a dramatic increase in BBB permeability as is shown in Fig. 2E. The figure shows the measured fluorescence intensity of the FITC-dextran molecules that diffused through the membrane normalized to the fluorescence intensity in the bottom channel. Note that the permeability of the BBBs on-chip that did not undergo treatment with bubbles and ultrasound was negligible as compared to the BBBs on-chip that did undergo ultrasound and bubble treatment.

An increased BBB permeability is also apparent from the TEER measurements shown in Fig. 2F. The TEER value drops after ultrasound insonation which is indicative of an increased membrane permeability. Note that the TEER value increases over time indicating full recovery of the BBB (decrease in permeability) after treatment with bubbles and ultrasound. Future work will focus on exploring the full parameter space of bubble size and acoustic driving conditions with the ultimate aim to correlate BBB permeability and recovery to the volumetric oscillation response of the microbubbles.

### Conclusions

BBB permeability is shown to dramatically increase after the exposure of microbubbles (floating against the BBB) by ultrasound of only 25 acoustic cycles at a moderate acoustic pressure amplitude (500 kPa). Furthermore, trans-endothelial electrical resistance (TEER) measurements indicate that the BBB is able to fully recover after ultrasound treatment over the course of several hours. The present study thereby shows that novel organ-on-a-chip technology is a promising route to study the fundamentals of BBB permeation induced by ultrasound-driven microbubbles.

### References

- [1]. Wong, A. D., Ye, M., Levy, A. F., Rothstein, J. D., Bergles, D. E., & Searson, P. C. (2013). The blood-brain barrier: An engineering perspective. In *Frontiers in Neuroengineering* (Issue JUL).
- [2]. van der Helm, M. W., Odijk, M., Frimat, J. P., van der Meer, A. D., Eijkel, J. C. T., van den Berg, A., & Segerink, L. I. (2017). Fabrication and validation of an organ-on-chip system with integrated electrodes to directly quantify transendothelial electrical resistance. *Journal of Visualized Experiments*, 2017(127).
- [3]. Segers, T., Gaud, E., Casqueiro, G., Lassus, A., Versluis, M., & Frinking, P. (2020). Foam-free monodisperse lipid-coated ultrasound contrast agent synthesis by flow-focusing through multi-gas-component microbubble stabilization. *Applied physics letters*, 116(17), 173701.

# The Influence of Nanobubble Size and Stability on In Vitro Ultrasound Mediated Sonoporation

*Damien V. B. Batchelor*<sup>1</sup>, *Fern J. Armistead*<sup>1</sup>, *Nicola Ingram*<sup>2,3</sup>, *Sally A. Peyman*<sup>1</sup>, *James R. McLaughlan*<sup>2,3</sup>, *P. Louise Coletta*<sup>3</sup>, *Stephen D. Evans*<sup>1</sup>

<sup>1</sup>*Molecular and Nanoscale Physics Group, School of Physics and Astronomy, University of Leeds, LS2 9JT, United Kingdom*

<sup>2</sup>*Leeds Institute of Medical Research, Wellcome Trust Brenner Building, St James's University Hospital, Leeds, LS9 7TF, United Kingdom*

<sup>3</sup>*Faculty of Electronic and Electrical Engineering, University of Leeds, LS2 9JT, United Kingdom*  
*Corresponding author: S.D.Evans@leeds.ac.uk*

## Introduction

Lipid-shelled nanobubbles (NBs) have recently emerged as potential dual diagnostic and therapeutic agents [1]. Similar to their micron-scale counterparts, microbubbles (1 – 10  $\mu\text{m}$ ), they can act as ultrasound (US) contrast agents, as well as locally enhance therapeutic uptake in a process known as sonoporation [2]. Recently, it has been shown that the reduced size of NBs ( $< 1 \mu\text{m}$ ) promotes increased uptake and accumulation in tumour interstitial space, which can enhance their diagnostic and therapeutic performance [3]. However, accurate characterisation of NB size and concentration is challenging, and may limit their transition into clinical use [4]. Their sub-micron nature limits accuracy of conventional microscopy techniques, whilst common light scattering techniques fail to distinguish between sub-populations present in NB samples (i.e. bubbles and liposomes). Due to this, reported NB size varies greatly throughout the literature and hence little is known about the influence of size on their therapeutic performance. In this study, we firstly describe a novel method of using a commercially available Nanoparticle Tracking Analysis (NTA) system, to distinguish between NBs and liposomes, owing to their differing optical properties. We used this technique to characterize NBs of varying mean size, isolated via centrifugation, and assessed their in vitro sonoporation performance on-chip, across a range of NB concentrations. The observed trends then led to investigation of NB stability, and highlighted important and potential stability mechanisms.

## Methods

Lipid-shelled (95:5 DPPC:DSPE-PEG2000) NBs were isolated from a MB suspension by centrifugation at either 100, 500 or 1,000 g (referred to as Sample I, II and III), yielding NBs of different modal sizes.

Nanoparticle Tracking Analysis (NTA) and Dynamic Light Scattering (DLS) were used to determine NB size (DLS, NTA) and concentration (NTA). During data acquisition, the camera level (a marker of image intensity) was set to between values of 3-4, such that highly scattering particles (i.e. NBs) were detected, but particles with a lower scattering intensity (i.e. lipid vesicles) were not (Figure 1a). Brightfield microscopy was used to determine the concentration of optically visible bubbles in NB samples. Sonoporation studies were conducted using SW480 cells cultured on the top of the channels in a microfluidic device ( $\mu$ -Slide VI 0.4, iBidi, Germany). Unfocused, 2.25 MHz central frequency US was used for sonoporation studies (Figure 1b). US parameters were as follows: MI = 0.6, PRF = 1 kHz, Duty Cycle = 1 %, Total Duration = 5 s.

A red fluorescence membrane probe (70 kDa Texas-Red Dextran, ThermoFisher) was used to quantify uptake, whilst a green fluorescence live stain (CellTracker Green CMFDA) was used to determine cell viability post treatment. NBs were added to the microfluidic channel and left for 60 mins at 21 °C to aid sonoporation by flotation. Microfluidic chips were imaged using a confocal microscope (Leica DMI8/SP8) to determine the location of live cells and quantify Dextran fluorescence. The Total Fluorescence Intensity (TFI) of Dextran inside viable, insonated cells was determined from confocal

fluorescence maps were analysed using image processing tools in MATLAB (2019b, Mathworks Inc, USA).

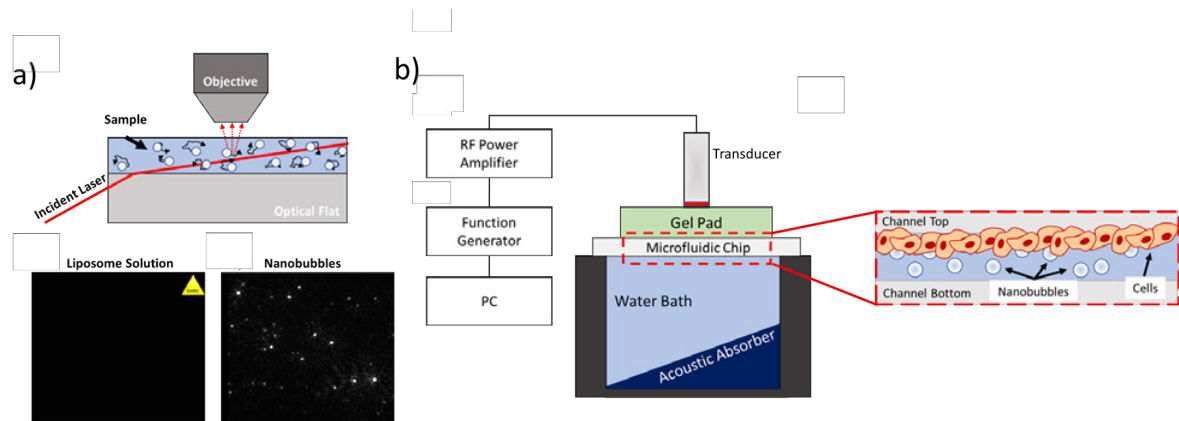


**Figure 1. a) Schematic showing the working principle of NTA, in which the random walk of nanoparticles is tracked by observing light scattered by individual particles. By utilizing a low camera gain setting compared to typical NTA measurements, we can distinguish between NBs and liposomes in a mixed population, due to the increased scattering associated with gas-core particles. b) The acoustic and microfluidic set-up used for sonoporation experiments, in which cells were cultured on the top of a microfluidic channel to allow for NB flotation towards the monolayer. Not to scale.**

## Results

For the first time using a commercial NTA instrument, we were able to distinguish between the NB and liposome sub-populations present in NB samples, due to the increased scattering associated with gas core particles (Figure 1a). Increasing RCF reduced mean NB size, characterised by NTA and DLS, and a reduced concentration of optically visible bubbles (Figure 1/Table 1).

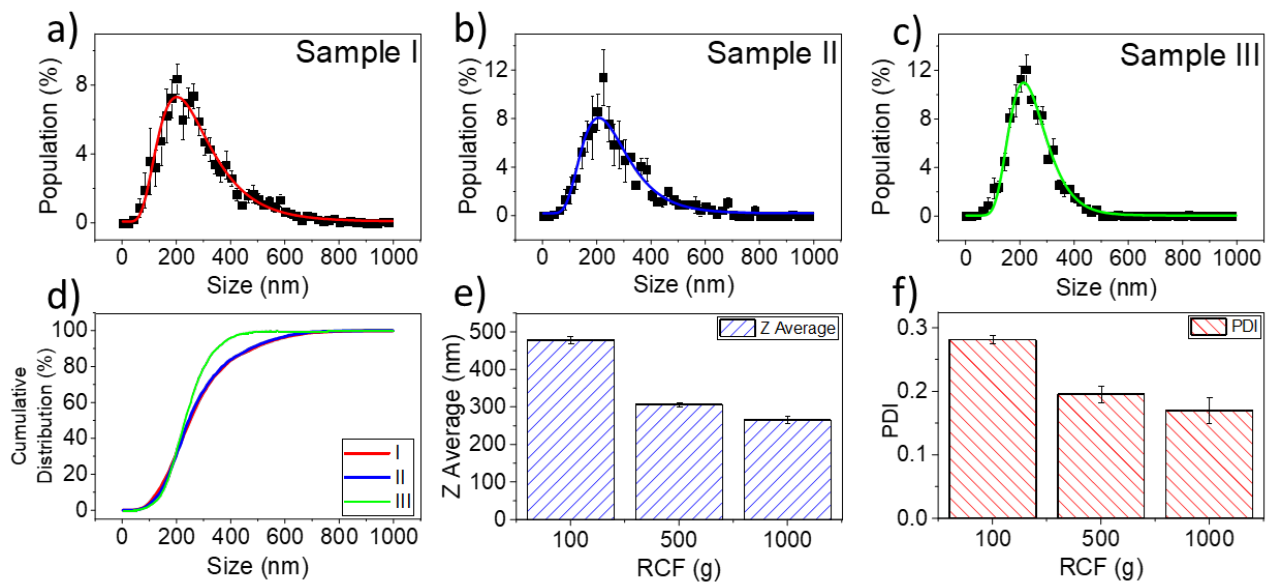


**Figure 2. Measured populations for samples separated via centrifugation at 100 g (a), 500 g (b), and 1000 g (c). d) Cumulative distribution for each NB sample, displayed as percentage of the population. e) Average size and (f) polydispersity index (PDI) of NB populations measured using DLS.**

Table 1. NB concentration and size data for populations isolated via centrifugation and characterized via NTA, DLS and brightfield microscopy. Stated values are mean  $\pm$  standard error across a minimum of 3 independent samples.

Sample	RCF (g)	NTA Mean Size (nm)	NTA Conc. ( $10^{10}$ /mL)	Microbubble Conc. ( $10^9$ /mL)
I	100	288 $\pm$ 23	4.91 $\pm$ 0.53	4.19 $\pm$ 0.90
II	500	265 $\pm$ 10	3.21 $\pm$ 0.86	1.34 $\pm$ 0.39
III	1000	251 $\pm$ 3	0.93 $\pm$ 0.10	0.02 $\pm$ 0.01

Sonoporation studies showed that all NB samples at their yield concentration could induce intracellular Dextran uptake when treated with US (Figure 3a), and the uptake decreased with NB concentration (Figure 3b). However, at matched NB concentration ( $10^{10}$  NBs/mL), Sample III outperforms Sample II contrary to what would be expected. By plotting the TFI against lipid concentration (comparable to sample dilution, assuming a final yield lipid concentration of 0.2 mg/mL), the observed trend between samples is similar to what would be expected, samples perform in the following order: I > II > III (Figure 3c).

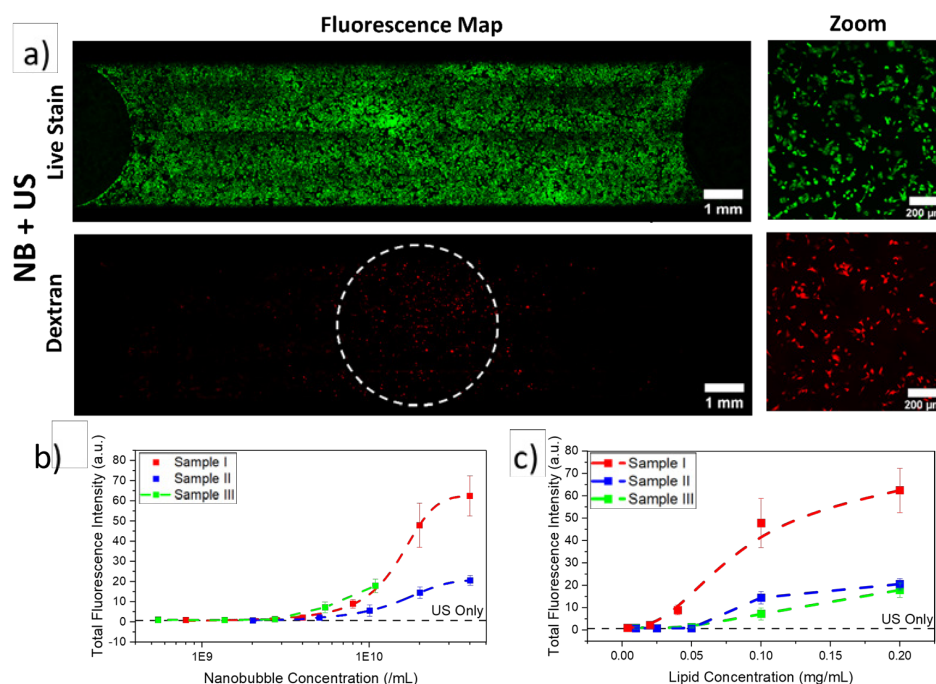
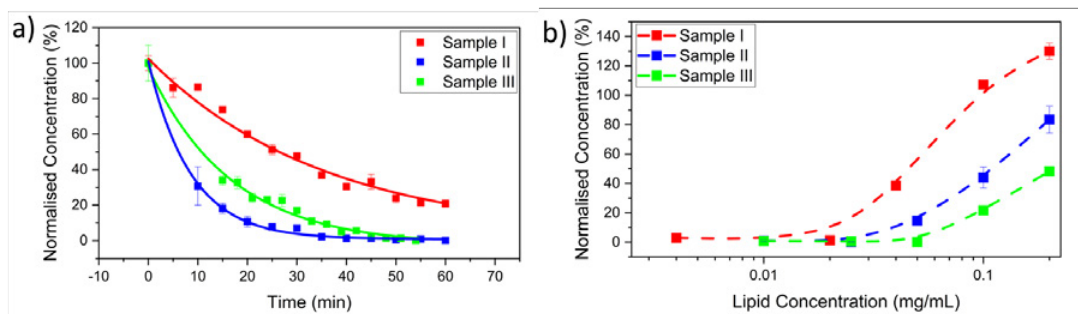


Figure 3. a) Confocal fluorescence imaging showing NB and US mediated Dextran uptake in SW480 cells, showing a full chip fluorescence map, and zoomed images showing co-localisation between Dextran fluorescence and viable cells. Quantitative analysis of Dextran uptake dependent on either (b) NB concentration or (c) total lipid concentration.

As only the initial ( $t=0$ ) NB concentration is directly measurable the actual concentration at the time of insonation ( $t = 60$  min) is not known. NB stability was measured *in situ* in the NTA system over 60 min at initial concentrations of  $10^9$ /mL (appropriate for NTA measurements) which replicated an on-chip environment. These results showed that stability of the samples was in the order of I > III > II (Figure 4a), which may explain the increased sonoporation performance of Sample II compared to Sample III. However, this trend was not expected as it is widely accepted that bubble stability decreases with size, due to the relationship between Laplace pressure,  $\Delta P$ , and bubble radius,  $r$  ( $\Delta P = -2\sigma/r^2$ , where  $\sigma$  is surface

tension). As *in situ* measurements were performed at matched NB concentration, and each sample had a different initial NB yield, the total lipid concentration across each sample will vary during measurement. For example, Sample II and III, had resultant lipid concentration of 6 and 20  $\mu\text{g/mL}$  respectively, during measurement.

From this, the dependency of NB stability on lipid concentration was investigated. NB concentration was initially measured ( $t=0$ ), and then diluted to various final lipid concentrations and concentration measure at  $t = 60$  min. For all measured lipid concentrations, comparisons between samples showed that Sample I was the most stable, with Sample III the least and that normalized NB concentration decreased with decreasing lipid concentration for all three samples. The results again mirrored those shown in the sonoporation study and highlight the importance of storage conditions on NB stability, whilst also giving insight into potential mechanisms behind NB stability. Recent studies by Segers et al. [5,6] show that the use of higher lipid concentrations can aid short-term and long-term MB stability, and our results suggest this model could also be applicable to NBs. It should also be noted that as well as being stored at varying lipid concentrations, the process of dilution required will also vary the total bubble concentration and hence the inter-bubble distance, and total dissolved gas concentration. Molecular dynamics simulations by Weijs et al. [7] predict that small inter-bubble distances,  $l$ , can shield gas diffusion due to high local gas concentrations, and that there exists a critical value ( $l_0/d < 10$ ,  $d =$  bubble diameter) at which NBs are found to be stable. Assuming  $d = 300$  nm, this model predicts that at their yield concentration Sample I is stable, and that Sample II and Sample III are unstable, concurrent with our results.



**Figure 4. Stability of NBs samples after separation via centrifugation at different RCF values. a) Normalised NB concentration measured *in situ* – “on-chip” over 60 min at matched initial NB concentration of  $10^9$  bubbles/mL. b) Normalised concentration of NB samples measured after 60 min of storage at varying lipid concentrations.**

## Conclusions

Accurate characterization of NB size and population has proved challenging in the research community and may limit their transition into clinical studies. Here we demonstrated novel use of a commercially available NTA system to determine the size and concentration of exclusively NBs, in a mixed population containing NBs and liposomes. We used this technique to characterize NBs of varying mean size, isolated via centrifugation, and assessed their *in vitro* sonoporation performance across a range of NB concentrations. Confocal fluorescence microscopy and image analysis showed that their sonoporation efficiency did not depend exclusively on size and concentration but was also dependent on NB stability. Using NTA, we revealed the relationship between NB stability, size, inter-bubble distance and lipid concentration in agreement with recently proposed models for stability, highlighting the importance of NB size, concentration, and stability on their therapeutic effectiveness. As such, our use of NTA to successfully characterize NBs is promising for the future development of stable NBs, opening a range of potential studies to investigate the effect of varying NB shell composition on stability and *in vitro* and *in vivo* performance.

## References

- [1]. Batchelor, D. V. B. et al. Nested Nanobubbles for Ultrasound-Triggered Drug Release. *ACS Appl. Mater. Interfaces* 12, 29085–29093 (2020).
- [2]. Bourn, M. D. et al. High-throughput microfluidics for evaluating microbubble enhanced delivery of Cancer therapeutics in spheroid cultures. *J. Control. Release* (2020)
- [3]. Pellow, C., Abenojar, E. C., Exner, A. A., Zheng, G. & Goertz, D. E. Concurrent visual and acoustic tracking of passive and active delivery of nanobubbles to tumors. *Theranostics* 10, 11690–11706 (2020).
- [4]. Batchelor, D. V. B. et al. Nanobubbles for therapeutic delivery: Production, stability and current prospects. *Curr. Opin. Colloid Interface Sci.* 54, 101456 (2021).
- [5]. Segers, T., Lohse, D., Versluis, M. & Frinking, P. Universal Equations for the Coalescence Probability and Long-Term Size Stability of Phospholipid-Coated Monodisperse Microbubbles Formed by Flow Focusing. *Langmuir* 33, 10329–10339 (2017).
- [6]. Segers, T., De Rond, L., De Jong, N., Borden, M. & Versluis, M. Stability of Monodisperse Phospholipid-Coated Microbubbles Formed by Flow-Focusing at High Production Rates. *Langmuir* 32, 3937–3944 (2016).
- [7]. Weijs, J. H., Seddon, J. R. T. & Lohse, D. Diffusive shielding stabilizes bulk nanobubble clusters. *ChemPhysChem* 13, 2197–2204 (2012).

## Microdroplet-DNA assemblies for tailored coalescing interaction and tumour cells transfection

*Fabio Domenici<sup>1</sup>, Angela Ditri<sup>1</sup>, Damiano Palmieri<sup>1</sup>, Martina Piermarini<sup>1</sup>, Letizia Oddo<sup>1</sup>, Yosra Toumia<sup>1</sup>, Federica Todaro<sup>1</sup>, Alessandro Porchetta<sup>1</sup>, Angelico Bedini<sup>2</sup>, Gaio Paradossi<sup>1</sup>*

<sup>1</sup>*Department of Chemical Sciences and Technologies, University of Rome Tor Vergata, Rome, Italy.*

<sup>2</sup>*INAIL, worker's Compensation Authority, Italy*

*Corresponding author: fabio.domenici@uniroma2.it*

### Introduction

The exploitation of microdroplets (MDs) has recently emerged as an exciting new technology platform for applications in the chemical and biological sciences, in order to tailor chemical reaction and to improve the efficiency of drug and gene delivery in the critical issues of modern cancer nanomedicine research [1]. In these frames, we have recently developed versatile and stable MDs made of dimethyldioctadecylammonium bromide (DDAB) shell and a liquid perfluorocarbon decafluoropentane (DFP) core, able to effectively load a drug into the core [2] and bind DNA on the DDAB shell at the aqueous interface (i.e., DDAB has a positive charge on the quaternary ammonium which attracts the negative charge of the DNA backbone) [3]. This high density and narrowly polydispersed DDAB-MDs system has already shown invaluable potential as a drug delivery carrier [2] in facilitating the transport of low hydrophilic drugs enclosed in MDs core through polar biological environments, and releasing them within tumour cells limiting the side effects of treatments. At the same time, the high affinity for cell membranes of the DDAB MDs shell could be exploited to transfect nucleic acids in cells [4] where specific tumour pathways can be modulated by means of siRNAs and specific consensus sequences transfection also to inhibit the drug resistance [5].

From then on, the aim of this work was the optimisation of DNA-MDs assemblies functional for two different applications. In the first one, the recognition and hybridisation of the two complementary oligonucleotides can be exploited to induce a rapid and selective coalescence of the micro-drops. In microfluidics, this system can be used to create microreactors as the coalescence mixes the reagents placed in the core of the MDs making them react to form a product. Tumour cells transfection represents the second application examined in this work. The affinity of DDAB shelled microdroplets for the cell membrane allow nucleic acids to be conveyed and introduced into the cell. Therefore, the drops could be widely used as vectors for the transfection of consensus genes in non-viral gene therapy.

### Methods

MDs with a DFP core enclosed in a DDAB shell were prepared according to [2] by adding, in this order, DFP, DDAB solution in EtOH and PBS (0,01M, pH 7,4) in a 15mL falcon. The mixture was sonicated using an ultrasonic processor 10s (0.7s pulse on and 0.3s pulse off, ~150W) and quickly diluted with additional PBS. This protocol allows to prepare ~ 10<sup>10</sup> MDs/mL as measured by microscope counting chamber. In order to obtain MDs containing fluorescent Nile Red (red) or Bodipy (green) in their DFP core, 20µL of the fluorophore solution (10µg/mL in EtOH) were added in the organic phase of the mixture immediately before the sonication.

All DNA samples (i.e., 24 bases Cy5\_ssDNA, 5'-marked with cyanine Cy5; and complementary Cy3\_ssDNA, 3'-modified with Cy3) were resuspended in PBS (0.01 M, pH 7.4) at the concentration of ~ 10 µM as quantified by NanoDrop UV-Vis spectrophotometer. The ssDNA hybridisation kinetics in solution was studied through fluorometric measurements with a Spark, Tecan fluorometer. Because of the hybridisation of the two ssDNAs induces a strong proximity of the two fluorophores Cy3 (donor) and Cy5 (acceptor), the binding kinetics was followed by an increase in the FRET signal.

In order to investigate the ssDNA-MDs interaction 10 nM of ssDNA was added to  $10^5$  MDs/mL in PBS suspension. The DNA and MDs molar ratio was chosen by evaluating the colloidal stability, the dimensions and the polydispersity of the DNA-MDs system. Image of DNA-MDs were carried out by confocal laser scanning microscopy (CLSM) using Nikon Eclipse Ti-E. The mean diameter and size distribution of the MDs were measured by dynamic light scattering (DLS). The measurements were carried out on the newly prepared system and were repeated on the same sample in the following days to verify the colloidal stability.

Binding kinetics of Cy3\_ssDNA and Cy5\_ssDNA hybridisation on the MDs surface, causing the specific binding interaction among the DNA-MDs, were followed in PBS solution by fluorescence.

For microfluidic collision experiments, the two ssDNA-MDs populations were converged separately in a micro-channel (Ibidi<sup>3in1</sup> channel) from two syringes pushed by a step by step pump at the set speed. The flow was observed by CLSM and the product was collected for a subsequent size analysis.

DNA transfection experiments using the MDs as carrier were performed on SK-Mel28 cell line cultured according to literature [6]. Cell samples were analysed with the addition of Cy3\_ssDNA-MDs, Cy5\_ssDNA-MDs and dsDNA-MDs. A further test was done by treating the cells with dsDNA without MDs. The treatments were performed by coating the MDs with 30 nM of DNA (single or double stranded) and the solution was then added to the cells in culture medium. After 1 hour incubation, the sample was washed several times and analysed by 2-D and 3-D confocal scan using NIS-Elements software (Nikon). Cell viability assays were performed by Trypan blue counting test using cell chip by Spark Tecan reader.

### Results

We developed MDs with a DFP core and a DDAB shell interacting with complementary DNA short strands (figure 1, A), exhibiting intriguing features of specific coalescence induction and DNA transfection. The ssDNA-MDs size distribution is centred at  $\sim 2.4 \mu\text{m}$  with low polydispersity. The system was optimised with a DNA surface coverage degree of  $10^3$  DNA strands per MDs (10 nM of DNA per  $10^5$  MDs/mL sample), which guarantees size stability and minimises the non-specific coalescences during the experiments. This allowed to detect specific coalescence events in the mixed population of Cy3\_ssDNA-MDs and Cy5\_ssDNA-MDs, triggered by the hybridisation of the two complementary ssDNA strands on the MDs surface.

The linking of ssDNA onto the MDs surface resulted in a significant reduction of the DNA hybridisation affinity (i.e.  $K_d$  from  $16.1 \pm 0.3 \text{ nM}$  to  $126.4 \pm 0.6 \text{ nM}$  according to scatchard plot). Although this, the affinity remains high enough to induce specific pairing and coalescence of the two different ssDNA-MDs populations. We found that after few minutes of 1:1 mixing the DNA-MDs size is doubled ( $\sim 5.6 \mu\text{m}$ ) with an increased polydispersity (figure 1, B).

Using time-lapse CLSM we investigated the possibility of transferring lipophilic organic molecules between the two different ssDNA-MDs populations through their specific coalescence. To this aim, we mixed two complementary ssDNA-MDs populations loaded with green donor (Bodipy) or red acceptor (Nile Red) fluorophores within the DFP core. We revealed that the coalescence process involves a progressive disappearance of the green donor fluorescence signal in favour of the red acceptor one. After approximately six minutes of coalescing, the whole DNA-MDs mixture exhibited only red fluorescent cores with the doubled average size. This means that after coalescence, Bodipy and Nile Red were both colocalised within a same DNA-MD (figure 1, B).

Microfluidic tracking experiments made it possible to optimise the collision and the specific coalescence process of the ssDNA-MDs (i.e., revealing the speed changes, analysing the product exiting the channel). The injection rate of the two populations was 0.89 mL/min which corresponds to a shear rate of  $5 \text{ dyn/cm}^2$ . This flow condition was chosen to favour an effective contact between the drops but not so fast to avoid separation and bouncing phenomena. Specific and non-specific coalescence events were 87% and 6% respectively.

We also present promising results about transfection and cytotoxicity of our MDs whose shell is modified with DNA sequences. We demonstrate that the DDAB-shelled MDs it is not only able to release drugs but it is also an efficient non-viral vector for DNA transfection into a human melanoma cell line (Sk-Mel 28) with very low cytotoxicity (figure 1,C). In addition, it seems that the dsDNA released in the cytosol by the MDs allows to trigger displacement reactions with subsequent uptake of DNA invading strands as observed by FRET confocal images.

## Conclusions

The DNA-MDs multifunctional system has shown promising results in combining stability, organic entity and DNA loading efficiency, and tranfection ability. The coalescence phenomenon - typical of hydrophobic systems in aqueous environment - is advantageously exploited in this work. Through the hybridisation of the complementary DNA strands that cover the MDs it is possible to induce a selective coalescence of the drops. This coalescence entails the mixing of reagents loaded inside them, allowing to conduct controlled reactions in small volumes. In addition to this application, we are confident that our DNA-MDs also deserve biomedical attention into design a valid approach of tumour treatment in the context of non-viral gene therapy.

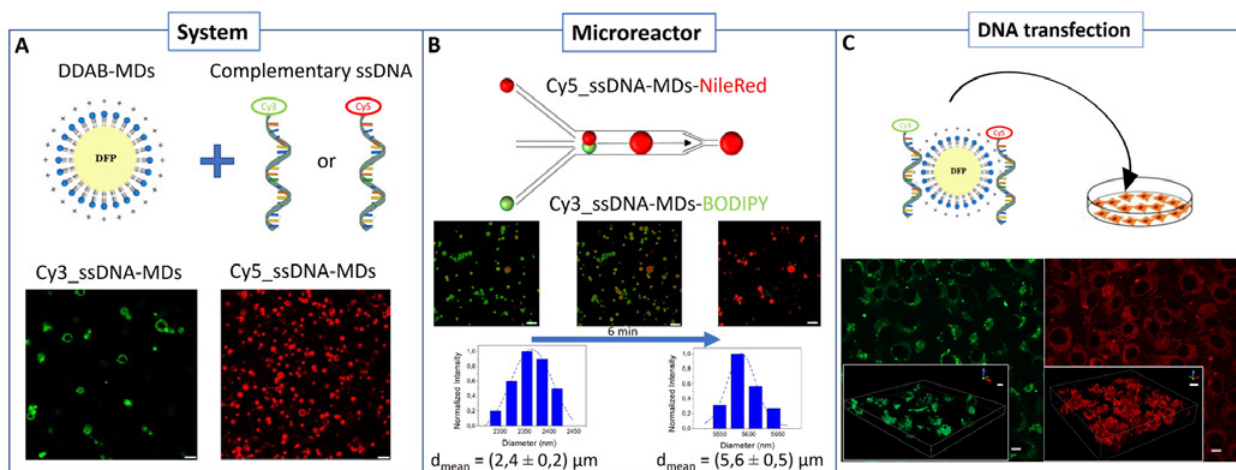


Figure 1. Panel A: sketch of the DDAB-MDs and complementary DNA strands marked with cyanine Cy3(green) or Cy5(red) composing the DNA-MDs system, with CLSM images of ssDNA-MDs; Panel B: sketch of the specific coalescence of the two ssDNA-MDs populations performed in microfluidic channel with respective CLSM images and DLS size distributions; Panel C: sketch of DNA-MDs transfection experiments with 2-D and 3-D CLSM images of ssDNA transfected Sk-Mel 28 cells. Scale bar 10  $\mu\text{m}$ .

## References

- [1]. Youn YS, Bae YH, Perspectives on the past, present, and future of cancer nanomedicine 2018, *Advanced Drug Delivery Reviews*, 130:3-11, 2018.
- [2]. Tortorella E, Palmieri D, Piermarini M, Gigante D, Oddo L, Toumia Y, Paradossi G, Domenici F, Phase Change Dimethyldioctadecylammonium-Shelled Microdroplets as a Promising Drug Delivery System: Results on 3D Spheroids of Mammalian Tumor Cells 2021, *Journal of Visualized Experiments*, 169, 2021.
- [3]. Zhang D, Seelig D, Dynamic DNA nanotechnology using strand-displacement reactions, 2011, *Nature Chemistry*, 3:103–113, 2011.
- [4]. Han K, An efficient DDAB-mediated transfection of Drosophila S2 cells, 1996, *Nucleic acids research*, 24:4362-3, 1996.
- [5]. Caffery B, Lee JS, Alexander-Bryant AA, Vectors for Glioblastoma Gene Therapy: Viral & Non-Viral Delivery Strategies, 2019, *Nanomaterials*, 9-105, 2019.

- [6]. Xiao P, Zheng B, Sun J, Yang J, Biochanin A induces anticancer effects in SK-Mel-28 human malignant melanoma cells via induction of apoptosis, inhibition of cell invasion and modulation of NF- $\kappa$ B and MAPK signaling pathways, 2017, *Oncol Lett.*,14(5):5989-5993, 2017.

### **Acknowledgements**

This project has received funding from the European Union's Horizon 2020 research and innovation Programme under grant agreement 766456 (AMPHORA) and from the Italian project BRiC19 ID 43 – INAIL.

# Encoding stimulus-responsiveness into microbubbles through lipid shell crosslinking

*Dragana Dubey<sup>1</sup>, Michael G. Christiansen<sup>1</sup>, Matej Vizovisek<sup>1</sup>, Samuel Gebhardt<sup>1</sup>, Jasmin Feike<sup>1</sup>, Simone Schuerle<sup>1</sup>*

*<sup>1</sup>Responsive Biomedical Systems Lab, ETH Zürich, Zürich, Switzerland  
Corresponding author: [simone.schuerle@hest.ethz.ch](mailto:simone.schuerle@hest.ethz.ch)*

## Introduction

Ultrasound imaging with contrast agents, especially with lipid-shelled microbubbles, has become a vital tool in clinical diagnostics. Efforts to adapt these agents for molecular imaging have typically focused on integrating targeting moieties that selectively bind them to sites of interest, without altering their physical properties.<sup>[1]</sup> A different approach is required for soluble biomarkers that do not provide anchor points for attachment such as secreted proteases, a highly informative class of enzymes centrally implicated in mechanisms of disease development and progression.<sup>[2]</sup> To visualize proteolytic activity using microbubbles, a change in chemical or backscattering behavior upon interaction with a target stimulus is needed. Reversible shell crosslinking has proven to be a viable strategy to incorporate responsiveness into microbubbles, enabling detection of changes in pH and other stimuli.<sup>[3]</sup> However, alternative strategies for cleavage-based detection of proteases with microbubbles have not been reported.

Here, we report on crosslinked microbubbles engineered to undergo irreversible decrosslinking of their shells upon exposure to a target stimulus. To inform the design of responsive microbubbles, we initially varied the crosslinker concentration and structure for non-responsive crosslinking, measuring its influence on acoustic and mechanical properties of microbubbles. By incorporating cleavable elements that respond to UV light or proteolysis, we demonstrate acoustic detection of these stimuli with kinetic resolution. In the future, the framework established in this study can be readily adapted to incorporate other substrates selectively cleaved by disease-relevant proteases, enabling ultrasound molecular imaging of proteolytic activity.

## Methods

PFB-filled microbubbles with shells consisting of DSPC and DSPE-PAA (poly acrylic acid) were prepared via amalgamation. Crosslinking of the microbubble shell with different concentrations of amine-terminated PEG crosslinkers was achieved via carbodiimide-mediated amidation (Figure 1a). After the reaction, microbubble size distribution and concentration were assessed using a Multisizer 4e (Beckman Coulter). Ultrasound imaging was performed in contrast mode on a LOGIQ E10 (GE Healthcare) clinical ultrasound scanner using a ML6-15 MHz probe (GE Healthcare). Acoustic characterization between 0.5 and 25 MHz was performed using a customized ultrasound attenuation measurement setup. For mechanical characterization, optical density of microbubble suspensions at 600 nm was measured as a function of increasing hydrostatic pressure. The pressure at which the optical density decreased to 50 % of the initial value was defined as  $p_{50\%}$ .

Responsive crosslinkers were synthesized and incorporated two terminal photocleavable units in the case of the UV-responsive crosslinker and a peptide with PEGylated termini in the case of the protease-responsive crosslinker. Stimulus exposure of the microbubbles was performed within the acoustic characterization chamber. For cleavage of the protease-responsive crosslinker, proteinase K was used because it exhibits broad substrate specificity. “Acoustic response” as a function of time was defined as the change in ultrasound signal intensity compared to the value before exposure to the stimulus and was normalized to the change observed at the maximum stimulus intensity. Measurements were performed at either the second or fourth harmonic of the microbubble resonance frequency.

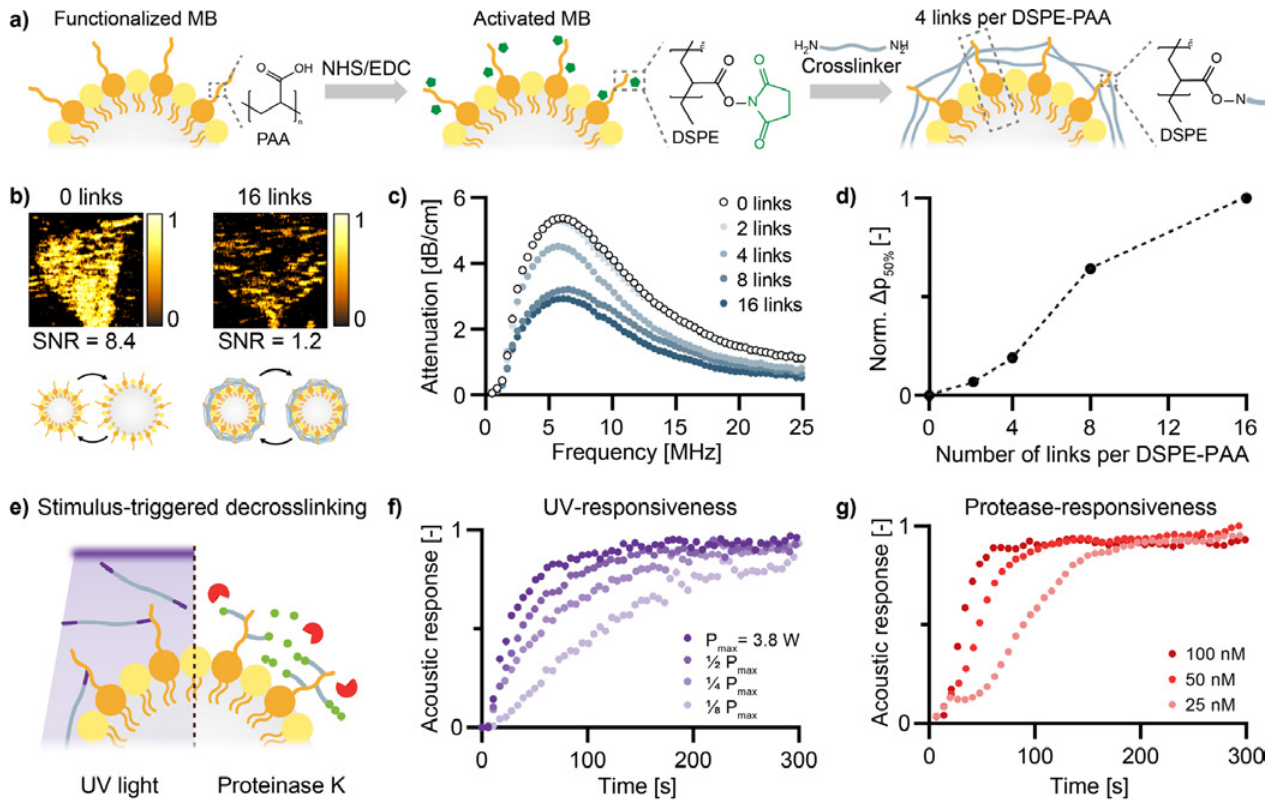


**Figure 1. Principle of microbubble shell crosslinking and stimulus-triggered decrosslinking.** (a) Schematic illustration of chemical crosslinking of the microbubble shell with amine-terminated crosslinkers via carbodiimide-mediated amidation (b) Contrast mode ultrasound images of control (0 links per DSPE-PAA lipid) and crosslinked (16 links per DSPE-PAA lipid) microbubbles (c) Attenuation spectra of microbubbles with different concentrations of crosslinker (d) Normalized change in  $p_{50\%}$  between crosslinked and non-crosslinked microbubbles (e) Schematic illustration of stimulus-triggered decrosslinking with UV light and proteinase K (f) Acoustic response of UV-responsive microbubbles crosslinked with 16 links per DSPE-PAA to UV light with different radiant powers (g) Acoustic response of protease-responsive microbubbles crosslinked with 16 links per DSPE-PAA to proteinase K at different concentrations.

## Results

Ultrasound imaging of control (0 links per DSPE-PAA lipid) and crosslinked (16 links per per DSPE-PAA lipid) microbubbles shows a 7-fold decrease in signal to noise ratio at the same microbubble concentration, indicating decreased echogenicity of crosslinked microbubbles (Figure 1b). Attenuation measurements of microbubbles crosslinked with different concentrations of the non-responsive crosslinker show a decrease in maximum attenuation for increasing number of links per DSPE-PAA (Figure 1c). Similarly, pressurized optical density measurements revealed increasing mechanical stability under hydrostatic pressure as a function of crosslinker concentration (Figure 1d). These results suggest that shell crosslinking affects the volumetric oscillations of microbubbles and that this effect is dependent on the crosslinker concentration. Such trends can be anticipated by the interconnected network of DSPE-PAA lipids that is formed on the microbubble shell.

Stimulus-triggered decrosslinking of the microbubble shell was initiated either via exposure to UV light or via addition of proteinase K (Figure 1e). Exposure of UV-responsive microbubbles to UV light of different radiant powers indicates a clear kinetic dependence of the response rate on stimulus intensity (Figure 1f). Protease-responsiveness to proteinase K, which is capable of cleaving the peptide at multiple sites, showed a clear dependence of the acoustic response on proteinase K concentration (Figure 1g). These results indicate that the observed acoustic response results from cleavage of the peptide crosslinker by proteinase K at nM concentrations.

### Conclusions

Restricting volumetric oscillations of microbubbles through shell crosslinking affects their acoustic and mechanical properties and is dependent on the crosslinker concentration. By incorporating labile units into crosslinkers, we demonstrated cleavage-based detection of UV light and the proteolytic activity of proteinase K. Studying systems responsive to a convenient model stimulus such as UV light can facilitate initial screening of various crosslinking conditions and ultimately inform the design of more sophisticated crosslinking strategies. Similarly, studying response to a protease with broad specificity such as proteinase K offers an ideal testbed to assess the response characteristics of future systems tailored to disease specific proteases. Ultimately, responsive microbubbles could be used as UCAs or in *ex vivo* diagnostic platforms to allow real-time sensing of proteolytic activity at the point-of-care.

### References

- [1]. S. A. Langeveld, B. Meijlink, K. Kooiman, *Curr. Opin. Chem. Biol.* 2021, 63, 171.
- [2]. M. Vizovišek, R. Vidmar, M. Drag, M. Fonović, G. S. Salvesen, B. Turk, *Trends in biochemical sciences* 2018, 43, 829.
- [3]. M. W. Burns, R. F. Mattrey, J. Lux, *ACS Appl. Mater. Interfaces* 2020, 12, 52298.

## Ultrasound molecular imaging using an anti-P-selectin aptamer for imaging bowel inflammation.

*Una Goncin<sup>1</sup>, Ron Geyer<sup>2</sup>, Steven Machtaler<sup>1</sup>*

*<sup>1</sup>Department of Medical Imaging, <sup>2</sup>Department of Pathology and Laboratory Medicine, University of Saskatchewan, Saskatoon, Saskatchewan, Canada  
Corresponding author: ung039@usask.ca*

### Introduction

Aptamers are single-stranded oligonucleotides (20-60 nucleotides) that bind with high affinity and specificity to targets ranging from inorganic molecules to large protein complexes [1]. They have several advantages over protein antibodies including cost, easy and rapid to synthesize, non-immunogenic, non-toxic and have been clinically translated. Despite seeming like the ideal targeted agent for molecular imaging, there are two important limitations to their use: 1) they are quickly degraded by nucleases and 2) rapidly filtrated via the kidneys due to their size. Those limitations can be overcome by coupling aptamers to microbubbles (MBs) for ultrasound molecular imaging. Our goal is to combine the strengths of aptamers and MBs to create a targeted MB to P-selectin, a validated vascular inflammatory marker [2,3], and use it to image inflammation in murine models of inflammatory bowel disease.

### Methods

Lipids were prepared at a molar ratio of 85:10:5 of DSPC, DSPE-PEG2K, and DSPE-PEG2K-DBCO (2 mg/ml). Perfluorobutane-purged vials were used to activate MBs via agitation with a VIALMIX for 45 sec. Size and concentration was measured by electrozone sensing (Multisizer 4e). After activation, MBs were concentrated and incubated in warm nuclease-free PBS with a fluorescent P-selectin aptamer (Fluor-P-Ap) (5'-azide-P-Ap-3'-Cy3; 10  $\mu$ l 100  $\mu$ M) or no aptamer for 20 min at 37°C (Fig. 1A) Confocal microscopy was used to confirm successful labelling of the fluorescent aptamer to the MB shell. Acute colitis was chemically induced using 2,4,6-trinitrobenzenesulfonic acid (TNBS) in 5 of 10 Balb/C mice and 6 transgenic IL-10 KO mice [4]. All remaining mice were administered with saline. All mice were imaged using non-linear contrast mode on a preclinical US system (Vevo3100) following i.v. bolus of  $1 \times 10^8$  MBs. Each mouse received a bolus injection of non-targeted (unlabelled DBCO-functionalized) MBs and P-selectin targeted (Fluor-P-Ap) MBs. Images were analyzed using VEVOQC. Following imaging, bowels were excised for histology and immunostaining.

### Results

The successful labeling of MBs with Fluor-P-Ap was verified with confocal microscopy (Fig. 1B). *Balb/C*: There was a significant increase in targeted US signal using P-selectin targeted MBs ( $3.82 \pm 2.08$  a.u.) in comparison to non-targeted MBs ( $1.21 \pm 0.21$  a.u.) in mice with acute colitis ( $p < 0.05$ ,  $n=5$ ). There was a significant difference between control and acute colitis mice with both non-targeted MBs ( $p < 0.01$ ) and P-selectin targeted MBs ( $p < 0.05$ ; Fig. 1C). *IL-10 KO*: There was a significant increase in targeted US signal using P-selectin targeted MBs ( $2.09 \pm 1.02$  a.u.) in comparison to non-targeted MBs ( $0.56 \pm 0.86$  a.u.;  $p < 0.05$ ; Fig. 1C). We validated the acute inflammatory phenotype in TNBS-induced Balb/C and IL-10 mice.

### Conclusions

We constructed a targeted MB to P-selectin using an aptamer, which generated a detectable ultrasound molecular imaging signal in mice with chemically-induced acute colitis. This approach for constructing quick, cost-efficient targeted MBs may represent a new generation of ultrasound molecular imaging contrast agents that can be clinically translated.

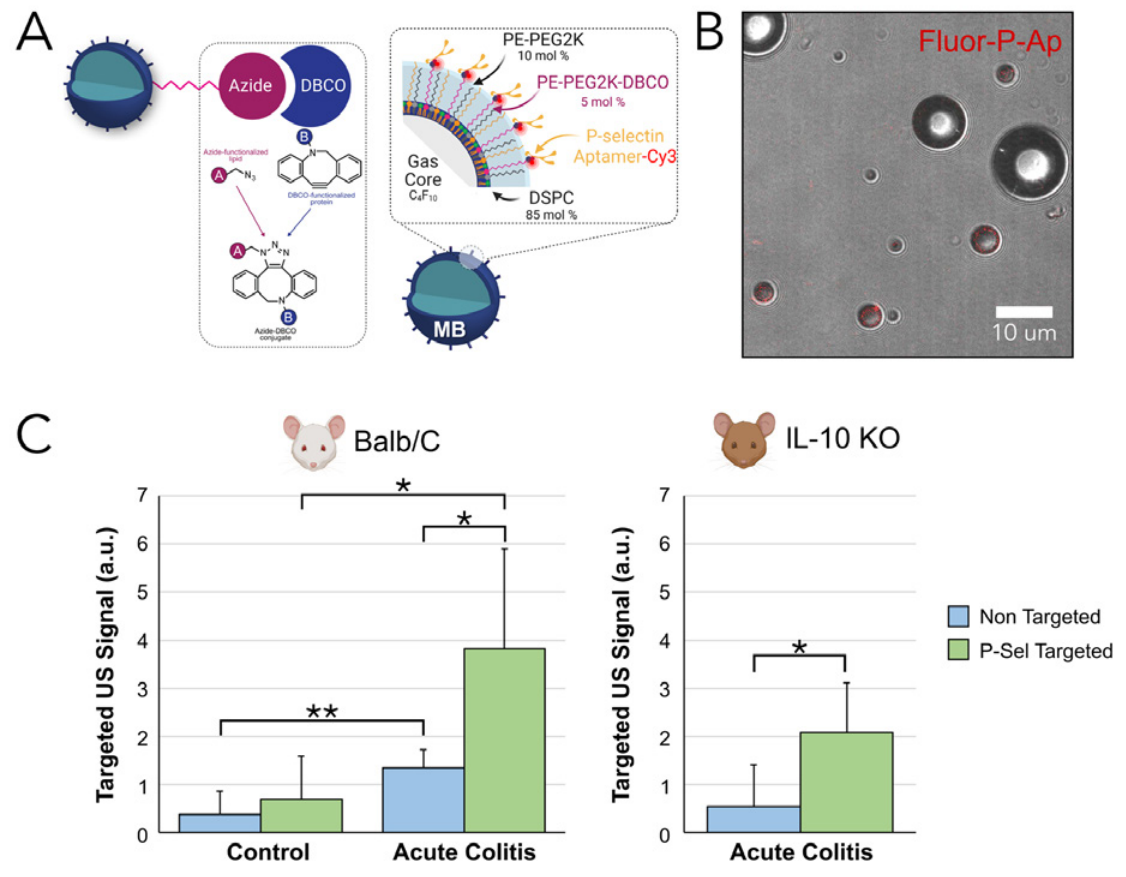


**Figure 1. Ultrasound molecular imaging using a fluorescent anti P-selectin aptamer for imaging inflammation in murine models of acute colitis.** A) Schematic of perfluorobutane(C<sub>4</sub>F<sub>10</sub>)-filled, lipid-shelled MBs with a fluorescent P-selectin aptamer (5'-azide-P-Ap-3'-Cy3) using a copper-free click chemistry approach. B) Fluorescent visualization of MBs successfully labelled with fluorescent P-selectin aptamer (Fluor-P-Ap; red). C) Bar graph summarized mean ± standard deviations of the targeted US signal (a.u.) using non-targeted MBs (blue) and P-selectin targeted MBs (green) in control and acute colitis induced Balb/C (left) and IL-10 KO mice (right; where \* p < 0.05, \*\* p < 0.01).

## References

- [1]. Lakhin, A. V., V. Z. Tarantul & L. V. Gening (2013) Aptamers: problems, solutions and prospects. *Acta naturae*, 5, 34-43.
- [2]. Deshpande, N., A. M. Lutz, Y. Ren, K. Foygel, L. Tian, M. Schneider, R. Pai, P. J. Pasricha & J. K. Willmann (2012) Quantification and monitoring of inflammation in murine inflammatory bowel disease with targeted contrast-enhanced US. *Radiology*, 262, 172-80.
- [3]. El Kaffas, A., K. Smith, P. Pradhan, S. Machtaler, H. Wang, R. von Eyben, J. K. Willmann & D. Hristov (2017) Molecular Contrast-Enhanced Ultrasound Imaging of Radiation-Induced P-Selectin Expression in Healthy Mice Colon. *Int J Radiat Oncol Biol Phys*, 97, 581-585.
- [4]. Wirtz, S., Neufert, C., Weigmann, B. & Neurath, M. F. Chemically induced mouse models of intestinal inflammation. *Nat Protoc* 2, 541-546, doi:10.1038/nprot.2007.41 (2007).

## Fibrin-Targeted Phase Shift Microbubbles Outperformed Fibrin-Targeted Microbubbles in Microvascular Obstruction Treatment

*Soheb Anwar Mohammed<sup>1</sup>, Muhammad Wahab Amjad<sup>1</sup>, Xucai Chen<sup>1</sup>, Maria F. Acosta<sup>2</sup>, Dillon Hanrahan<sup>2</sup>, Evan C. Unger<sup>2</sup>, Emmanuelle J. Meuliet<sup>2</sup>, John J. Pacella\*<sup>1</sup>*

<sup>1</sup>Center for Ultrasound Molecular Imaging and Therapeutics, Heart and Vascular Medicine Institute, University of Pittsburgh, 200 Lothrop St, Pittsburgh, PA.

<sup>2</sup>Microvascular Therapeutics, LLC, 1635 E. 18<sup>th</sup> Street, Tucson, Az.

[pacellajj@upmc.edu](mailto:pacellajj@upmc.edu)

### Introduction:

Cardiovascular disease is the leading cause of morbidity and mortality in the United States [1]. More than 1 million Americans are estimated to have a new or recurrent acute myocardial infarction (AMI) each year [2]. Although the mortality from AMI has decreased in recent years, post-MI congestive heart failure is increasing due to microvascular obstruction (MVO), ultimately limiting myocardial salvage [3]. It has been estimated that up to 60% of all acute ST-elevated myocardial infarction (STEMI) patients receiving the percutaneous coronary intervention (PCI) develop MVO, with subsequent decreased left ventricular (LV) systolic function and major adverse cardiac events including cardiac death, stroke, myocardial infarction, and heart failure requiring hospitalization [4–6]. Conventional strategies for treating MVO include administration of vasodilators, antiplatelet therapy, thrombus aspiration, embolic protection devices, and even hyperoxemic intracoronary reperfusion therapy [7]. Even with the strategies mentioned above, no definitive therapeutic consensus for MVO exists, and many clinical trials have yielded conflicting results [5,8,9]. Therefore, we aim to address an urgent unmet need by devising an image-guided acute therapy, termed ‘sonoreperfusion’ (SRP), that resolves MVO by ultrasound-targeted microbubble cavitation (UTMC) [10,11]. To further improve this therapy, currently, we are evaluating safe and stable lipid-based fibrin-targeted phase shift microbubbles (FTPSMB) (Microvascular Therapeutics, Inc) to treat MVO owing to their smaller size and more efficient microthrombi penetration, compared to standard fibrin targeted microbubbles (FTMBs) (~200 nm vs. 3 µm).

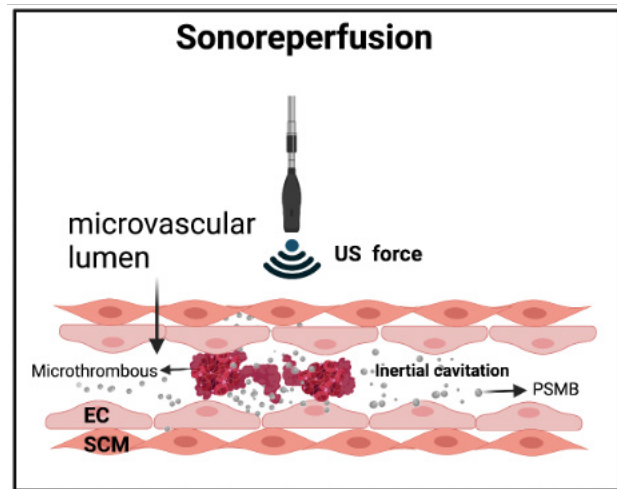


Figure 1: Depicts ultrasound-targeted phase shift microbubbles cavitation in the obstructed microvessels.

### Methods:

MVO of the rat ( $n=6$ ) hindlimb was created by directly injecting freshly prepared porcine microthrombi into the left femoral artery under contrast-enhanced ultrasound imaging (CEUS) guidance. DEFINITY<sup>®</sup> MBs (Lantheus Medical Imaging) were infused (2 ml/hr) through the right external jugular vein for CEUS. Following a stable ten min. of MVO, a therapeutic transducer (1 MHz, 1.5 MPa, 5 ms pulse duration, 5-sec pulse interval) was positioned vertically above the hindlimb for therapeutic US pulses during concomitant administration of fibrin-targeted MBs/PSMBs (3 ml/hr). CEUS cine loops with burst replenishment were obtained by imaging transducer (7 MHz CPS, Imaging MI 0.2, 200 ms frame interval, burst MI 1.9) at baseline (BL), 10 min post-MVO, and after each of the two SRP treatment sessions (TX1, TX2) and analyzed (MATLAB\_R2021a).

**Results:**

We successfully created MVO in both groups. FTPSMB treatment resulted in a greater increase in the blood volume (dB) and flow rate (dB/sec) when compared with FTMB (Figure 2) after each 10-minute treatment session.

**Conclusions:**

US-guided FTPSMB cavitation causes more rapid and complete reperfusion of rat hindlimb following MVO compared to FTMB, likely owing to their small size and more effective thrombus penetration. Studies to explore the underlying molecular mechanisms associated with sonoreperfusion treatments are underway.

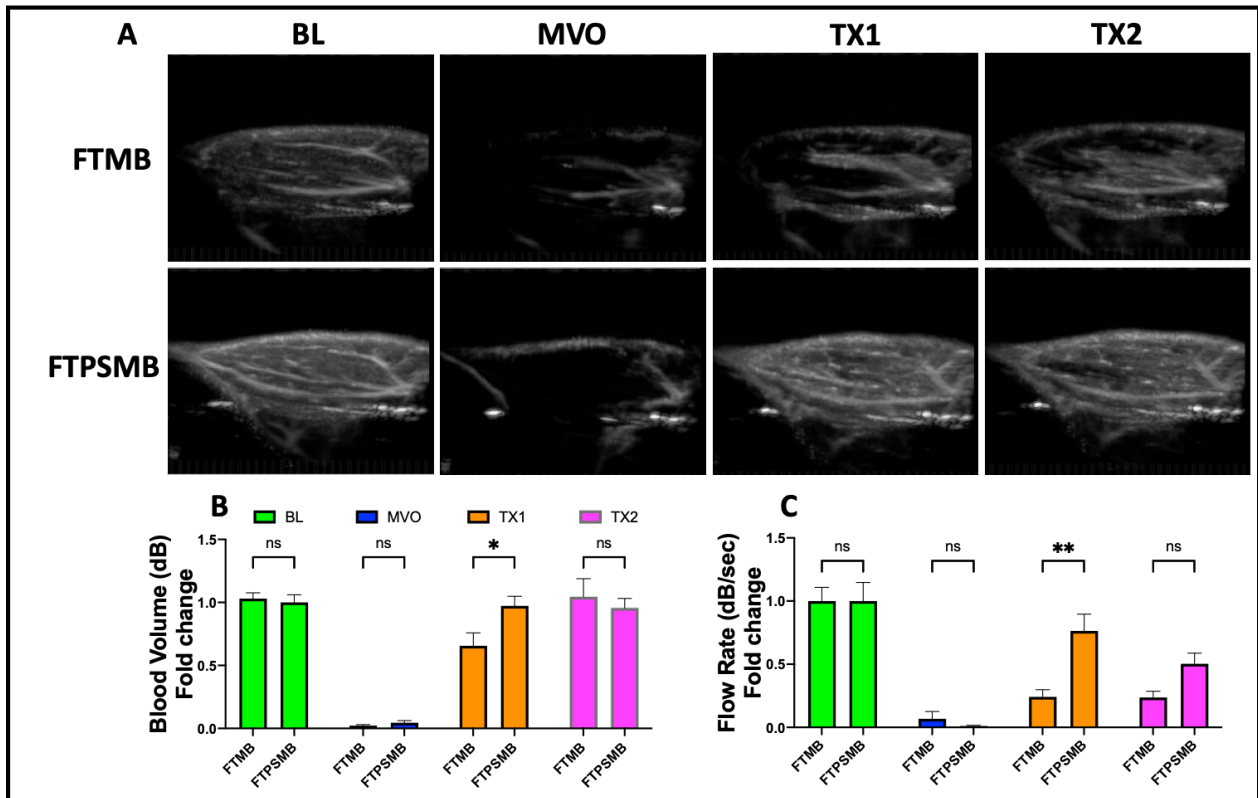


**Figure 3:** Fibrin-targeted Phase shift microbubbles (FTPSMBs) rescued microvascular obstruction. [A] contrast-enhanced ultrasound images of rat hindlimb. [B] peak plateau video intensity which reflects vascular cross-sectional area. [C] flow rate. Data expressed as mean ± standard error (n=6). \*p < 0.05, \*\*p < 0.001.

**References**

[1] S.S. Virani, A. Alonso, H.J. Aparicio, E.J. Benjamin, M.S. Bittencourt, C.W. Callaway, A.P. Carson, A.M. Chamberlain, S. Cheng, F.N. Delling, M.S.V. Elkind, K.R. Evenson, J.F. Ferguson, D.K. Gupta, S.S. Khan, B.M. Kissela, K.L. Knutson, C.D. Lee, T.T. Lewis, J. Liu, M.S. Loop, P.L. Lutsey, J. Ma, J. Mackey, S.S. Martin, D.B. Matchar, M.E. Mussolino, S.D. Navaneethan, A.M. Perak, G.A. Roth, Z. Samad, G.M. Satou, E.B. Schroeder, S.H. Shah, C.M. Shay, A. Stokes, L.B. VanWagner, N.-Y. Wang, C.W. Tsao, American Heart Association Council on Epidemiology and Prevention Statistics Committee and Stroke Statistics Subcommittee, Heart Disease and Stroke Statistics-2021 Update: A Report From the American Heart Association, *Circulation*. 143 (2021) e254–e743. <https://doi.org/10.1161/CIR.0000000000000950>.

[2] E.J. Benjamin, P. Muntner, A. Alonso, M.S. Bittencourt, C.W. Callaway, A.P. Carson, A.M. Chamberlain, A.R. Chang, S. Cheng, S.R. Das, F.N. Delling, L. Djousse, M.S.V. Elkind, J.F. Ferguson, M. Fornage, L.C. Jordan, S.S. Khan, B.M. Kissela, K.L. Knutson, T.W. Kwan, D.T. Lackland, T.T. Lewis, J.H. Lichtman, C.T.

Longenecker, M.S. Loop, P.L. Lutsey, S.S. Martin, K. Matsushita, A.E. Moran, M.E. Mussolino, M. O’Flaherty, A. Pandey, A.M. Perak, W.D. Rosamond, G.A. Roth, U.K.A. Sampson, G.M. Satou, E.B. Schroeder, S.H. Shah, N.L. Spartano, A. Stokes, D.L. Tirschwell, C.W. Tsao, M.P. Turakhia, L.B. VanWagner, J.T. Wilkins, S.S. Wong, S.S. Virani, American Heart Association Council on Epidemiology and Prevention Statistics Committee and Stroke Statistics Subcommittee, Heart Disease and Stroke Statistics-2019 Update: A Report From the American Heart Association, *Circulation*. 139 (2019) e56–e528. <https://doi.org/10.1161/CIR.0000000000000659>.

- [3] B. Ibáñez, G. Heusch, M. Ovize, F. Van de Werf, Evolving therapies for myocardial ischemia/reperfusion injury, *J. Am. Coll. Cardiol.* 65 (2015) 1454–1471. <https://doi.org/10.1016/j.jacc.2015.02.032>.
- [4] A. Galli, F. Lombardi, Postinfarct Left Ventricular Remodelling: A Prevailing Cause of Heart Failure, *Cardiol. Res. Pract.* 2016 (2016) 2579832. <https://doi.org/10.1155/2016/2579832>.
- [5] J. Mazhar, M. Mashicharan, A. Farshid, Predictors and outcome of no-reflow post primary percutaneous coronary intervention for ST elevation myocardial infarction, *Int. J. Cardiol. Heart Vasc.* 10 (2016) 8–12. <https://doi.org/10.1016/j.ijcha.2015.11.002>.
- [6] C. Bouleti, N. Mewton, S. Germain, The no-reflow phenomenon: State of the art, *Arch. Cardiovasc. Dis.* 108 (2015) 661–674. <https://doi.org/10.1016/j.acvd.2015.09.006>.
- [7] S.H. Rezkalla, R.V. Stankowski, J. Hanna, R.A. Kloner, Management of No-Reflow Phenomenon in the Catheterization Laboratory, *JACC Cardiovasc. Interv.* 10 (2017) 215–223. <https://doi.org/10.1016/j.jcin.2016.11.059>.
- [8] R. Jaffe, A. Dick, B.H. Strauss, Prevention and treatment of microvascular obstruction-related myocardial injury and coronary no-reflow following percutaneous coronary intervention: a systematic approach, *JACC Cardiovasc. Interv.* 3 (2010) 695–704. <https://doi.org/10.1016/j.jcin.2010.05.004>.
- [9] G. Niccoli, F. Burzotta, L. Galiuto, F. Crea, Myocardial no-reflow in humans, *J. Am. Coll. Cardiol.* 54 (2009) 281–292. <https://doi.org/10.1016/j.jacc.2009.03.054>.
- [10] F.T.H. Yu, X. Chen, A.C. Straub, J.J. Pacella, The Role of Nitric Oxide during Sonoreperfusion of Microvascular Obstruction, *Theranostics*. 7 (2017) 3527–3538. <https://doi.org/10.7150/thno.19422>.
- [11] J.J. Pacella, J. Brands, F.G. Schnatz, J.J. Black, X. Chen, F.S. Villanueva, Treatment of microvascular micro-embolization using microbubbles and long-tone-burst ultrasound: an in vivo study, *Ultrasound Med. Biol.* 41 (2015) 456–464. <https://doi.org/10.1016/j.ultrasmedbio.2014.09.033>.

## ***In vivo* Pharmacokinetics of Microbubble Volume Dose: A Direct Blood Characterization Study**

***J. Angel Navarro-Becerra<sup>1</sup>, Kang-Ho Song<sup>1</sup>, Payton Martinez<sup>2</sup>, and Mark Borden<sup>1,2</sup>***

<sup>1</sup>*Mechanical Engineering Department, University of Colorado Boulder, Boulder, CO, USA*

<sup>2</sup>*Biomedical Engineering Department, University of Colorado Boulder, Boulder, CO, USA*

*Corresponding author: mark.borden@colorado.edu*

### **Introduction**

Successful translation of microbubbles (MBs) as a drug delivery system into clinical applications depends on the complete understanding of the *in vivo* biological effects and pharmacokinetics behavior. Variations in MB compositions, injection dose, and size distributions result in different acoustic responses [1] and variability in permeability effects [2], making it extremely difficult to standardize conventional metrics to report the parameters used and compare the observed bioeffects. Microbubble volume dose (MVD) represents a promising unifying dose metric that captures the MB size and concentration into MB gas volume to obtain consistent and comparable permeability effects [2,3]. To establish MVD as a metric, optimization, and better understanding of the *in vivo* pharmacokinetics characteristics play a key role. *In vivo* studies have measured the pharmacokinetics of MBs using indirect methods, including ultrasound contrast images [3,4] and gas chromatography [5,6]. However, these methods have limitations related to the sensitivity in the MB detection and gas content, making it difficult to characterize the complete MB pharmacokinetics. Therefore, to overcome these limitations and offer a broad characterization of the MVD pharmacokinetics profiles, the goal of this work was to demonstrate for the first time the feasibility of measuring the *in vivo* pharmacokinetics of size selected MBs at different MVDs directly in the blood.

### **Methods**

Size-selected microbubbles (2-, 3- and 5-  $\mu\text{m}$  diameter, DSPC/PEG40S/PFB gas) were made. The gas volume fraction ( $\phi_{\text{MB}}$ ) was calculated by plotting MB concentration vs. MB volume and integrating the area under the curve. For *in vivo* pharmacokinetic studies, three Sprague – Dawley rats (280-470 g) per MVD were injected with a 5-,10-,20-, and 40- MVD of each MB size via the jugular vein. 100  $\mu\text{L}$  of blood was then withdrawn from 1 to 5- and 10-min after injection (Fig. 1A). Blood samples were analyzed using a hemocytometer, and MVD variations as a function of time were determined by image analysis. Pharmacokinetics curves for each size and MVD were used to estimate the MVD absorption (area under the curve, AUC), half-life ( $t_{1/2}$ ), and other relevant pharmacokinetic parameters.

### **Results**

Size-isolated MBs had median volume diameters close to 2-, 3-, and 5  $\mu\text{m}$  (Fig. 1B). The corresponding  $\phi_{\text{MB}}$  was  $78 \pm 17$ ,  $84 \pm 11$ , and  $169 \pm 18$   $\mu\text{L}/\text{mL}$  (Fig. 1C). Intravenous injection for 2- and 3-  $\mu\text{m}$  administered at 5-, 10-, and 20- MVD and for 5  $\mu\text{m}$  at 5- and 10- MVD, MVD decreases exponentially as a function of time following a one-compartment pharmacokinetic model (Fig.1 D-F, solid lines), with typical  $R^2 > 0.94$ . Opposite, for 2- and 3-  $\mu\text{m}$  injected at 40 MVD and 5  $\mu\text{m}$  at 20 MVD, MVD decreased biexponentially over time following a two-compartment pharmacokinetic model (Fig. 1 D-F, dashed lines), with typical  $R^2 > 0.98$ . The fitted curves demonstrate that MBs were eliminated from the circulation in 10 min. Half-life values ( $t_{1/2}$ ) for first-order kinetic models showed slight increases as the MVD increased without significant changes while second-order kinetic models had significant decreases in half-life as MVD increased (Fig. 1G). However, when the MVDs are compared between sizes the half-life is almost the same, with times no longer than 2.5 min. Finally, MVD absorption in the central compartment was dependent on the pharmacokinetics, under the first-order regime MB absorption increased as the MVD increased while for the second-order regime MB absorption decreased (Fig. 1H).

## Conclusions

We present the first direct blood microbubble pharmacokinetic study that enable us to analyze the complete MVD pharmacokinetics profiles and establish thresholds in which MVD changes from first- to second- order. Therefore, we propose this novel technique to directly study and understand the pharmacokinetics of different microbubbles compositions used in clinical and research applications to evaluate in a unified way the possible therapeutic effects.

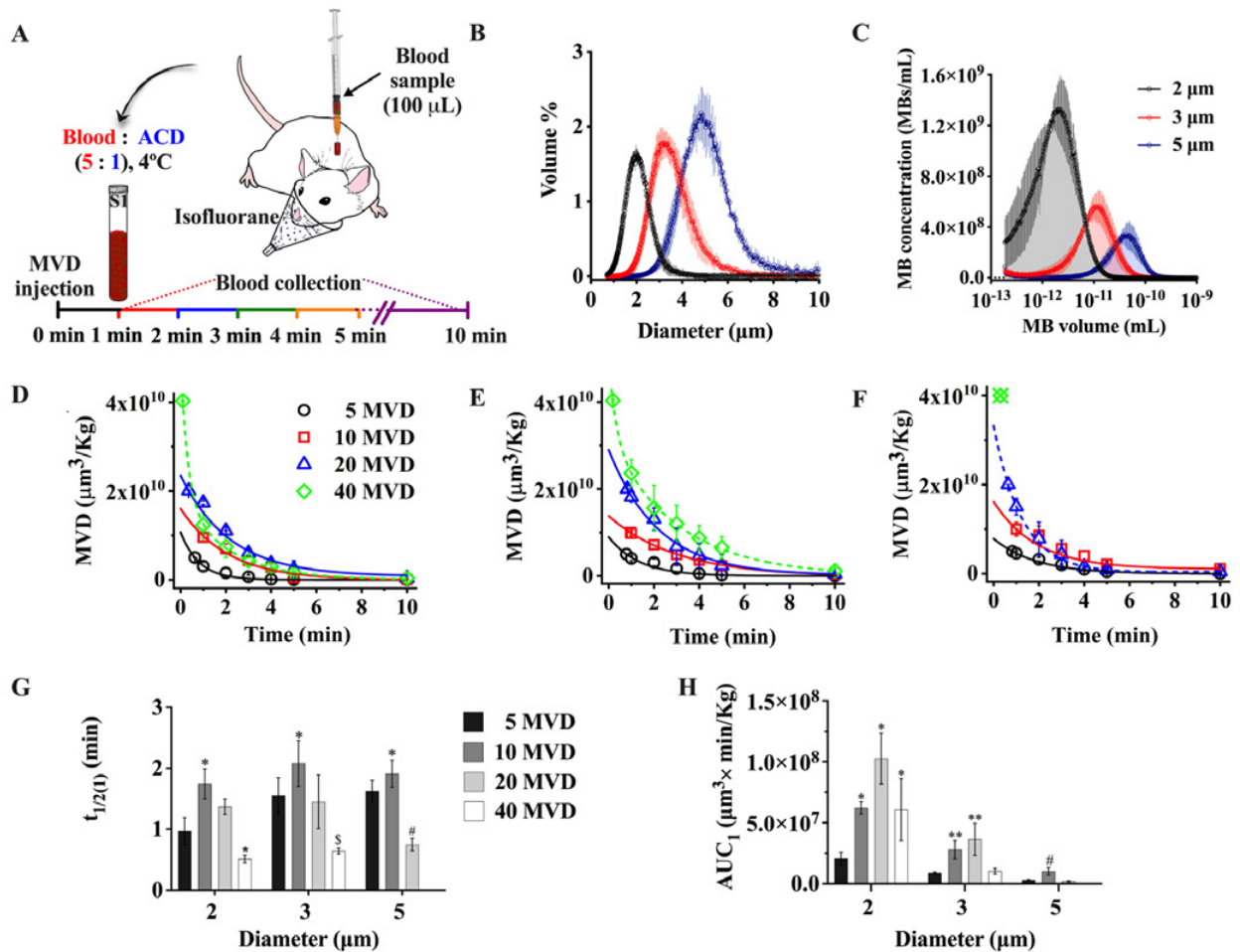


Figure 1. A) Schematic of blood samples collection after microbubble (MB) injection. B) Volume – weighted and microbubble size distributions. C) MB concentration vs. volume, the shadow shows the area under the curve that represents the microbubble gas volume fraction ( $\phi_{\text{MB}}$ ). D-F) *In vivo* pharmacokinetics curves obtained from blood analysis after intravenous injection of 2-, 3-, and 5-  $\mu$ m diameter microbubbles at 5, 10, 20, and 40 MVD. Fitted solid and dashed lines represent the one- and two-compartment pharmacokinetic model ( $R^2 > 0.94$ ). G-H) Half-life ( $t_{1/2}$ ) and MVD absorption as a function of MVD and microbubble diameter. Data represent the mean  $\pm$  standard deviation for three different experiments.

## References

- [1]. Sonne, C., Xie, F., Lof, J., Oberdorfer, J., Phillips, P., Everbach, E. C., & Porter, T. R. (2003). Differences in definity and optison microbubble destruction rates at a similar mechanical index with different real-time perfusion systems. *Journal of the American Society of Echocardiography*, 16(11), 1178-1185.
- [2]. Song, K. H., Fan, A. C., Hinkle, J. J., Newman, J., Borden, M. A., & Harvey, B. K. (2017). Microbubble gas volume: A unifying dose parameter in blood-brain barrier opening by focused ultrasound. *Theranostics*, 7(1), 144.
- [3]. Bing, C., Hong, Y., Hernandez, C., Rich, M., Cheng, B., Munaweera, I., ... & Chopra, R. (2018). Characterization of different bubble formulations for blood-brain barrier opening using a focused ultrasound system with acoustic feedback control. *Scientific reports*, 8(1), 1-12
- [4]. Chen, C. C., Sirsi, S. R., Homma, S., & Borden, M. A. (2012). Effect of surface architecture on in vivo ultrasound contrast persistence of targeted size-selected microbubbles. *Ultrasound in medicine & biology*, 38(3), 492-503.
- [5]. Li, P., Hoppmann, S., Du, P., Li, H., Evans, P. M., Moestue, S. A., ... & Liu, L. (2017). Pharmacokinetics of perfluorobutane after intra-venous bolus injection of Sonazoid in healthy Chinese volunteers. *Ultrasound in medicine & biology*, 43(5), 1031-1039.
- [6]. Morel, D. R., Schwieger, I., Hohn, L., Terretaz, J., LLULL, J. B., CORNIOLEY, Y. A., & Schneider, M. (2000). Human pharmacokinetics and safety evaluation of SonoVue™, a new contrast agent for ultrasound imaging. *Investigative radiology*, 35(1), 80.

## Shell characterization of single microbubbles using a novel stress-strain analysis

Charlotte Nawijn<sup>1</sup>, Sander Spijkhouw<sup>2</sup>, Jason Voorneveld<sup>2</sup>, Hans Bosch<sup>2</sup>,  
Michel Verluis<sup>1</sup>, Tim Segers<sup>3</sup>, and Guillaume Lajoinie<sup>1</sup>

<sup>1</sup>Physics of Fluids Group, Technical Medical (TechMed) Center and MESA+ Institute for Nanotechnology, University of Twente, The Netherlands

<sup>2</sup>Department of Biomedical Engineering, Thorax Center, Erasmus MC University Medical Center, Rotterdam, the Netherlands

<sup>3</sup>BIOS Lab-on-a-Chip group, Max-Planck Center Twente for Complex Fluid Dynamics, MESA+ Institute for Nanotechnology, University of Twente, The Netherlands

Corresponding author: c.l.nawijn@utwente.nl

### Introduction

Microbubbles are of great interest for both ultrasound imaging, where they are used as contrast agents, and in ultrasound therapy, where they are investigated for drug and gene delivery. In both cases, a full characterization of the response of microbubbles to ultrasound driving is crucial to predict and exploit the (nonlinear) features of the bubbles, which strongly depend on the viscoelastic shell parameters [1]. The role of the viscoelastic shell is most pronounced at low driving amplitudes as the lipid shell is typically strain softening [1]. Typically, acoustic attenuation measurements allow characterization at low acoustic pressure amplitudes, however, since these are performed on a microbubble suspension, high-precision characterization is only possible by using monodisperse bubbles [2, 3]. On the other hand, single microbubbles can be characterized using ultra-high-speed optical imaging in combination with microbubble spectroscopy [3], but this can only be done at relatively large oscillation amplitudes, and only with great difficulty for bubbles oscillating in the free-field.

Here we propose a novel method to characterize the viscous and elastic shell properties of single microbubbles using a ramp-up in acoustic pressure in an acoustical camera setup [4, 5]. Considering the stress balance on the bubble wall, the resulting strain, and strain rate allows us to individually measure the elastic and viscous contributions with few assumptions. Not only does this technique allow the investigation of the properties of single bubbles and their distribution in the population, but it also opens new possibilities to unravel the dissipation caused by the shell as a function of strain and strain rate.

### Methods

From the Rayleigh-Plesset equation for a coated bubble it follows that the elastic and viscous pressure contributions (which we call function  $f$ ) are the result of a pressure balance resulting from inertia, thermodynamic behavior of the gas inside the bubble, sound re-radiation, atmospheric pressure, and the incident acoustic pressure [1]:

$$f = P_{elas} + P_{visc} = -\rho_L \left( R \frac{d^2 R}{dt^2} + \frac{3}{2} \frac{dR}{dt} \right) + \left( P_0 + \frac{2\sigma(R_0)}{R_0} \right) \left( \frac{R_0}{R} \right)^{3\kappa} \left( 1 - \frac{3\kappa}{c_L} \frac{dR}{dt} \right) - P_0 - P_{ac},$$

where  $R$  is the bubble radius,  $R_0$  the initial radius,  $\sigma(R)$  the radius-dependent surface tension,  $\rho_L$  the density of the medium,  $\kappa$  the polytropic exponent of the gas,  $c_L$  the speed of sound in the medium,  $P_0$  the atmospheric pressure, and  $P_{ac}$  the incident acoustic pressure. The elastic and viscous contribution are commonly modeled as [1]:

$$f = P_{elas} + P_{visc} = \frac{2\sigma(R)}{R} + \frac{4}{R} \frac{dR}{dt} \left( \mu_L + \frac{\kappa_s}{R} \right),$$

where  $\mu_L$  is the viscosity of the medium and  $\kappa_s$  the shell viscosity. Through non-dimensionalization of the Rayleigh-Plesset equation, the viscous and elastic pressure contributions can be written as a function of the strain  $(R(t) - R_0)/R_0$ , and its time derivatives. The elastic contribution - and thereby the effective surface tension - is independent of the strain rate and can thus be determined from the non-dimensionalized function

$f$  by considering the data where the strain rate is zero. The remainder of the shell contribution is due to the viscosity of the shell and of the medium. Note that this approach does not require any a priori knowledge on the physical description of the viscoelastic shell parameters.

The viscoelastic contribution of the shell of a single microbubble as a function of the radius and bubble wall velocity is determined by slowly increasing the incident acoustic pressure, while measuring radial strain and strain rate, using an ‘acoustical camera’ setup as described in [4, 5], see Fig. 1A. Briefly, this setup consists of a tank filled with a microbubble suspension, in which an ultrasound transducer drives the radial oscillations of the microbubbles at a frequency of 1.5 MHz. The wave is programmed to increase in amplitude from 0 to 25 kPa in a time span of 100  $\mu$ s. Simultaneously, two high-frequency transducers (25 MHz frequency) are used to probe the bubble oscillations: the first transmits ultrasound with an amplitude of 500 kPa for 120  $\mu$ s, starting 10  $\mu$ s before the low-frequency pulse, while the second records the (amplitude modulated) pressure that is geometrically scattered by the bubble. The radial strain time trace is then recovered using amplitude demodulation following [5].

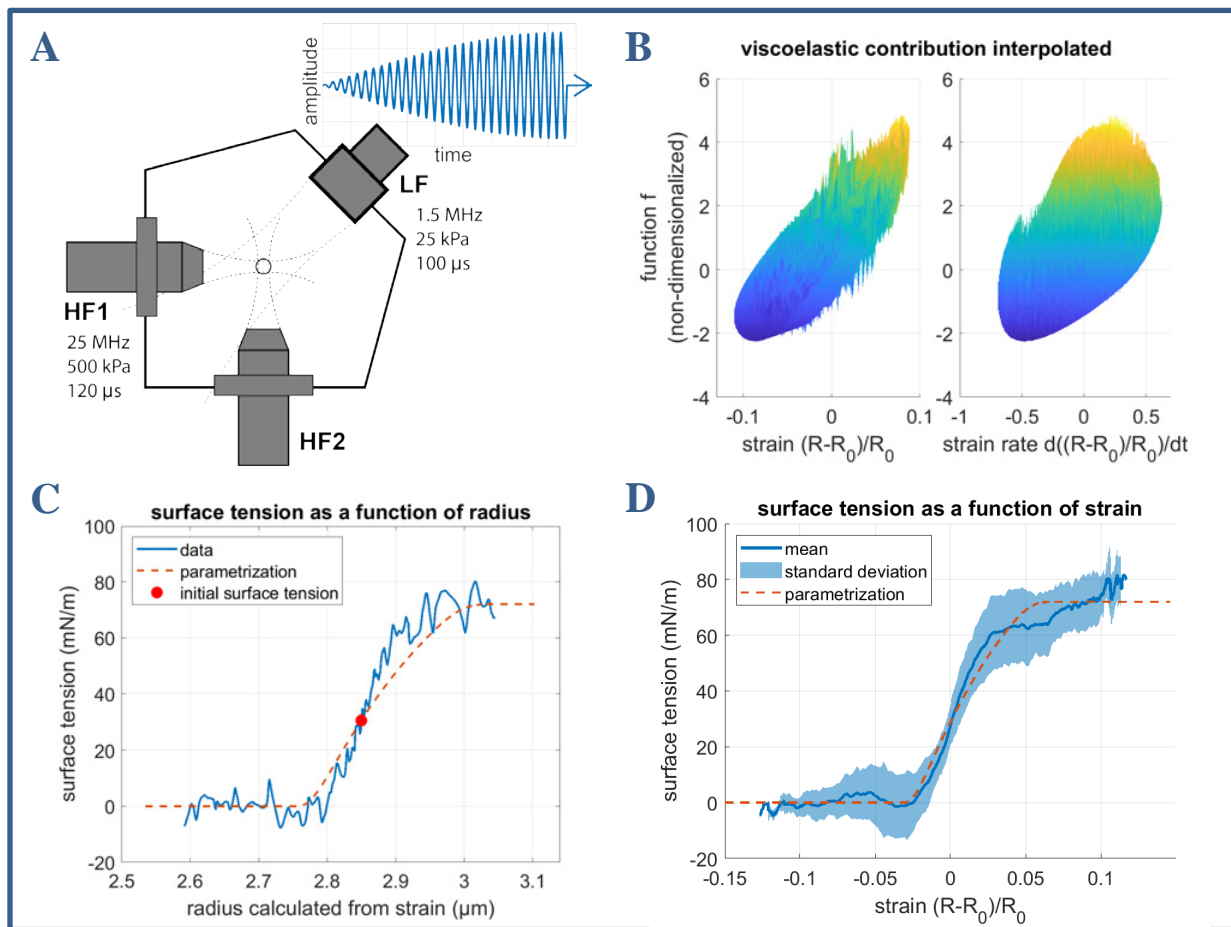


Figure 1. A. Schematic of the acoustical camera setup, with low-frequency (LF) and high-frequency (HF) transducers [5]. B. The viscoelastic pressure contribution of a single microbubble as a function of strain and strain rate. C. The strain-dependent surface tension as determined from the viscoelastic pressure contribution in 1B. The orange dashed line shows a measured surface tension curve of DPPC-based bubbles of the same size [3], and the red dot indicates the initial surface tension as found from error minimization. D. The combined surface tension curves of all bubbles analyzed in this work. The solid blue line indicates the mean, and the shaded region the standard deviation. The orange dashed line again shows the measured surface tension curve [3].

To validate this novel characterization approach, we use lipid-shelled (DSPC mixed with DPPE-PEG5000, 9:1 molar ratio) monodisperse  $C_4F_{10}$ -filled microbubbles, made in-house using a flow-focusing device at 55°C and using a gas mixture of 13 v%  $C_4F_{10}$  in  $CO_2$ , as described in [6, 7]. The bubbles had a

mean radius of 2.8  $\mu\text{m}$ , and a concentration of about 150 bubbles/mL. The surface tension as a function of bubble radius (strain) is recovered by applying an error minimization routine that enforces a zero surface tension when the bubble is fully compressed, and a surface tension equal to that of water when the bubble shell is fully ruptured. From the error minimization we characterize three parameters that significantly influence the bubble response: the initial radius (within the narrow size distribution), the initial surface tension, and the phase of the incident acoustic pressure wave (experimentally unknown).

### Results

The total viscoelastic pressure contribution as a function of the strain and strain rate of a single microbubble is shown in Fig 1B. Starting at a zero strain and near zero strain rate, the hyperplane is travelled in successively larger spirals as the driving pressure increases. A typical extracted surface tension curve for a single bubble is shown Fig. 1C. The orange dashed line depicts the surface tension curve experimentally measured for a monodisperse bubble suspension (DPPC:DPPE-PEG5k, 9:1 molar ratio) with this particular mean size [3]. Good agreement is found between the surface tension resulting from our stress-strain analysis with error minimization, and the curves measured previously on the whole population.

The surface tension curves from 197 bubbles as a function of strain are shown in Fig. 1D, where the mean is indicated by the solid blue line, and the standard deviation by the shaded region. From the waist of the curve at zero strain, it can be concluded that the initial surface tension is comparable for this bubble population. Good agreement is found between the size distributions determined through error minimization ( $R_0 = 2.7 \pm 0.67 \mu\text{m}$ ) and using the Coulter Counter.

### Conclusion

The combined viscoelastic pressure contributions of lipid-shelled microbubbles are determined from the radial strain of single microbubbles recorded by an acoustical camera. The elastic contribution, corresponding to a zero strain rate, provides the surface tension as a function of the bubble radius. The surface tension is found to be in good agreement with prior measurements on a monodisperse bubble population. This stress-strain analysis and error minimization also provides statistics on the size and the initial surface tension of single microbubbles. Future work will investigate the dependence of the viscous contribution of the shell on the strain and strain rate.

### References

- [1]. M. Versluis, E. Stride, G. Lajoinie, B. Dollet, and T. Segers, "Ultrasound Contrast Agent Modeling: A Review", *Ultrasound in Medicine & Biology*, 46.9: 2117-2144, 2020.
- [2]. M. A. Parrales, J. M. Fernandez, M. Perez-Saborid, J. A. Kopechek, and T. M. Porter, "Acoustic characterization of monodisperse lipid-coated microbubbles: Relationship between size and shell viscoelastic properties", *The Journal of the Acoustical Society of America*, 136.3: 1077-1084, 2014.
- [3]. T. Segers, E. Gaud, M. Versluis, and P. Frinking, "High-precision acoustic measurements of the nonlinear dilatational elasticity of phospholipid coated monodisperse microbubbles", *Soft Matter*, 14.47: 9550-9561, 2018.
- [4]. G. Renaud, J. G. Bosch, A. F. W. Van Der Steen, and N. De Jong, "Low-Amplitude Non-linear Volume Vibrations of Single Microbubbles Measured with an 'Acoustical Camera'", *Ultrasound in Medicine & Biology*, 40.6: 1282-1295, 2014.
- [5]. S. Spiekhout et al., "Observations of monodisperse microbubble resonance by an 'Acoustical Camera'", presented at the 26th European Symposium on Ultrasound Contrast Imaging, 2021.
- [6]. T. Segers, A. Lassus, P. Bussat, E. Gaud, and P. Frinking, "Improved coalescence stability of monodisperse phospholipid-coated microbubbles formed by flow-focusing at elevated temperatures," *Lab on a Chip*, 19.1: 158-167, 2019.
- [7]. T. Segers, E. Gaud, G. Casqueiro, A. Lassus, M. Versluis, and P. Frinking, "Foam-free monodisperse lipid-coated ultrasound contrast agent synthesis by flow-focusing through multi-gas-component microbubble stabilization", *Applied Physics Letters*, 116.17: 173701, 2020.

## First *in-vivo* metabolomics characterization of acoustically-mediated blood-brain barrier opening

Antoine Preetet<sup>1</sup>, Sylvie Bodard<sup>1</sup>, Antoine Lefèvre<sup>1,2</sup>, Anaïs Millet<sup>1</sup>, Edward Oujagir<sup>1</sup>, Camille Dupuy<sup>1</sup>, Tarik Iazourène<sup>1</sup>, Ayache Bouakaz<sup>1</sup>, Patrick Emond<sup>1,2</sup>, Jean-Michel Escoffre<sup>1\*</sup>, Lydie Nadal-Desbarats<sup>1,2\*</sup>

<sup>1</sup>UMR 1253, iBrain, Université de Tours, Inserm, Tours, France

<sup>2</sup>Département Analyses Chimique et Métabolomique, PST Analyse des Systèmes Biologiques, Université de Tours, Tours, France

Corresponding author: antoine.preetet@univ-tours.fr

### Introduction

Microbubble-assisted ultrasound has emerged as a promising method for the intracerebral delivery of drugs (1). Microbubbles (MB) are intravenously injected and locally activated by ultrasound (US), thus increasing the permeability of blood-brain barrier (BBB) for facilitating extravasation and drug uptake into the brain tissue. The safety of this method has been investigated using complementary analytical strategies including transcriptomics, histology, brain imaging, and behavioral tests (2-16). The present study aimed to investigate for the first time the *in-vivo* metabolic consequences of acoustically-mediated BBB opening (BBBO). To achieve this goal, a longitudinal study of these metabolic consequences on brain tissue, cerebrospinal fluid (CSF), serum, and urine metabolomes was performed using NMR spectroscopy (<sup>1</sup>H NMR) and high-performance liquid chromatography coupled with mass spectrometry (HPLC-MS).

### Methods

After intravenous injection of MB (100 µL at 10<sup>8</sup> MB/mL; Visualsonics Fujifilm), rats' right striata were exposed to ultrasound (1 MHz, 10 ms BL, 0.6 MPa PNP, 30 s) to open its BBB. Brain, cerebrospinal fluid (CSF), serum and urine were collected from control group (w/o US treatment) and three other rat groups sacrificed 3 hrs, 48 hrs, 1 week after the MB-assisted US. A well-established analytic routines using <sup>1</sup>H-NMR and non-targeted and targeted HPLC-MS spectrometries were performed to assess the metabolites levels and quantify tryptophan derivatives implied into inflammatory and neurotransmission processes on control and sonicated matrices (17). Significant metabolites identified by univariate analyses depending on the temporality comparisons were used to perform pathway analyses using hypergeometric test with false discovery rate (FDR) p-value adjustment, based on definitions of KEGG database (Kyoto Encyclopedia of Genes and Genomes). Further, multivariate data analyses were achieved using unsupervised principal component analysis (PCA) to determine potential outliers and global metabolic profiles and supervised partial least square discriminant analysis (PLS-DA) was used to establish models between two-time groups.

### Results

For the first time, we explored the metabolomic consequences of MB-assisted US in several biological compartments. Cerebral, peri-cerebral and peripheral metabolomes depict specific and sequential kinetics after acoustically-mediated BBBO. As expected, metabolic perturbations observed in the serum metabolome were significantly more important than in CSF, striatum and urine metabolomes. The CSF metabolome returned to the basal level more quickly than serum metabolome. There is no longer any metabolic disturbance in CSF 3-hrs after BBBO in comparison with the serum metabolome, which showed metabolic perturbations up to 1-week post-BBBO. In contrast, metabolic disturbances within the striatum metabolome were greatest at 2-days after BBBO and persisted for up to 1 week, as well as urine metabolome showed metabolic perturbations up to 1-week after the BBBO procedure. In addition, pathway analyses on cerebral and peripheral metabolomes reveal several metabolic dysregulations over the time. Our data revealed that arginine, proline, alanine, aspartate and glutamate metabolisms are mainly and significantly disrupted in all

matrices. In addition, nucleotides metabolisms involved into genetic processes (*i.e.*, DNA replication, RNA transcription) are also observed in CSF and serum metabolomes.

Some metabolic pathways (*i.e.*, arginine and glutamate metabolism) involved into bioenergetic metabolism were disturbed in the serum and CSF metabolomes immediately after the BBBO, but also in the brain metabolome, 1-week later. Alanine, aspartate, asparagine, glutamate and glutamine are input metabolites for arginine-associated metabolic processes (*i.e.*, urea cycle, tricarboxylic acid cycle, nitrogen metabolism). The arginine plays a key role in the energetic cell supply and in the homeostasis maintenance by regulating the nitrogen levels and immune processes. Thus, the dysregulation of arginine-associated seems to constitute the first metabolomic characterization of MB-mediated BBBO.

We also investigated tryptophan derivate dosage, that reveals some minor changes upon serotonergic neurotransmission and inflammation, especially in striatum, in CSF and in serum metabolomes. These investigations showed a dysregulation of the sub-pathway related to the inflammation in the serum metabolome (kynurine pathway) and other ones in the CSF and striatum metabolomes related to the neurotransmission (degradation of serotonin).

### Conclusions

In conclusion, multimodal and multimatrix metabolomic approaches provided the first metabolic signature related to the acoustically-mediated BBBO within the striatum and its surrounding biological compartments. Stronger metabolic response to the BBBO was observed in vascular compartment with in particular the presence of a vascular inflammation. The acoustically-mediated BBBO in the striatum disturbed the serotonergic neurotransmission. Nevertheless, further investigations are still required to explore the influence of US and MB-related parameters on brain metabolism and neurological processes including neuroinflammation and neurotransmission.

### References

- [1]. A. Presset *et al.*, Endothelial Cells, First Target of Drug Delivery Using Microbubble-Assisted Ultrasound. *Ultrasound Med Biol* 46, 1565-1583 (2020).
- [2]. Z. I. Kovacs *et al.*, Disrupting the blood-brain barrier by focused ultrasound induces sterile inflammation. *Proc Natl Acad Sci U S A* 114, E75-E84 (2017).
- [3]. D. McMahon, R. Bendayan, K. Hynynen, Acute effects of focused ultrasound-induced increases in blood-brain barrier permeability on rat microvascular transcriptome. *Sci Rep* 7, 45657 (2017).
- [4]. D. McMahon, K. Hynynen, Acute Inflammatory Response Following Increased Blood-Brain Barrier Permeability Induced by Focused Ultrasound is Dependent on Microbubble Dose. *Theranostics* 7, 3989-4000 (2017).
- [5]. D. McMahon, W. Oakden, K. Hynynen, Investigating the effects of dexamethasone on blood-brain barrier permeability and inflammatory response following focused ultrasound and microbubble exposure. *Theranostics* 10, 1604-1618 (2020).
- [6]. B. Baseri, J. J. Choi, Y. S. Tung, E. E. Konofagou, Multi-modality safety assessment of blood-brain barrier opening using focused ultrasound and definity microbubbles: a short-term study. *Ultrasound Med Biol* 36, 1445-1459 (2010).
- [7]. N. McDannold, N. Vykhodtseva, S. Raymond, F. A. Jolesz, K. Hynynen, MRI-guided targeted blood-brain barrier disruption with focused ultrasound: histological findings in rabbits. *Ultrasound Med Biol* 31, 1527-1537 (2005).
- [8]. N. Sheikov *et al.*, Brain arterioles show more active vesicular transport of blood-borne tracer molecules than capillaries and venules after focused ultrasound-evoked opening of the blood-brain barrier. *Ultrasound Med Biol* 32, 1399-1409 (2006).
- [9]. N. Sheikov, N. McDannold, S. Sharma, K. Hynynen, Effect of focused ultrasound applied with an ultrasound contrast agent on the tight junctional integrity of the brain microvascular endothelium. *Ultrasound Med Biol* 34, 1093-1104 (2008).
- [10]. N. Sheikov, N. McDannold, N. Vykhodtseva, F. Jolesz, K. Hynynen, Cellular mechanisms of the blood-brain barrier opening induced by ultrasound in presence of microbubbles. *Ultrasound Med Biol* 30, 979-989 (2004).

- [11]. C. Horodyckid et al., Safe long-term repeated disruption of the blood-brain barrier using an implantable ultrasound device: a multiparametric study in a primate model. *J Neurosurg* 126, 1351-1361 (2017).
- [12]. H. L. Liu et al., Hemorrhage detection during focused-ultrasound induced blood-brain-barrier opening by using susceptibility-weighted magnetic resonance imaging. *Ultrasound Med Biol* 34, 598-606 (2008).
- [13]. T. Mainprize et al., Blood-Brain Barrier Opening in Primary Brain Tumors with Non-invasive MR-Guided Focused Ultrasound: A Clinical Safety and Feasibility Study. *Sci Rep* 9, 321 (2019).
- [14]. H. Kim et al., PETCT imaging evidence of FUS-mediated (18)F-FDG uptake changes in rat brain. *Med Phys* 40, 033501 (2013).
- [15]. O. Olumolade, S. Wang, G. Samiotaki, E. E. Konofagou, Longitudinal Motor and Behavioral Assessment of Blood-Brain Barrier Opening with Transcranial Focused Ultrasound. *Ultrasound Med Biol* 42, 2270-2282 (2016).
- [16]. H. C. Tsai, W. S. Chen, C. Inserra, K. C. Wei, H. L. Liu, Safety evaluation of frequent application of microbubble-enhanced focused ultrasound blood-brain-barrier opening. *Sci Rep* 8, 17720 (2018).
- [17]. A. Lefevre *et al.*, Validation of a global quantitative analysis methodology of tryptophan metabolites in mice using LC-MS. *Talanta* **195**, 593-598 (2019).

## Freeze-dried Monodisperse Microbubbles as Ultrasound Contrast Agent

Ugur Soysal<sup>1</sup>, Pedro N. Azevedo<sup>1,2,3</sup>, Flavien Bureau<sup>2</sup>, Alexandre Aubry<sup>2</sup>, Marcio S. Carvalho<sup>3</sup>, Amanda C. S. N. Pessoa<sup>4</sup>, Lucimara G. de la Torre<sup>4</sup>, Olivier Couture<sup>5</sup>, Arnaud Tourin<sup>2</sup>, Mathias Fink<sup>2</sup>, Patrick Tabeling<sup>1</sup>

<sup>1</sup>Laboratoire de Microfluidique, MEMS et Nanostructures, ESPCI Paris, France;

<sup>2</sup>Institut Langevin, ESPCI Paris, Université PSL, CNRS, France;;

<sup>3</sup>Department of Mechanical Engineering, PUC-Rio, Brazil;

<sup>4</sup>School of Chemical Engineering, University of Campinas, Brazil;

<sup>5</sup>Laboratoire d'Imagerie Biomédicale, Sorbonne Université, CNRS, INSERM, France;

### Introduction

Over the last few years, the advantages of using monodisperse bubbles, as ultrasound contrast agents (UCA) have been underlined. Today, monodisperse bubbles, produced by microfluidic technology, have coefficients of variation (CV) less than 5%, and resonance spectra standard deviations below 15% [1]. With monodisperse bubbles, by using an appropriate excitation, one obtains higher signal-to-noise ratios. This, in turn, improves the image quality[2]. In the field of molecular diagnostics, monitoring of resonance frequency facilitates the detection of bound bubbles [3]. Delivery of drugs, genes or therapeutic gases can also be optimized [4]. In addition, monodisperse bubbles facilitates the realisation of non-invasive pressure measurements.

However, thus far, contrarily to polydisperse bubbles, freeze-drying monodisperse populations of fresh microbubbles, without deteriorating their monodispersivity, remains a challenge. Thereby, today, monodisperse bubbles can neither be stored nor transported. This represents a bottleneck for their use in clinical applications. Attempts made to solve the problem have used toxic solvents, raising regulatory issues [5]. In this work, we propose an approach to freeze-dry large populations of fresh monodisperse bubbles without deteriorating their monodispersivity, and without using any solvent.

### Methods

The microbubbles were generated using a flow focusing and step-emulsification microfluidic PDMS (polydimethylsiloxane)-based device. The design also included an anti-clogging system to avoid large aggregates and to ensure long-term stable production. The shell material used was polyvinyl alcohol (PVA) due to its high echogenicity and stability [6]. The gas phase used is perfluorohexane (C<sub>6</sub>F<sub>14</sub>) because of its high hydrophobicity, lower solubility and higher molecular weight compared to air. The microbubbles were produced with diameters of 40µm and 5µm at a rate of up to ~6×10<sup>5</sup> bubbles/min, with CV <5%. The microbubbles were outspread as monolayers over a glass plate to suppress coalescence, Ostwald ripening, and creaming effect, which are found to be major responsible mechanisms of the monodispersity degradation. Each process steps from production, to resuspension were controlled and investigated with optical microscopy to perform geometrical characterization. The resonance behavior of microbubble populations, fresh and freeze-dried, were characterized by backscattering measurements under same conditions. The bubbles were introduced in a PDMS sample container (35mm×10mm×1mm), where they were characterized with the use of an emitter/receiver focal transducer (bandwidth approximately 50%, 38mm focal length, center frequency 2.25 MHz). In order to compare the acoustic properties of freshly generated and resuspended PVA monodisperse microbubble, both populations were excited by a broadband sinusoidal 1-cycle burst signal, with a pulse repetition frequency of 1kHz, and a peak negative pressure of 134kPa (characterized by hydrophone). The waveform data's recording frequency was 22Hz, and the sampling rate was 65MSamples/s, yielding 3125 data points per waveform. Fast Fourier Transform (FFT) was performed on the region of interest located in the focal zone of the transducer.

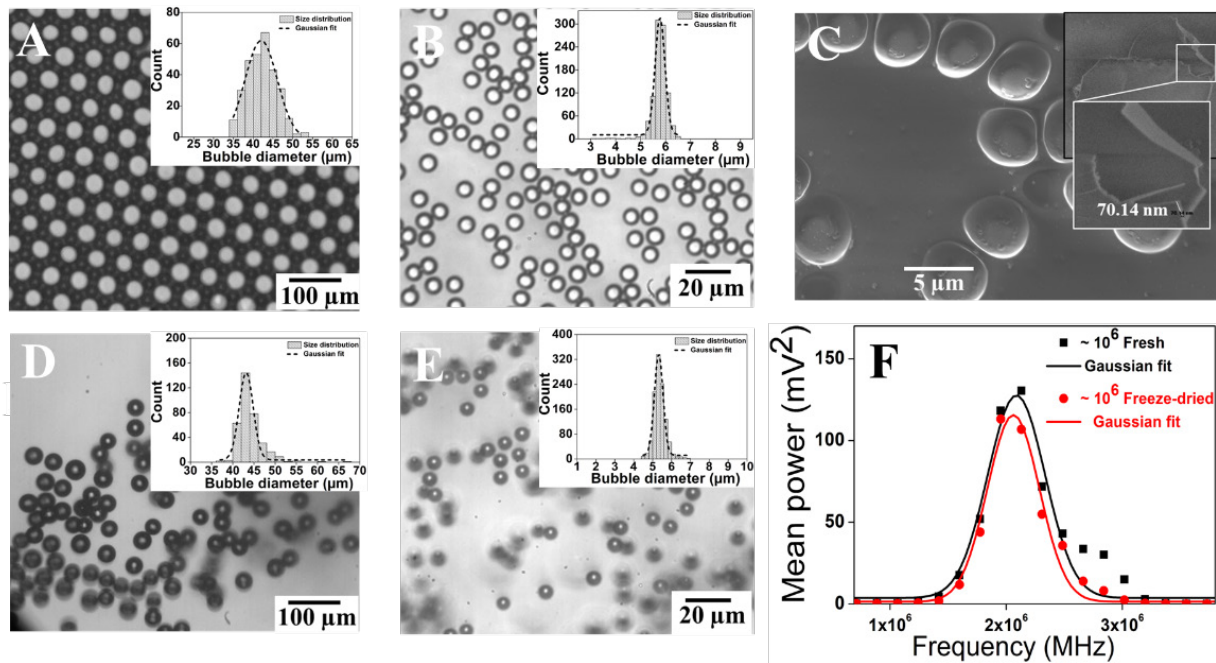


Figure 1: Image and size distribution of freeze-dried monodisperse microbubbles (A) 42  $\mu\text{m}$  mean diameter with  $\sigma$  of 4 and CV of 9%, and (B) 5.8  $\mu\text{m}$  mean diameter  $\sigma$  of 0.3 and CV of 5% in average diameters. (C) A SEM image of the 5  $\mu\text{m}$  freeze-dried microbubble powder. The inset shows an estimate of the shell thickness ( $\sim 70$  nm) from a magnified image of a broken bubble. (D and E) Shows the image and size distribution of the resuspended bubbles with average diameters of the bubbles as 44  $\mu\text{m}$  (with 6% CV) and 5.4  $\mu\text{m}$  (5% CV), respectively. (F) Backscattered spectra of fresh and freeze-dried PVA bubbles, for the same concentrations, with an almost identical acoustic responses (the difference of  $\pm 2\%$  in the resonance frequency and  $\pm 10\%$  in the maximum amplitude).

## Results

The geometrical characteristic of freeze-dried microbubbles populations with mean diameter of 44 and 5  $\mu\text{m}$  are presented in Fig.1A and Fig.1B, respectively. The insert of both figures show their SD, which was calculated using MATLAB's *imfindcircles* function, which employs a Circular Hough Transform (CHT) based algorithm. In both cases, the monodispersity is conserved as shown by their narrow size distribution. A shape deformation resulted from a close packing of the bubbles with 44  $\mu\text{m}$  diameter resulted in a larger CV (10%) for that population in comparison with the 5  $\mu\text{m}$  group. Fig.1C shows a SEM image of lyophilized microbubble, where the shell thickness of  $\sim 70$  nm is indicated. After resuspension with DI water we obtained a CV of 6% and 5% for the 44  $\mu\text{m}$  and 5  $\mu\text{m}$  bubbles, respectively (Fig.1D and 1E). These values are not significantly different, within the experimental error, from fresh bubbles, indicating that the monodispersity is conserved throughout the process, until the resuspension. Fig.1F shows the resonance spectrum obtained from broadband *in vitro* backscatter acoustic measurements of freshly generated and lyophilized bubbles of 5  $\mu\text{m}$ . The difference between the two spectra is in the resonance frequencies of  $\pm 2\%$  and  $\pm 10\%$  in the maximum amplitudes. Both resonance responses have a standard deviation of 10%, ensuring a narrow bandwidth for monodisperse bubbles. These results confirm that the acoustic properties of the monodisperse microbubbles were preserved after resuspension. An important feature we found, consistent with literature [2], is that monodisperse bubbles show a backscatter signal that is an order of magnitude larger than that of polydisperse bubbles for the same bubble concentration, as shown in Fig. 2.

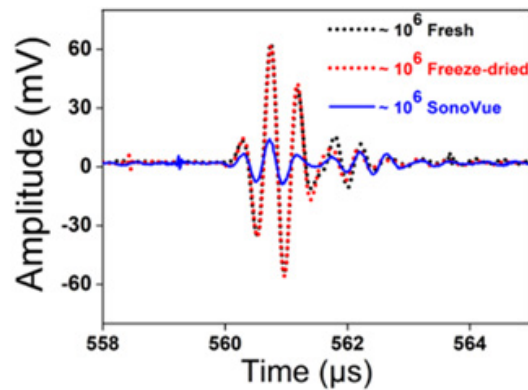


Figure 2: Shows a typical backscattered acoustic response of fresh, freeze-dried PVA monodisperse bubbles, and polydisperse (SonoVue) at the same bubble concentrations.

### Conclusions

The geometric and acoustic characterization of the microbubbles before and after the freeze-drying process shows that by using a specific collection process at the outlet of the microfluidic device, we maintain the monodispersity of the microbubbles. The technology we use makes thus possible to transport and store monodisperse microbubbles, opening the way for a new generation of ultrasound contrast agents that can be directly used in clinical applications. With the rate of production we achieve (in the kHz range), we could produce  $10^{14}$  bubbles per year with 1000 devices parallelization. This figure can be compared with the world production ( $10^{17}$  bubbles annually). Moreover, by optimizing production conditions, there is room to improve again the production.

### References

- [1]. Tremblay-Darveau C, Williams R, Burns PN. *Ultrasound in Medicine and Biology* Elsevier, 2014;40:775–78.
- [2]. Segers T, Kruizinga P, Kok MP, Lajoinie G, de Jong N, Versluis M. *Ultrasound in Medicine&Biology* 2018b; 44:1482–1492.
- [3]. Overvelde M, Garbin V, Dollet B, de Jong N, Lohse D, Versluis M. *Ultrasound in Medicine&Biology* 2011; 37:1500–1508.
- [4]. Dixon AJ, Li J, Rickel J-MR, Klivanov AL, Zuo Z, Hossack JA. *Ann Biomed Eng* 2019;47:1012–1022.
- [5]. Song R, Peng C, Xu X, Wang J, Yu M, Hou Y, Zou R, Yao S. *ACS Appl Mater Interfaces* 2018;10:14312–14320.
- [6]. Grishenkov D, Kari L, Brodin L-Å, Brismar TB, Paradossi G. *Ultrasonics* 2011;51:40–48.

# Ultrasonic Cavitation-Assisted and Acid-Activatable Liposomes for Universal Active Tumor Penetration

**Guowei Wang,<sup>1,2,3</sup> Chao Zhang,<sup>1</sup> Yifan Jiang,<sup>1</sup> Yue Song,<sup>1</sup> Jifan Chen,<sup>1</sup> Yu Sun,<sup>1</sup> Qunying Li,<sup>1</sup> Zhuxian Zhou,<sup>2,3</sup> Youqing Shen,<sup>2,3</sup> and Pintong Huang<sup>1</sup>**

<sup>1</sup> *Department of Ultrasound in Medicine, The Second Affiliated Hospital of Zhejiang University School of Medicine, Zhejiang University, Hangzhou 310009, China.*

<sup>2</sup> *Key Laboratory of Biomass Chemical Engineering of Ministry of Education and Zhejiang Key Laboratory of Smart Biomaterials, College of Chemical and Biological Engineering, Zhejiang University, Hangzhou 310027, China.*

<sup>3</sup> *ZJU-Hangzhou Global Scientific and Technological Innovation Center, Hangzhou 311215, China.*

*Corresponding author: wangguowei@zju.edu.cn, and huangpintong@zju.edu.cn*

## Introduction

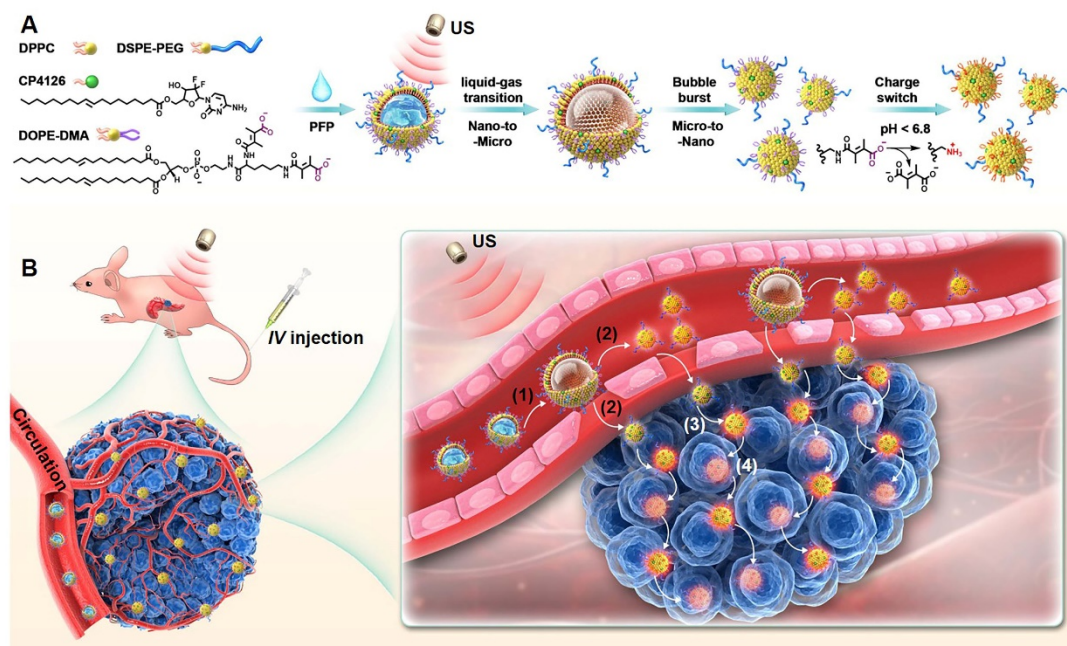
Active tumor penetration that nanoparticles enter tumors through the transcytosis of blood endothelial cells rather than the leaky gaps of blood wall is recently considered as a new and promising strategy for cancer nanomedicine delivery, but it is challenging to develop active transporting nanocarriers. In previous work, we developed many types of enzyme-responsive active penetrating nanomedicines that undergo transcytosis in tumor endothelial cells and tumor cells, delivering chemotherapeutic drugs throughout the whole tumor, completely erasing various tumors in mice model. However, the endogenous stimuli, e.g., enzymes in the tumor microenvironment, are heterogeneous even in the single type tumor in different patients, which may result in non/low-responsive of the nanocarriers in the clinic. Therefore, it is acquisitive to design an active penetration strategy that can be applied to a broad range of tumors.

The acidic tumor microenvironment ( $\sim$  pH = 6.0-6.8), generated by the excess production of lactate and protons during tumor cell metabolism, has virtually been characterized as a hallmark of all solid tumors both in animal model and patients. The acidic pH of the tumor microenvironment has been used as a universal stimulus for developing smart cancer nanomedicines. We have developed a type of pH-triggered charge-reversal nanoparticles to generate cationic charges in tumors for enhanced drug delivery. However, the pH of the perivascular site is physiologically neutral and the acidic tumor region is usually 100-200  $\mu$ m away from the tumor vasculatures. Ultrasonic cavitation can improve nanomedicines' extravasation from the blood vessel in a non-intrusive and homogeneous manner. Microbubbles irradiated by ultrasound (US) can create stable and inertial cavitation effects to induce transient or lethal pores on cell membranes. Accordingly, we propose to develop a universal active transporting strategy for cancer nanomedicine, which transports to tumor periphery by ultrasonic cavitation, generates cationic charge under the acidic tumor microenvironment, and undergoes cationization-initiated transcytosis in tumor cells.

## Methods

To demonstrate the strategy, we designed a size and charge dual-conversional gemcitabine prodrug-integrated liposomal nanodroplet (SCGLN) (**Scheme 1**). SCGLN was prepared using an acidity-cleavable dimethylmaleic amide-modified 1, 2-dioleoyl-sn-glycero-3-phosphoethanolamine lipid (DOPE-DMA), 1, 2-dipalmitoyl-sn-glycero-3-phosphocholine (DPPC), 1, 2-distearoyl-sn-glycero-3-phosphoethanolamine-N-[methoxy(polyethylene glycol)-2000] (DSPE-PEG) and a lipophilic fatty acid ester derivative of gemcitabine (CP4126), and loaded with perfluoropentane. Once in tumor blood vessels, SCGLN changes from nanodroplets to microbubbles via liquid-gas phase transition of perfluoropentane irritated by US, opens the tight vascular wall by acoustic droplet vaporization, and ultrasonic cavitation, converts from microbubbles to nano-sized liposomes, and extravasates from blood vessels into tumor periphery. Thereafter, SCGLN undergoes charge-reversal in the acidic tumor microenvironment after the hydrolysis of dimethylmaleic amides, triggers fast cationization-initiated transcytosis, penetrates deep into tumor

parenchyma, and delivers the loaded gemcitabine (GEM) throughout the tumor to achieve potent antitumor activity.



**Scheme 1.** Schematic representation of SCGLN for active tumor penetration *via* acoustic transformation and transcytosis.

## Results

The liposomal nanodrops SCGLN were prepared using the lipid mixture of DPPC, DSPE-PEG, DOPE-DMA, and CP4126 at the mass ratio of 1.5:1:1.5:1 and following with the encapsulation of perfluoropentane. CP4126's lipid amphipathic structure can wholly integrate with phospholipid membrane, resulting in 100% encapsulation efficiency and a GEM-loading rate of about 9.98%. SCGLN were liposomal nanodroplets with particle size of  $377.7 \pm 60.2$  nm and zeta potential of  $-11.6 \pm 4.8$  mv in PBS buffer at 25 °C and pH 7.4. With transitory US irradiation (20 sec, 2 W/cm<sup>2</sup>), SCGLN underwent phase transition from nanodroplet to microbubble at 37 °C. Prolonged US irradiation (ca. 5-10 min) disrupted the microbubble of SCGLN, and the microbubble could reassemble into nano-sized liposomes with particle size of  $179.3 \pm 27.6$  nm. The zeta potential of SCGLN changed quickly from about -7 mV to +4 mV within 30 min at pH 6.5, but remained unchanged at about -11 mv at pH 7.4 during the experiment.

In 3D culture of multicellular tumor spheroids, the cytotoxicity of SCGLN was significantly higher than the control liposomes and GEM. The IC<sub>50</sub> of SCGLN was 0.17 μM to BxPC3 multicellular tumor spheroids, which was about 3-7 times of the other treatments. In orthotopic pancreatic tumor-bearing mice, SCGLN showed the highest fluorescence in tumors than the control liposomes. The fluorescence intensity of SCGLN in the tumor was 8.33-fold that of CGLN and 3.59-fold that of SGLN. In the experiment of *in vivo* real-time ultrasonic cavitation-induced tumor accumulation and penetration using CLSM and US apparatus, SCGLN could rapidly extravasate from capillaries and penetrated the tumor parenchyma within 60 min. The gemcitabine-loaded SCGLN exhibited potent antitumor activity in multiple poorly permeable tumor models, which completely erased subcutaneous U251 glioma and stopped the progression of orthotopic BxPC3 pancreatic ductal adenocarcinoma.

## Conclusions

In summary, we demonstrated a universal active tumor penetration strategy for low permeable tumors. The design combines ultrasonic cavitation, acidity-responsive charge-reversal, and cationization-initiated transcytosis to enhance the nanomedicine's blood extravasation and tumor penetration capability. The

designated active penetrating SCGLN liposomes achieved superior tumor accumulation and deep penetration and exhibited potent antitumor activity in the poorly permeable tumors, including glioma and PDA mice tumor model.

**References**

- [1]. Guowei Wang, Chao Zhang, Yifan Jiang, Yue Song, Jifan Chen, Yu Sun, Qunying Li, Zhuxian Zhou, Youqing Shen, and Pintong Huang. Ultrasonic Cavitation-Assisted and Acid-Activated Transcytosis of Liposomes for Universal Active Tumor Penetration. *Advanced Functional Materials*, 2021, 31(34), 2102786.

# Development and Characterization of Nitro-Fatty Acid Microbubbles (NFABs) for the Treatment of Microvascular Obstruction

Muhammad Wahab Amjad<sup>1</sup>, Soheb Anwar Mohammed<sup>1</sup>, Xucai Chen<sup>1</sup>, Terry O. Matsunaga<sup>2</sup>, Bruce A. Freeman<sup>3</sup>, Marco Fazzari<sup>3</sup>, John J. Pacella<sup>\*1</sup>

<sup>1</sup>Center for Ultrasound Molecular Imaging and Therapeutics, Heart and Vascular Medicine Institute, University of Pittsburgh, Pittsburgh, PA, USA

<sup>2</sup>Department of Biomedical Engineering and Department of Medical Imaging, University of Arizona, Tucson, AZ, USA

<sup>3</sup>Department of Pharmacology and Chemical Biology, School of Medicine, University of Pittsburgh, Pittsburgh, PA, USA

Corresponding author: pacellajj@upmc.edu

## Introduction

Cardiovascular disease (CVDs) is the leading cause of global death. In 2019, 17.9 million people died from CVD; 85% of which were due to acute myocardial infarction (AMI) [1]. Post-MI congestive heart failure is increasing due to obstruction (MVO). MVO is blockage of the microcirculation by thrombi and tends to occur after coronary stenting for AMI, and results in hypoperfusion. Current therapeutic strategies for MVO are not consistently effective. Hence, we have been developing ultrasound (US)-targeted microbubble cavitation (UTMC) as a potential treatment for MVO. In its current form, UTMC only mechanically restores the blood flow in the obstructed vessels by disintegrating the microthrombi; it does not address the accompanying harmful oxidative stress and inflammation. Nitro-fatty acids (NFA) pleiotropically modulate cell signaling and inflammatory cell responses, resulting in antioxidant and anti-inflammatory actions [2]. We have been developing US-targeted perfluorobutane gas-filled NFA microbubbles (NFABs). These dual function NFABs will address not only the mechanical obstruction but also the accompanying inflammatory milieu associated with MVO.

## Methods

NFABs were prepared using a sonication method followed by investigation of microbubble (MB) concentration (MBs/ml) and mean size using a Beckman particle counter. The concentration of NFA incorporated into the MBs was calculated using liquid chromatography-mass spectrometry (LC-MS). NFAB dynamics were tested *in vitro* using a flow loop and ultra-high frame microscopy. To study the *in vivo* efficacy of NFABs, rat hindlimb ischemia reperfusion experiments were performed wherein focal tissue concentration of NFA, microvascular blood flow rate (dB/s) and gene expression (ICAM1, VCAM1 and MCP) were studied.

The *in vitro* and *in vivo* experiments demonstrated promising results and motivated further optimization of NFA loading in MBs and understanding of NFAB storage stability. To achieve high loading efficiency, a series of NFAB formulations comprising varying molar ratio combinations of Distearoyl-phosphatidylcholine (DSPC) and NFA were prepared and analyzed. Other constituents including DSPE-mPEG(2000) and Polyoxyethylene stearate (STPEG) remained constant in all formulations.

## Results

NFABs were prepared and their number and size investigated. The number was found to be in the range of 0.8-1.2 x 10<sup>9</sup> MBs/ml having a mean size of 2.5-3.3 μm. No major difference was observed in the number and size of blank MBs and NFABs.

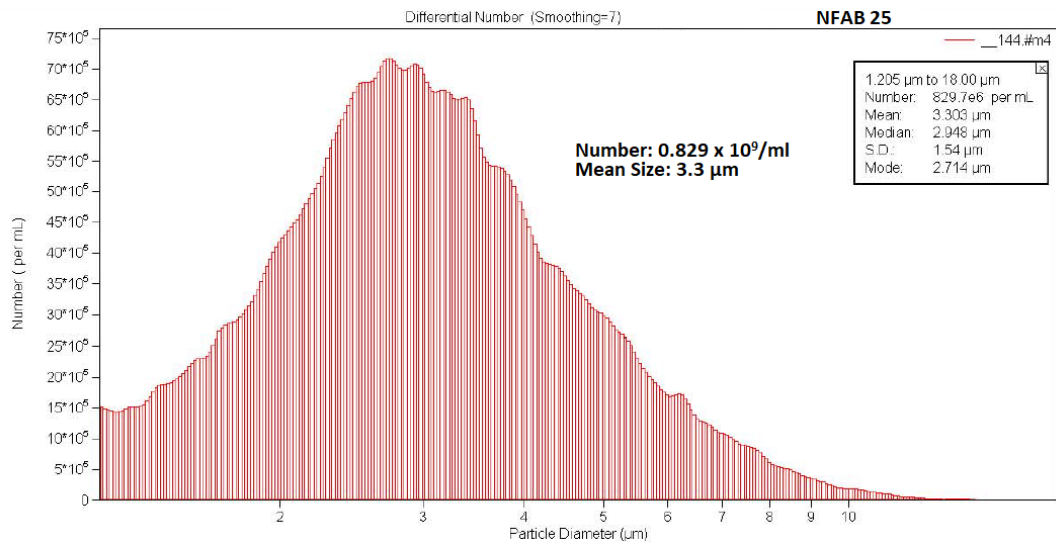


Figure 1. Multisizer image showing NFAB 25 number and mean size.

Ultra high frame rate microscopy analyses confirmed that the incorporation of NFA in the MB shell did not compromise the performance of the NFABs with respect to stability and cavitation activity in response to ultrasound.

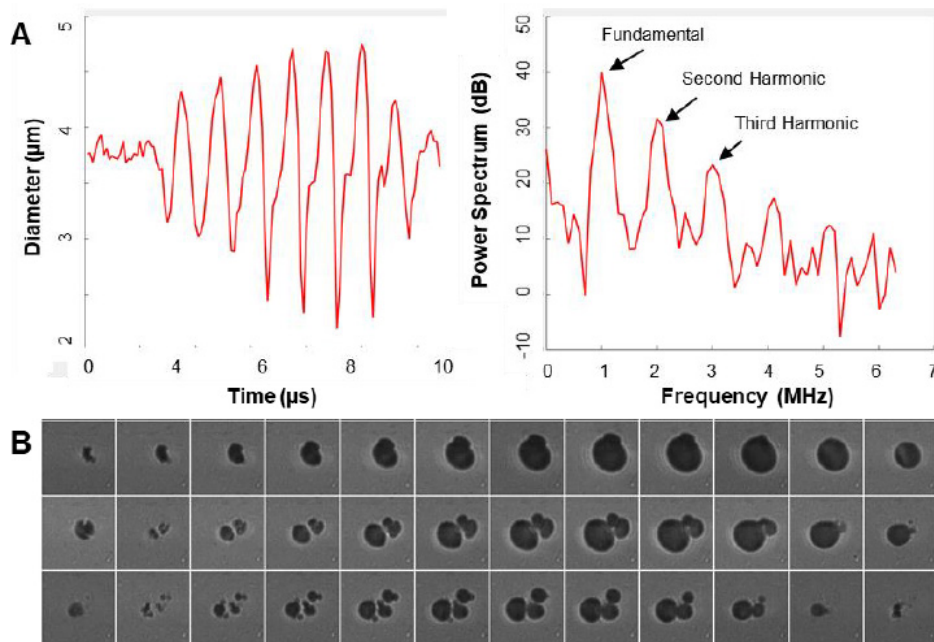


Figure 2. Ultra-high frame microscopy imaging. A) MB size vs. time derived from high speed movie (left) and the corresponding power spectrum (right) (B) Montage of high speed movie showing NFAB going through inertial cavitation, breaking, and daughter bubble formation.

In a rat hindlimb ischemia-reperfusion injury model, UTMC with NFABs resulted in the highest local tissue concentration of NFA (40 fmol/mg) the highest microvascular blood flow rate (7.5 dB/s) and the greatest reduction in pro-inflammatory gene expression (ICAM1, VCAM1 and MCP) following ischemia reperfusion in comparison to NFA alone or NFA+blank MBs.

To further optimize NFA loading and enhance local delivery of NFA to the target site (goal 230 fmol/mg) in the hindlimb, six different NFAB formulations were prepared. Of the formulations assessed, the highest NFA loading was 109.31  $\mu$ M in NFAB 75, see Table 1).

Table 1. NFAB Formulations and NFA loading

NFAB Formulations	Molar Ratios		NFA Loading Concentration ( $\mu\text{M}$ )
	DSPC	NFA	
NFAB 25	18	15	10.06
NFAB 50	12	30	97.84
NFAB 75	6	45	109.31
NFAB 100	0	61	85.23
NFAB 90	2	54	42.84
NFAB 1:1	25	61	18.27

The storage stability study of NFABs was performed at 4°C. NFABs were systematically analyzed for number and size over 30 days and were found to be stable during that time frame.

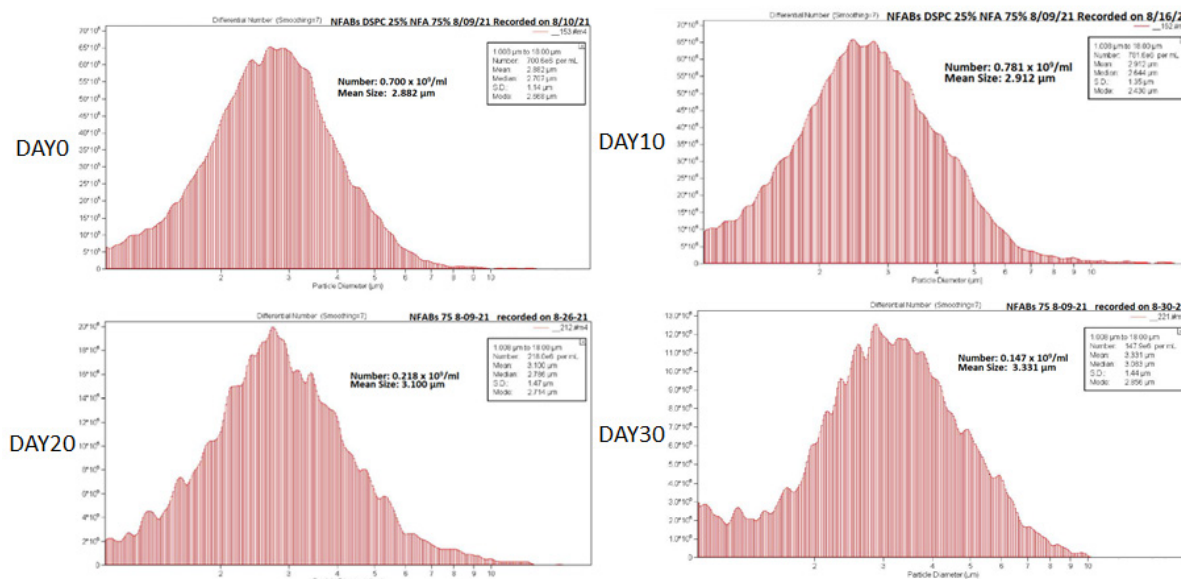


Figure 3. Stability Study of NFAB 75 for 30 days.

## Conclusions

NFABs exhibit promising *in vitro* and *in vivo* physicochemical characteristics. The formulation NFAB75 yielded the greatest NFA loading and were stable for up to one month. Now that we have optimized NFA loading, studies testing the therapeutic efficacy of NFAB in a rat model of myocardial ischemia reperfusion are underway.

## References

- [1]. World Health Organization, Cardiovascular diseases (CVDs) key facts, (2021). [https://www.who.int/news-room/fact-sheets/detail/cardiovascular-diseases-\(cvds\)](https://www.who.int/news-room/fact-sheets/detail/cardiovascular-diseases-(cvds)).
- [2]. N.K. Khoo, L. Li, S.R. Salvatore, F.J. Schopfer, B.A. Freeman, Electrophilic fatty acid nitroalkenes regulate Nrf2 and NF- $\kappa\text{B}$  signaling: A medicinal chemistry investigation of structure-function relationships, *Sci Rep.* 8 (2018) 2295. DOI:10.1038/s41598-018-20460-8.

# Evaluating the Stability of Perfluorocarbon Nanodroplets for Antimicrobial Therapies

***Christopher Campbell<sup>1</sup>, Gareth LuTheryn<sup>2</sup>, Nicholas D Evans<sup>1</sup>, Peter Glynne-Jones<sup>1</sup>,  
Jeremy Webb<sup>3</sup>, Dario Carugo<sup>2</sup>***

<sup>1</sup>*Faculty of Engineering and Physical Sciences, University of Southampton, Southampton, U.K.*

<sup>2</sup>*School of Pharmacy, University College London, London, U.K.*

<sup>3</sup>*National Biofilms Innovation Centre (NBIC), School of Biological Sciences, University of Southampton, Southampton, U.K.*

*Corresponding author: c.k.campbell@soton.ac.uk*

## Introduction

Perfluorocarbon nanodroplets (NDs) are a promising technology in the field of anti-microbial therapies, particularly for the treatment of biofilm-associated infections such as those found in chronic wounds. Previous work on the anti-microbial effect of gas-filled microbubbles highlighted the potential of microbubbles to enhance the delivery of bioactive compounds, such as nitric oxide [1]. Nitric oxide (NO) is a potent signalling molecule known to induce biofilm dispersal; however, it has an extremely short half-life making it difficult to deliver to a biofilm in therapeutically relevant amounts. Nanodroplets consisting of a liquid perfluorocarbon (PFC) core stabilised by a lipid shell can be loaded with NO [2]. Moreover, PFC NDs are responsive to ultrasound exposure and can be converted into gas-filled microbubbles through acoustic droplet vapourisation (ADV) [3]. Microbubble cavitation can then be induced, and has the potential to increase temporal control over the release of therapeutic molecules loaded into the droplet.

This study aims to develop a stable formulation of PFC NDs and test their ability to disperse bacterial biofilms through the delivery of nitric oxide and other bioactive compounds.

## Methods

To formulate nanodroplets, a lipid solution and liquid perfluorocarbon are emulsified by 2-stage sonication. The first stage is used to disperse a rehydrated lipid film in phosphate-buffered saline (PBS). The second stage emulsifies perfluoro-n-pentane with the lipid solution through pulsed sonication, creating an emulsion of nanodroplets. 1,2-distearoyl-sn-glycero-3-phosphocholine (DSPC) was combined with either polyoxyethylene (40) stearate (PEG40S) or 1,2-distearoyl-sn-glycero-3-phosphoethanolamine-N-[amino(polyethylene glycol)-2000] (DSPE-PEG2000) in a 9:1 molar ratio to make the lipid-shell of the nanodroplets.

DSPC:PEG40S NDs were incubated at both storage (4 °C) and physiological wound (35 °C) temperature. Additionally, DSPC:DSPE-PEG2000 NDs were incubated at physiological temperature. The effect of varying the second sonication duration on the mean diameter of DSPC:PEG40S NDs was also tested. The standard sonication protocol uses pulsed sonication, with 2s ON and 5s OFF, for a total of 60s of sonication. Nanoparticle tracking analysis (NTA) was used to measure the size distribution of the nanodroplet samples. NTA measures the hydrodynamic diameter of the particles and reveals the overall size dispersity of a sample.

Currently, these formulations are being tested to assess the anti-microbial effects on *Pseudomonas aeruginosa* biofilms. Biofilms grown in 96-well plates will be incubated with unloaded (NO-free) NDs and then stained with crystal violet (1% w/v). Relative changes in biofilm biomass will be measured using a plate reader at 584 nm once the biofilm is solubilized using acetic acid.

## Results

Both formulations remained consistent in size over a 6-hour period at 35 °C (Fig. 1), with DSPC:PEG40S NDs having an initial (0h) mean diameter of  $165.1 \pm 64.0$  nm (Fig. 1, S.D. error bars). DSPC:DSPE-PEG2000 NDs had an initial (0h) mean diameter of  $185.7 \pm 95.9$  nm. After incubation at 35 °C for 6h, the DSPC:PEG40S NDs had a mean diameter of  $166.4 \pm 68.2$  nm, and DSPC:DSPE-PEG2000 NDs had a mean diameter of  $206.7 \pm 111.3$  nm. DSPC:PEG40S NDs remained consistent in size over a 5-day period at 4 °C, with an initial (Day 0) mean diameter of  $199.3 \pm 104.1$  nm. After 5 days incubation at 4 °C, the NDs mean diameter was  $199.8 \pm 108.3$  nm.

The effect of varying the second sonication time on ND diameter was assessed. Sonication lengths of 15, 30, 60, 90 and 120s were tested. NDs made with 15s of sonication had a mean diameter of  $236.7 \pm 134.8$  nm, while NDs made with 30s of sonication had a mean diameter of  $230.3 \pm 130.1$  nm. NDs manufactured with the standard 60s sonication time had a mean diameter of  $199.3 \pm 104.1$  nm, with 90s of sonication time resulting in a mean diameter of  $187.9 \pm 96.8$  nm. NDs made with 120s of sonication time had a mean diameter of  $209.6 \pm 116.1$  nm. Of the formulations investigated, DSPC:PEG(40)S NDs have been selected for testing on biofilms, with a 60s sonication time used for manufacture.

## Conclusions

This study has optimised the manufacture of perfluorocarbon-core lipid-shelled nanodroplets and assessed their stability at both storage and physiological wound temperatures over time. The effect of varying sonication time on mean diameter has been tested, with a general trend of smaller droplets with increasing sonication time.

Ongoing work includes testing the effect PFC NDs on *Pseudomonas aeruginosa* biofilms. Bioactive gases such as nitric oxide (NO) will be loaded into the droplets, and passive release will be assessed. Antibiofilm effects will be assessed with both NO-loaded and unloaded droplets.

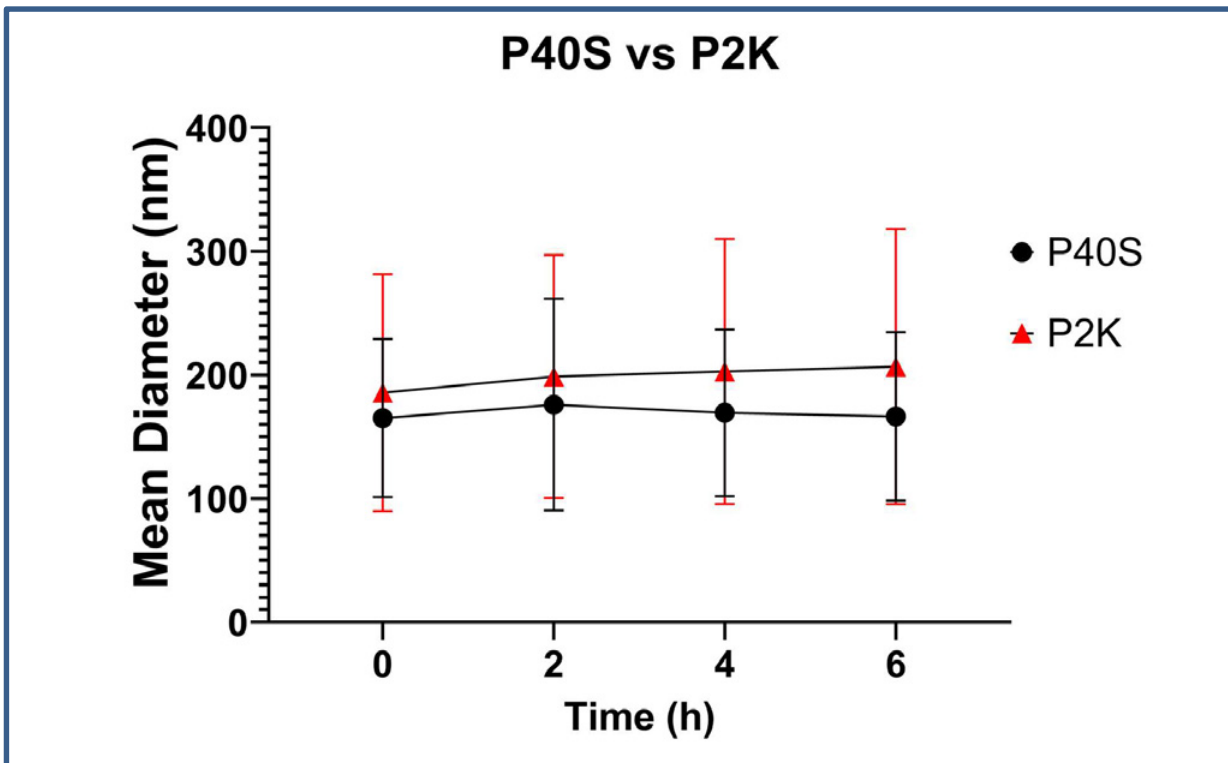


Figure 1. Mean diameter of DSPC:PEG40S (P40S) and DSPC:DSPE-PEG2000 (P2K) perfluorocarbon nanodroplets over a 6-hour period at 35 °C.

## References

- [1]. Lafond, M. et al. Bactericidal Activity of Lipid-Shelled Nitric Oxide-Loaded Microbubbles. *Front. Pharmacol.* 10, (2019).
- [2]. Ortiz, D., Cabrales, P. & Briceño, J. C. Transport of Nitric Oxide by Perfluorocarbon Emulsion. *Biotechnol. Prog.* 29, 1565 (2013).
- [3]. Zhou, Y. Application of acoustic droplet vaporization in ultrasound therapy. *Journal of Therapeutic Ultrasound* vol. 3 1–18 (2015)

## Can Ultrasound Contrast Agents swim?

*Georges Chabouh<sup>1</sup>, Catherine Quilliet<sup>1</sup>, Gwennou Coupier<sup>1</sup>*

<sup>1</sup>Université Grenoble Alpes, CNRS, LIPhy, F-38000 Grenoble, France  
Corresponding author: [georges.chabouh@univ-grenoble-alpes.fr](mailto:georges.chabouh@univ-grenoble-alpes.fr)

### Introduction

Microbubbles, which were initially created as vascular contrast agents for ultrasound (US) imaging are now taking US in promising new directions in various areas of medicine. The opening of the brain-blood-barrier, thanks to microbubbles cavitation, made the delivery of antibody therapy possible in a first-in-world clinical trial (Sunnybrook Health Sciences Centre, Toronto, Canada) for breast cancer that has metastasized to the brain [1]. However, under high-intensity acoustic excitations, current Ultrasound Contrast Agents (UCAs) cannot stay long enough on the target and are rapidly destroyed [2]. Thus, the use of micro-robots for targeted-drug-delivery is of great importance.

We evidenced a swimming motion of UCAs through a buckling mechanism activated by pressure waves. When submitted to an increase of external pressure, a spherical elastic shell filled with gas first shrinks isotropically, then destabilizes above a certain pressure threshold towards a buckled shape. This swift buckling transition involves an important volume of fluid set into motion in a short time. The reinflation after external pressure decrease follows a different path, involving a sequence of stable shapes followed by an unbuckling instability of much weaker amplitude. This velocity and shape hysteresis opens several possibilities for triggering a swimming motion.

### Methods

Experiments were conducted in a custom-built chamber mounted vertically on a 90 degrees flipped microscope (Fig. 1-a). A dilute suspension of SonoVue microbubbles (MBs) was injected into the chamber using a pressure controller (Elvesys, France), and the pressure inside the chamber is monitored using a pressure sensor mounted in series. Cospheric beads (air + glass shell) are mixed with the MBs. As they have a comparable density and they do not buckle when the pressure is applied, they serve as reference particles.

A quasi-static pressure variation ( $f = 2$  Hz) is used with a pressure cycle ranging from 0 to 20 kPa in order to make the MBs buckle without any destruction as seen in Fig. 1-b.

### Results

Both SonoVue MBs and the reference beads float against gravity due to the buoyancy force. The particles' position and speed as a function of time are obtained from the recorded videos using homemade tracking software based on two-dimensional (2D) Gaussian fitting with subpixel resolution from a pixelized image of light intensity.

In order to quantify the buckling, we define the aspect ratio  $\lambda$ , as the ratio between the two widths of the 2D-Gaussian in the direction of buckling and perpendicular to it. In Fig. 2a, we show that at around 0.2 seconds of every cycle, the aspect ratio suddenly decreases to reach a plateau when the buckling pressure is reached, and in the same time a motion of the MB at the same direction as the center-to-buckling-spot vector can be seen (Fig. 2b), in the unbuckling phase,  $\lambda$  increases, and a reverse motion of the MB is measured. Overall, a positive net displacement is achieved while the velocity of the reference beads oscillates around 0, as a consequence of Brownian motion.

### Conclusions

We have experimentally proven that a net positive displacement of the MB can be achieved thanks to the intrinsic properties of shell buckling. The next step is to engineer shells that have different visco-elastic properties and thicknesses in order to increase the net positive displacement. On the other hand, to activate more this mechanism, the driving acoustic frequency has to be 'gently' increased, just before the natural

buckling frequency of the shell [3] in order to let time for complete buckling/de-buckling cycles to take place. As an answer to the problem of directivity as seen in the acoustic radiation force technique [4], ultrasound molecular imaging and drug delivery can benefit from this novel micro-robot powering.

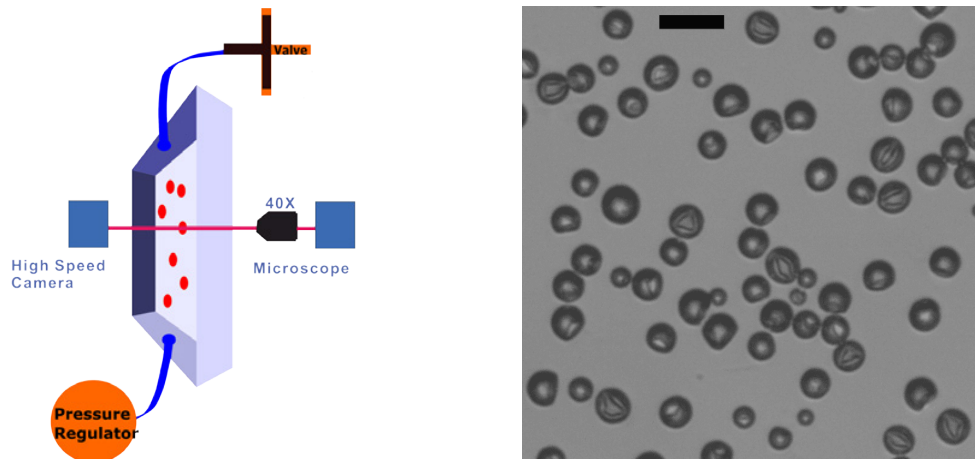


Figure 1. a) Experimental apparatus and b) Buckled SonoVue MBs close to the wall. The scale bar represents 10 microns.

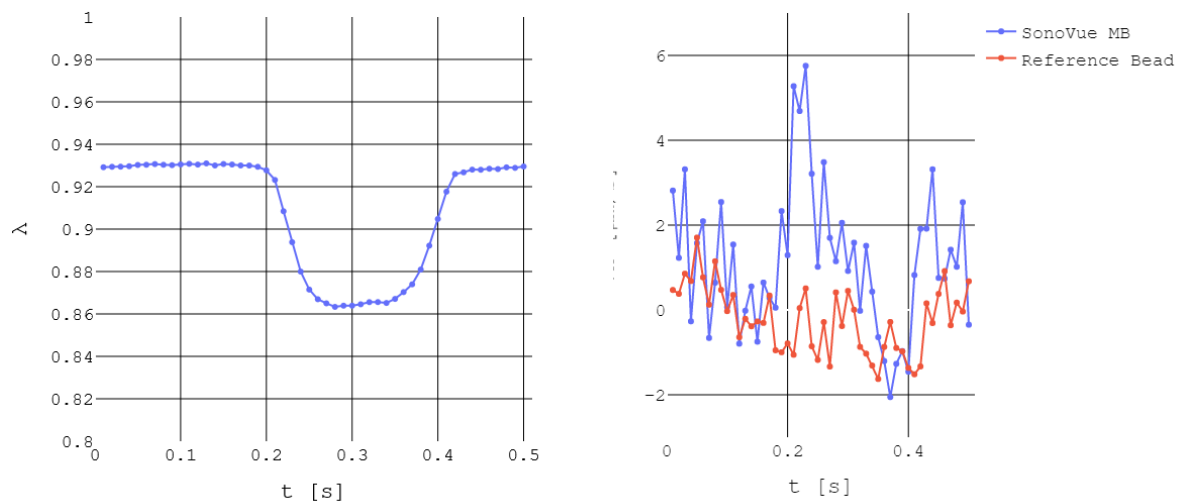


Figure 2. a) Aspect ratio of the MB on one cycle, and b) Velocity in x-direction perpendicular to gravity. The signal is averaged 25 times in both cases. The chosen shell buckles in the  $x > 0$  direction

### References

[1]. Meng, Y., Reilly, R. M., Pezo, R. C., Trudeau, M., Sahgal, A., Singnurkar, A., ... & Lipsman, N. (2021). MR-guided focused ultrasound enhances delivery of trastuzumab to Her2-positive brain metastases. *Science Translational Medicine*, 13(615), eabj4011.

- [2]. Fan, Z., Chen, D., & Deng, C. X. (2014). Characterization of the dynamic activities of a population of microbubbles driven by pulsed ultrasound exposure in sonoporation. *Ultrasound in medicine & biology*, 40(6), 1260-1272.
- [3]. Mokbel M, Djellouli A, Quilliet C, Aland S, Coupier G., Post-buckling dynamics of spherical shells, Proc. R. Soc. A, 477, 20210378, 2021.
- [4]. Supponen, O., Upadhyay, A., Lum, J., Guidi, F., Murray, T., Vos, H. J., ... & Borden, M. (2020). The effect of size range on ultrasound-induced translations in microbubble populations. *The Journal of the Acoustical Society of America*, 147(5), 3236-3247.

# Investigating microvascular phantom and case materials for ultrasound perfusion imaging

P.Chen<sup>1</sup>, A. Pollet<sup>2</sup>, A. Panfilova<sup>1</sup>, M. Zhou<sup>1</sup>, S. Turco<sup>1</sup>, J. den Toonder<sup>2</sup>, M. Mischì<sup>1</sup>

<sup>1</sup>Department of Electrical Engineering, Eindhoven University of Technology, Eindhoven, Netherlands

<sup>2</sup>Department of Mechanical Engineering, Institute for Complex Molecular Systems, Eindhoven University of Technology, Eindhoven, Netherlands

Corresponding author: p.chen1@tue.nl

## Introduction

Imaging and quantification of blood perfusion reveals a fundamental property of tissue that varies in many important physiological and pathological processes [1]. Current methods for perfusion imaging by ultrasound are based on Doppler ultrasound and contrast-enhanced ultrasound (CEUS). In designing novel Doppler ultrasound techniques, there is a need to assess the accuracy of flow measurements and the sensitivity of flow imaging in small vessels. CEUS provides real-time imaging of blood flow with the help of intravenously-injected ultrasound contrast agents (UCAs). By quantitatively analyzing CEUS acquisitions, several advanced techniques have been developed for perfusion quantification, enabling the estimation of parameters related to blood flow dynamics [2, 3]. Although *in-vivo* studies have shown promising results, the relationship between the underlying (micro)vascular architecture and the UCA kinetics, along with the resulting CEUS image enhancement and ultimately the estimated hemodynamic parameters, is not well understood.

In this context, *in-vitro* studies, especially on perfusable (micro)vascular phantoms, play a crucial role in developing ultrasound perfusion imaging techniques and validation. Materials with well-characterized acoustic properties, good optical transparency, longevity and stability are of great interest for the development of perfusable phantoms with designed (micro)vasculature networks. In the past years, several tissue-mimicking materials such as gelatin and polyvinyl alcohol (PVA) have been investigated for the realization of (micro)vasculature phantoms. Typical phantoms are soft hydrogels that have low mechanical stiffness, leading to the challenges in connecting tubing for reliable perfusion without leakage, and to changes of position and geometry of the (micro)vasculature while imaging. To overcome these issues, a rigid phantom case that is suitable for ultrasound imaging is valuable [4].

In this work, we investigate the acoustic properties, optical transparency and longevity of seven tissue-mimicking phantom materials including gelatin, agarose, polyacrylamide (PAA), polydimethylsiloxane (PDMS), polyvinyl alcohol (PVA), alginate and polyethylene glycol diacrylate (PEGDA), and five different phantom case materials including polycarbonate (PC), polymethyl methacrylate (PMMA), polymethylpentene (TPX), cyclic olefin copolymer (COC) and polyether block amide (PEBA). Moreover, perfusable (micro)vascular phantoms made of optimal phantom and case materials as well as their ultrasound perfusion imaging are demonstrated.

## Methods

The through-transmission technique was used to measure the acoustic properties, including speed of sound ( $SoS$ ), acoustic impedance ( $Z$ ) and attenuation coefficient ( $\alpha$ ), of the phantom and case materials [5]. The parameter of nonlinearity ( $B/A$ ), which quantifies the nonlinear propagation effects of acoustic waves in a medium, was also measured for the phantom materials. In this technique, water is employed as a reference by comparing ultrasonic waves propagating through water with waves propagating through the materials. All the experiments were conducted in a water tank. A dedicated rail system was used to fix the transmitter, material samples and receiver, ensuring that they were aligned along their longitudinal axis. A schematic diagram of the experimental set-up is depicted in Fig. 1.

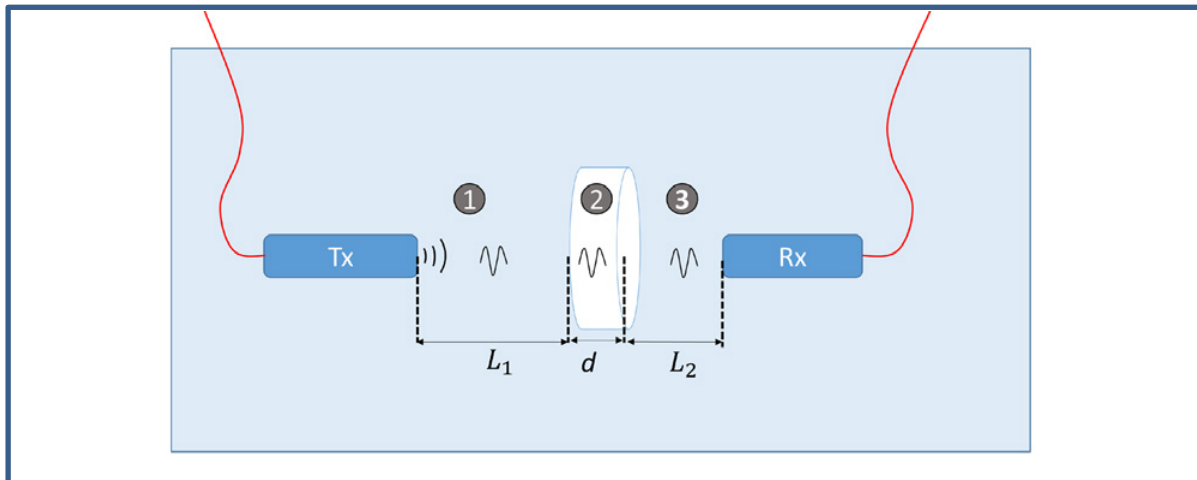


Figure 1. Experimental set-up scheme: transmitted (Tx) ultrasound signals propagate to the receiver (Rx), passing through three parts: (1) water with interval distance  $L_1$ , (2) sample with thickness  $d$ , (3) water with interval distance  $L_2$ .

For the measurement of  $SoS$ ,  $Z$  and  $\alpha$ , two transducers (V306 with a diameter of 13 mm and C304 with a diameter of 25 mm; Panametrics, Olympus Inc., Waltham, MA, USA) with 2.25-MHz center frequency were used to transmit and receive in a frequency range varying from 1 MHz to 3 MHz. Additionally, two transducers (V309 with a diameter of 13 mm and V307 with a diameter of 25 mm; Panametrics, Olympus Inc., Waltham, MA, USA) with 5-MHz center frequency were used for the frequency range varying from 4 to 6 MHz. An extra transmission at 3.5 MHz was conducted for both sets to validate the measurement consistency. By comparing the received signals propagating through water and through the materials, the  $SoS$ ,  $Z$  and  $\alpha$  for phantom and case materials were calculated. For the measurement of the parameter  $B/A$ , the finite amplitude insertion substitution (FAIS) method was used based on this through-transmission experimental set-up [6, 7]. The FAIS method is a comparative method based on the measurement of the amplitude of the second harmonic generated during the wave propagation through a sample with unknown  $B/A$  relative to that generated during the propagation through a reference medium (typically water) with known  $B/A$ . In this method, the ultrasonic sources are assumed to be finite amplitude plane waves. By modelling the nonlinear propagation of ultrasonic waves as a function of the distance between two transducers, we conducted the measurements with multiple distances between two transducers and then performed a least square curve fitting to estimate the  $B/A$  for each phantom material. In our measurement, high-pressure ultrasound pulses were transmitted using a transducer with 2.25-MHz center frequency (V306 with a diameter of 13 mm; Panametrics, Olympus Inc., Waltham, MA, USA) and received by a transducer with 5-MHz center frequency (V307 with a diameter of 25 mm; Panametrics, Olympus Inc., Waltham, MA, USA).

Long-term observation of these materials was conducted to compare their optical transparency, longevity and stability.

Based on the acoustic measurement results and the long-term observations, the optimal phantom material, PAA, and the optimal case material, TPX, were determined. These materials were therefore employed to design and fabricate a perfusion system, consisting of a PAA phantom including a sugar-printed dual-bifurcation microvascular structure with diameter varying from 330 to 650  $\mu\text{m}$  in a rigid TPX case [8]. To demonstrate the performance of the perfusion system for ultrasound perfusion imaging, CEUS imaging of the UCA flow at a rate of 0.08 mL/min through the microvascular structure in the system was performed using a Verasonics ultrasound system (Verasonics Vantage 128, Verasonics Inc., USA) equipped with a L11-4v probe transmitting at 3.5 MHz in a contrast-specific mode.

## Results

Our measurements show a wide range in speed of sound ( $SoS$ ) varying from 1057 to 1616 m/s, acoustic impedance ( $Z$ ) varying from 1.09 to  $1.71 \cdot 10^6$  kg/m<sup>2</sup>s, and attenuation coefficients ( $\alpha$ ) varying from 0.1 to 22.18 dB/cm at frequencies varying from 1 to 6 MHz for different phantom materials. The nonlinearity parameter  $B/A$  varies from 6.1 to 12.3 for most phantom materials. Among them, PAA has the measured  $SoS$  ranging from 1445 to 1538 m/s,  $Z$  ranging from 1.45 to  $1.58 \cdot 10^6$  kg/m<sup>2</sup>s,  $\alpha$  ranging from about 0.1 to 0.9 dB/cm at frequencies varying from 1 to 6 MHz, and  $B/A$  ranging from 6.1 to 11.6, which are close to the acoustic properties of human soft tissues. Moreover, PAA has good optical transparency, longevity and stability. For the case materials, TPX has the measured  $SoS$  and  $Z$  similar to that of soft tissues. Especially its low  $\alpha$ , ranging from about 3.3 to 11.3 dB/cm, makes TPX the preferred choice as a case material. Therefore, the measurements suggest PAA and TPX to be the optimal phantom and case materials, respectively.

Figure 2 depicts an example of a perfusion system consisting of a PAA perfusable phantom including a sugar-printed dual-bifurcation microvascular structure in a rigid TPX case. One frame of its CEUS imaging and the maximum intensity persistence of the CEUS imaging are shown, in which the dual-bifurcation structure can be clearly observed.

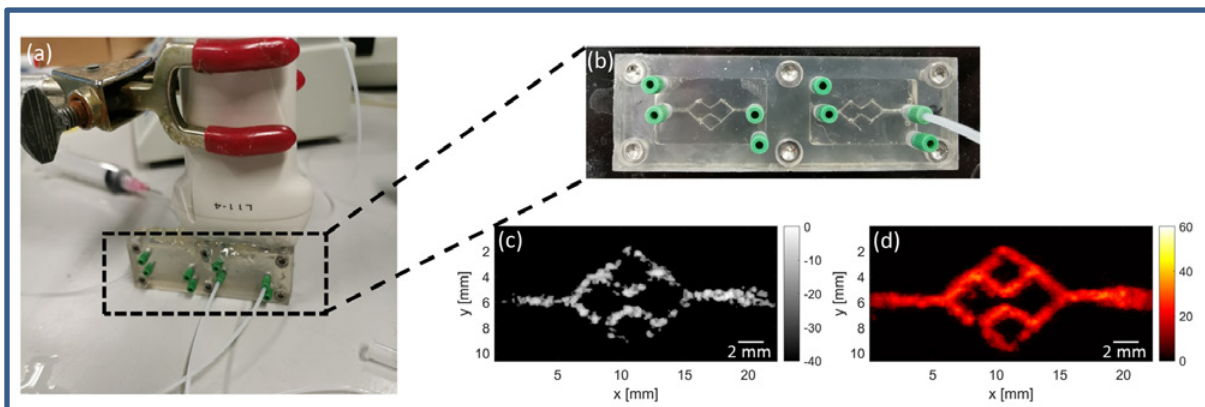


Figure 2. (a) and (b): a perfusion system consisting of PAA perfusable phantom in a rigid TPX case imaged by an ultrasound probe. The system contains two chambers, each with dimensions of  $25 \times 15 \times 5$  mm. (c): one CEUS frame of the UCA flow through the dual-bifurcation structure. (d): maximum intensity persistence of the CEUS imaging.

## Conclusions

In this work, a systematic comparison of tissue-mimicking phantom and case materials in terms of their acoustic properties, optical transparency and longevity was performed. We conclude that PAA and TPX are the optimal choice for phantom and case materials, respectively. Based on this choice, perfusion systems consisting of a perfusable phantom in a rigid case, similar to that proposed in Fig. 2, can be designed and fabricated for ultrasound perfusion imaging, allowing *in-vitro* investigation of the flow dynamics in the microvasculature.

## References

- [1]. Cosgrove D, Lassau N. Imaging of perfusion using ultrasound. *European Journal of Nuclear Medicine and Molecular Imaging*, 37: 65-85, 2010.
- [2]. Mischi M, Turco S, Soliman O, ten Cate F, Wijkstra H, Schoots I. *Quantification of contrast kinetics in clinical imaging*. Springer, 2018.

- [3]. Turco S, Frinking P, Wildeboer R, Arditi M, Wijkstra H, Lindner J, Mischi M. Contrast-enhanced ultrasound quantification: From kinetic modeling to machine learning. *Ultrasound in Medicine and Biology*, 46: 518-543, 2020.
- [4]. Chen P, Pollet A, Panfilove A, Zhou M, Turco S, den Toonder J, Mischi M. Acoustic characterization of tissue-mimicking materials for ultrasound perfusion imaging research. *Ultrasound in Medicine and Biology*, 2021.
- [5]. Cafarelli A, Verbeni A, Poliziani A, Dario P, Menciassi A, Ricotti L. Tuning acoustic and mechanical properties of materials for ultrasound phantoms and smart substrates for cell cultures. *Acta Biomaterialia*, 49: 368-378, 2017.
- [6]. Gong X, Zhu Z, Shi T, Huang J. Determination of the acoustic nonlinearity parameter in biological media using FAIS and ITD methods. *J Acoust Soc Am.*;86(1):1-5, 2005.
- [7]. Zeqiri B, Cook A, Rétat L, Civalé J, Haar G Ter. On measurement of the acoustic nonlinearity parameter using the finite amplitude insertion substitution (FAIS) technique. *Metrologia.*;52(2):406-422, 2015.
- [8]. Pollet A, Homburg E, Cardinaels R, den Toonder J. 3D sugar printing of networks mimicking the vasculature. *Micromachines*, 11(1):43, 2020.

# Refined models for oscillations of ultrasound contrast agents in the spherical and buckled configurations

G. Chabouh<sup>1</sup>, M. Mokbel<sup>2</sup>, B. Dollet, C. Quilliet<sup>1</sup>, S. Aland<sup>2</sup>, G. Couplier<sup>1</sup>

<sup>1</sup>Université Grenoble Alpes, CNRS, LIPhy, F-38000 Grenoble, France

<sup>2</sup>Technische Universität Bergakademie Freiberg, Akademiestrasse, 609599 Freiberg, Germany

Corresponding author: gwennou.couplier@univ-grenoble-alpes.fr

## Introduction

Hollow microshells have been used for decades as ultrasound contrast agents (UCAs), and their resonance frequencies in the spherical configuration have been widely studied [1]. Noteworthy, even in such a simple configuration, the existing models lack to describe accurately all experimental observations.

Vibration experiments on UCAs should a priori allow the determination of the rheological constants of the shell material, that are associated with the chosen model. Indeed, experimental determinations based on various techniques (Spectroscopy, Light scattering, Attenuation) have led to unexpected dependences of the viscoelastic moduli on shell radius, which are often observed to increase with the shell radius [2-8]. This dependence on radius of the material properties was not substantiated by physical arguments, suggesting that extra modeling was required.

Depending on the applied acoustic field, UCAs may also buckle. In [9], the current state of a suspension of UCAs is controlled by a low-frequency acoustic field while the propagation velocity of a high-frequency acoustic signal is measured. The authors observe a decrease of this sound speed while the ambient pressure is increased above a certain threshold, in marked contrast with the standard results in a simple fluid. As in other preceding works [10,11], this is interpreted as a ‘softening’ of the shell due to its buckling. This interpretation is consolidated by the existence of a hysteretic loop as the ambient pressure is varied, which is also a signature of the buckling–unbuckling transitions. A very different study reaches the same conclusion: in [12], primary Bjerkness forces on hollow micrometric shells are measured; a strong rise of this force above a given amplitude of the applied acoustic field is interpreted again as a signature of the sudden ‘softening’ of the shell. This interpretation is supported by independent measurements of the buckling pressure by pressing the probe of a Scanning Electron Microscope against the shell.

In all the above-mentioned studies, the data are not quantitatively fitted by a model. Indeed, to our knowledge, the sole model accounting for shell response in the buckled state is that of Marmottant et al. [13], which has been refined in [14]. These models assume that in the buckled configuration, the elastic response of the whole shell is simply that of the encapsulated gas while that due to shell material has disappeared, as if the shell was broken.

## Methods

Models describing spherical oscillations of UCAs were either considering zero-thickness shells or incompressible material [1]. In a recent contribution [15], we modeled the solid shell as a compressible viscoelastic isotropic material, which was then generalized to an anisotropic material – a highly relevant consideration for lipidic shells. A Rayleigh–Plesset-like equation was derived and solved analytically.

For the buckled configuration, we have stucked to a homogeneous, incompressible material as a first step, and we have described the oscillations as that of a two-variable oscillator, in a simplified model aiming at capturing the main dependency of the oscillation frequencies with the parameters of the problem. The model was confronted to 3D axisymmetric numerical simulations [16].

## Results and conclusions

For spherical oscillations, we have found exact expressions for the free pulsation of an encapsulated bubble, which could be used to interpret more accurately experimental characterization of UCAs. Our results suggest that neglecting compressibility will lead to underestimation of the shear modulus and that adding

some compressibility in the model may contribute to explain the apparent growth of the elastic moduli with the shell radius. As in a recent paper introducing more complex laws for surface tension [17], we have also shown that a precise knowledge of the inner pressure or, equivalently, of the polytropic coefficient that depends on the chosen gas and on the details of the thermodynamics process, is necessary to well understand the observed behaviours in experiments.

In spite of the potentially huge number of deformation modes of a buckled shell, its dynamics can be described by a pair of coupled oscillators. The two resulting modes decouple in the high inner pressure limit and can be identified as the surface oscillation mode and the volume oscillation mode. The former corresponds to the lowest frequency and contributes more to the overall signal than the high frequency mode. Both frequencies are much lower than that in the spherical case. This confirms and quantifies the apparent softening of buckled shells observed in the literature. By contrast with previous models [13,14], we show that this softening is mainly due to the absence of contribution of the inner gas.

### References

- [1]. Helfield B., A review of phospholipid encapsulated ultrasound contrast agent microbubble physics, *Ultrasound Med. Biol.* 45, 282–300, 2018.
- [2]. Tu, J., Guan, J., Qiu, Y., and Matula, T. J., Estimating the shell parameters of SonoVueVR microbubbles using light scattering, *J. Acoust. Soc. Am.* 126, 2954–2962, 2009.
- [3]. van der Meer, S. M., Dollet, B., Voormolen, M. M., Chin, C. T., Bouakaz, A., de Jong, N., Versluis, M., and Lohse, D., Microbubble spectroscopy of ultrasound contrast agents, *J. Acoust. Soc. Am.* 121, 648–656, 2007.
- [4]. Parrales, M. A., Fernandez, J. M., Perez-Saborid, M., Kopechek, J. A., and Porter, T. M., Acoustic characterization of monodisperse lipid-coated microbubbles: Relationship between size and shell viscoelastic properties, *J. Acoust. Soc. Am.* 136, 1077–1084, 2014.
- [5]. Helfield, B. L., and Goertz, D. E., Nonlinear resonance behavior and linear shell estimates for Definity and Micromarker assessed with acoustic microbubble spectroscopy, *J. Acoust. Soc. Am.* 133, 1158–1168, 2013.
- [6]. Doinikov, A. A., Haac, J. F., and Dayton, P. A., Modeling of non-linear viscous stress in encapsulating shells of lipid-coated contrast agent microbubbles, *Ultrasonics* 49, 269–275, 2009.
- [7]. Li, Q., Matula, T. J., Tu, J., Guo, X., and Zhang, D., Modeling complicated rheological behaviors in encapsulating shells of lipid-coated microbubbles accounting for nonlinear changes of both shell viscosity and elasticity, *Phys. Med. Biol.* 58, 985–998, 2013.
- [8]. Chetty, K., Stride, E., Sennoga, C. A., Hajnal, J. V., and Eckersley, R. J., High-speed optical observations and simulation results of SonoVue microbubbles at low-pressure insonation, *IEEE Trans. Ultrason. Ferroelectr. Freq. Control* 55, 1333–1342, 2008.
- [9]. Renaud G, Bosch JG, van der Steen AFW, de Jong N., Dynamic acousto-elastic testing applied to a highly dispersive medium and evidence of shell buckling of lipid-coated gas microbubbles, *J. Acoust. Soc. Am.* 138, 2668–2677, 2015.
- [10]. Trivett D, Pincon H, Rogers P., Investigation of a three-phase medium with a negative parameter of nonlinearity. *J. Acoust. Soc. Am.* 119, 3610–3617, 2006.
- [11]. Zaitsev V, Dyskin A, Pasternak E, Matveev L., Microstructure-induced giant elastic nonlinearity of threshold origin: mechanism and experimental demonstration. *Europhys. Lett.* 86, 44005, 2009.
- [12]. Memoli G, Baxter KO, Jones HG, Mingard KP, Zeqiri B., Acoustofluidic measurements on polymer-coated microbubbles: primary and secondary Bjerknes forces. *Micromachines* 9, 404, 2018.
- [13]. Marmottant P, van der Meer S, Emmer M, Versluis M, de Jong N, Hilgenfeldt S, Lohse D., A model for large amplitude oscillations of coated bubbles accounting for buckling and rupture. *J. Acoust. Soc. Am.* 118, 3499–3505, 2005.
- [14]. Sijl J, Overvelde M, Dollet B, Garbin V, de Jong N, Lohse D, Versluis M., ‘Compression-only’ behavior: a second-order nonlinear response of ultrasound contrast agent microbubbles, *J. Acoust. Soc. Am.* 129, 1729–1739, 2011.
- [15]. Chabouh G, Dollet B, Quilliet C, Coupier G., Spherical oscillations of encapsulated microbubbles: effect of shell compressibility and anisotropy, *J. Acoust. Soc. Am.* 149, 1240–1257, 2021.
- [16]. Mokbel M, Djellouli A, Quilliet C, Aland S, Coupier G., Post-buckling dynamics of spherical shells, *Proc. R. Soc. A*, 477, 20210378, 2021.
- [17]. Dash N., Tamadapu G., Radial dynamics of an encapsulated microbubble with interface energy, *Arxiv* 2105:03039, 2021.

# Normalized Singular Spectrum Area Measurement of Simulated Microbubble Signals in a Vessel Phantom

Yi Huang<sup>1</sup>, Elizabeth B. Herbst<sup>1</sup>, John A. Hossack<sup>1</sup>

<sup>1</sup>Department of Biomedical Engineering, University of Virginia, Charlottesville, USA  
Corresponding author: jh7fj@virginia.edu

## Introduction

Targeted contrast agents, comprising gas-filled microbubbles (MBs) conjugated with disease specific ligands, are used to enhance the utility of diagnostic ultrasound molecular imaging. The differentiation between the adherent (molecularly bounded) MBs and non-adherent (free) MBs can provide us with a better understanding about the MB dynamics during exposure to blood flow. Previous studies from our lab [1], both *in vitro* and *in vivo*, have demonstrated that the normalized singular spectrum area (NSSA) measurement had excellent performance in terms of differentiating the adherent MB signals (intermediate NSSA value) from non-adherent MB signals (high NSSA value) as well as identifying tissue signals (low NSSA value). In this study, we developed a simulation method to test the hypothesis that the intermediate NSSA values observed in adherent MBs are due to their micro scale displacements along the vessel wall.

## Methods

NSSA is a singular value decomposition (SVD) derived metric, which calculates the ratio between the summation of all singular values and the highest singular value of the matrix [2]. The simulated image was generated by the convolution of the input objects and the point spread function (PSF) of the imaging system. We set the PSF to match the imaging configuration of the ATL L12-5 transducer used in our prior *in vitro* experiments. A single scatterer point, with high signal intensity, was located in the vessel region to represent a MB. A population of random scatterers, of moderate intensity, outside the vessel region were used to provide background static tissue speckle.

The non-adherent MBs were distributed randomly throughout the lumen of simulated vessel, and they were set to displace at a rate of 2-10 mm per frame in lateral dimension. To simulate the adherent MBs bounding to the vessel wall and oscillating under blood flow, we located them in a specific region on the bottom wall and allowed them to displace at a rate of 1-10  $\mu\text{m}$  per frame moving back and forth along the vessel.

To closely match the loss of signal to noise ratio (SNR) with depth in prior experiments [3], we added the background noise simulated as a Gaussian noise increasing from 10dB to 20dB through the image depth. To study the sensitivity of NSSA to frequency shift, the frequency set in PSF was varied from 5% to 20% to match the reported resonance frequency differences between adherent MBs and non-adherent MBs [4].

## Results

The comparison between our simulated result and prior experimental result is shown in Fig. 1 (a) and (b). The corresponded NSSA mapping results were able to highlight the adherent MB signal as intermediate NSSA value and differentiate it from the free MB signal and the background tissue. We include receiver operating characteristic (ROC) analysis based on the histogram counts of NSSA value in Fig. 1(c) for quantitative specificity study. For the static tissue and adherent MBs, the AUC=0.98. For the adherent MBs and non-adherent MBs, the AUC=0.90. After the frequency shifted by 15%, the distribution of intermediate NSSA value on adherent MBs had a significant difference from the initial result as shown in Fig. 1(d).

## Conclusions

Our work successfully simulated the physical interactions of MBs and the micro scale displacements of adherent MBs led to detectable intermediate NSSA values, which can be used to differentiate adherent MBs from free MBs and background tissues. The frequency shift will give rise to detectable higher singular values

of adherent MB signals and change the NSSA, which provides a good perspective to analyze the sensitivity of NSSA measurement in the future.

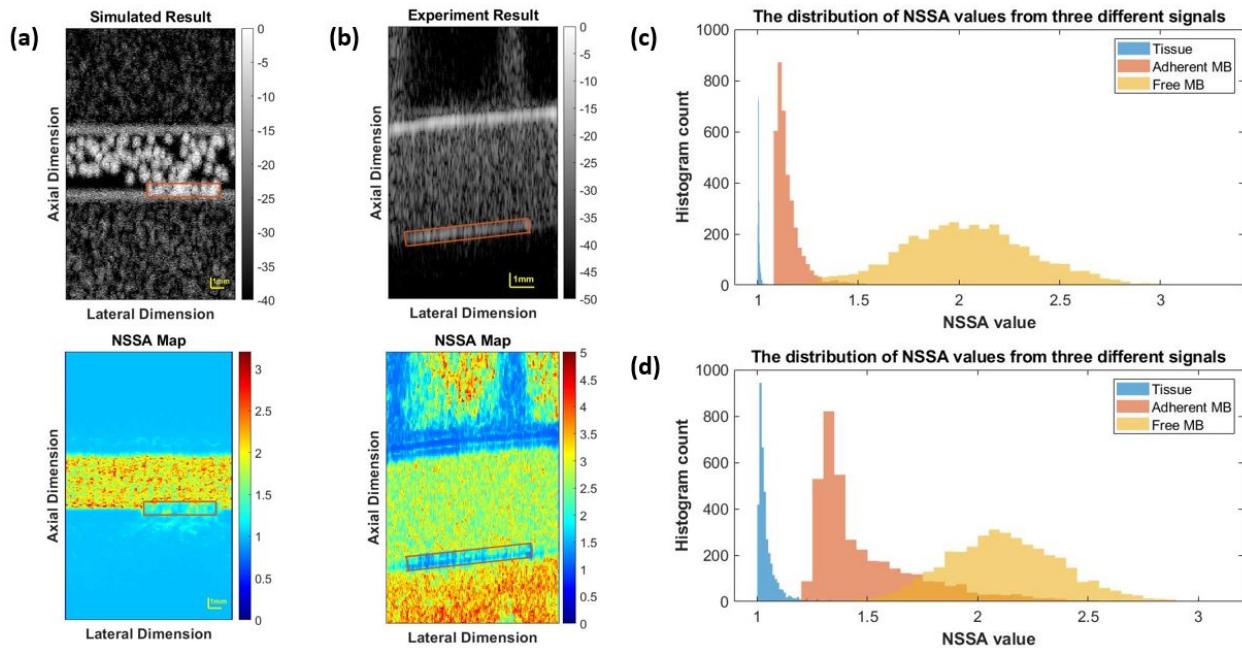


Figure 1. (a) Above: the simulated ultrasound image; Below: NSSA measurements from the simulated image. Red rectangular represents the adherent MBs and their intermediate NSSA value. (b) Above: the *in vitro* ultrasound image; Below: NSSA measurements from the experimental image. Red rectangular represents the adherent MBs and their intermediate NSSA value. (c) The histogram of NSSA values. (d) The histogram of NSSA values after the frequency shifted by 15%.

## References

- [1] E. B. Herbst, S. Unnikrishnan, A. L. Klibanov, F. W. Mauldin, and J. A. Hossack, "Validation of Normalized Singular Spectrum Area as a Classifier for Molecularly Targeted Microbubble Adherence," *Ultrasound Med. Biol.*, vol. 45, no. 9, pp. 2493–2501, Sep. 2019, doi: 10.1016/j.ultrasmedbio.2019.05.026.
- [2] F. W. Mauldin, D. Lin, and J. A. Hossack, "The Singular Value Filter: A General Filter Design Strategy for PCA-Based Signal Separation in Medical Ultrasound Imaging," *IEEE Trans. Med. Imaging*, vol. 30, no. 11, pp. 1951–1964, Nov. 2011, doi: 10.1109/TMI.2011.2160075.
- [3] S. Wang, F. W. Mauldin, A. L. Klibanov, and J. A. Hossack, "Shear forces from flow are responsible for a distinct statistical signature of adherent microbubbles in large vessels," *Mol. Imaging*, vol. 12, no. 6, pp. 396–408, Sep. 2013.
- [4] J. S. Lum, V. Daeichin, D. F. Kienle, D. K. Schwartz, T. W. Murray, and M. A. Borden, "Changes in microbubble dynamics upon adhesion to a solid surface," *Appl. Phys. Lett.*, vol. 116, no. 12, p. 123703, Mar. 2020, doi: 10.1063/1.5135017.

# Volumetric Imaging of Microbubbles Using a Sparse Array and Deep Learning based Adaptive Beamforming

***Boudewine W. Ossenkoppele<sup>1</sup>, Luxi Wei<sup>2</sup>, Ben Luijten<sup>3</sup>, Hendrik J. Vos<sup>1,2</sup>, Nico de Jong<sup>1,2</sup>, Ruud J.G. van Sloun<sup>3,4</sup>, Martin D. Verweij<sup>1,2</sup>***

<sup>1</sup>*Laboratory of Medical Imaging, Department of Imaging Physics, Delft University of Technology, Delft, The Netherlands,*

<sup>2</sup>*Thoraxcenter, Dept Biomedical Engineering, Erasmus University Medical Center Rotterdam, Rotterdam, the Netherlands*

<sup>3</sup>*Department of Electrical Engineering, Eindhoven University of Technology, Eindhoven, The Netherlands,*

<sup>4</sup>*Philips Research, Eindhoven, The Netherlands*

*Corresponding author: B.W.Ossenkoppele@tudelft.nl*

## Introduction

Three-dimensional imaging for ultrasound localization microscopy has significant advantages. It enables motion correction in all three dimensions and can provide a more complete picture of the micro-vasculature compared to a single intersecting plane. Sparse arrays have advantages in realizing three-dimensional images compared to fully populated matrix arrays in terms of cost, cable count and data rate. However, sparse arrays come with other challenges including a low SNR and high variation of magnitude and pulse shape within the field. When beamforming with Delay-And-Sum (DAS), strong clutter due to grating lobes from contrast agents will be present, which can prevent the correct detection and localization of microbubbles. Deep learning based methods have been introduced to improve microbubble localization [1], both on beamformed images and in combination with deep learning based adaptive beamforming (ABLE) [2], [3] for linear and phased arrays. Here we implement deep learning based adaptive beamforming for a sparse array and compare the 3D detection and localization of microbubbles in w.r.t. that achieved with traditional DAS beamforming.

## Methods

A 5 MHz prototype sparse array with a tapered spiral design consisting of 256 elements of 200  $\mu\text{m}$  x 200  $\mu\text{m}$  was used [4]. Of the 1.6 cm diameter aperture only the center 120 elements within a 7 mm diameter were used to transmit a diverging wave with 30° opening angle, as described in [5]. The RF echoes were beamformed with either a DAS beamformer or modified ABLE beamformer. ABLE learns adaptive apodization weights and the network is trained with a signed-mean-squared-logarithmic loss function. The ABLE beamformer was modified to increase the receptive field to 2.5 wavelengths in all directions and was trained with simulations of point scatterers, generated with Field II. The target data consisted of volumetric data patches, containing the actual location of the point scatterer convolved with a small 3D gaussian. The input data consisted of the pre-delayed RF data. Individual microbubbles were segmented based on voxel intensity, followed by the estimation of their center of mass according to the identification algorithm in [6].

## Results

The ABLE beamformed images visually contain less clutter than the DAS beamformed images. When DAS beamforming is used more localization errors of the simulated microbubbles are made than after beamforming with ABLE (see Figure 1).

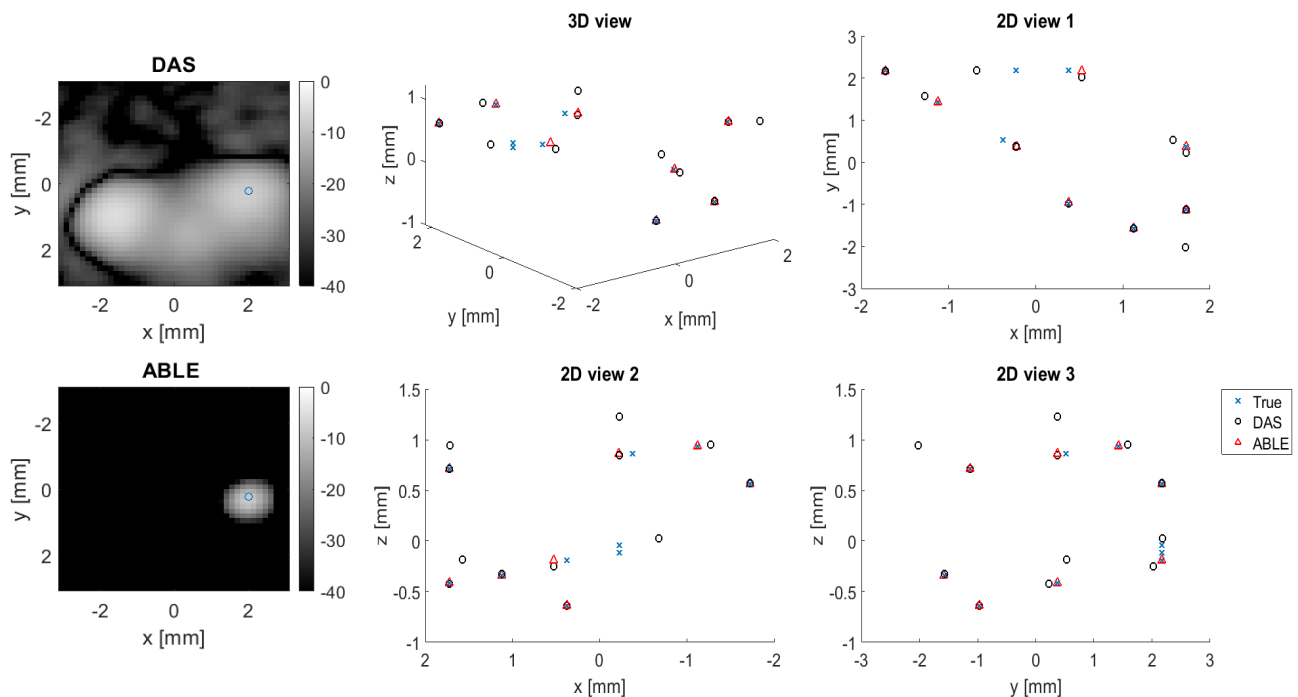


Figure 1. *Left)* An axial image slice after beamforming with DAS and ABE, the true location of the simulated microbubble is also shown as the blue circle. *Right)* A comparison of the 3D localization of simulated microbubbles after DAS and ABE beamforming. True locations are also shown.

## Conclusions

We implemented a deep learning based adaptive beamformer for microbubble imaging with a spiral array. We showed that ABE enabled better detection and localization of simulated microbubbles than the traditional DAS beamformer.

## References

- [1]. R. J. G. Van Sloun, O. Solomon, M. Bruce, Z. Z. Khaing, H. Wijkstra, Y. C. Eldar, and M. Mischi, "Super-Resolution Ultrasound Localization Microscopy through Deep Learning," *IEEE Trans. Med. Imaging*, 2021.
- [2]. B. Luijten, R. Cohen, F. J. De Bruijn, H. A. W. Schmeitz, M. Mischi, Y. C. Eldar, and R. J. G. van Sloun, "Adaptive ultrasound beamforming using deep learning," *IEEE Trans. Med. Imag.*, 2020.
- [3]. J. Youn *et al.*, "Model-based Deep Learning on Ultrasound Channel Data for Fast Ultrasound Localization Microscopy," *2021 IEEE International Ultrasonics Symposium (IUS)*, 2021, pp. 1-4.
- [4]. A. Ramalli, E. Boni, A. S. Savoia, and P. Tortoli, "Density-tapered spiral arrays for ultrasound 3-D imaging," *IEEE Trans. Ultrason., Ferroelectr., Freq. Control*, vol. 62, no. 8, pp. 1580–1588, Aug. 2015.
- [5]. L. Wei, G. Wahyulaksana, B. Meijlink, A. Ramalli, E. Noothout, M. D. Verweij, E. Boni, K. Kooiman, A. F. W. Van Der Steen, P. Tortoli, N. De Jong, and H. J. Vos, "High Frame Rate Volumetric Imaging of Microbubbles Using a Sparse Array and Spatial Coherence Beamforming," *IEEE Trans. Ultrason. Ferroelectr. Freq. Control*, vol. 68, no. 10, pp. 3069–3081, 2021.
- [6]. O. Couture and V. Hingot, "Super-resolution ultrasound," in *Proc. IEEE Ultrason. Symp.*, Sep. 2020.

## Size-Dependance of Microbubble Cavitation Threshold

*Alexis Vivien, Anne Lassus, Emmanuel Gaud, Victor Jeannot*

*Bracco Suisse SA, CH-1228 Plan-les-Ouates, Geneva, Switzerland*

*Corresponding author: [Alexis.Vivien@bracco.com](mailto:Alexis.Vivien@bracco.com)*

### Introduction

Microbubble cavitation is an efficient way to temporarily permeabilize blood vessels to allow therapeutic molecules, otherwise too big, to extravasate. The mechanism is efficient but relatively poorly understood, especially when it comes to link the microbubble size and the thresholds of the different cavitation regime. Indeed, most clinic microbubble formulations are polydisperse hence potentially hiding many behaviours in one.

In this study, the relation between microbubble size and cavitation threshold is addressed both *in-vitro* and *in-silico* with model-based simulations.

### Methods

For this study, a low ultrasound frequency typically used for therapeutic microbubble-enhanced ultrasound was considered, namely 250 kHz.

The study is divided in two parts, the first one comprises Matlab simulations, modeling the radius evolution of a single microbubble with time, following Marmottant's model [1], under specific acoustic conditions. Based on this simulation, the cavitation threshold was defined as the acoustic pressure for which the maximal radius expansion reaches the Blake critical radius [2] leading to explosive growth.

The other part is the result of *in-vitro* cavitation experiments, recording microbubble acoustic response as a function of acoustic pressure. The metrics used to characterize stable and inertial cavitation are respectively the ultraharmonics (UH) and broadband noise (BB) levels. Once the levels are collected, the acoustic pressure at which either ultraharmonic or broadband noise signal arises is defined as the cavitation threshold respectively stable and inertial.

A home-made polydisperse microbubble formulation, with diameter ranging roughly from 0.2 to 7  $\mu\text{m}$ , was used for *in-vitro* experiment. Cavitation thresholds were measured for the native formulation as well as for sub-populations of different sizes obtained by centrifugation/washing process. Three sub-populations were considered, namely diameter  $< 1 \mu\text{m}$ , 1-3  $\mu\text{m}$  diameter and diameter  $> 3 \mu\text{m}$ .

In addition, based on the initial Coulter Counter distribution of the polydisperse agent, the excursion radius of each microbubble size present in the distribution was calculated using Marmottant's model for different acoustic pressures and Coulter-like distributions were calculated with the maximum diameter reached during the oscillation.

## Results

Modeling clearly shows a decrease of the cavitation threshold when the microbubble size increases (Figure 1).

*In vitro* measurements confirm this behaviour, since the sub-population with a maximum microbubble size of 1  $\mu\text{m}$  shows a cavitation threshold significantly higher than other samples containing microbubbles of 3  $\mu\text{m}$  or larger (Figure 1).

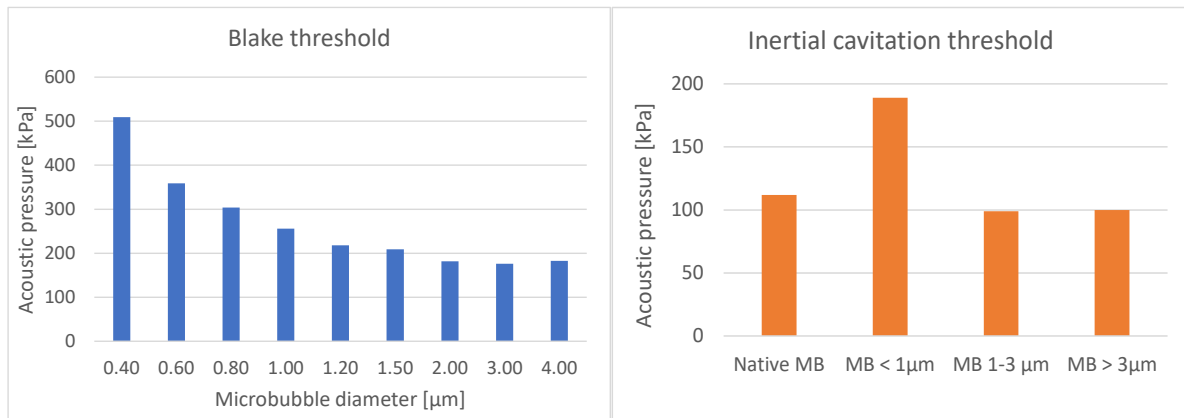


Figure 1: Left: Simulated Blake threshold as a function of microbubble size. Right: Measured inertial cavitation threshold (broadband noise onset) of the different sub-populations (Native, < 1  $\mu\text{m}$ , 1-3  $\mu\text{m}$  and > 3  $\mu\text{m}$ )

Interestingly the simulated Blake threshold appears higher than the inertial cavitation threshold measured *in vitro*: 250 kPa vs. 190 kPa for 1  $\mu\text{m}$  microbubble and 180 kPa vs. 100 kPa for 3  $\mu\text{m}$  microbubbles. This means that inertial cavitation (generating broadband noise echo) already exists at acoustic pressure lower than Blake threshold which corresponds to explosive growth of the microbubble.

The Coulter-like distributions of the expansion diameter at different acoustic pressures (Figure 2) show that, at 250 kPa, microbubbles up to 1  $\mu\text{m}$  experience very little expansion whereas for larger microbubbles, expansion explodes in agreement with Blake threshold. At 400 kPa, all the microbubbles of the distribution (0.7  $\mu\text{m}$  and higher) show this large expansion ratio.

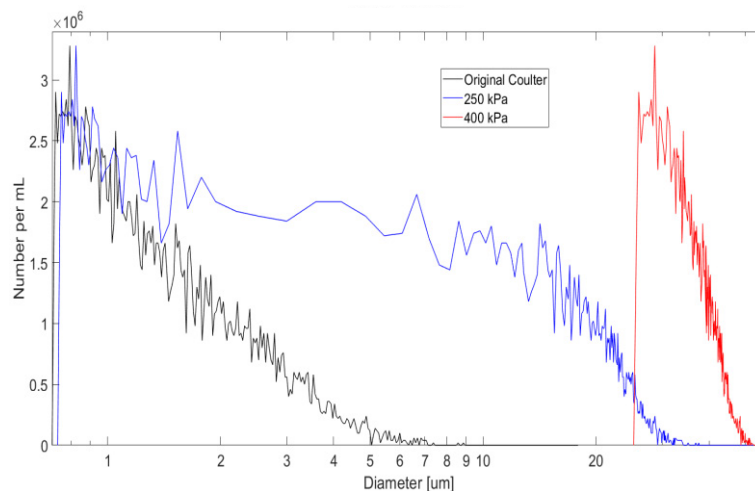


Figure 2: Simulated Coulter-like distribution of the maximum expansion diameter at 0, 250 and 400 kPa

## Conclusion

This study clearly shows the strong dependency existing between microbubble size and cavitation threshold, the smallest microbubbles having the hardest time entering either of the cavitation regime.

This relation has to be carefully considered when tuning acoustic parameters for therapeutic applications.

It should be mentioned that measurements performed at 500 kHz showed similar results (not shown) with slightly higher cavitation thresholds.

This work also highlights the fact that microbubbles can in theory reach immense radius while expanding, this at relatively low acoustic pressures, but it must be noted that modeling describes microbubble dynamic in a free-field environment without taking into account the confinement in the vessels which may dampen oscillation.

Cavitation thresholds experimentally assessed through broadband noise onset are slightly lower than the threshold for explosive growth given by Blake model. This supports the use of passive cavitation detection as a valuable tool to prevent these large excursion radii from occurring during microbubble-enhanced ultrasound therapy.

## References

- [1]. Marmottant, van der Meer, Emmer, Versluis, de Jong, Hilgenfeldt, Lohse. A model for large amplitude oscillations of coated bubbles accounting for buckling and rupture. *J.Acoust.Soc.Am.* 118(6), 3499-3505. 2005.
- [2]. T.G Leighton. *The Acoustic Bubble*. Academic Press, 1994, pp 85-86

## Microbubble dynamics in brain microvessels

*James H. Bezer<sup>1</sup>, Paul Prentice<sup>2</sup>, William Lim Kee Chang<sup>1</sup>, Sophie V Morse<sup>1</sup>,  
Christopher J. Rowlands<sup>1</sup>, Kirsten Christensen-Jeffries<sup>3</sup>, Andrei S. Kozlov<sup>1</sup>, James J. Choi<sup>1</sup>*

<sup>1</sup>Department of Bioengineering, Imperial College London, United Kingdom

<sup>2</sup>School of Engineering, University of Glasgow, United Kingdom

<sup>3</sup>Department of Biomedical Engineering, King's College London

Corresponding author: j.choi@imperial.ac.uk

### Introduction

Blood-brain barrier (BBB) disruption using ultrasound-driven microbubbles is a promising technique for delivering drugs to the brain. However, its physical mechanisms are not fully understood. This study aimed to directly observe the physical interactions between single microbubbles and brain microvessels using high- and ultra-high-speed microscopy.

### Methods

Acute brain slices were obtained from juvenile rats which had been transcidentally perfused with SonoVue, heparin, and dye. In each slice, a suitable bubble in a microvessel (5-15  $\mu\text{m}$  diameter) was found and its behaviours during an ultrasound pulse were observed using high-speed microscopy. Typical BBB opening pulses were used, with a centre frequency of 1 MHz, peak negative pressures of 0.2-1 MPa, and pulse lengths of up to 10,000 cycles. Bubble dynamics were tracked at both microsecond and millisecond time scales. Volumetric oscillations were observed over 15 cycles at 10 Mfps using a Shimadzu HPV-X2 ultra-high speed camera. Bubble and tissue motions over 10 ms pulses were observed at 5.58 kfps.

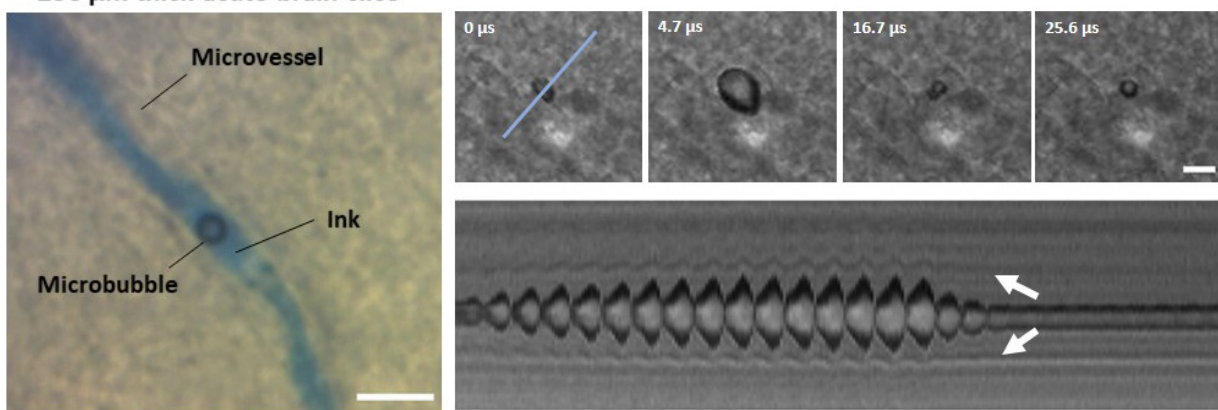
### Results

Oscillating microbubbles caused microvessel walls to distend and invaginate at the ultrasound driving frequency. In many instances, the oscillations generated micron-scale tissue displacements well beyond the vessel boundary. Bubble oscillations in small microvessels are often asymmetric. Microbubbles can be forced out of small microvessels due to the primary radiation force; this was more common at higher pressures.

### Conclusions

Under typical BBB opening ultrasound parameters, microbubbles can exert significant forces on brain microvessels, generating rapid micrometre-scale tissue displacements. Microbubble extravasation due to the primary radiation force may be a mechanism of BBB disruption or of tissue damage. These results enhance our understanding of bubble behaviours in brain tissue, and may aid the development of safer and more effective clinical therapies.

#### 250 $\mu\text{m}$ thick acute brain slice



Left: Example microbubble in a microvessel of a brain slice. Right: Frames from 10 Mfps video of microbubble sonicated at 1 MHz, 0.8 MPa, with streak image along blue line (below). Arrows: vessel walls. Scale: 10  $\mu\text{m}$

## Smart biomaterials: Exploiting protein mechanics for ultrasound stimulated drug release

*Christa P. Brown<sup>1</sup>, Sally A. Peyman<sup>1</sup>, P. Louise Coletta<sup>2</sup>, Stephen D. Evans<sup>1</sup>, Lorna Dougan<sup>1,3</sup>*

<sup>1</sup>*School of Physics and Astronomy, University of Leeds, Leeds, U.K.*

<sup>2</sup>*Leeds Institute of Medical Research, St James' University Hospital, Leeds, U.K.*

<sup>3</sup>*Astbury Centre for Structural Molecular Biology, University of Leeds, Leeds, U.K.*

*Corresponding author: py14cpb@leeds.ac.uk*

### Introduction

Folded proteins have a variety of different functions in biological systems: incorporating these functions into rationally designed, folded protein hydrogels provides opportunity for developing responsive drug delivery systems [1,2]. Acoustic responsive hydrogels from the inclusion of microbubbles and acoustic responsive droplets have shown success in controlling the stiffness of the gel to mimic tissues and release drugs [3,4]. In this study, we investigate the potential for ultrasound responsive drug release from protein hydrogels by embedding microbubbles [5,6] within bovine serum albumin (BSA) as a model protein hydrogel. Initial findings show that the inclusion of microbubbles significantly changes the mechanics of the BSA hydrogels, without affecting the folded fraction of protein (Fig. 1B and 1C). After characterising the MB embedded within the BSA hydrogel, we will move on to the use of ultrasound on MB in BSA hydrogels for on-demand drug system.

### Methods

Phospholipid stabilised MBs with a C4F10 gas core were produced in 25 mM sodium phosphate and 1% (v/v) glycerol buffer. Due to their buoyancy, MBs greater than 2  $\mu\text{m}$  were separated via floatation. Optical microscopy (Nikon 90i) was used to determine the size distribution and concentration of population of the MBs [7]. The BSA pre-gel solution was prepared as stated previously [8], but with the addition of 1% glycerol to the buffer. BSA hydrogels were produced by exposing the pre-gel solution to a blue lamp (452 nm, 9W) source for 5 minutes causing the crosslinking of dityrosines between BSA monomers. To produce BSA hydrogels with embedded MBs, were diluted and mixed into the pre-gel solution with the same gelation procedure.

Circular dichroism spectra (CD) was used to determine the folded fraction of the BSA gelation using the set up described in [8]. Rheology experiments on the BSA hydrogels were performed with a stress controlled rheometer (Anton Parr MCR 502) using a parallel plate. Oscillatory time sweeps of BSA hydrogel were used to determine the storage ( $G'$ ) and loss ( $G''$ ) moduli with oscillation frequency of 1 Hz and shear strain of 0.5%. In each time sweep the pre-gel solution is exposed to the blue light after 30 seconds for 5 mins. To prevent evaporation of the sample throughout the experiment, silicone oil with a low viscosity (5ct) covered the air-sample interface.

### Results

Fig. 1A shows that the stiffness of the BSA hydrogels was reduced with increasing concentrations of MBs, characterised by a lower storage modulus ( $G'_{\infty}$ ); the standard hydrogel in the absence of MBs had a storage modulus of  $1900 \pm 100$  Pa, and was reduced to  $1600 \pm 200$  Pa with the addition of  $10^9$  MB/mL. The CD spectra found that BSA gel without MBs had a folded protein fraction of  $81.4 \pm 0.9\%$  and the inclusion  $10^9$  MB/mL had a folded protein fraction of  $79.9 \pm 0.8\%$ . The addition of microbubbles to the BSA hydrogel does not significantly cause unfolding of the protein, therefore changes in the BSA hydrogel mechanics can be ruled out as not due to protein unfolding shown in Fig. 1D and 1E. This therefore suggests that the microbubbles reduce the chance for crosslinks to form between BSA monomers, and as a result reduces the overall stiffness of the final BSA hydrogel.

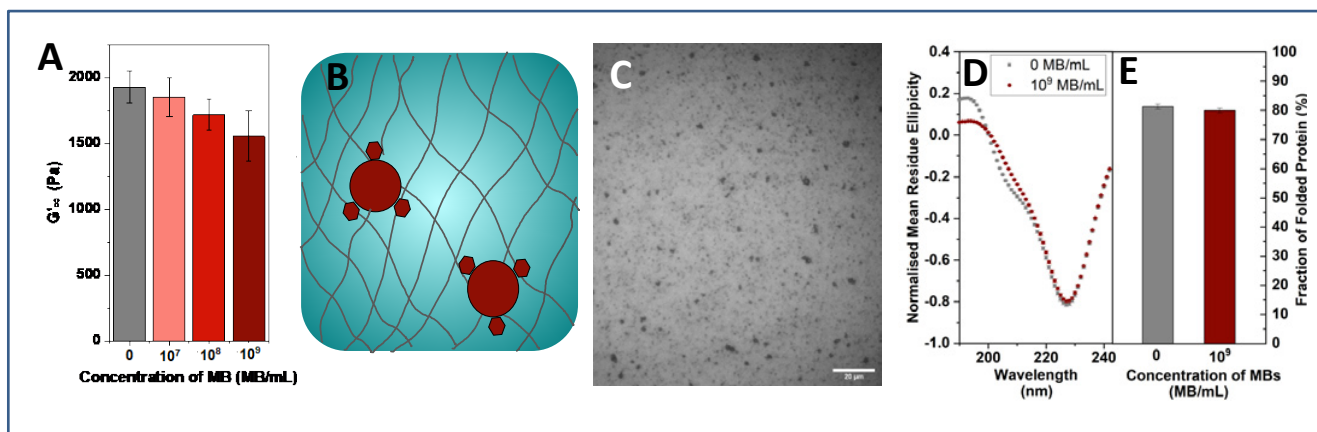


Figure 1. (A) The mechanical properties of the cross-linked protein hydrogels are measured using rheology and the impact of increasing concentrations of embedded microbubbles (MBs) are determined. With increasing concentration of MB the final storage modulus ( $G'_{\infty}$ ) decreases. (B) Schematic (not to scale) of drug-loaded MBs (red) encapsulated in a cross-linked protein hydrogel, with inset showing the expected network of folded bovine serum albumin (BSA) protein (grey) clusters connected by chains of folded BSA molecules. (C) Bright field microscopy of MBs encapsulated in the cross-linked BSA protein hydrogel, scale bar is 20  $\mu\text{m}$ . (D) CD spectra of the cross-linked BSA protein hydrogel (grey) and the BSA hydrogel with 10<sup>9</sup> MBs/mL (red), (E) compares the folded fraction of BSA protein in the absence (grey) and presence (red) of MBs.

## Conclusions

The inclusion of microbubbles has shown that the stiffness of BSA hydrogel can be finely controlled without affecting the folded fraction of the protein. The addition of 10<sup>9</sup> MB/mL caused a reduction the final storage modulus of hydrogel from 1900  $\pm$  100 for the standard BSA hydrogel to Pa 1600  $\pm$  200 Pa in the presence of 10<sup>9</sup> MB/mL, allowing for matching the stiffness to the appropriate tissue. Further work is required to understand how the use of ultrasound on BSA hydrogels effects the percentage of folded BSA and mechanics of the hydrogel, before moving on to investigating the system for ultrasound responsive drug release.

## References

- [1]. Hughes, M, et al., (2020) *Soft Matter*, 16, 6389-6399
- [2]. Hanson, SB, Dougan L (2020) *Macromolecules*, 53, 17, 7335-7345
- [3]. Huang D, et al., (2019) 7, 14, 2330-2337
- [4]. Lima, E, et al., (2012) *Acta Biomaterialia*, 8, 12, 4334-4341
- [5]. Abou-Saleh R, et al., (2013) *Langmuir*, 29, 4096-4103
- [6]. Bourn, MD et al., (2020) *Journal of Controlled Release*, 326, 13-24
- [7]. Abouh-Saleh R, et al. (2021) *Review of Scientific Instruments*, 92, 074105
- [8]. Hughes M, et al., (2021) *ACS Nano*. 15, 17, 11296-113808

# High-intensity focused ultrasound to induce and boost anti-tumor immunity

Y. Engelen<sup>1</sup>, H. Dewitte, S. De Smedt<sup>1</sup>, G.P.R. Lajoinie<sup>2\*</sup>, I. Lentacker<sup>1\*</sup>

<sup>1</sup> Ghent Research Group on Nanomedicines, Laboratory of General Biochemistry and Physical Pharmacy, Faculty of Pharmaceutical Sciences, Ghent University, Ottergemsesteenweg 460, 9000, Ghent, Belgium

<sup>2</sup> Physics of Fluids group, MIRA Institute of Biomedical Technology and Technical Medicine, University of Twente, Enschede, Netherlands

\*shared senior authorship

Corresponding author: yanou.engelen@UGent.be

## Introduction

The aim of cancer immunotherapy is to activate T cells to drive anticancer immunity which partially depends on antigen presentation by mature dendritic cells. Personalized vaccines comprising patient-derived DCs loaded *ex vivo* with tumor antigens, have seen some extensive research and progress in the past decade<sup>1</sup>. However, the costly and laborious manufacturing process remain substantial bottlenecks for the widespread use and application of personalized DC-vaccines, as such the focus has shifted to *in vivo* delivery of tumor antigens to DCs. One strategy that can achieve this is an immunogenic cell death (ICD) inducing therapy.

An immunogenic tumor microenvironment (TME) can be created by exploiting ICD, a common denominator for a variety of cell death pathways, resulting in the presence of damage-associated molecular patterns (DAMPs) that recruit and activate DCs in the TME. DAMPs linked to ICD are calreticulin (CRT), ATP, HMGB1 and type I IFNs<sup>2,3</sup>. It has been shown that inducing tumor ICD provides a first onset of antitumor immunity. These findings initiated large studies to screen which known cancer therapies are *bona fide* ICD-inducers<sup>4</sup>. While these studies largely focus on chemotherapy drugs, more physical techniques to tackle cancer are also studied, incl. high-intensity focused ultrasound (HIFU)<sup>5,6</sup>.

HIFU uses ultrasound (US) waves to locally heat (thermal HIFU) or mechanically disrupt (mechanical HIFU) tumors and is used to non-invasively treat a.o. prostate and breast cancer<sup>7,8</sup>. In the clinic, the main focus currently lies on thermal HIFU to rapidly and non-invasively debulk solid tumors by locally heating tumors to temperatures that cause coagulative necrosis. Few studies reported that thermal HIFU caused a pronounced increase in immune cell infiltration around the treated region, incl. tumor-specific T cells<sup>9,10</sup>. However, study outcome was often disappointing as only a limited increase in overall survival was shown, even when HIFU therapy was combined with immune checkpoint inhibitors and immune adjuvants<sup>7,11</sup>. A possible explanation for these disappointing results can be found in the specific HIFU parameters that were based on clinical settings developed to induce quick and complete tumor destruction via thermal ablation. Making is of continuous US and high acoustic pressures (>15 MPa)<sup>5,8</sup>. However, a coagulated tumor becomes impermeable for immune cells and it is unlikely that these cells or therapeutics that are delivered at later time points can reach the tumor tissue efficiently<sup>12,13</sup>. Also, experimental data indicate a higher immune cell infiltration after mechanical compared to thermal HIFU<sup>5,8,14</sup>. In these settings short (100 to 1000 cycles) but intense acoustic pulses (>60 MPa) are applied to induce tumor ablation via histotripsy promoting the release of tumor antigens via cell fractionation<sup>5,14,15</sup>.

## Methods

CT26 colon cancer cells (ATCC<sup>®</sup>, CRL-2638<sup>™</sup>) were treated with mechanical soft HIFU *in vitro* in our custom build HIFU set-up. The custom HIFU software allows control over the sample holder, the HIFU transducer and the backscatter transducer (Sonic Concepts, H-151). Also a CCD camera is built-in, which is controlled by external software. The water bath is temperature controlled, allowing to maintain the temperature of the water constant. (Fig. 1A) The cells are seeded on acoustically transparent Lumox<sup>™</sup> cell culture dishes for adherent cells. For HIFU treatment the dishes are placed in custom 3D-printed lids. (Fig. 1B) These are filled with degassed RPMI 1640 medium before they are placed in the water bath.

This set-up allows to physically validate the applied HIFU treatment by collecting and storing the acoustical signal that is received by the backscatter transducer. By linking this physical data of the applied HIFU to the biological outcome of the flow cytometry experiments, a deeper insight and understanding of the treatment can be achieved. A custom MATLAB analysis script, was used to create “heat maps” of the cavitation activity of the treated samples, and also to extract quantitative physical data for analysis. (Fig. 3)

For the flow cytometric analysis a mitochondrial probe was used, namely the Mitoprobe (DiIC<sub>1</sub>(5)) (ThermoFisher, M34151), in combination with Propidium Iodide (PI) (ThermoFisher, P1304MP). The mitoprobe accumulates in the mitochondria with active membrane potentials. The Mitoprobe staining intensity decreases when the mitochondrial membrane potential is lost or decreased. PI is not permeant to live cells, as such PI can be used to detect dead cells. The combination of a Mitoprobe (DiIC<sub>1</sub>(5)) and Propidium Iodide allows discrimination between 3 distinct populations, namely healthy, early regulated cell death and dead cells. Also, the flow cytometer in our lab, namely the MACSQuant Analyzer 16, allows us to determine the amount of cell that are still present in the sample by flowing distinct volumes. This is vital to assess how many cells have been fully destroyed by the HIFU treatment.

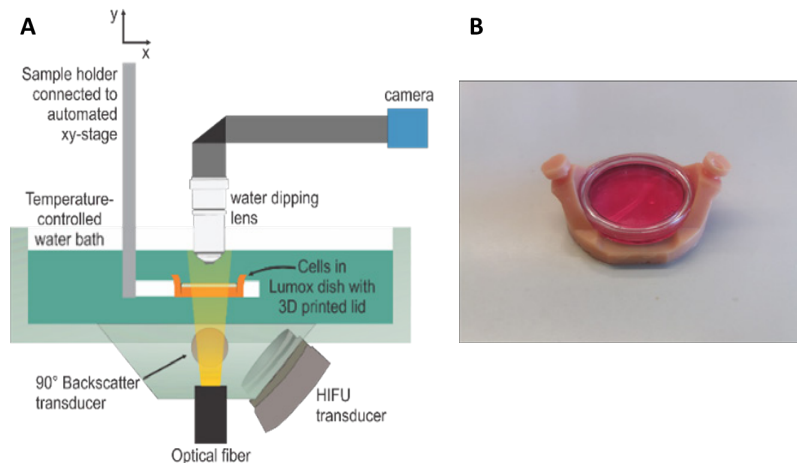


Figure 1. (A) Schematic overview of the HIFU set-up. The sample holder, the CCD camera, the HIFU transducer and the backscatter transducer are all connected to a computer, allowing full control over the set-up and HIFU regimes during treatment. The water bath in which the samples are treated is temperature controlled. The HIFU transducer is used to treat the cells and the backscatter transducer collects the acoustic backscatter signal coming from the treatment area. The collection of the backscatter signal allows quantification and visualization of the cavitation activity, and also the linking of the physical data to the biological results from the performed flow cytometry assays. (B) Custom-made 3D-printed lids that fit the acoustically transparent Lumox<sup>™</sup> adherent cell culture dishes are used to treat the CT26 cells *in vitro*.

## Results

CT26 cells were treated in our set-up with soft mechanical HIFU (1,1 MHz) consisting of varying acoustic pressures and number of cycles. Flow cytometric analysis indicates that all treated samples have strong decreases in the mitochondrial membrane potential, indicating they endured severe physical stress. (Fig. 1). However, the induced biological effect did not vary in function of the applied acoustic pressure. The analysis of the collected backscatter signal shows clear alterations between the different HIFU settings.

For instance, a significant increase in cavitation activity can be observed when comparing the “heat maps” of HIFU settings with higher acoustic pressures to those with lower acoustic pressures. (Fig. 2B-C)

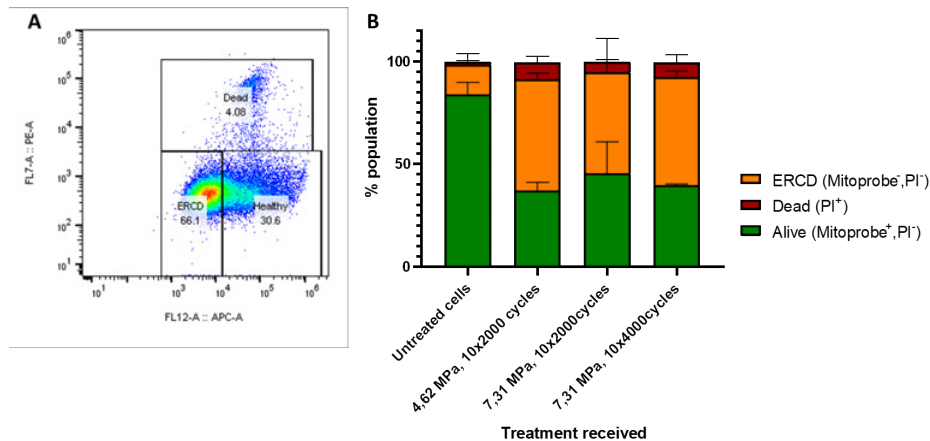


Figure 2. (A) A dot plot of the flow cytometric result of CT26 cells treated with HIFU (1,1MHz) consisting of 7,21 MPa, 2000 cycles and 10 bursts. On the x-axis the intensity for the Mitoprobe (DiIC<sub>15</sub>) and on the y-axis the intensity for PI are plotted. A decrease in intensity for the Mitoprobe indicates a loss of the mitochondrial membrane potential. The combination of these 2 dyes allow discrimination between 3 populations, namely the alive (Mitoprobe<sup>+</sup>,PI<sup>-</sup>), early regulated cell death (Mitoprobe<sup>-</sup>,PI<sup>+</sup>) and a dead population (PI<sup>+</sup>). (B) Graphical representation of flow cytometric results, showing the population distribution 6 hours after HIFU treatment.

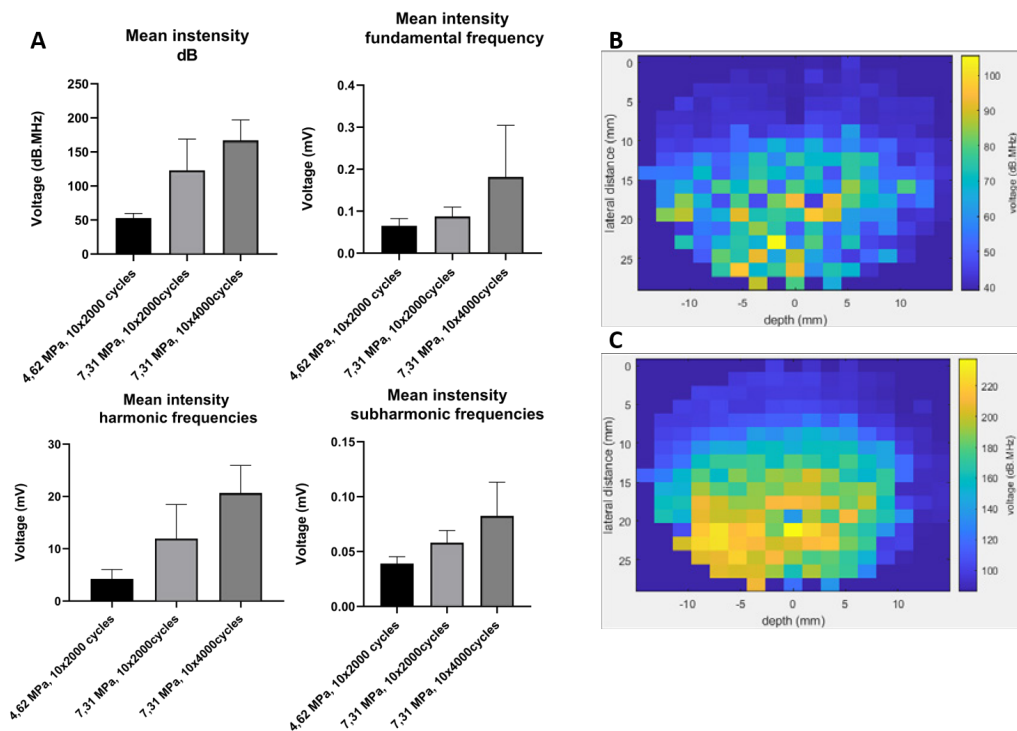


Figure 3. Physical analysis of the collected acoustical backscatter signal. (A) Graphical representation of mean intensities (dB.MHz or mV) measured in function of their respective frequencies. (B) “Heat map” of the cavitation activity of HIFU treatment consisting of 4,62 MPa, 2000 cycles and 10 bursts; (C) “Heat map” of the cavitation activity of HIFU treatment consisting of 7,31 MPa, 2000 cycles and 10 bursts.

## Conclusions

Our custom build set-up allows us to expose cancer cells to specific HIFU settings *in vitro* while simultaneously quantify cavitation activity. The cavitation maps collected during HIFU treatment show a clear increase in acoustical activity when the acoustic intensity of the HIFU signal is increased while this results in a pronounced decrease in mitochondrial membrane potential. Further experiments are planned to evaluate the expression of their ICD hallmarks and elucidate the impact of different HIFU parameters.

## References

- [1] Perez CR, De Palma M. Engineering dendritic cell vaccines to improve cancer immunotherapy. *Nat Commun.* 2019;10(1):1-10. doi:10.1038/s41467-019-13368-y
- [2] Kielbik M, Szulc-kielbik I, Klink M. Calreticulin — Multifunctional Chaperone in Immunogenic Cell Ovarian Cancer Patients. Published online 2021.
- [3] Solari JIG, Filippi-Chiela E, Pilar ES, et al. Damage-associated molecular patterns (DAMPs) related to immunogenic cell death are differentially triggered by clinically relevant chemotherapeutics in lung adenocarcinoma cells. *BMC Cancer.* 2020;20(1):1-14. doi:10.1186/s12885-020-06964-5
- [4] Kroemer G, Galluzzi L, Kepp O, Zitvogel L. Immunogenic cell death in cancer therapy. *Annu Rev Immunol.* 2013;31:51-72. doi:10.1146/annurev-immunol-032712-100008
- [5] Hoogenboom M, Eikelenboom D, den Brok MH, Heerschap A, Fütterer JJ, Adema GJ. Mechanical High-Intensity Focused Ultrasound Destruction of Soft Tissue: Working Mechanisms and Physiologic Effects. *Ultrasound Med Biol.* 2015;41(6):1500-1517. doi:10.1016/j.ultrasmedbio.2015.02.006
- [6] Bastianpillai C, Petrides N, Shah T, Guillaumier S, Ahmed HU, Arya M. Harnessing the immunomodulatory effect of thermal and non-thermal ablative therapies for cancer treatment. *Tumor Biol.* 2015;36(12):9137-9146. doi:10.1007/s13277-015-4126-3
- [7] Silvestrini MT, Ingham ES, Mahakian LM, et al. Priming is key to effective incorporation of image-guided thermal ablation into immunotherapy protocols. *JCI insight.* 2017;2(6):e90521. doi:10.1172/jci.insight.90521
- [8] MAuri GA, Nicosia luc A, Xu Z, et al. Focused ultrasound: tumour ablation and its potential to enhance immunological therapy to cancer. *Br J Radiol.* 2018;91(1083). doi:10.1259/bjr.20170641
- [9] Liu HL, Hsieh HY, Lu LA, Kang CW, Wu MF, Lin CY. Low-pressure pulsed focused ultrasound with microbubbles promotes an anticancer immunological response. *J Transl Med.* 2012;10(1):1-14. doi:10.1186/1479-5876-10-221
- [10] Zhou Y-F. High intensity focused ultrasound in clinical tumor ablation. *World J Clin Oncol.* 2011;2(1):8. doi:10.5306/wjco.v2.i1.8
- [11] Chavez M, Silvestrini MT, Ingham ES, et al. Distinct immune signatures in directly treated and distant tumors result from TLR adjuvants and focal ablation. *Theranostics.* 2018;8(13):3611-3628. doi:10.7150/thno.25613
- [12] Martins I, Wang Y, Michaud M, et al. Molecular mechanisms of ATP secretion during immunogenic cell death. *Cell Death Differ.* 2014;21(1):79-91. doi:10.1038/cdd.2013.75
- [13] Dewitte H, Verbeke R, Breckpot K, De Smedt SC, Lentacker I. Nanoparticle design to induce tumor immunity and challenge the suppressive tumor microenvironment. *Nano Today.* 2014;9(6):743-758. doi:10.1016/j.nantod.2014.10.001
- [14] van den Bijgaart RJE, Eikelenboom DC, Hoogenboom M, Fütterer JJ, den Brok MH, Adema GJ. Thermal and mechanical high-intensity focused ultrasound: perspectives on tumor ablation, immune effects and combination strategies. *Cancer Immunol Immunother.* 2017;66(66):247-258. doi:DOI 10.1007/s00262-016-1891-9
- [15] Schade GR, Wang YN, D'Andrea S, Hwang JH, Liles WC, Khokhlova TD. Boiling Histotripsy Ablation of Renal Cell Carcinoma in the Eker Rat Promotes a Systemic Inflammatory Response. *Ultrasound Med Biol.* 2019;45(1):137-147. doi:10.1016/j.ultrasmedbio.2018.09.006

# Ultrasound-mediated delivery of microRNA-126 to endothelial cells

***Stephanie He<sup>1</sup>, Davindra Singh<sup>1</sup>, Hossein Yusefi<sup>2</sup>, Brandon Helfield<sup>1,2</sup>***

<sup>1</sup>*Department of Biology, Concordia University, Montreal, Canada*

<sup>2</sup>*Department of Physics, Concordia University, Montreal, Canada*

*Corresponding author: Stephanie.He@concordia.ca*

## **Introduction**

Endothelial-specific microRNA-126 (miR-126) modulates angiogenesis through the decreased expression of two negative regulators PIK3R2 and SPRED1 [1], and is downregulated in ischemic tissue. Site-specific gene delivery with ultrasound-responsive microbubbles has demonstrated effectiveness *in vivo* as a non-viral and image-guided tool, and while previous work has shown the feasibility of miR-126 delivery with microbubbles [2], the optimal ultrasound conditions, microbubble constructs and downstream biological effects remain unexplored. Here, we present the characterization of a miR-126 loaded microbubble formulation and explore ultrasound parameters that initiate the release and delivery of pro-angiogenic miR-126 into endothelial cells while maintaining cell viability.

## **Methods**

Cationic microbubbles were synthesized by dissolving polyethyleneglycol-40 stearate, distearoyl phosphatidylcholine and 1,2-disrearoil-3-trimethylammoniumpropane (Avanti Polar Lipids) at molar ratios of 0.50:0.41:0.09 [3] in PBS with 1mM EDTA, propylene glycol and glycerol at volume ratios of 0.80:0.15:0.05. The lipid dispersion resulted in a 4 mg/ml solution to which decafluorobutane gas was added and microbubbles were created by mechanical agitation (Lantheus Vialmix). Size, concentration and stability measurements were conducted using a Coulter Counter Multisizer 4e, and the zeta potential was measured by dynamic light scattering (Malvern Zetasizer Nano ZS). Microbubbles were incubated with miR-126 for 15 minutes and were washed at 400g for 3 min prior to use. The quantification of miR-126 loading on the microbubbles was assessed by gel electrophoresis.

Human umbilical vein endothelial cells (HUVEC) were cultured in EGM-2 (Lonza) and were used from passage 4 to 9. Suspensions of miR-126-loaded microbubbles were incubated with HUVECs (50:1 microbubble to cell ratio) within a custom sonication chamber maintained at 37°C and insonicated at 1 MHz (50-250 kPa, 1k-50k cycles, duty cycles from 20-50%) for a treatment duration of 2 min. Quantification of miR-126 delivery was performed by RT-qPCR, the expression levels of PIK3R2 and SPRED1 target proteins were assessed by Western blotting, and the cell viability was evaluated via an MTT assay.

## **Results**

We formulated a stable cationic microbubble formulation measured over 80 minutes, resulting in a concentration ranging from  $1.11 \times 10^9$  to  $1.27 \times 10^9$  MB/ml and a volume-weighted mean diameter ranging from 3.1-3.4  $\mu\text{m}$ . The zeta potential yielded +38.08 mV after synthesis and +27.60 mV following miR-126 attachment. Through densitometry, we have determined a microbubble loading capacity of 6  $\mu\text{g}$  of miR-126 per  $10^9$  microbubbles. Under acoustic conditions that maintain cell viability (>90%), we were able to deliver modest amounts of miR-126 ranging from 1-1.7 fold compared to sham treatment controls, with expression levels increasing with duty cycle. For a subset of ultrasound conditions, downstream miR-126 protein targets PIK3R2 and SPRED1 exhibited decreased expression by 58% and 9%, respectively, compared to controls.

## **Conclusions**

The present work detailed a methodology to synthesize, characterize and quantify a stable, gene-loaded microbubble suitable for miRNA delivery. Our data demonstrates evidence of functional miR-126 delivery into HUVEC for therapeutic angiogenesis purposes.

**References**

- [1]. Qu, M., Pan, J., Wang, L., Zhou, P., Song, Y., Wang, S., Jiang, L., Geng, J., Zhang, Z., Wang, Y., Tang, Y. and Yang, G., 2019. MicroRNA-126 Regulates Angiogenesis and Neurogenesis in a Mouse Model of Focal Cerebral Ischemia. *Molecular Therapy - Nucleic Acids*, 16, pp.15-25.
- [2]. Cao, W., Rosenblat, J., Roth, N., Kuliszewski, M., Matkar, P., Rudenko, D., Liao, C., Lee, P. and Leong-Poi, H., 2015. Therapeutic Angiogenesis by Ultrasound-Mediated MicroRNA-126-3p Delivery. *Arteriosclerosis, Thrombosis, and Vascular Biology*, 35(11), pp.2401-2411.
- [3]. Christiansen, J., French, B., Klibanov, A., Kaul, S. and Lindner, J., 2003. Targeted tissue transfection with ultrasound destruction of plasmid-bearing cationic microbubbles. *Ultrasound in Medicine & Biology*, 29(12), pp.1759-1767.

## Acoustic Cluster Therapy (ACT®) increases blood-brain barrier permeability and enhances accumulation of core-crosslinked polymeric micelles

*Melina Mühlenpfordt<sup>1</sup>, Marieke Olsman<sup>2</sup>, Emma Bøe Olsen<sup>1</sup>, Sverre Helge Torp<sup>2,3</sup>, Spiros Kotopoulos<sup>4,5</sup>, Cristianne J.F. Rijcken<sup>6</sup>, Qizhi Hu<sup>7</sup>, Marielle Thewissen<sup>6</sup>, Sofie Snipstad<sup>7</sup>, Catharina de Lange Davies<sup>1</sup>*

<sup>1</sup>Department of Physics, Norwegian University of Science and Technology, Trondheim, Norway

<sup>2</sup>Department of Clinical and Molecular Medicine, Norwegian University of Science and Technology, Trondheim, Norway

<sup>3</sup>Department of Pathology, St. Olavs Hospital, Trondheim University Hospital, Trondheim, Norway

<sup>4</sup>National Centre for Ultrasound in Gastroenterology, Haukeland University Hospital, Bergen, Norway

<sup>5</sup>Exact Therapeutics, Oslo, Norway

<sup>6</sup>Cristal Therapeutics, Maastricht, The Netherlands

<sup>7</sup>Cancer Clinic, St. Olavs Hospital, Trondheim, Norway

\* Authors contribute equally

Corresponding author: melina.muhlenpfordt@ntnu.no

### Introduction

The restrictive nature of the blood-brain barrier (BBB) imposes a challenge for cerebral drug delivery. Acoustic Cluster Therapy (ACT®), a novel ultrasound mediated drug delivery platform, is a promising approach to circumvent the BBB (Fig. 1) [1,2]. Intravenously injected microdroplet-microbubble clusters are activated by localized insonation, forming large ACT®-bubbles. Further low intensity insonation results in controlled volume oscillation of the ACT®-bubbles, inducing biomechanical effects on the cerebral endothelium. In this study, we evaluated the effect of ACT® on the permeability of the BBB and subsequent accumulation of core-crosslinked polymeric micelles (CCPM) in the brain parenchyma.

### Methods

Fluorescently labelled CCPM were intravenously administered into mice and brains were treated with ACT®. Changes in BBB permeability were assessed using contrast-enhanced magnetic resonance imaging. Near infrared fluorescence imaging was used to measure the accumulation of CCPM in excised brains. Extravasation and penetration of CCPM into the brain parenchyma was imaged by confocal laser scanning microscopy (CLSM). Histology was used to evaluate the safety of the treatment.

### Results

In animals receiving ACT® a 1.5-fold increase in BBB permeability was observed. Near infrared fluorescence-images revealed a 3.7-fold increase in accumulation of CCPM in ACT® treated animals compared to control animals, which was further verified by CLSM showing improved extravasation and penetration of CCPM into the parenchyma. Histological analysis of ACT® treated brains showed no signs of tissue damage.

### Conclusions

ACT® transiently and locally enhanced the permeability of the BBB and facilitated local parenchymal accumulation and penetration of CCPM. These findings provide important insights into ACT® highly relevant for future clinical development using ACT® and nanomedicines to treat brain disorders.

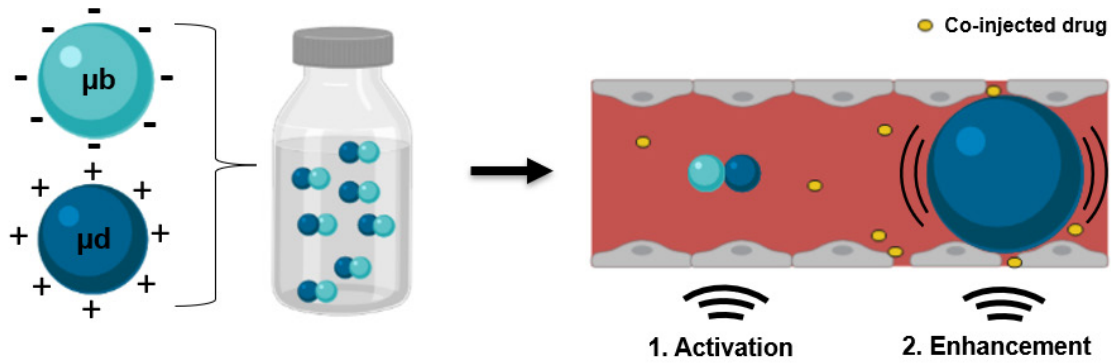


Figure 1: ACT<sup>®</sup> cluster dispersion for injection (left) and the principle of ACT<sup>®</sup> (right). Figure created with Biorender.

### References

- [1]. P. Sontum, S. Kvåle, A. Healey, R. Skurtveit, R. Watanabe, M. Matsumura, J. Ostensen. Acoustic Cluster Therapy (ACT) - A novel concept for ultrasound mediated, targeted drug delivery, *Int J Pharm*, 495 (2015) 1019-1027.
- [2]. A. Healey, P. Sontum, S. Kvåle, M. Eriksen, R. Bendiksen, A. Tornes, J. Ostensen. Acoustic Cluster Therapy: In Vitro and Ex Vivo Measurement of Activated Bubble Size Distribution and Temporal Dynamics, *Ultrasound Med Biol*, 42 (2016) 1145–1166.

# Ultra-High Speed Quantification of Cell Strain During Cell-Microbubble Interactions

*Oliver Pattinson<sup>1</sup>, Dario Carugo<sup>2</sup>, Fabrice Pierron<sup>1</sup>, Nicholas D Evans<sup>1</sup>*

<sup>1</sup>*Faculty of Engineering and Physical Sciences, University of Southampton, Southampton, U.K.*

<sup>2</sup>*School of Pharmacy, University College London, London, U.K.*

*Corresponding author: op1g15@soton.ac.uk*

## Introduction

Recent developments in microbubble-based therapies have led to a range of opportunities for their use as ultrasound-responsive drug delivery systems. Previous work has demonstrated the ability to resolve microbubble oscillations at high frequencies [1], [2], and qualitatively identify cell deformation during cell-microbubble interactions [3], [4], [5]. However, technical constraints associated with information capture at the high frequencies necessary for ultrasound-stimulated microbubble cavitation, have hindered spatially resolved quantification of cell and bubble mechanics. The mechanical response of cells not only dictates therapeutic effectiveness, but also may predict the safety and viability of microbubble treatments. Similarly, mechanical effects on the cell are of much greater importance when the applications involve a mechanosensitive process, such as in bone repair [6]. Advances in ultra-high speed imaging and the inclusion of experimental mechanics techniques presents the opportunity to accurately quantify the mechanical effects of cell-microbubble interactions. This study will explore the use of a custom designed acoustofluidic device for ultra-high speed imaging and deformation analysis, to resolve the strains experienced by a cell upon interaction with an ultrasound-activated microbubble.

## Methods

To image the complex interaction of cells and microbubbles at ultra-high speed, an acoustofluidic device was computationally modelled and developed to create an appropriate ultrasound field environment on a compact scale that maximised image resolution and magnification. Briefly, a polydimethylsiloxane (PDMS) casing was plasma bonded to a 170  $\mu\text{m}$  thick, cell culture microscopy cover glass with an inlet for a custom designed 1 MHz ultrasound transducer (Fig 1). Lipid-shelled microbubbles were manufactured via two stage sonication, following lipid film hydration. In this project, microbubbles were prepared using both 1,2-distearoyl-sn-glycero-3-phosphocholine (DSPC) and 1,2-dibehenoyl-sn-glycero-3-phosphocholine (DBPC), with the inclusion of electrostatically charged 1,2-distearoyl-sn-glycero-3-ethylphosphocholine (DSPEC) to promote microbubble attachment to cells (Table 1). MG-63, osteosarcoma cells were cultured on the cover glass for 24 hours following assembly of the device, and interaction between cells and microbubbles was initiated via inversion of the device. Ultra-high speed images were obtained using an Olympus IX-71 inverted microscope and a Shimadzu Hypervision HPV-X camera illuminated with a pulsed laser (400 W Cavitar Cavilux Smart). Upon ultrasound stimulation of the cell-microbubble layer, videos were taken at 2 and 5 million frames per second, at a magnification of 80  $\times$ . The resultant images showing oscillating microbubbles and deformation of neighbouring cells were analysed using digital image correlation (DIC) to identify deformation directions and the strain experienced throughout the cell. The effect of microbubble oscillation amplitude, driving ultrasound pressure and cell interaction methods on the strains experienced were explored to demonstrate the mechanics of cell-microbubble interactions.

**Table 1. Different microbubble formulations utilised throughout the project, and corresponding molar ratios of the microbubble shell constituents used.**

Microbubble Formulation	Microbubble Shell Constituents (Number of Moles)				
	DSPC	DBPC	PEG40s	DSPE-PEG2000	DSEPC
DBPC-Microbubbles	0	9	0	1	0
DSPC-Microbubbles	9	0	0.5	0	0

DSEPC-Microbubbles	9	0	0.5	0	2
--------------------	---	---	-----	---	---

## Results

Cell-microbubble interactions were captured inside the acousto-fluidic device at frame rates of 2 and 5 million frames per second, under 1 MHz ultrasound stimulation. Images were obtained at 80x magnification, resulting in a spatial resolution of 50 pixels across a cell of size 30  $\mu\text{m}$ . Using edge detection, a microbubble of size 9  $\mu\text{m}$  was observed to oscillate with a stable diameter change of 5.3% over a time period of 64  $\mu\text{s}$ . DIC was performed on the videos, spatially resolving the deformation and strain experienced by a cell in close proximity to the oscillating microbubble. The microbubble oscillation inflicted cell deformation mainly in a localised region, with peak deformations of  $\sim 350$  nm and peak strains of  $\sim 5\%$  (Fig. 1).

## Conclusions

The results of this study have demonstrated a new methodology with the ability to obtain a more quantitative determination of cell-microbubble interactions at ultra-high speed than previously reported. Microbubble oscillation has been time-resolved at 5 MHz frequency, with a precision of 10 nanometers. In addition, the applicability of DIC has produced complex deformation and strain patterns of a microbubble-deformed cell for the first time. This finding can give insight into the mechanoreponse of cells and membrane permeabilisation during cell-microbubble interactions.

The resultant image quality also highlights the potential to analyse various parameters of microbubble therapy, including real time mechanical results and post-treatment biological outcomes. Future work will include comparisons of the mechanical results from different interaction parameters and analysis of fluorescent drug uptake in accordance with the magnitude and spatial properties of the cell strain distribution.

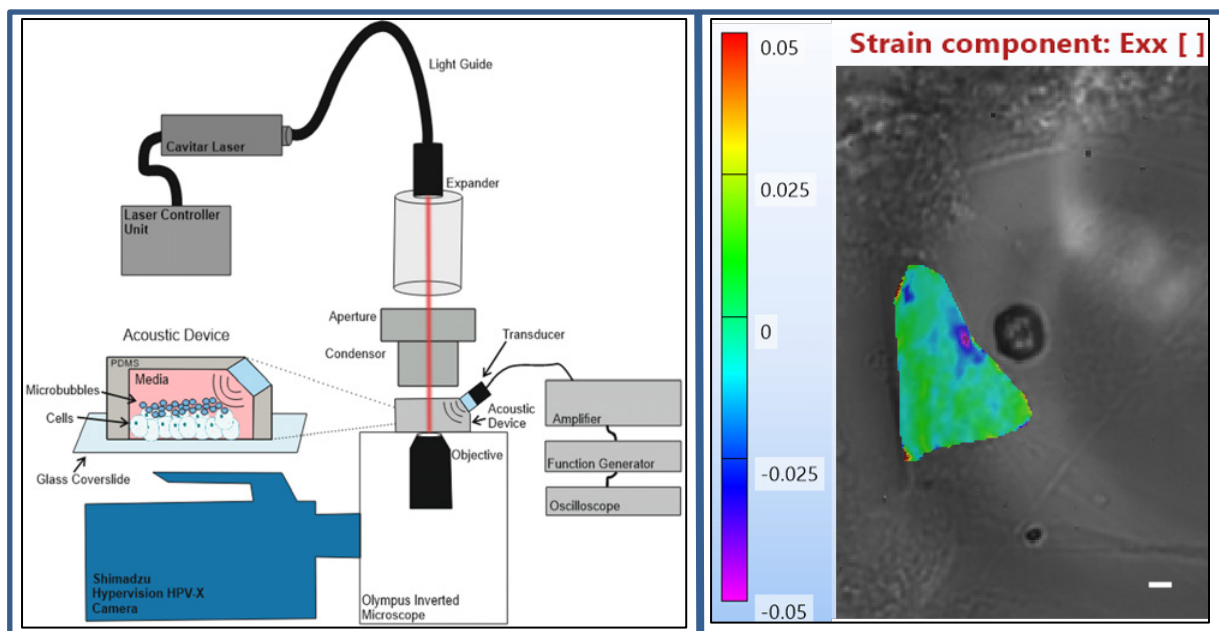


Figure 1. Schematic of the ultra-high speed imaging set up including custom design acoustofluidic device and ultrasound transducer (Left). Resultant strain map obtained using DIC on a 2 MHz video of microbubble oscillation in the presence of an MG-63 cell (coloured) at 80 x magnification, mapping strain in the horizontal direction. Scale bar = 5  $\mu\text{m}$  (Right).

## References

- [1] K. Chetty, C. A. Sennoga, J. V. Hajnal, R. J. Eckersley, and E. Stride, "High speed optical observations and simulation results of lipid based microbubbles at low insonation pressures," Proc. - IEEE Ultrason. Symp., vol. 1, no. 6, pp. 1354–1357, 2006.
- [2] I. Beekers et al., "Combined Confocal Microscope and Brandaris 128 Ultra-High-Speed Camera," Ultrasound Med. Biol., vol. 45, no. 9, pp. 2575–2582, Sep. 2019.
- [3] A. Van Wamel, A. Bouakaz, M. Versluis, and N. De Jong, "Micromanipulation of endothelial cells: Ultrasound-microbubble-cell interaction," Ultrasound Med. Biol., 2004.
- [4] A. van Wamel et al., "Vibrating microbubbles poking individual cells: Drug transfer into cells via sonoporation," J. Control. Release, vol. 112, no. 2, pp. 149–155, May 2006.
- [5] I. De Cock et al., "Ultrasound and microbubble mediated drug delivery: acoustic pressure as determinant for uptake via membrane pores or endocytosis," J. Control. Release, vol. 197, pp. 20–28, 2015.
- [6] F. Padilla, R. Puts, L. Vico, and K. Raum, "Stimulation of bone repair with ultrasound: A review of the possible mechanic effects," Ultrasonics, vol. 54, no. 5, pp. 1125–1145, 2014.

## Ultrasound-assisted intravesical chemotherapy: preliminary safety results in a dog model

*Noboru Sasaki<sup>1</sup>, Nobuki Kudo<sup>2</sup>, Kensuke Nakamura<sup>1</sup>, Mitsuyoshi Takiguchi<sup>1</sup>*

<sup>1</sup>*Faculty of Veterinary Medicine, Hokkaido University, Sapporo, Japan*

<sup>2</sup>*Faculty of Information Science and Technology, Hokkaido University, Sapporo, Japan*

*Corresponding author: n.sasaki@vetmed.hokudai.ac.jp*

### Introduction

Bladder cancer is the second most common urological cancer, and almost 70% are non-muscle invasive bladder cancer (NMIBC) at the initial diagnosis. The standard therapy for NMIBC is transurethral resection of visible tumor, followed by intravesical Bacillus Calmette-Guérin (BCG) therapy or intravesical chemotherapy. However, 50-70% of patients relapse within 5-year and up to 30% of those progress to muscle invasive cancer [1]. In addition, current shortage of BCG requires alternative intravesical therapy [2]. Ultrasound-triggered microbubble cavitation may have potential for enhancing the efficacy of intravesical chemotherapy for NMIBC. Intravesical instillation enables microbubbles to directly attach to tumor cells lining the surface of bladder tumor. Stimulation of those microbubbles adjacent to tumor cells may directly enhance the cellular uptake of chemotherapeutic agents. Moreover, US-triggered microbubble cavitation may increase penetration of drugs in tumor, and thus enhance concentration gradient-motive diffusion into tumor cells. Meanwhile, an increase in the permeability of the bladder by US-triggered microbubble cavitation may change pharmacokinetics of drugs in the blood. An advantage of intravesical chemotherapy is that cytotoxic agents are applied to only bladder lumen and not to normal tissues. Therefore, it is critical for the development of US-assisted intravesical chemotherapy to restrict the effects of chemotherapeutic agents to the bladder. In this study, we evaluated the safety of the combination of US-triggered microbubble cavitation and intravesical chemotherapy.

### Methods

Three healthy female beagle dogs were used in this preliminary safety study. The median body weight of the dogs was 10.25 kg (range 9.7-11.2 kg). All animal experiment was approved by the Experimental Animals Committee of Hokkaido University (No. 20-0081). Pirarubicin (4'-O-tetrahydropyranyldoxorubicin), an anthracycline derivative, was chosen as an intravesical therapeutic agent. Pirarubicin (10mg) in 20mL saline and 0.1 mL Sonazoid® microbubbles (Daiichi-Sankyo, Tokyo, Japan) were administrated into bladder via an indwelling catheter. Right after the administration, ultrasound was exposed to the bladder for 1 min (Fig. 1). The mixture of pirarubicin and microbubbles was removed from the bladder 30 min after the US exposure, and the bladder was washed 3 times using a 0.9% sodium chloride irrigation.

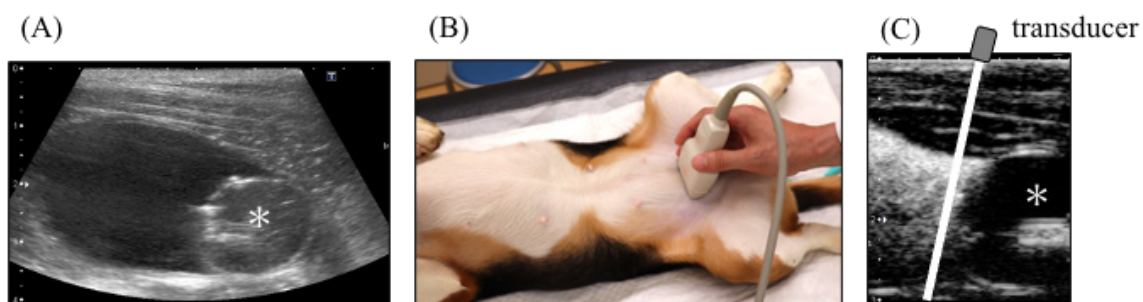


Figure 1. Images of ultrasound-assisted intravesical chemotherapy. (A) An ultrasound image after pirarubicin instillation. \* indicates the tip of the catheter. (B) Transducer position during the treatment. (C) An ultrasound image of after microbubble instillation. White line indicates the scan plane of ultrasound during the treatment. \* indicates the tip of the catheter.

Ultrasound exposure was performed using a linear array scanner (PLT-704SBT, Canon Medical Systems, Tochigi, Japan) and a diagnostic US machine (APLIO XG SSA-790, Canon Medical Systems). The scanner was operated in a pulse subtraction imaging mode. The field of view depth was set to 2 cm and a single focus was placed at a depth of 1 cm from the scanner surface. Acoustic parameters were as follows; the transmitting frequency of 5 MHz, the peak-negative pressure of -1.2 MPa, the pulse duration of 0.44  $\mu$ sec, and the pulse repetition frequency of 7.7 kHz.

For the measurement of pirarubicin concentration in plasma, blood was collected 15, 30 min, 1, 2, 4, 8, and 24 hr after the instillation. In order to assess the bladder mucosa soon after the treatment, another treatment was conducted four weeks after the first treatment. The sonicated region of bladder wall and the apex of the bladder (non-sonicated region) were dissected into two pieces, respectively. One piece was fixed in 10% neutral buffered formalin for the histopathological evaluation, and the other was stored in -80°C for the quantification of pirarubicin in the bladder tissue. Pirarubicine was quntified using an Agilent 6495B Triple Quadrupole LC/MS (Agilent Technologies, Santa Clara, CA, USA).

## Results

Plasma concentration of intravesically instilled pirarubicine was lower than the detection limit in all samples (Fig. 1). Hematoxylin and eosin staining did not show any observable changes in the bladder mucosa at sonicated region. Table 1 shows the tissue concentration of pirarubicin after the theatment. In two dogs, tissue pirarubicin of sonicated region was higher than that of non-sonicated region. However, the average concentration of pirarubicin was not statistically different between sonicated region and non-sonicated region (pared *t*-test, *p* = 0.09).

**Table1. Plasma concentration of intravesical pirarubicin.**

	15 min after	30 min after	1 hr after	2 hr after	4 hr after	8 hr after	24 hr after
<b>intravesical instillation</b>	< 0.5 ng/mL	< 0.5 ng/mL	< 0.5 ng/mL	< 0.5 ng/mL	< 0.5 ng/mL	< 0.5 ng/mL	< 0.5 ng/mL
<b>intravesical instillation &amp; US-triggered microbubble cavitation</b>	< 0.5 ng/mL	< 0.5 ng/mL	< 0.5 ng/mL	< 0.5 ng/mL	< 0.5 ng/mL	< 0.5 ng/mL	< 0.5 ng/mL

**Table2. Pirarubicin concentration in the bladder tissue.**

	Dog 1	Dog 2	Dog 3
<b>non-sonicated region</b>	0.21 $\mu$ g/g-tissue	0.21 $\mu$ g/g-tissue	1.04 $\mu$ g/g-tissue
<b>sonicated region</b>	1.65 $\mu$ g/g-tissue	0.19 $\mu$ g/g-tissue	2.43 $\mu$ g/g-tissue

## Conclusions

Ultrasound-triggered microbubble cavitation may be a safe method for local delivery of chemotherapeutic agents in the bladder. An efficacy of the treatment would be evaluated in a future clinical study.

## References

- [1]. Eifler JB, Scarpato KR, Clark PE, Management of noninvasive bladder cancers, *Current Opinion in Oncology*, 27: 185-190, 2015.
- [2]. Fankhauser CD, Teoh JYC, Mostafid H, Treatment options and results of adjuvant treatment in nonmuscle-invasive bladder cancer (NMIBC) during the Bacillus Calmette-Guérin shortage, *Current Opinion in Urology*, 30: 365-369, 2020.

## On the size dependency of sonoporation efficiency: a monodisperse microbubble study

***Benjamin Van Elburg*<sup>1\*</sup>, *Joke Deprez*<sup>2\*</sup>, *Guillaume Lajoinie*<sup>1</sup>, *Stefaan C. De Smedt*<sup>2</sup>,  
*Michel Versluis*<sup>1</sup>, *Ine Lentacker*<sup>2#</sup>, *Tim Segers*<sup>1#</sup>**

<sup>1</sup>*Physics of Fluidics Group, University of Twente, Enschede, The Netherlands*

<sup>2</sup>*Ghent Research Group on Nanomedicines, Laboratory of General Biochemistry and Physical Pharmacy, Ghent University, Ghent, Belgium*

<sup>3</sup>*BIOS Lab-on-a-Chip Group, Max-Planck Center for Complex Fluid Dynamics, MESA+ Institute for Nanotechnology, University of Twente, Enschede, The Netherlands*

Corresponding author: [b.vanelburg@utwente.nl](mailto:b.vanelburg@utwente.nl)

\*, # Both authors contributed equally

### Introduction

Ultrasound in combination with ultrasound contrast agents (UCA) can be used for both diagnostic and therapeutic applications [1]. A therapeutic implementation is sonoporation, where drug delivery into the cell is enhanced by a mechanical stimulus, or the formation of pores in the cell membrane induced by volumetric oscillations of the microbubbles. Microbubbles resonate to the driving ultrasound field, where the resonance frequency is inversely proportional to the microbubble size. At resonance, the amplitude of oscillation is at maximum and therefore, it is expected that the sonoporation efficiency is at maximum for resonantly driven microbubbles [2]. In order to demonstrate the sonoporation size-dependency we utilize monodisperse microbubble suspensions with radii ranging from 2 to 6  $\mu\text{m}$  and a single insonifying ultrasound frequency of 1 MHz. The sonoporation efficiency was characterized through the uptake patterns of FITC-dextran [3]. Microbubble resonance was investigated with ultra-high-speed imaging at 10 million frames/s.

### Methods

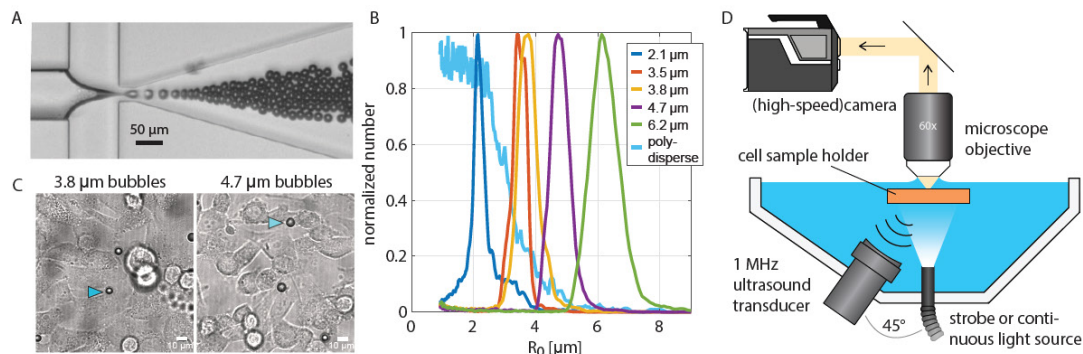


**Figure 1. A) Monodisperse microbubble formation in a flow focusing device. B) By controlling the liquid and gas flow rates monodisperse microbubble suspensions with different mean radii were produced. C) Monodisperse microbubbles floating against the confluent cell layer before ultrasound exposure. D) Schematic of the setup employed to record bubble oscillations.**

Polydisperse microbubbles were also prepared, namely by vigorously shaking (Capmix) a vial filled with an aqueous lipid mixture comprising DSPC and DPPE-PEG5000 mixed at a 9:1 molar ratio. Monodisperse microbubbles were filled with a gas-mixture (13 v%  $\text{C}_4\text{F}_{10}$  in  $\text{CO}_2$ ) as described in [2] and coated using the same phospholipid mixture as used for the polydisperse bubbles. The monodisperse bubbles were formed in a flow-focusing device exactly as described in [4], and as displayed in Figure 1A. Different bubble sizes (Figure 1B) were obtained by controlling the gas and liquid flow-rate as described by van Elburg *et al.* [5].

For the sonoporation experiments, Bowes Lung Metastasis (BLM) cells were seeded in Lumox dishes. After reaching full confluency, microbubbles (mono- or polydisperse, see Fig. 1C) and FITC-dextran (4 kDa or 2 MDa) were added to the cells. Subsequently, the Lumox dish was inverted, immersed into a

water tank (Fig. 1D) and exposed to a single ultrasound burst of 1000 cycles with a frequency of 1 MHz, and at acoustic pressure amplitudes of either 500 kPa or 750 kPa. After insonation, the exposed area was cut out of the Lumox dish and the cells were harvested for flow cytometry, where the efficiency of sonoporation was evaluated as described in [3].

For the optical bubble dynamics characterization experiments, a Lumox dish was coated with a 50  $\mu\text{m}$  thick cell-layer-mimicking polyacrylamide hydrogel. Polydisperse microbubbles were diluted such that the bubble spacing was at least 20 bubble radii, a similar concentration as used during the sonoporation experiments. The microbubble dynamics was recorded with an ultra-high-speed camera (Shimadzu HPV-X2) operated at 10 Mfps. The bubbles were exposed to 1 MHz frequency ultrasound bursts of 10 cycles at an acoustic pressure amplitude of 500 kPa. Radius-time curves were obtained from automated image analysis in MATLAB where the bubble size was measured from the inflection point of the angle-averaged intensity profile of the bubble. The amplitude of oscillation was obtained from the Fourier-transformed amplitude spectrum.

## Results

The FITC-dextran uptake induced with the different microbubble suspensions is plotted in Fig. 2A. Monodisperse microbubbles with a radius of 4.7  $\mu\text{m}$  showed the highest sonoporation efficiency, i.e., 4 times higher than that for the polydisperse bubbles, while both smaller and larger bubbles showed a decrease in efficiency. The radial amplitude of oscillation of the microbubbles is shown in Fig. 2B. Note that the amplitude of oscillation is highest for microbubbles of a size between 1.5 and 4.5  $\mu\text{m}$  in radius, while the radial amplitude quickly decreases for bubbles larger than 4.5  $\mu\text{m}$ . Remarkably, the trends observed in Fig. 2A and B do not match. While bubbles smaller than 4  $\mu\text{m}$  in radius are observed to oscillate at a similar amplitude of oscillation and therefore, in a simplified linear picture, are expected to exert equal shear-stress, we observe a strong increase in sonoporation efficiency with bubble radius up to a radius of 4.7  $\mu\text{m}$ . Thus, the results indicate that sonoporation efficiency is not governed by the oscillation amplitude *alone*. Therefore, another mechanism besides the oscillation amplitude is expected to contribute to sonoporation efficiency. Candidates may include the length scale over which the bubble interacts with the cell layer and the strain or strain-rate of the cell membrane induced by the bubble oscillations. The present results highlight the need for a more thorough physical understanding of microbubble-cell interaction.

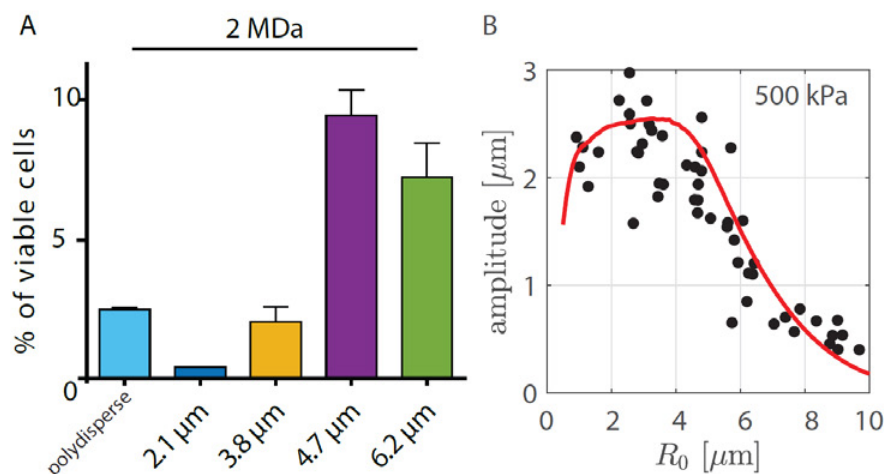


Figure 2. A) Sonoporation percentage of the live cells exposed to ultrasound. The large 4.7- $\mu\text{m}$ -radius bubble results in the highest sonoporation percentage. B) The radial amplitude of oscillation of microbubbles at 500 kPa acoustic driving and characterized by high-speed imaging. Note that bubbles smaller than 4  $\mu\text{m}$  in radius oscillate at the largest amplitude of oscillation. The red line is a guide to the eye obtained from a Rayleigh-Plesset simulation.

## Conclusions

Monodisperse microbubbles show a significant increase in sonoporation efficiency compared to polydisperse microbubbles. Surprisingly, the maximum radial amplitude of oscillation does not correlate with sonoporation percentage. This result suggests that sonoporation efficiency cannot be predicted by microbubble resonance alone.

## References

- [1] S. Roovers, J. Deprez, D. Priwitaningrum, G. Lajoinie, N. Rivron, H. Declercq, O. De Wever, E. Stride, S. Le Gac, M. Versluis, J. Prakash, S. C. De Smedt & I. Lentacker. Sonoprinting liposomes on tumor spheroids by microbubbles and ultrasound. *J.Control Release*. 316(October), 79–92 (2019).
- [2] B. Helfield, X. Chen, S. C. Watkins & F. S. Villanueva. (2016). Biophysical insight into mechanisms of sonoporation. *Proceedings of the National Academy of Sciences*, 113(36), 9983-9988.
- [3] I. De Cock, E. Zagato, K. Braeckmans, Y. Luan, N. de Jong, S. C. De Smedt, I. Lentacker. (2015). Ultrasound and microbubble mediated drug delivery: acoustic pressure as determinant for uptake via membrane pores or endocytosis. *Journal of controlled release*, 197, 20-28.
- [4] T. Segers, E. Gaud, M. Versuis & P. Frinking. High-precision acoustic measurements of the nonlinear dilatational elasticity of phospholipid coated monodisperse microbubbles. *Soft Matter*. 14(47), 9550–61 (2018).
- [5] B. van Elburg, G. Collado-Lara, G. Bruggert, T. Segers, M. Versluis, G. Lajoinie. Feedback-controlled microbubble generator producing one million monodisperse bubbles per second. *Review of Scientific Instruments*. 92 (2021).

## The 27<sup>th</sup> European Symposium on Ultrasound Contrast Imaging Rotterdam is sponsored by:

### ***Bracco Suisse SA***

Marco Graf, Senior  
Communication Events Manager  
Cadempino, Switzerland

### ***Mindray Medical Germany GmbH***

Hongbo Zhu  
Marketing Ultrasound Europe  
Darmstadt, Germany

### ***Erasmus University MC - Thorax Center***

Prof.dr. Felix Zijlstra,  
Head of the department  
Rotterdam  
The Netherlands

### ***Siemens Healthineers***

Helen Cleminson  
SHS US IN ADGI  
United Kingdom

### ***GE Healthcare***

Christopher (Scott) Lee  
Product Leader – Optison  
Missouri USA

### ***Samsung Medison***

Luc van Dalen, account  
manager HME of the  
Samsung Electronics Benelux

### ***Philips Healthcare***

Radjen Ganpat  
Senior Field Marketing  
General Imaging Ultrasound  
Eindhoven, The Netherlands

### ***Verasonics, Inc***

Sara Shager  
Marketing and Sales Associate  
Kirkland, WA

### ***Oldelft Ultrasound***

Stefan Roggeveen  
Commercial Manager  
Delft, the Netherlands

### ***Fujifilm VisualSonics***

Adrie Gubbels, Sales Manager  
Visualsonics  
Amsterdam, the Netherlands

### ***Solstice Pharmaceutic Managing directorals***

Wim van Hoeve, Sales Manager  
Enschede, the Netherlands

# Sponsors:

## Golden sponsor



GE Healthcare



SIEMENS  
Healthineers

## Silver sponsor

**mindray**  
healthcare within reach

**SAMSUNG**



 **Solstice**  
pharmaceuticals

**PHILIPS**

 **Oldelft**  
Ultrasound

**FUJIFILM**  
VISUALSONICS

 **Verasonics**<sup>®</sup>  
The leader in Research Ultrasound™

# The 27<sup>th</sup> European Symposium on Ultrasound Contrast Imaging, Rotterdam is sponsored by:



LIFE FROM INSIDE

GE Healthcare



Verasonics®  
The leader in Research Ultrasound™

 Solstice  
pharmaceuticals

Erasmus MC

*Erasmus*

THORAX CENTRUM

FUJIFILM  
VISUAL SONICS

SAMSUNG

mindray  
healthcare within reach

PHILIPS

SIEMENS  
Healthineers